UNIVERSIDADE FEDERAL DE UBERLÂNDIA
FACULDADE DE ENGENHARIA QUÍMICA
Programa de Pós-Graduação em Engenharia Química

Study of catalysts for the hydrodeoxygenation reaction of phenol

Estudo de catalisadores para a reação de Hidrodesoxigenação do fenol

Karen Abreu Resende

Uberlândia – MG

2017

UNIVERSIDADE FEDERAL DE UBERLÂNDIA
FACULDADE DE ENGENHARIA QUÍMICA
Programa de Pós-Graduação em Engenharia Química

Study of catalysts for the hydrodeoxygenation reaction of phenol

Estudo de catalisadores para a reação de Hidrodesoxigenação do fenol

Karen Abreu Resende

Orientadora: Profª. Dra. Carla Eponina Hori
Co-orientador: Dr. Fábio Bellot Noronha

Tese submetida ao Programa de Pós-Graduação em Engenharia Química da Universidade Federal de Uberlândia como parte dos requisitos necessários à obtenção do título de Doutor em Engenharia Química, área de concentração em Pesquisa e Desenvolvimento de Processos Químicos.

Uberlândia - MG
2017

Dados Internacionais de Catalogação na Publicação (CIP)
Sistema de Bibliotecas da UFU, MG, Brasil.

R433s
2017

Resende, Karen Abreu, 1989-
Study of catalysts for the hydrodeoxygenation reaction of phenol / Karen Abreu Resende. - 2017.
209 f. : il.

Orientadora: Carla Eponina Hori.
Coorientador: Fábio Bellot Noronha
Tese (doutorado) -- Universidade Federal de Uberlândia, Programa de Pós-Graduação em Química.
Disponível em: http://dx.doi.org/10.14393/ufu.te.2017.6
Inclui bibliografia.

1. Engenharia química - Teses. 2. Fenóis - Teses. 3. Termodinâmica - Teses. 4. Nióbio - Teses. I. Hori, Carla Eponina. II. Noronha, Fábio Bellot. III. Universidade Federal de Uberlândia. Programa de Pós-Graduação em Química. IV. Título.

CDU: 66.0

TESE DE DOUTORADO SUBMETIDA AO PROGRAMA DE PÓS-GRADUAÇÃO EM ENGENHARIA QUÍMICA DA UNIVERSIDADE FEDERAL DE UBERLÂNDIA COMO PARTE DOS REQUISITOS NECESSÁRIOS PARA OBTENÇÃO DO TÍTULO DE DOUTOR EM ENGENHARIA QUÍMICA, EM 11 DE AGOSTO DE 2017.

BANCA EXAMINADORA

Profª. Drª. Carla EponinaHori
Orientadora (PPGEQ/UFU)

Fabio Bellot Noronha
Dr. Fábio Bellot Noronha
Coorientador (INT)

Lucienne L. Romanielo
Profª. Drª. Lucienne Lobato Romanielo
(PPGEQ/UFU)

Dr. Marco André Fraga
(INT)

Sandra C. Dantas
Profª. Drª. Sandra Cristina Dantas
(ICTE/UFTM)

Prof. Dr. Victor Luis dos Santos Teixeira da Silva
(PEQ/COPPE/UFRJ)

Agradecimentos

Esse trabalho foi realizado ao longo dos últimos quatro anos, e é o resultado do esforço em conjunto de muitas pessoas. Tenho muito a agradecer aos meus orientadores Carla Eponina Hori e Fábio Bellot Noronha que se dedicaram com muito afinco para a realização desse trabalho. Eles estiverem presentes em todos os momentos e sempre me ajudaram a buscar um alto grau de excelência. A Prof. Carla Eponina Hori agradeço por toda a amizade e por sempre investir em mim desde a iniciação cientifica. Tenho a agradecer não apenas por todas as horas de dedicação, mas também pela confiança, pelos conselhos e por sempre representar um exemplo a ser seguido. Igualmente importante, também tenho muito há agradecer ao meu orientador Fábio Bellot Noronha, que apesar da distância sempre se fez muito presente, ajudando com a parte experimental e também com orientações essenciais. A sua determinação e grau de exigência é um grande exemplo a ser seguido. Obrigado, por me aceitar no seu grupo e me permitir trabalhar com pessoas tão inspiradoras. Aqui se fecha um ciclo e surgem novas possibilidades.

Gostaria de agradecer aos meus pais: Maria Lúcia e Péricles por todo o suporte que eles me deram durante toda a minha vida acadêmica. Afinal de contas, dentre todas as escolhas que eles tiveram na vida, eles optaram por me propiciar essa família maravilhosa que nós somos. Também tenho muito a agradecer a minha irmã Milena, o seu apoio me ajudou muito na realização desse trabalho.

Gostaria de agradecer ao Professor Johannes Lecher por ter me recebido no seu grupo no PNNL durante 1 ano. Essa experiência me proporcionou grandes oportunidades de aprendizagem. Também tenho muito a agradecer a todos do grupo nos EUA que me acolheram e sempre me ajudaram: Don Camaioni, John Fulton, Zizwe, Meng Wand and Hui Shi. Em especial, ao Hui Shi que me ajudou muito com todo o experimental, discussão dos resultados e me orientou na construção desse trabalho. Tenho muito a agradecer aos amigos que fiz nos EUA, que durante esse ano se tornaram inesquecíveis: Dana, Hyejung, Raea, Patrick, Marton, Sebastian, Zbyněk e Richard, em especial ao Mohamed, que me ajudou muito durante toda a realização desse trabalho.

Também tenho muito a agradecer ao grupo do Rio de Janeiro, que sempre me receberam muito bem e me ajudaram com todo o experimental. Quero agradecer principalmente a Camila, Priscilla, Adriana, Cris e a Erika. Obrigada por discutir os resultados comigo, por me auxiliarem com o experimental e principalmente com as minhas estádias no Rio.

Agradeço ao Adriano Braga por me ajudar com as caracterizações da última série dos catalisadores e principalmente por me ajudar a tratar e discutir os resultados. Também agradeço ao pessoal do LNLS pelo suporte nas análises realizadas, especialmente a Daniela Coelho por ter me ensinado muito sobre XPS e a Ameli pela orientação no tratamento de dados de XANES e EXAFS.

Tenho muito a agradecer aos amigos do laboratório de Uberlândia, que se tornaram amigos para a vida. Rondi, Letícia, Rafinha, Sarah, Dyovani, Lucas, Thalles, Carol. Vocês fizeram e fazem a vida no laboratório muito mais alegre. São amigos que eu sempre posso contar. Também quero agradecer aos amigos que sempre me ajudaram muito a lidar com todo o stress emocional do doutorado, Jessika, Diego e Ana Carolina muito obrigada por serem amigos tão especiais. Também quero agradecer ao Rafael que apesar do pouco tempo de convívio é um grande companheiro.

Gostaria de agradecer ao CNPq pela bolsa de doutorado e também pelo auxílio para realizar parte desse trabalho nos EUA.

As palavras nunca serão suficientes para agradecer a todos da maneira que vocês merecem. Porém, mesmo assim deixo meu muito OBRIGADA!!

SUMMARY

LIST OF FIGURES

TABLE LIST

ABSTRACT

The conversion of biomass into bio-oil through fast pyrolysis followed by its upgrading via hydrodeoxygenation (HDO) is considered a potential route for the production of renewable fuels. The present work aimed to develop new catalysts for the hydrodeoxygenation (HDO) of phenol, which is a typical bio-oil model compound. The work section was divided in 5 independent chapters: (i) a thermodynamic study in order to determine the most favorable operational conditions for the HDO of phenol. According to this study when methane was added to the system, the equilibrium composition calculated indicated only the formation of methane for all the conditions evaluated. However without CH_4, the best operational conditions to perform the phenol HDO reaction are at intermediate temperatures and with high H_2/phenol ratio; (ii) In sequence, the effect of to the addition of a second metal (Cu, Ag, Zn, Sn) on the performance of Pd/ZrO_2 catalyst for HDO of phenol in the gas phase was studied. The incorporation of dopants to Pd/ZrO_2 resulted in the formation of Pd–X (Cu, Ag, Zn) alloys, which reduced the reaction rate for HDO and increased the selectivity to hydrogenation products (cyclohexanone and cyclohexanol). However, the oxophilic sites generated by Sn cations promoted the hydrogenation of the carbonyl group of the keto-tautomer intermediate formed, producing benzene as the main product; (iii) The impact of particle size of ZrO_2-supported Pd and of alloying with Ag was explored for hydrogenation of phenol in aqueous phase. This study was performed during an internship at PNNL (Pacific Northwest National Laboratory). Kinetic assessments were performed in a batch reactor, on monometallic Pd/ZrO_2 samples with different Pd loadings (0.5%, 1% and 2%), as well as on a 1% PdAg/ZrO_2 sample. In general, the lower activity of the small Pd particles was attributed to low activation entropies for the strongly bound species and the presence of Ag increases catalyst activity by decreasing the apparent energy of activation and increasing the coverages of phenol and H_2, without negatively affecting the transition entropy; (iv) After that, based on the recent insides reported about the HDO reactions, the hydrodeoxygenation of phenol was studied using Rh, Pd and Ni catalysts supported on Nb_2O_5. This part allowed understanding how the SMSI (strong metal-support interaction) affects the selectivity of the HDO reaction. In general, an increase in the reduction temperature favored benzene selectivity, all the samples showed selectivity of approximately 95% for benzene for high reduction temperatures; (v) In the final chapter of this work the effect of doping cerium oxide support with niobium was investigated for HDO of phenol at 573K in the gas phase. The incorporation of niobium altered the lattice parameters of cerium based oxides, favored the reduction of the cerium and increased the selectivity to deoxygenated products (benzene). Small amounts of niobium affected the surface area of the support and promoted the formation of more dispersed nickel particles, which disfavored the hydrogenolysis of benzene. In general, the data presented in this thesis contributed to a better understanding of the HDO reaction.

Keywords: hydrodeoxygenation, phenol, bimetallic, thermodynamics, niobium, oxides.

RESUMO

O processo de conversão da biomassa em bio-óleo através da pirólise rápida seguida do melhoramento do produto final por meio da reação de hidrodesoxigenação (HDO) é considerada uma importante via para a produção de combustíveis renováveis. O presente trabalho teve como objetivo desenvolver novos catalisadores para serem aplicados na reação de HDO do fenol (típico modelo do bio-óleo). O trabalho foi dividido em 5 capítulos independentes: (i) No primeiro capitulo realizou-se um estudo termodinâmico para determinar as condições operacionais mais favoráveis para realizar a reação de HDO do fenol. De acordo com este estudo, quando o metano é adicionado ao conjunto de compostos presentes no sistema, a composição de equilíbrio indica apenas a formação de CH_4, independente das condições avaliadas. No entanto, sem CH_4, as melhores condições operacionais para a realização da reação de HDO do fenol são com temperaturas intermediárias e uma alta relação H_2/fenol; (ii) Em sequência, estudou-se o efeito da adição de um segundo metal (Cu, Ag, Zn, Sn) no desempenho catalítico da amostra Pd/ZrO_2 na reação de HDO realizada na fase gasosa. A incorporação de dopantes resultou na formação de ligas Pd-X (Cu, Ag, Zn), que reduziram a taxa reacional e aumentaram a seletividade para produtos hidrogenados (cicloexanona e cicloexanol). No entanto, os sítios oxofílicos gerados pela presença dos cátions Sn promoveram a hidrogenação do grupo carbonila do intermediário ceto-tautômero, produzindo benzeno como o principal produto; (iii) Em sequência, explorou-se o impacto do tamanho da partícula de Pd suportada em ZrO_2 e o efeito da formação de liga entre o Pd e a Ag para a reação de hidrogenação do fenol em fase aquosa. Este estudo foi realizado durante um estágio no PNNL (Pacific Northwest National Laboratory). O estudo cinético foi realizado em um reator batelada, utilizando amostras de Pd/ZrO_2 com diferentes teores de Pd (0,5%, 1% e 2%), bem como em uma amostra de $PdAg/ZrO_2$. Em geral, as partículas de Pd menores apresentaram uma menor atividade, o que foi atribuída à baixa entropia de ativação das espécies fortemente ligadas nas partículas menores. A presença de Ag aumentou a atividade do catalisador, diminuindo a energia aparente de ativação e melhorando a cobertura de fenol e H_2, sem afetar negativamente a entropia das moléculas de transição; (iv) Com base nos estudos recentes reportados na literatura, a reação de HDO foi estudada utilizando catalisadores de Rh, Pd e Ni suportados em Nb_2O_5. Esta parte do trabalho permitiu entender como o efeito SMSI (forte interação metal-suporte) afeta a seletividade da reação. Em geral, um aumento na temperatura de redução favoreceu a seletividade do benzeno e todas as amostras apresentaram seletividade de aproximadamente 95% para esse composto; (V) No capítulo final deste trabalho, o efeito causado pela adição de Nb na estrutura do óxido de cério foi investigado para HDO de fenol na fase gasosa. A incorporação de nióbio alterou os parâmetros da rede de óxidos à base de cério, favoreceu a redução do Ce e aumentou a seletividade para os produtos desoxigenados (benzeno). Pequenas quantidades de nióbio afetaram a área superficial do suporte e promoveram a formação de partículas de níquel mais dispersas, que desfavoreceram a hidrogenólise do benzeno. Em geral, os dados apresentados nesta tese contribuíram para uma melhor compreensão da reação de HDO.

Palavras chaves: hidrodesoxigenação, fenol, bimetálicos, termodinâmica, nióbio, óxidos.

1.CHAPTER I

1.1. Introduction

The bio oil obtained from pyrolysis usually has an energy content that is nearly half of petroleum due to extremely high oxygen contents in the range 35–40 wt% [1]. Thus, the direct applications of the bio oil are limited also due to its high viscosity, high water and ash contents, low heating values, solid content, chemical instability, and high corrosiveness. Despite of the bio oil short coming properties it has some promising characteristics, such as less toxicity, good lubricity and greater biodegradation than petroleum fuels [2-4]. In general, the bio oil obtained from biomass pyrolysis is a complex mixture of reactive compounds. The average composition of pyrolysis oils is around 55wt% organic components, that include organic acids, ketones, phenolic compounds, furans, syringols, guaiacols and others compounds, 15–30wt% water and 20wt% lignin fraction. Phenolic compounds represent the major part of the lignin fraction of the bio oil [5,6], which explains the use of these reagents as model compounds of bio oil [7].

In order to specifically convert bio oils into valuable fuels, the hydrodeoxygenation (HDO) reactions have been investigated intensively in the last decade [3]. HDO of bio oil involves the presence of a catalyst and hydrogen at moderate temperatures. The oxygen is removed from the molecules to form water. According to Bu et al. [4] the overall reaction stoichiometry of HDO may be schematically represented by the follow equation:

$$-(CH_2O)- + H_2 \rightarrow -(CH_2)- + H_2O \qquad \textbf{1.1}$$

The HDO reaction may be performed in gas or liquid phase, however the liquid treatments have some disadvantages, such as, the consumption of solvent, the cost of high pressure equipment and the difficulties to separate catalyst, char, products, solvent and non-reacted lignin from the reaction media [5]. In this work, all the catalytic system studied was tested in the HDO reaction in the gas phase using phenol as a model compound. The HDO reaction in a liquid phase was evalued with one catalytic system also using phenol as a model compound.

The HDO reaction is considered a bifunctional mechanism that requires a metallic site for hydrogenation/dehydrogenation as well as an oxophilic site that adsorbs the oxy compound. Conventional sulfide catalysts used for petroleum hydroprocessing and precious metal catalysts have been studied for their reactivity in model oxygenate compound HDO [3,6]. Tan et al. [13] showed that on a strong oxophilic metal, the direct deoxygenation is the favorable path, while on weaker oxophilic metals such as Pt, the direct deoxygenation become less favorable and the tautomerization-hydrogenation-dehydration mechanism is the favorable path. The addition of a second metal is often found to induce variations in both catalytic and adsorptive properties [14]. For example, Cu improved the activity of Ni-based catalysts during HDO of guaiacol [15]. Similarly, bimetallic PdFe/C exhibited a significantly enhanced HDO activity compared to Fe/C in the conversion of guaiacol [16]. In general, there are several ways that oxygen can be removed from the compounds that are found in bio oil, such as phenol. One pathway is direct hydrodeoxygenation (direct deoxygenation, DDO), which leads to the formation of aromatics and water. Another is hydrogenation of the phenolic ring followed by dehydration to form cyclohexene derivatives [8]. Also there is the tautomerization path [9-12].

The choice of carrier material is an important aspect of catalyst formulation for HDO, as it has the potential to influence the activity and selectivity observed during the deoxygenation of bio oil model compounds over metallic catalysts [17]. Particularly interesting results have been observed over reducible metal oxides such as TiO_2, and CeO_2, where deoxygenation is hypothesized to involve oxygen vacancies [18].The reducible metal oxide supports may contribute to the deoxygenation of model bio oil compounds.

In the present study, phenol is chosen as model compound for hydrodeoxygenation because the bio oil has a relatively high concentration of phenolic compounds. Pd bimetallic samples supported on ZrO_2 were studied iniciallty to evalued if the alloy formation favored the stability of the samples in the HDO reaction. This study was based on a previus works from the group that showed Pd samples supported on ZrO_2 as a potencial support for the HDO reaction in a gas phase. In sequence these samples also were studied in the liquid phase, aiming to evalued the kinetic of the hydrogenation of phenol. The recent literature indicated the important role of the support in the HDO reaction. Then, in the next part, we studied transition metal supported on niobium and cerium oxides. In this second part of the work we are aiming to study the activity, selectivy and estabiliy of these samples in the HDO reaction.

1.2. Structure of dissertation

This doctoral dissertation is divided in additional 8 chapters, as described below:

1.2.1. Chapter II- Literature Review

A small overview of phenol HDO reaction mechanism, metals and supports used.

1.2.2. Chapter III – Experimental Part

A description of materials, catalyst preparation, characterization/analytical methods, and the experimental setups used for all the chapters on this doctoral thesis.

1.2.3. Chapter IV – Thermodynamic Analysis of the hydrodeoxygenation reaction of phenol in gas phase

The thermodynamics analysis of the HDO reaction of phenol was performed. was and then related to experimental tests of gas phase phenol HDO over 5%Ru/ZrO_2 and 2%Pd/ZrO_2catalysts.

1.2.4. Chapter V – Hydrodeoxygenation of phenol over zirconia supported Pd bimetallic catalysts: The effect of second metal on catalyst deactivation

In sequence, the HDO of phenol over bimetallic Pd catalysts supported on ZrO_2 (PdAg, PdZn, PdCu and PdSn) was investigated. The formation of Pd alloy with the reduction temperature was studied by in situ X-ray photoelectron spectroscopy (XPS) and X-ray absorption spectroscopy (XAS) experiments.

1.2.5. Chapter VI – Aqueous phase hydrogenation of phenol catalyzed by Pd and PdAg on ZrO_2

The effects of Pd particle size and of Pd-Ag bimetallic particles on the activity and selectivity in aqueous phase hydrogenation of phenol, using ZrO_2 as the support, were investigated. Physicochemical characterizations are combined with kinetic measurements to develop a description of the HDO reaction.

1.2.6. Chapter VII – Hydrodeoxygenation of phenol over Niobia supported catalysts: Effect of different metals and reduction temperature

Different metals (Ni, Pd and Rh) supported on Nb_2O_5 were evaluated for the gas phase phenol HDO reaction. A systematic study was performed using phenol as a model compound of the bio oil to investigate the effect of the different metals and the reduction temperature on this reaction.

1.2.7. Chapter VIII – Hydrodeoxygenation of phenol over doped cerium oxide with niobium

The effects of the addition of different contents of Nb in the ceria structure was investigated. The activity and selectivity of these catalysts were evaluated over the gas phase hydrogenation of phenol, using nickel as a metallic phase. The structural modification of Nb addition in different environments was studied by in situ X-ray photoelectron spectroscopy (XPS), X-ray absorption spectroscopy (XAS) and In situ X-ray diffraction (XRD) experiments.

1.2.8. Chapter IX – Conclusion

The main conclusions of the thesis were presented along with recommendations for further work.

Reference

[1] M. M . Ahmad , M . Fitrir R . Nordin and M . T. Azizan, Upgrading of Bio-Oil into High-Value Hydrocarbons via Hydrodeoxygenation, American Journal of Applied Sciences 7 (2010) 746–755.https://doi.org/10.3844/ajassp.2010.746.755

[2] A.R.K. Gollakota, M. Reddy, M.D. Subramanyam, N. Kishore, A Review on the Upgradation Techniques of Pyrolysis Oil, Renew. Sustain. Energy Rev. 58 (2016) 1543–1568.https://doi.org/10.1016/j.rser.2015.12.180

[3] E. Furimsky, Catalytic hydrodeoxygenation, Appl. Catal. A Gen. 199 (2000) 147–190.https://doi.org/10.1016/S0926-860X(99)00555-4

[4] Q. Bu, H. Lei, A.H. Zacher, L. Wang, S. Ren, J. Liang, Y. Wei, Y. Liu, J. Tang, Q. Zhang, R. Ruan, A review of catalytic hydrodeoxygenation of lignin-derived phenols from biomass pyrolysis, Bioresour. Technol. 124 (2012) 470–477.https://doi.org/10.1016/j.biortech.2012.08.089

[5] R.N. Olcese, M. Bettahar, D. Petitjean, B. Malaman, F. Giovanella, A. Dufour, Gas-phase hydrodeoxygenation of guaiacol over Fe/SiO2 catalyst, Appl. Catal. B Environ. 115–116 (2012) 63–73.https://doi.org/10.1016/j.apcatb.2011.12.005

[6] H.Y. Zhao, D. Li, P. Bui, S.T. Oyama, Hydrodeoxygenation of guaiacol as model compound for pyrolysis oil on transition metal phosphide hydroprocessing catalysts, Appl. Catal. A Gen. 391 (2011) 305–310.https://doi.org/10.1016/j.apcata.2010.07.039

[7] A. Gutierrez, R.K. Kaila, M.L. Honkela, R. Slioor, A.O.I. Krause, Hydrodeoxygenation of guaiacol on noble metal catalysts, Catal. Today. 147 (2009) 239–246.https://doi.org/10.1016/j.cattod.2008.10.037

[8] J. He, C. Zhao, J.A. Lercher, Impact of solvent for individual steps of phenol hydrodeoxygenation with Pd/C and HZSM-5 as catalysts, J. Catal. 309 (2014) 362–375.https://doi.org/10.1016/j.jcat.2013.09.009

[9] V.N. Bui, D. Laurenti, P. Afanasiev, C. Geantet, Hydrodeoxygenation of guaiacol with CoMo catalysts . Part I : Promoting effect of cobalt on HDO selectivity and activity Applied Catalysis B : Environmental, 101 (2011) 239–245.https://doi.org/10.1016/j.apcatb.2010.10.025

[10] A.J.R. Hensley, Y. Wang, J. Mcewen, Phenol deoxygenation mechanisms on Fe (110) and Pd (111), ACS Catal. 5 (2015) 523–536.https://doi.org/10.1021/cs501403w

[11] P.M. De Souza, R.C. Rabelo-neto, L.E.P. Borges, G. Jacobs, B.H. Davis, T. Sooknoi, D.E. Resasco, F.B. Noronha, Role of Keto Intermediates in the Hydrodeoxygenation of Phenol over Pd on Oxophilic Supports, ACS Catal. 5 (2015) 1318−1329.https://doi.org/10.1021/cs501853t

[12] M. Saidi, F. Samimi, D. Karimipourfard, T. Nimmanwudipong, B.C. Gates, M.R. Rahimpour, Upgrading of lignin-derived bio-oils by catalytic hydrodeoxygenation, Energy Environ. Sci. 7 (2014) 103–129.https://doi.org/10.1039/C3EE43081B

[13] Q. Tan, G. Wang, L. Nie, A. Dinse, C. Buda, J. Shabaker, D.E. Resasco, Different Product Distributions and Mechanistic Aspects of the Hydrodeoxygenation of m-Cresol over Platinum and Ruthenium Catalysts, ACS Catal. 5 (2015) 6271–6283.https://doi.org/10.1021/acscatal.5b00765

[14] B. Coq, F. Figueras, Bimetallic palladium catalysts : influence of the co-metal on the catalyst performance, 173 (2001) 117–134. https://doi.org/10.1016/S1381-1169(01)00148-0

[15] M. V. Bykova, D.Y. Ermakov, V. V. Kaichev, O.A. Bulavchenko, A.A. Saraev, M.Y. Lebedev, V. Yakovlev, Ni-based sol-gel catalysts as promising systems for crude bio-oil upgrading: Guaiacol hydrodeoxygenation study, Appl. Catal. B Environ. 113–114 (2012) 296–307.https://doi.org/10.1016/j.apcatb.2011.11.051

[16] J. Sun, A.M. Karim, H. Zhang, L. Kovarik, X.S. Li, A.J. Hensley, J.S. McEwen, Y. Wang, Carbon-supported bimetallic Pd-Fe catalysts for vapor-phase hydrodeoxygenation of guaiacol, J. Catal. 306 (2013) 47–57.https://doi.org/10.1016/j.jcat.2013.05.020

[17] P.M. Mortensen, J.D. Grunwaldt, P.A. Jensen, K.G. Knudsen, A.D. Jensen, A review of catalytic upgrading of bio-oil to engine fuels, Appl. Catal. A Gen. 407 (2011) 1–19.https://doi.org/10.1016/j.apcata.2011.08.046

[18] M.B. Griffin, G.A. Ferguson, D.A. Ruddy, M.J. Biddy, G.T. Beckham, J.A. Schaidle, Role of the Support and Reaction Conditions on the Vapor-Phase Deoxygenation of m-Cresol over Pt/C and Pt/TiO2 Catalysts, ACS Catal. 6 (2016) 2715–2727.https://doi.org/10.1021/acscatal.5b02868

2.CHAPTER II

2.1. Literature Review

The global energy consumption is increasing, thus renewable energy should be widely explored in order to diversify energy sources and keep sustainable development safe. The use of biomass has been intensely investigated as a source of renewable energy. Most processes that convert biomass to liquid fuels begin with pyrolysis, followed by catalytic upgrading of the resulting biocrude liquids [1]. In pyrolysis process, biomass decomposes to generate mostly vapors and aerosols. After cooling and condensation, a dark brown homogenous liquid (bio-oil) is formed which has a heating value about half that of conventional fuel oil [2].

The production of third generation fuels is mostly based on bio-oils and vegetable oils. Bio-oils have gained considerable importance as potential feedstock for the production of hydrocarbons through catalytic processes. This oil is a complex mixture of water with different types of organic compounds such as carboxylic acids, ketones, aldehydes, sugars, alcohols, phenols with more complex compounds such as lignin and carbohydrates with higher chain [3]. In general, the bio-oil composition, chemical and physical characteristics are closely linked to the type of raw material used and the conditions used in its production [4].

According to Mohan et al. [4] the use of bio-oil has several environmental advantages over fossil fuels, as it is cleaner and causes less pollution. Also the production of the bio-oil can be viable economically in countries with large volumes of organic wastes, which is the case of Brazil. Besides that, the thermochemical conversion of biomass (pyrolysis, gasification, combustion) is a promising, non-nuclear form of future energy. Table 2.1 presented by Qi et al. [5] shows a comparison between the physical properties of a bio-oil and a particular fossil oil. The most important difference observed between these two oils is the ratio of the chemical elements. The amount of oxygen present in the bio-oil is greater than on the oil derived from diesel. This high oxygen content is responsible for problems with polymerization during storage and it also decreases the calorific value of the bio-oil. Because of its low energy value, the bio-oil cannot be used directly as diesel and gasoline, or another fuel attached to transport [6].

Table 2-1. Typical properties of wood pyrolysis bio-oil and of heavy fuel oil. Adapted from Zhang Qi et al. [5].

	Bio-oil	**Fuel oil**
Moisture content [wp%]	15-30	0.1
pH	2.5	-
Specific gravity	1.2	0.94
Elemental composition [wt%]		
C	54-58	85
H	5.5-7	11
O	35 - 40	1.0
N	0 – 0.2	0.3
Ash	0 – 0.2	0.1
HHV(MJ/kg)	16-19	40
Solids [wp%]	0.2-1	1
Distillation residue [wp%]	Above 50	1

The deleterious properties of the bio-oil, such as, high viscosity, thermal instability and corrosiveness are obstacles to the substitution of fossil derived fuels by the renewable oils. So, an upgrading process to reduce the oxygen content is required before its application. Hydrodeoxygenation (HDO), hydrodesulfurization (HDS) and hydrodenitrification (HDN) are the main processes that can be used to improve the bio-oil. The literature review of this study will be restricted to the hydrodeoxygenation reaction that is the main focus of this work.

2.2. Hydrodeoxygenation reaction (HDO)

Hydrodeoxygenation reaction is reported to be the most suitable method to upgrade bio-oil [7]. Industrialization of HDO process was first done by Neste oil in Porvoo, Finland using vegetable oils as the primary feed stock. Upgrading biomass-derived oils to hydrocarbon fuels requires oxygen removal and molecular weight reduction. As a result, typically there is formation of an oil phase and an aqueous phase product, as shown generically in equation 2.1:

$$-(CH_2O)- + H_2 \rightarrow -(CH_2)- + H_2O \qquad \textbf{2.1}$$

Catalytic upgrading of bio-oil is a complex reaction network due to the high diversity of compounds in the feed. Cracking, decarbonylation, decarboxylation, hydrocracking, hydrodeoxygenation, hydrogenation, and polymerization have been reported to take place in HDO process [8]. Fig. 2.1 shows examples of these reactions.

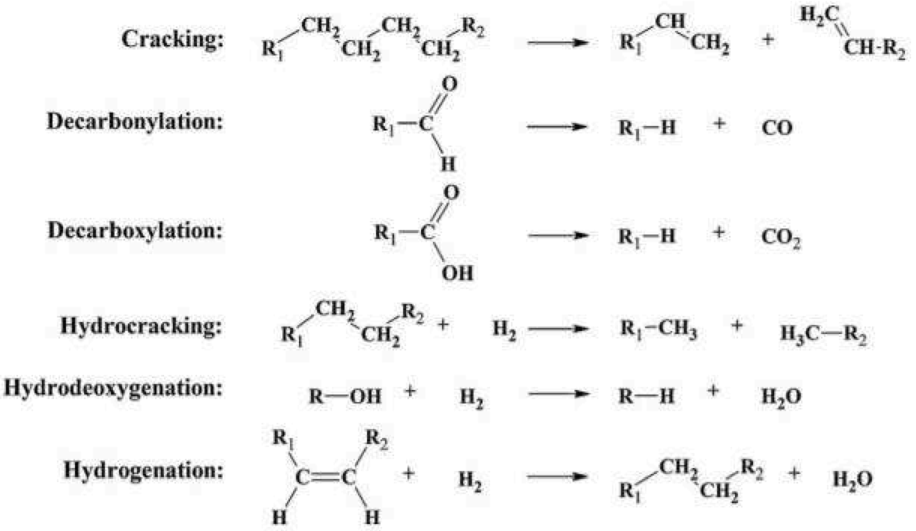

Figure 2-1. Examples of reactions associated with catalytic bio-oil upgrading. The figure was presented by [8].

Hydrodeoxygenation (HDO) of phenolic compounds to cycloalkanes in liquid phase has been reported using heterogeneous metallic catalysts at moderate temperatures (573–873 K) and high hydrogen pressures in fixed bed reactors [9,10]. According to Mortensen et al. [8] high pressure is generally used to ensure better solubility of hydrogen in the oil and thereby a higher availability of hydrogen in the vicinity of the catalyst, which increases the reaction rate and further decreases coking in the reactor.

Due to the diversity of compounds found in the bio-oil many authors choose to use model compounds to study the performance of the catalysts in this reaction [11-13]. The average composition of raw pyrolysis oil is 50–65% of organic components, 15–30% of water and 20% of colloidal lignin fraction. More than 400 different organic components have been detected, which can be classified in several groups: organic acids, aldehydes, ketones, furans, phenolic compounds, guaiacols (methoxyphenols), seryngols and sugar based compounds [10-14].

2.3. Thermodynamic analysis

Before starting to develop catalysts for the HDO reaction it is important to perform a thermodynamic analysis of this process. This analysis may help to determine the optimal operation conditions for the process. Once the best operating conditions are known, the performance tests of the catalysts can be executed in order to obtain a viable process. There are not many thermodynamic studies of phenol HDO reaction in the literature. Therefore this review focus was studiesthat analyzed similar reactions. Velu et al. [15] studied the hydrogenation of phenol over palladium catalysts and calculated Gibbs free energies for the main reactions. In general, the Gibbs free energies of these reactions are negative for each hydrogenolysis/hydrogenation step except for the partial hydrogenation of benzene to cyclohexene. The results obtained by these authors are presented in Figure 2.2 Phenol can be hydrogenated by two initial routes: (1) the first one leading to cyclohexanone or cyclohexanol and the second that produces benzene (8).

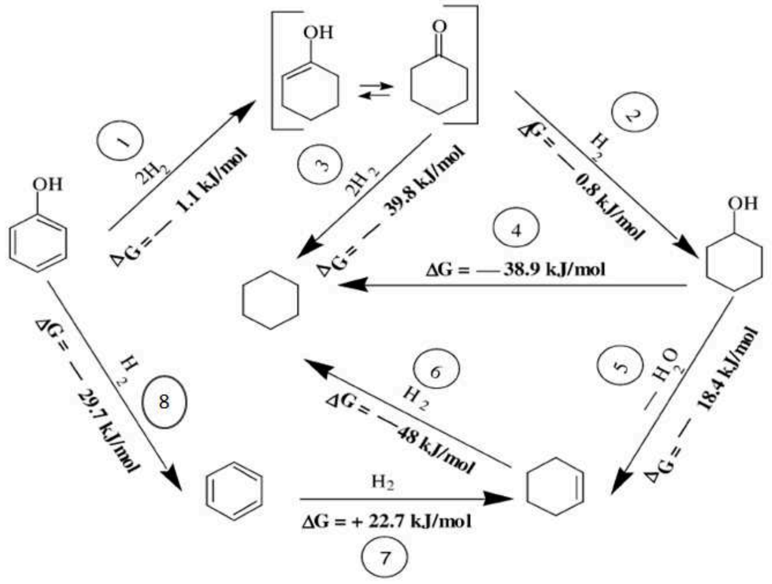

Figure 2-2. Reaction network showing thermodynamically favorable steps in the hydrogenation of phenol. Adapted from Velu et al. [15]

Shin e Keane [16] studied the gas-phase hydrogenation/hydrogenolysis of alcoholic solutions of phenol. The authors calculated the possible thermodynamic limitations by estimating the equilibrium constants using the NIST database. The calculated ΔG free energies (taking 498 K as a representative temperature) for all the possible reaction steps in the conversion of phenol are given in Table 2.2. The thermodynamic calculations indicate that the standard free energies of reaction are negative for each hydrogenolysis/hydrogenation step with the exception of the partial hydrogenation of benzene to cyclohexene.

Table 2-2. Gibbs Free Energies at 498 K for the possible reaction steps observed in the hydrogen treatment of Phenol [16].

Reaction	**ΔG, kJ mol^{-1}**
$C_6H_5OH + 2H_2 \leftrightarrow C_6H_{10}O$	-1.1
$C_6H_5OH + 3H_2 \leftrightarrow C_6H_{11}OH$	-2.0
$C_6H_5OH + H_2 \leftrightarrow C_6H_6 + H_2O$	-29.7
$C_6H_5OH + 3H_2 \leftrightarrow C_6H_{10} + H_2O$	-20.1
$C_6H_5OH + 4H_2 \leftrightarrow C_6H_{12} + H_2O$	-40.8
$C_6H_{10}O + H_2 \leftrightarrow C_6H_{11}OH$	-0.8
$C_6H_{10}O \leftrightarrow C_6H_5OH + 2H_2$	0.9
$C_6H_{10}O \leftrightarrow C_6H_6 + H_2O + H_2$	-28.6
$C_6H_{10}O + H_2 \leftrightarrow C_6H_{10} + H_2O$	-18.9
$C_6H_{10}O + 2H_2 \leftrightarrow C_6H_{12} + H_2O$	-39.8
$C_6H_{11}OH \leftrightarrow C_6H_{10}O + H_2$	0.9
$C_6H_{11}OH \leftrightarrow C_6H_5OH + 3H_2$	1.5
$C_6H_{11}OH \leftrightarrow C_6H_6 + H_2O + 2H_2$	-27.9
$C_6H_{11}OH \leftrightarrow C_6H_{10} + H_2O$	-18.4
$C_6H_{11}OH + H_2 \leftrightarrow C_6H_{12} + H_2O$	-38,9
$C_6H_6 + 2H_2 \leftrightarrow C_6H_{10}$	22.7
$C_6H_6 + 3H_2 \leftrightarrow C_6H_{12}$	-26.1
$C_6H_{10} + H_2 \leftrightarrow C_6H_{12}$	-48.0

Olcese et al. [11] presented a thermodynamic analysis for guaiacol HDO reaction. The chemical equilibrium compositions were calculated using GASEQ software. The following compounds were used in this study: phenols (phenol, cresols, catechols and guaiacol), hydrogenated ring compounds (cyclohexane, cyclohexene, cyclohexanol, etc.), HDO products (benzene, toluene and xylene), carbon, methanol, water, carbon dioxide and monoxide and alkanes (methane- C_6). The starting feed was 1% guaiacol, 90% H_2, 9% Ar, at 1 atm and 673

K. CH_4 was the final product when the thermodynamic equilibrium was achieved, considering 31 possible compounds.

Newman et al. [17] presented the temperature dependence of the standard state Gibbs Free Energy of the following reaction: $xH_2 +$ phenol → product + yH_2O. The number of moles of H_2 (x) and H_2O (y) varies for each of the products: benzene, cyclohexanone, cyclohexene, cyclohexane, cyclohexanol. They concluded that hydrogenation is thermodynamically favorable at lower temperatures (below 500K) and it becomes unfavorable at high temperature. On another hand, the ΔG for deoxygenation of phenol to benzene is essentially independent of temperature and therefore becomes the thermodynamically favored reaction above 550 K.

2.4. HDO mechanism

Three reaction paths can be observed during HDO process: (i) hydrogenation of the C_{Arom}-C (HYD) bond (ii) direct deoxygenation (DDO) and (iii) tautomerization - hydrogenation-dehydration [10, 18]. Figure 2.3 was presented by Ghampson et al. [19] and shows the possible routes for the HDO reaction of phenol. Route 1 is initiated by ring hydrogenation (HYD) of phenol to hydrogenated products, which is in turn transformed into cyclohexene by dehydration. Cyclohexane and benzene are then produced from hydrogenation and dehydrogenation, respectively, of cyclohexene. Finally, isomerization of cyclohexane yields methylcyclopentane while hexane is formed from ring opening reaction of cyclohexane [19]. This route was partially reported by Zhao et al. [20] that studied the catalytic hydrodeoxygenation of phenol on the dual-functional catalyst system Pd/C and H_3PO_4 in a liquid phase. The authors divided the elementary reactions for the aqueous-phase phenol hydrodeoxygenation into four processes: (1) phenol hydrogenation to cyclohexanone on Pd/C; (2) cyclohexanone hydrogenation to cyclohexanol on Pd/C; (3) cyclohexanol dehydration to cyclohexene on HZSM-5, and (4) cyclohexene hydrogenation to cyclohexane on Pd/C.

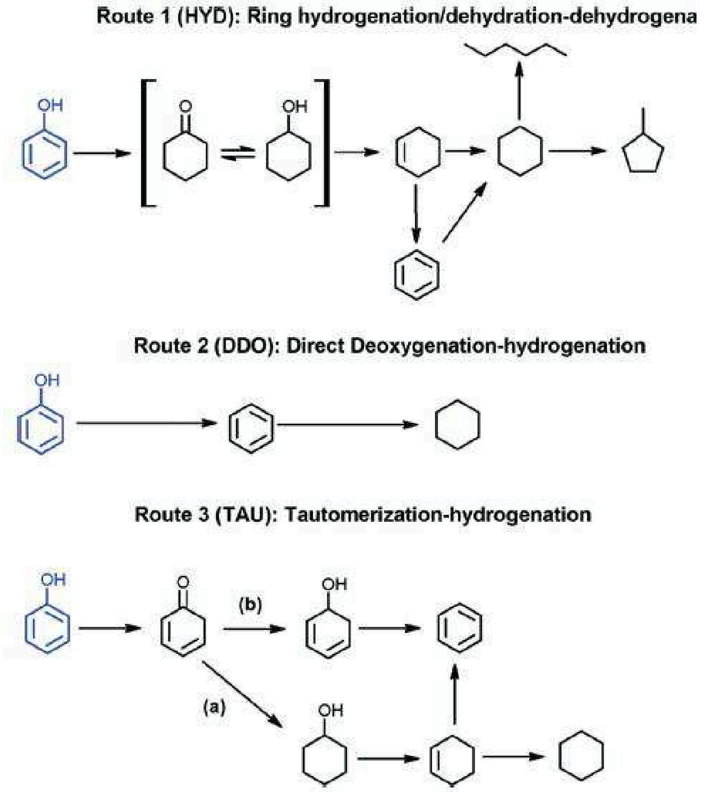

Figure 2-3. Reaction scheme for the conversion of phenol. Adapted from Ghampson et al. [19].

Route 2 depicts direct deoxygenation (DDO) of the C–O σ bond to produce benzene. Hensley et al. [21] studied the deoxygenation mechanism for the conversion of phenol to benzene on Fe(110) and Pd(111) using density functional theory. Five distinct deoxygenation mechanisms were examined as presented in Figure 2.4. Two mechanisms were identified as competing for the most favorable mechanism: the DHOx and H-DHOx. Therefore, the most favorable phenol deoxygenation mechanism was the DHOx, because each step in this mechanism is both energetically and kinetically favorable. Hensley et al. [21] observed that the majority of the deoxygenation reactions on the Pd(111) surface are highly endothermic, while on the Fe(110) surface, almost all deoxygenation reactions are exothermic.

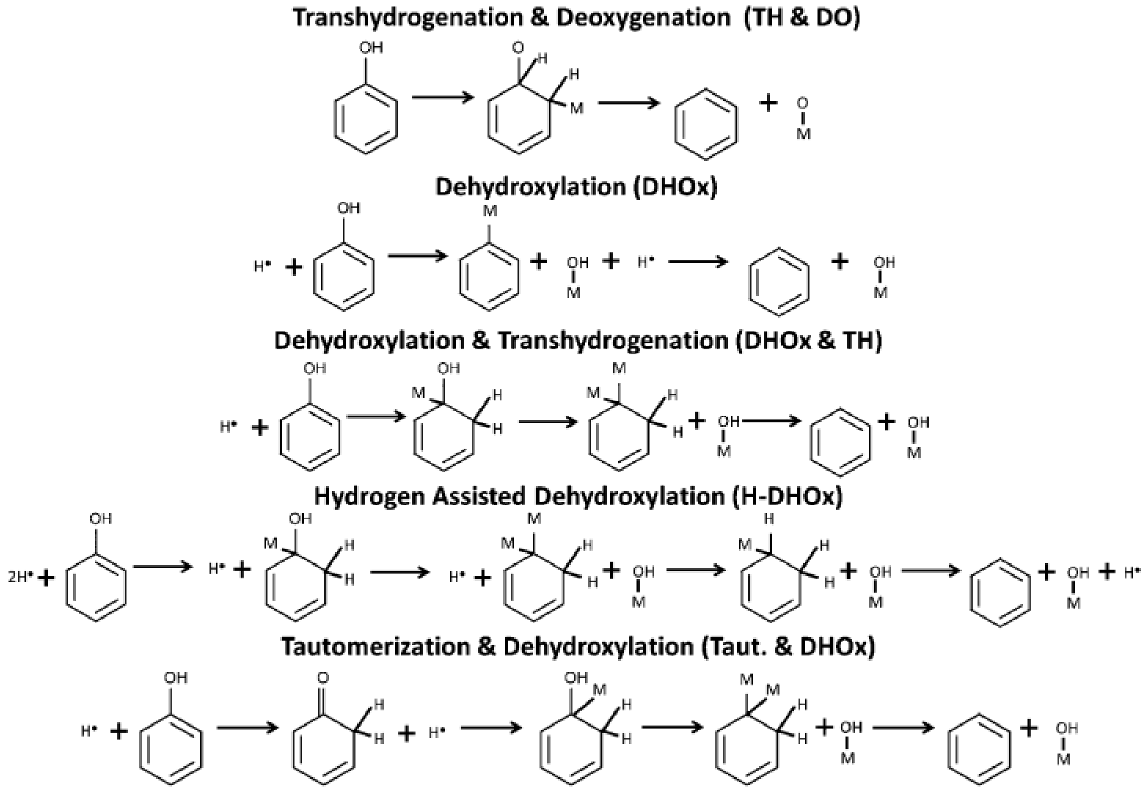

Figure 2-4. Possible deoxygenation reaction mechanisms for phenol on a metal catalyst surface. Adapted from Hensley et al. [21].

Figure 2.5 suggests that the deoxygenation reactions are not likely to occur on the Pd(111) surface at reasonable operating temperatures because of the highly endothermic nature of these key reaction steps and the probability of significantly large activation energies. Based on the exothermic nature of the elementary deoxygenation reaction energies, these reactions have a higher probability of producing the deoxygenated products on the Fe(110) surface.

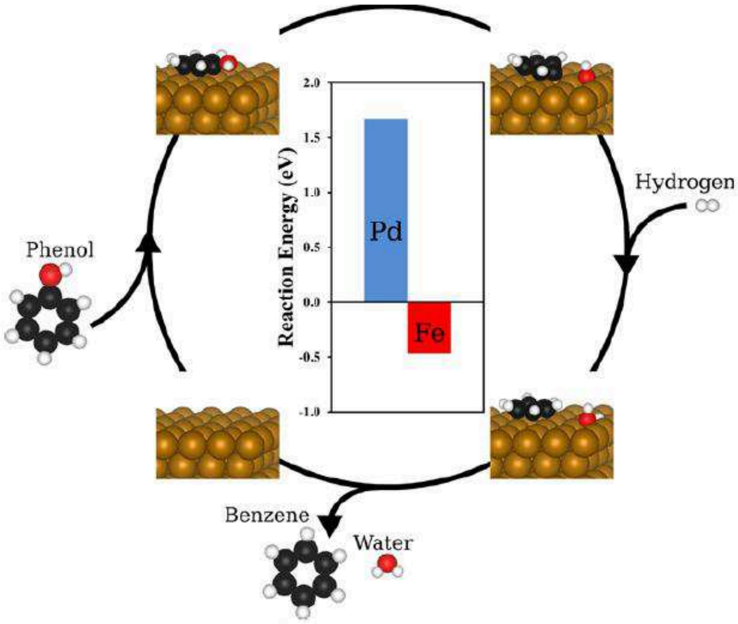

Figure 2-5. Reaction energy for each surface studied. Adapted from Hensley et al. [21].

Route 3 proceeds first through keto-enol tautomerization (TAU) of phenol to form an unstable cyclohexadienone intermediate, followed by two potential pathways: (1) hydrogenation of the carbonyl group to form 2,4-cyclohexadienol and subsequent rapid dehydration to benzene, or (2) hydrogenation to cyclohexanol which is then dehydrated to form cyclohexene, and a final hydrogenation step to cyclohexane. De Souza et al. [22] studied the performance of Pd catalysts supported on SiO_2, Al_2O_3 and ZrO_2 for the hydrodeoxygenation (HDO) of phenol in the gas phase, at 573K and 1 atm using a fixed bed reactor. According to the authors the pathway for phenol HDO is through this route 3. For Pd/SiO_2 and Pd/Al_2O_3 catalysts, the ring is preferentially hydrogenated to produce cyclohexanone and cyclohexanol. On the other hand, over Pd/ZrO_2 the intermediate is hydrogenated to 2,4-cyclohexadienol, which is subsequently dehydrated to benzene. The differences in the reaction pathways were attributed to the presence of oxophilic sites on the ZrO_2 surface (Zr^{4+} cations). Based on the reaction mechanism proposed by de Souza et al. [22] and using similar operational conditions, Teles et al. [23] investigated the effect of the metal type on the product distribution for HDO of phenol (Fig. 2.6). According to the authors, for Pt/SiO_2, Pd/SiO_2 and Rh/SiO_2 catalysts, phenol is mainly tautomerized, followed by hydrogenation of the C–C bond of the tautomer intermediate formed, producing cyclohexanone and cycloexanol (Fig. 2.6). By contrast, the direct dehydroxylation of phenol followed by hydrogenolysis might also occur over more oxophilic metals such as Ru, Co and Ni.

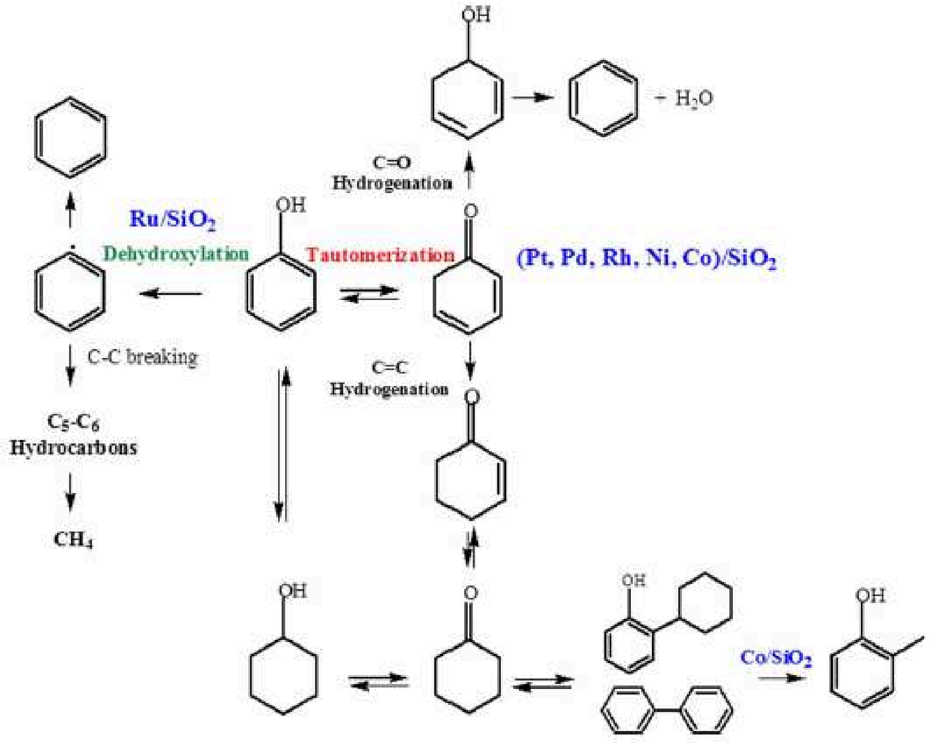

Figure 2-6. Reaction pathways for HDO of phenol over silica supported metal catalysts. Adapted from Teles et al. [23]

2.5. Catalysts for HDO process

Different samples have been studied as catalysts for HDO process: transition metals sulfides, carbides, nitrides, oxynitride, phosphides, noble and metal oxides [24]. Details of the role of some of these catalysts are presented below. Mortensen et al. [25] performed a study to identify efficient catalysts for HDO of phenol at intermediate temperature and pressure (548K and 100 bar) in a batch reactor. The authors investigated four groups of catalysts, totaling 23 samples: oxide catalysts, methanol synthesis catalysts, reduced noble metal catalysts, and reduced non-noble metal catalysts. The following activity order was observed: Ni/ZrO_2 > $Ni-V_2O_5/ZrO_2$ > $Ni-V_2O_5/SiO_2$ > Ru/C > Ni/Al_2O_3 > Ni/SiO_2 >>Pd/C > $Ni/MgAl_2O_4$ > Ni/CeO_2-ZrO_2 ~ Ni/CeO_2 > Pt/C >> $Cu/ZnO/Al_2O_3$ ~ $NiO-MoO_3/Al_2O_3$ ~ $NiCu/SiO_2$ > Cu/SiO_2 > Co/SiO_2 > Ni/C > Fe/SiO_2; MnO/C; WO_3/C; V_2O_5/C; $CoO-MoO_3/Al_2O_3$. The oxides and methanol synthesis catalysts had low activity for HDO of phenol at the given conditions, which was linked to their inability to hydrogenate the phenol ring. On other hand, reduced metal catalysts of both noble and non-noble metals were significantly more active.

Mortensen et al. [26] studied the hydrodeoxygenation (HDO) of phenol over nickel nano-particles of different size (5–22 nm) supported on SiO_2 in a batch reactor at 548 K and

100 bar. The authors concluded that an intermediate nickel particle size is needed for optimal phenol HDO over Ni/SiO_2 at temperatures below 573 K. Both the hydrogenation and deoxygenation reaction were considered Ni-particle size dependent. Surface site population theory evidenced that the deoxygenation reactions were favored on step/corner sites, giving higher deoxygenation rates on small particles. For hydrogenation, the influence of particle size on the rate could be related to the size of Ni facets, with larger facets being better.

Ghampson et al. [19] investigated the hydrodeoxygenation of phenol over supported Co catalysts as a function of the oxide support (alumina, silica-alumina, zirconia and titania). They used a batch reactor at 573 K and a hydrogen pressure of 3 MPa. The reaction time was 4h. Cobalt supported on Al_2O_3 and SiO_2–Al_2O_3 followed the sequential ring hydrogenation–dehydration–hydrogenation route typical of metal/acidic support catalysts, while phenol tautomerization followed by hydrogenation/dehydration sequence was evident over Co/ZrO_2. However, over Co/TiO_2 the sequential direct deoxygenation–hydrogenation pathway occurred preferentially. According to the authors the catalytic activity is related to the total acidity of the Co–support interface, while the product selectivity is a function of the nature of the acid sites determined by cyclohexanol dehydration.

In the literature many studies proposed a correlation between the affinity of the metals to bind oxygen and their deoxygenation activity [21, 25, 27]. Teles et al. [23] investigated this relationship between the deoxygenation activity and the affinity of the metals to bond with oxygen from carbonyl group. The authors conclude that oxygen binds more strongly to Ru than to other metals. The following binding energies of atomic oxygen were observed: Ru (-5.90 eV) <Co(-5.58 eV) < Ni (-5.40 eV) < Rh (-5.04 eV) < Pd (-4.48 eV) < Pt (-4.20 eV). The selectivity to deoxygenated products increased in the same order of binding energies of atomic oxygen, which demonstrated that stronger bonds of oxygen from carbonyl group to the metal, favors the formation of deoxygenated products.

Nelson et al. [28] performed a study with isotopically labeled phenol and DFT (Density Functional Theory) calculations to provide insight into the HDO mechanism over Ru/TiO_2 catalyst. The authors showed the importance of interface sites between Ru nanoparticles and the TiO_2 support. They proposed that the amphoteric nature of TiO_2 facilitates H_2 heterolysis to generate an active site that promotes the catalytic C−O bond scission of phenol. Also, they highlighted that the DDO selectivity of Ru/TiO_2 catalyst with small Ru particles is enhanced by the presence of water. The authors proposed a novel DDO mechanism for phenol when the reaction is performed with water. In this mechanism, water molecules adsorb on hydroxylated or partially reduced TiO_2. This support can easily accept and donate protons across the

Ru/TiO_2 interface and lower the C−O scission barrier by donating a proton during the abstraction of the phenolic OH group. The OH group is replaced in a hydride attack with a single reductive proton. Small Ru particles that create a maximal number of interface sites are necessary for optimal DDO performance. Because of the strong C_{aryl}−O bond, the direct scission pathway has received very little attention in the past. However, the DFT results identified a bifunctional site with metal and Brønsted acid functionality at Ru/TiO_2 interface that provides a lower C− O bond scission barrier (Ea = 0.42 eV) than the most favorable hydrogenation step (Ea = 0.81 eV).

2.5.1. Bimetallic Catalysts

Bimetallic catalysts have been studied for different reactions, such as, hydrogenation in general, hydrogenolysis, CO oxidation, among others. These materials can be a combination of noble metals (Pt, Pd, Rh) with transition metals such as Cu, Zn and Ag. The presence of the second metal may cause the dilution of the active metal, which can affect the selectivity and stability of the reaction studied. Moreover, the dopant also can improve the thermal stability of the noble metal, which helps to avoid the sintering of the primary metal in the reduction and reaction process [29]. Coq and Figueras [30] reviewed the main effects caused by the addition of a second metal to Pd catalysts. The influence of the dopant on Pd catalyst may be determined by two factors: the degree of interaction between the two components and the chemical state of the dopant metal. In general, alterations of the catalytic properties of Pd were discussed according to the following effects: (i) electronic, (ii) geometric effects and (iii) the formation of mixed active sites, which can catalyze two reactions at the same time. According to Coq and Figueras [30] the electron effects play an important role in the selectivity and stability of the hydrogenation reaction of unsaturated hydrocarbons, while the geometric effect affects the structure-sensitive reactions. The geometric effect, known as "ensemble-size", can be caused by the addition of an inactive metal B to an active metal A. A direct consequence of this effect is the decrease in TOF (number of molecules transformed per unit time per atom A exposed on the metal surface). This was observed by Sinfelt et al. [31] that studied the hydrogenolysis of ethane to methane over a series of copper-nickel alloys. The catalytic activity decreased markedly and continuously with addition of copper to nickel over the whole range of alloy composition.

Wang et al. [32] tested Ni–Mo–B amorphous bimetallic catalyst in the phenol hydrodeoxygenation (HDO). The catalysts were prepared by chemical reduction of nickel nitrate and ammonium heptamolybdate with sodium borohydride aqueous solution. According to the authors MoO_2 acted as Brønsted acid site, while B^0 donated partial electrons to Ni, enhanced the catalytic activity. Nie et al. [33] investigated the catalytic conversion of m-cresol in the presence of H_2 on SiO_2-supported Ni, Fe, and bimetallic Ni–Fe catalysts at 573 K and atmospheric pressure, which are the HDO conditions. Over the monometallic Ni catalyst, the products from the hydrogenation were dominant (3-methylcyclohexanone and 3-methylcyclohexanol). By contrast, on Fe and Ni–Fe bimetallic catalysts, the dominant product is toluene. The deoxygenation path would mostly occur on Fe and Ni–Fe catalysts that contain an oxophilic metal (Fe), while the hydrogenations path would occur on Ni, which has a higher affinity for the aromatic ring. In the work published by Huynh et al. [34] Ni-, Cu-, or Co-containing HZSM-5-supported catalysts and two series of bimetallic catalysts (NiCo/HZSM-5 and NiCu/HZSM-5) were prepared, characterized, and tested in the hydrodeoxygenation (HDO) of phenol as a model compound for bio-oil in batch experiments. As expected, Ni/HZSM-5 is more active than monometallic Cu/HZSM-5 and Co/HZSM-5 for phenol HDO, which is related to the Ni capability of H_2 activation and dissociation. The addition of Cu to Ni/HZSM-5 strongly promotes Ni reducibility and leads to the formation of the NiCu alloy but generates separate Cu species with larger particle size. Ni-Cu/HZSM-5 showed lower conversion and selectivity toward deoxygenated products, which may be expected since Cu is less active for the studied reaction. In contrast, the addition of Co to Ni/HZSM-5 increases the catalytic activity and also changes the distribution of deoxygenated products. The addition of Co also suppresses the coke deposition as compared with monometallic catalysts.

Cu/C, Fe/C, Pd/C, Pt/C, PdFe/C, and Ru/C were characterized and evaluated for vapor-phase hydrodeoxygenation (HDO) of guaiacol (GUA) by Sun et al. [35]. Cu and Fe metal catalysts exhibit lower activity than the precious metal catalysts, however they showed higher selectively to deoxygenated products (Benzene and toluene). Compared to Fe/C and Pd/C, PdFe/C catalysts exhibit a substantially enhanced activity while maintaining the high selectivity to HDO products without ring saturation or ring opening. Bimetallic PdFe/C catalysts were found to exhibit a significantly enhanced hydrodeoxygenation activity, which was related to the modification of Fe by Pd as confirmed by high-resolution STEM imaging complemented by EDS, temperature-programmed reduction, EXAFS, and theoretical calculations. The reaction pathways for guaiacol HDO were dependent on the type of catalyst. Figure 2.7 shows the proposed reaction pathways on the supported metal catalysts studied by Sun et al. [35]. In general, over Fe, Cu, and PdFe phenol was the major intermediate formed through either demethylation of guaiacol followed by HDO of catechol or demethoxylation of guaiacol.

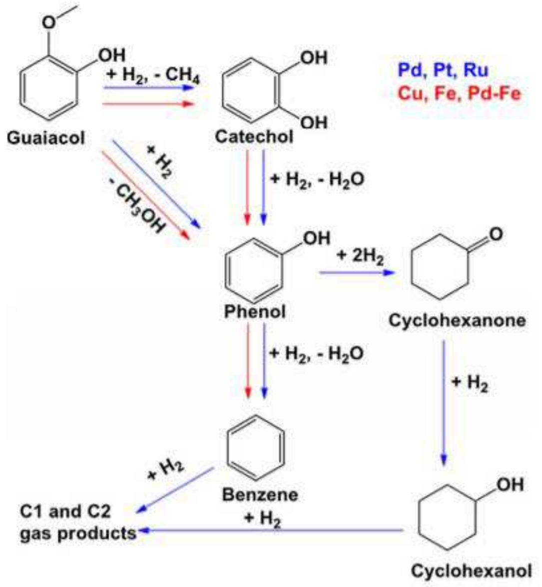

Figure 2-7. Reaction pathways on precious metals (Pd, Pt, Ru) as indicated by blue arrows vs. reaction pathways on base metals (Cu, Fe) and bimetallic Pd–Fe as indicated by red arrows. Adapted from Sun et al. [35]

The alloying of an oxophilic metal to a noble metal has a positive effect for the hydrodeoxygenation reactions. These bimetallic systems have been proposed to reduce the barrier for C–O scission through a strong interaction of the oxophilic metal with the oxygen-containing in the aromatic compound. Hong et al. [36] investigated a series of Pd/Fe_2O_3 catalysts for the hydrodeoxygenation (HDO) of m-cresol. The authors showed that the addition of a noble metal (Pd, Pt, Ru, and Rh) significantly improves the activity of Fe. The presence of Pd facilitated the reduction of Fe and improved the resistance of the Fe surface to the oxidation by reactant and water generated during the HDO process. Similar to the Pd/Fe_2O_3 catalysts, M/Fe_2O_3 catalysts (M =Pt, Ru, and Rh) showed high selectivity to toluene, with a similar product distribution iron catalyst. A possible mechanism is presented in Figure 2.8. H_2 preferentially adsorbs and dissociates on Pd entities attached to Fe surface, followed by spillover to the metallic Fe sites where the substrate, m-cresol, adsorbs and activates. The unique adsorption mode of m-cresol on the Fe metallic surface enables the high selectivity toward direct HDO products (toluene, benzene, and xylene). Meanwhile, Pd is the active site for activating hydrogen and maintains the high hydrogen coverage on the metallic Fe surface.

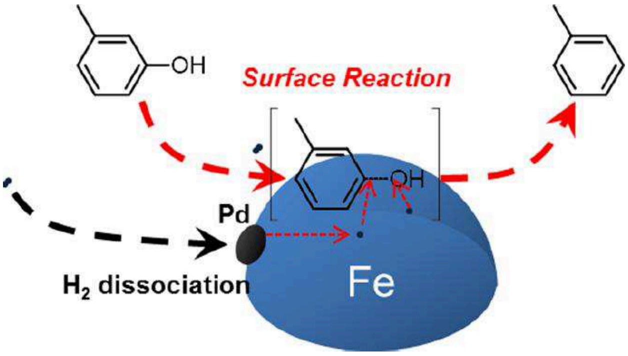

Figure 2-8. Mechanism of HDO reaction over Pd-Fe. Adapted from Hong et al. [36].

The addition of Co or Ni to γ-Al_2O_3-supported Pt catalyst improved the HDO of m-cresol conversion and modified the product distribution [37]. The enhancement in the overall HDO activity is related to the better hydrogenation activity of bimetallic Pt–Co and Pt–Ni catalysts and the generation of additional sites for alcohol dehydration. Consequently, more saturated cyclic hydrocarbon product, methylcyclohexane, is observed on bimetallic catalysts with respect to the monometallic Pt catalyst. The authors highlighted that efficient catalysts for upgrading of phenolic compounds can be designed by tuning different catalyst active functions based on the knowledge of reaction mechanisms. Robinson et al. [38] reported that the addition of Mo to supported Pt catalysts increased the selectivity to deoxygenated products by creating sites that introduce a new preferred reaction pathway by changing the kinetic barriers. They conclude that PtMo can catalyze m-cresol deoxygenation via a pathway involving an initial tautomerization step, while the mechanism on monometallic Pt/Al_2O_3 was the ring hydrogenation, followed by dehydration on the support. The Mo sites on the PtMo bimetallic surface dramatically lower the barrier for m-cresol tautomerization and subsequent deoxygenation. The accessibility of this pathway arises from the increased interaction between the oxygen of m-cresol and the Mo sites on the Pt surface.

2.6. Support effect

The supports play an important role in the HDO reaction process, since they can improve the dispersion and stability of the active phase. In addition, some supports also present active sites, such a Brønsted or Lewis acid sites, which may influence the catalytic activity, coke formation and product distribution of the different reactions involved in the

HDO process. In general, the effects caused by the support can be related to the following factors: water tolerance, surface acidity, porosity, metal-support interaction, surface area, etc [39]. Lee et al. [40] studied the catalytic roles of the metal nanoparticles and acidic supports in the hydrodeoxygenation of guaiacol. They demonstrated that metals were responsible for the hydrogenation of aromatic rings while metal deposited on acidic supports were indispensable to the deoxygenation of oxygenates. Figure 2.9 shows the main products obtained for different support and the metals. In general, it is noted that the support has a more significant effect on the yield of the products than the metal.

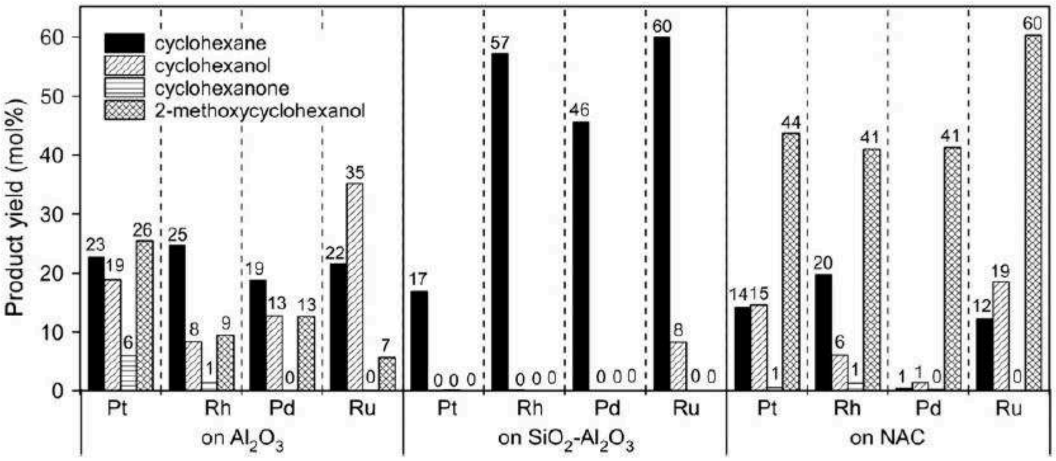

Figure 2-9. Product distributions of the hydrodeoxygenation of guaiacol with Pt, Rh, Pd, and Ru supported on Al_2O_3, SiO_2-Al_2O_3, and NAC. Adapted from Lee et al. [40].

Newman et al. [17] studied Ru-supported catalysts for hydrodeoxygenation (HDO) process using phenol as a model compound. According to the authors the reactivity data is consistent with a parallel mechanism, involving direct deoxygenation (DDO) or hydrogenation (HYD) of phenol. They did not observe effects of the different supports, pore size or morphology in the HYD pathway, however for the DDO pathway, the selectivity varied with support. Among the studied supports (carbon, silica, alumina, and titania) TiO_2 was the one that showed the most dramatic effect on reactivity of the HDO reaction. The role of TiO_2 was explained by a "spillover mechanism", in which small Ru particles could facilitate hydrogen dissociation and the hydrogen in turn could diffuse to the support where Ti^{4+} is reduced to Ti^{3+} Lewis acid sites. The authors also supposed that this effect may be related to the strong metal–support interaction (SMSI). However, the most probably hypothesis presented by Newman et al. [17] to justify the positive effect caused by TiO_2 was related to the difference observed in the Ru particle size on each support. Large Ru particles presented in the other supports interact with the aromatic ring and facilitate hydrogenation, while on the TiO_2 surface, small metal particles create a bifunctional catalyst with the phenyl ring interacting with the metal particle, while the oxygen adsorbs on a reduced Ti^{3+} site.

De Souza et al. [41] investigated the effect of the type of support (SiO_2, Al_2O_3, TiO_2, ZrO_2, CeO_2 and $CeZrO_2$) on the performance of Pd-based catalysts for the hydrodeoxygenation of phenol at 573 K using a fixed bed reactor. In general, the product selectivity was affected by the type of support: Pd/TiO_2 and Pd/ZrO_2 favored the formation of benzene, while cyclohexanone was a major product over the other supports (Pd/SiO_2, Pd/Al_2O_3, Pd/CeO_2 and Pd/$CeZrO_2$). The high selectivity to benzene over Pd/TiO_2 and Pd/ZrO_2 catalysts was related to the oxophilic sites of these supports represented by incompletely coordinated Ti^{4+}/ Ti^{3+} and Zr^{4+}/Zr^{3+} cations near the periphery of metal particles.

2.6.1. Zirconium oxide

The zirconia is a promising catalytic support, which exhibits high thermal stability and basic/acidic properties. As discussed before, Mortensen et al. [25] performed a study of different catalysts for HDO of phenol in a batch reactor. In this work, the authors also evaluated the influence of support. On general, the choice of support influenced the activity significantly. The following apparent order of activity for HDO of phenol with nickel supported on different materials was observed: Ni/ZrO_2 > Ni-V_2O_5/ZrO_2 > Ni-V_2O_5/SiO_2 > Ni/Al_2O_3 > Ni/SiO_2 >> Ni/$MgAl_2O_4$ > Ni/CeO_2-ZrO_2 ~Ni/CeO_2 >>Ni/C. Ni/ZrO_2 had the best performance under the studied conditions with almost complete conversion of phenol and a high selectivity toward cyclohexane. According to the authors nickel based catalysts require a metal oxide as carrier. They proposed a possible reaction mechanism for the HDO over Ni/ZrO_2, which involves the presence of a bifunctional catalyst, as presented in figure 2.10. The presence of oxide support is important to promote the activation of phenol through heterolytic dissociation of the O-H bond. Then, the hydrogen from phenol is adsorbed on an oxygen site at the oxide surface layer and a metal vacancy site stabilizes the phenoxide ion.

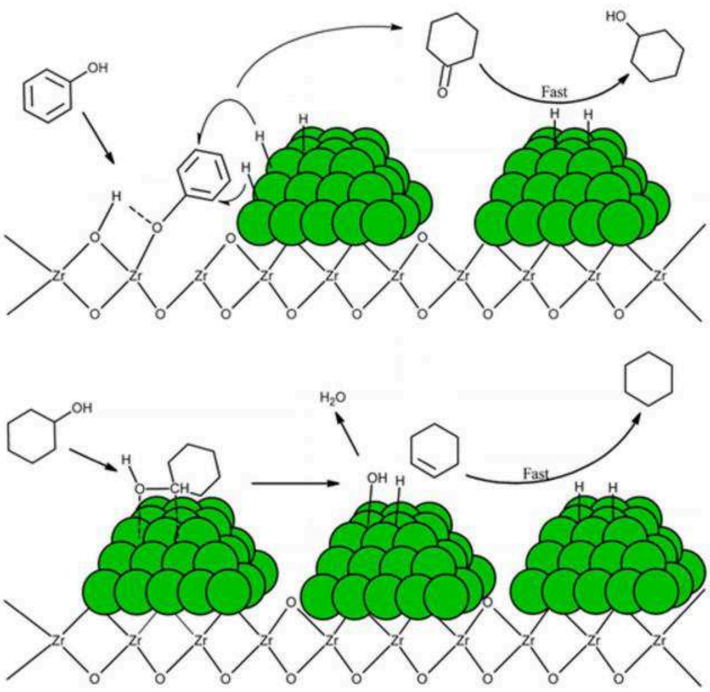

Figure 2-10. Proposed reaction mechanism for HDO of phenol over an oxide supported nickel catalyst (Ni/ZrO_2). Adapted from Mortesen et al. [25].

According to the preparation methodology, zirconium oxide can present different crystalline phases: monoclinic, tetrahedral and cubic. De Souza et al. [42] studied the effect of zirconia structure on the performance of Pd/ZrO_2 catalysts for hydrodeoxygenation of phenol. They conclude that the presence of the tetrahedral ZrO_2 phase (Pd/t-ZrO_2) crystal favors the benzene formation, while the monoclinic phase (Pd/m-ZrO_2) promoted the hydrogenation of phenol to cyclohexanone. The difference in the density of oxophilic sites affected the reaction pathway over zirconia supported Pd catalysts. For Pd/t-ZrO_2, the support has enough acidity to promote the dehydration of cyclohexanol formed to cyclohexene, followed by the formation of benzene, while Pd/m-ZrO_2 promoted the tautomerization of phenol to a cyclohexadienone intermediate. Bui et al. [18] compared zirconia, titania and alumina in guaiacol HDO reaction. In general, the catalytic system CoMoS/ZrO_2 was the most selective toward C_{arom}–O hydrogenolysis. The main pathways observed were DMO (demethoxylation) and DDO (direct deoxygenation). The presence of ZrO_2 decreased the methylation reactions and the formation of heavier products, which occur in large extent with alumina support.

2.6.2. Niobium Oxide

Niobium oxide is a potential catalyst support for HDO reaction, however it has not been intensively studied. Niobium oxides species show a wide variation of Nb–O connection and structure. As a result of these different structures and properties, niobium compounds exhibit unique activity, selectivity and stability for many different catalytic reactions [43]. Niobium can have the follow formal oxidation states: +5 to -1. However, its most stable state is +5. The +4 oxidation state is represented in halide compounds, while the +2 and +3 states appear in cluster compounds based on octahedral M_6X_{12} units [44]. Norwak and Ziolek [44] reported that the amorphous niobium oxide (V) begins to crystallize around 773 K to the **T** (orthorhombic, space group: Pbam) form. Crystallization occurs until 1103 K, where **M-** form (monoclinic, space group: I4/mmm) becomes apparent. At higher temperatures, a third transformation to a "high temperature" **H**-form (monoclinic, space group: P2/m) has been reported.

Niobium oxide may be synthesized from niobic acid [43]. When this acid is thermally treated below 573 K it exhibits strong Brønsted acidity, which decreases with increasing the calcination temperature [45]. The decrease of Brønsted acid sites is attributed to the crystallization of amorphous niobic acid into niobium oxide. Lebarbier et al. [46] analyzed the texture, structure, acidity of a series of Nb-based catalysts obtained by calcination of niobic acid between 423-823 K. Increasing the calcination temperature brings a surface area decrease and changes in the acidy of these materials.

Niobia is a typical SMSI (strong metal support interaction) oxide. In the SMSI process, a thin Nb_2O_x layer covers the transition metal stabilizing reduced Nb^{5+} sites in the thin oxide overlayer. In general, this effect affects the catalysts activities due to surface decoration. The catalytic activities of the structure-sensitive reactions are usually affected, such as the hydrogenolysis of hydrocarbons, which was observed by Uchijima [47]. Brown et al. [48] investigated the effect caused by raising the reduction temperature from 523 to 773 K in the catalytic properties of Pt/Nb_2O_5 and Rh/Nb_2O_5 for the hydrogenolysis of 2-methylbutane and n-pentane. The strong metal-support interaction (SMSI) caused by the high reduction temperature decreased the rates of hydrogenolysis of both catalysts. However, the effects of SMSI were reversible and eliminated by oxidation at 673 K followed by reduction at 523 K.

The direct hydrodeoxygenation of raw woods into liquid alkanes over a multifunctional $Pt/NbOPO_4$ catalyst was investigated by Xia et al. [49] using computational calculations. They evaluated the interaction of the C-O group present in phenol with the surface of $NbOPO_4(100)$ and $Re_2O_7(010)$, which is related to respective active sites: Nb^{5+} and Re^{5+}. The high catalytic activity of $NbOPO_4$ can be ascribed to better adsorption capability of surface Nb_{5c} and a lower activation barrier in comparison to Re_2O_7. Figure 2.11 shows the energy profiles of the C-O bond breakdown for C_6H_5OH (phenol) calculated by Xia et al. [49].

Phenol is preferably absorbed through the O- at the Nb^{5+} site present on $NbOPO_4$ (100), with an adsorption energy of -0.89 eV, while for Re_2O_7 (010), this energy is -0.37 eV. After adsorption, phenol opens the C-O bond in a radical with a C-O distance of 1.98 Å in the TS2 transition state, which has an activation energy of 1.17eV. During product dissociation, the hydroxyl and phenyl groups adsorb on Nb^{5+} sites with a reaction enthalpy of -1.66eV. The adsorption energy of the phenol on the calculated Re_2O_7 (010) was much lower (-0.37 eV) than that observed for $NbOPO_4$ (100). In addition, the dissociation process is endothermic with a high activation energy (1.38 eV).

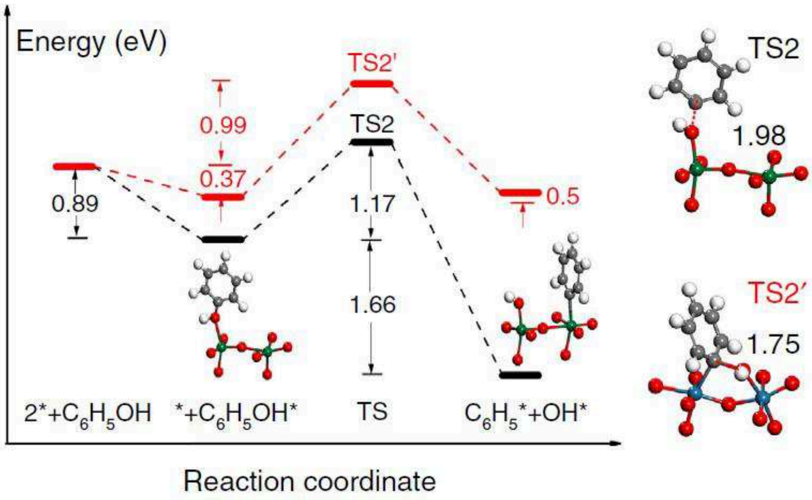

Figure 2-11. Power profiles of the breakage of the C-O bond to the C_6H_5OH. The black line represents the $NbOPO_4$ (100) and the red line represents the Re_2O_7 (010). The green balls represent the Nb atoms, the blue balls the Re, gray the C and the red the O [49].

Xia et al. [49] also reported that there is a correlation between the C–O bond dissociation barriers and their corresponding adsorption energies. Stronger bond strengths of M_{5c}–O (M=Nb, Re) lead to easier the C–O bond cleavage, which is in line with the principle of Brønsted–Evans–Polanyi relationship. In other words, the outstanding binding ability of $NbOPO_4$ is one determining factor in the efficient deoxygenation of cellulose and lignin. They also calculated and compared the adsorption energies of different intermediate species (OH, O, etc.) on niobium phosphate with other supports, such as ZrO_2. The results obtained are presented in Table 2.3. It was observed that $NbOPO_4$ demonstrates the strongest binding capacity, while ZrO_2, with the weakest adsorption.

Table 2-3. Bonding energy (eV) calculated for some important intermediates in $NbOPO_4$ (100), Re_2O_7 (010) and ZrO_2 (010). Adapted from Xia et al. [49].

Species	**Reaction**	**$NbOPO_4$(100)**	**Re_2O_7(010)**	**ZrO_2(010)**
O	$1/2O_2 + * \rightarrow O*$	-4.44	-1.99	1.43
OH	$H_2O + * \rightarrow OH* + 1/2H_2$	-1.95	-0.13	1.06
H	$1/2H_2 + * \rightarrow H*$	-0.59	0.43	2.17
C_4H_8O	$C_4H_8O + * \rightarrow C_4H_8O*$	-1.15	-0.83	-0.80
C_4H_9OH	$C_4H_9OH + * \rightarrow C_4H_9OH*$	-1.20	-0.76	-0.69
OC_4H_9	$C_4H_9OH + * \rightarrow C_4H_9O* + 1/2H_2$	-2.12	-0.32	1.14
C_4H_9	$C_4H_{10} + * \rightarrow C_4H_9* + 1/2H_2$	-0.09	0.94	1.94

Recently, Barrios et al. [50] compared the performance of Pd supported on SiO_2 and Nb_2O_5 for the HDO of phenol reaction at different temperatures using a fixed-bed reactor. The type of support significantly affects activity and product distribution. The reaction rate for HDO of phenol over Pd/Nb_2O_5 was higher than that observed for silica supported catalyst. Cyclohexanone was the dominant product for Pd/SiO_2, whereas benzene was mainly formed on Pd/Nb_2O_5. The high activity and selectivity to deoxygenated products of Pd/Nb_2O_5 for HDO of phenol is likely due to the strong interaction between the oxophilic sites represented by Nb^{5+}/Nb^{4+} cations and the oxygen from the phenol molecule, as previous calculated by Xia et al. [49].

2.6.3. Cerium mixed oxides

Over the past several years, CeO_2-containing materials have been intensively studied as catalysts of heterogeneous reactions. The presence of cerium in a catalyst is justified by some factors, such as, the beneficial effect of precious metal-ceria interactions or the presence of the redox couple Ce^{iv}-Ce^{iii}. Cerium has an ability to change from Ce^{iv} (CeO_2) under oxidizing conditions to Ce^{iii} (Ce_2O_3) under reducing conditions, which may affect the catalytic activity and selectivity. In general, ceria is known to (a) affect the dispersion of supported metals; (b) promote the water gas shift and steam reforming reactions; (c) increase the thermal stability of the support; (d) promote noble metal reduction and oxidation; (e) store and release oxygen, hydrogen, and sulfur; (f) form surface and bulk vacancies; and (g) form inter-metallic M-Ce compounds [51]

Several cerium mixed oxides Ce–M–O (with M = Eu, Pr, Sm, Nd) were recently investigated with the aim of improving oxygen mobility of this oxide [52]. The distortion of the O_2 sublattices caused by the presence of another element in the mixed oxides permits a higher mobility of lattice oxygen. The reduction occurs not only on the surface but also extends deep into the bulk [53]. For example, the mixed $Ce_xZr_{1-x}O_2$ has good stability and redox properties, which attracted attention to its application as catalysts [53].

Schimming et al. [54] investigated the hydrodeoxygenation of guaiacol over bulk ceria and ceria–zirconia oxide with different elemental compositions. The reactions were performed in a flow reactor at 1 atm and 548–673K. They showed that ceria–zirconia catalysts without fully reduced metal particles are active for the studied reaction and phenol and catechol are formed as the primary products. Benzene is formed as the completely deoxygenated product, but the final deoxygenation step is much slower than the hydrogenation. This activity was related to the fact that ceria dissociates hydrogen and creates oxygen vacancy sites under mild conditions, which is a requirement for HDO catalysts. Zirconium has a slightly smaller ionic radius than cerium, which causes a slight strain in the ceria–zirconia crystal lattice and facilitates structural relaxation after the formation of an oxygen vacancy. Figure 2.12 shows a linear correlation between the concentration of oxygen vacancies at 573 K and the guaiacol conversion at the same temperature. There is a clear indication that oxygen vacancies play a critical role in the conversion of guaiacol. In addition to the electronic effects, the presence of zirconium also partially suppresses crystallization during the synthesis of the catalysts and results in smaller, more active crystallites. According to the authors optimized synthesis methods could increase the concentration of oxygen vacancies under specific reaction conditions and reduce the energy required for their formation.

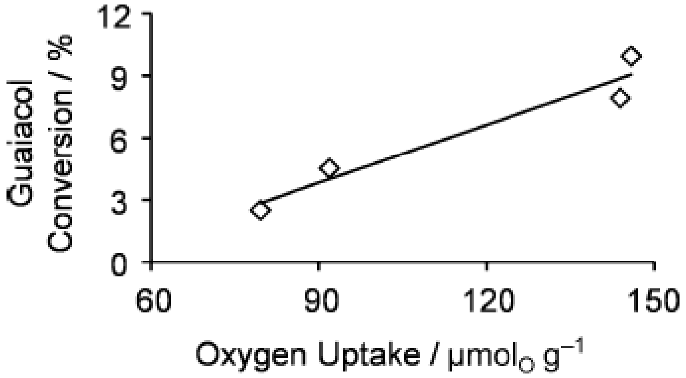

Figure 2-12. Correlation of the concentration of oxygen vacancy sites with guaiacol conversion over ceria and ceria–zirconia at 573K. Adapted from Schimming et al. [54].
]

Besides zirconium, other metals can be added to the cerium oxide structure to improve its properties, although there is no study of this type for the HDO reaction. According to Zhang et al. [55] among the various multivalent dopants Pr is a promising one, because it may dissolve into the host CeO_2 to form a solid solution. This is expected due to the similarity of ionic radius to Ce ions and the same fluorite structure of PrO_2 and CeO_2. Doping CeO_2-based materials with multivalent Pr ($Pr^{3+/4+}$) is known to enhance the formation and migration of oxygen vacancies [55]. Sn also can be an option as a dopant. Ayastuy et al. [56] studied a series of $Ce_XSn_{1-X}O_{2-\delta}$ oxides with low amount of tin ($X \geq 0.85$). The oxides were synthesized by co-precipitation method. The incorporation of tin to cerium oxide prevented growth of ceria crystallites and also increased the amount of lattice defects. Oxygen vacancies in the ceria lattice increased linearly with the amount of tin. The incorporation of tin into the ceria lattice also increased the total surface acidity. XPS analysis indicated both 4+ and 3+ oxidation states for Ce, and the most abundant species on the surface were Ce^{4+} and $Sn^{4+/2+}$.

Niobium is another possible dopant to be added to cerium oxide. $CeNbO_{4+\delta}$ is known to exhibit a wide range of oxygen hyperstoichiometry (δ) varying from 0 to 0.33. $CeNbO_{4+\delta}$ materials may be oxidized to yield four different phases: monoclinic $CeNbO_{4.08}$, $CeNbO_{4.25}$, $CeNbO_{4.33}$ and tetragonal $CeNbO_4$, which depends on the heating regime. The coexistence of Ce^{3+} and Ce^{4+} cations in these complex oxides have been reported to be originated from the occupancy of the interstitial oxygen sites and associated relaxation of the surrounding oxygen array [57-58]. $CeNbO_4$ samples were synthesized via solid state reactions and characterized by XRD, XPS, internal friction and impedance measurements [59]. XRD patterns showed that the sample cooled from 1173 K to room temperature was mainly composed of monoclinic $CeNbO_4$ phase. XPS analysis showed that the oxygen lattice can be present in form of Ce–O and Nb–O while niobium exists in Nb^{5+} state and cerium exists in both Ce^{3+} and Ce^{4+} states.

2.7. Stability

The high deactivation rates are the biggest problem of the catalysts to be used in the HDO reactions. According to Furimsky e Massoth [60] a main reason for deactivation of the catalysts in the hydroprocessing reactions involves the loss of active sites, which may happen by: (i) deactivation caused by coke; (ii) poisoning of the sites present in the catalyst by adsorption or (iii) sintering of the active phase. Velu et al. [15] investigated the stability of Pd supported samples over the vapor phase hydrogenation of phenol. Pd/CeO_2 exhibited stable activity during on-stream operation, but produced a mixture of cyclohexanone, cyclohexanol and cyclohexane. On the other hand, Pd/ZrO_2 produced exclusively the desired product (cyclohexanone), but undergoes deactivation. De Souza et al. [41] also observed that Pd samples supported on cerium oxides were more stable among several other Pd catalysts. The authors reported that the growth of Pd particle size and the reduction in acidic sites density during HDO of phenol were the primary routes of catalyst deactivation, which may be related to the fact that HDO of phenol takes place at the metal-support interface. The higher stability of Pd/CeO_2 and Pd/$CeZrO_2$ catalysts was related to the higher amount of oxygen vacancies of these supports. The formation of oxygen vacancies expose additional cationic sites that turn over oxygenate intermediates and/or allow facile desorption of oxygenate products. However, the adsorption strength also contributed to catalyst deactivation. The stronger adsorption between the carbonyl function with oxides such as TiO_2, ZrO_2, SiO_2, and Al_2O_3 resulted in an accumulation of O-containing byproducts and led to catalyst deactivation.

Reference

[1] A. Bridgwater, Fast pyrolysis processes for biomass, Renew. Sustain. Energy Rev. 4 (2000) 1–73.https://doi.org/10.1016/S1364-0321(99)00007-6

[2] A. V Bridgwater, Review of fast pyrolysis of biomass and product upgrading, Biomass and Bioenergy. 38 (2011) 68–94.https://doi.org/10.1016/j.biombioe.2011.01.048

[3] M. Garcia-Perez, A. Chaala, H. Pakdel, D. Kretschmer, C. Roy, Characterization of bio-oils in chemical families, Biomass and Bioenergy. 31 (2007) 222–242.https://doi.org/10.1016/j.biombioe.2006.02.006

[4] D. Mohan, C.U. Pittman, P.H. Steele, Pyrolysis of wood/biomass for bio-oil: A critical review, Energy and Fuels. 20 (2006) 848–889.https://doi.org/10.1021/ef0502397

[5] Q. Zhang, J. Chang, T. Wang, Y. Xu, Review of biomass pyrolysis oil properties and upgrading research, Energy Convers. Manag. 48 (2007) 87–92.https://doi.org/10.1016/j.enconman.2006.05.010

[6] J. Kim, Production, separation and applications of phenolic-rich bio-oil –A review, Bioresour. Technol. 178 (2014) 90-98.https://doi.org/10.1016/j.biortech.2014.08.121

[7] N. Arun, R. V. Sharma, A.K. Dalai, Green diesel synthesis by hydrodeoxygenation of bio-based feedstocks: Strategies for catalyst design and development, Renew. Sustain. Energy Rev. 48 (2015) 240–255.https://doi.org/10.1016/j.rser.2015.03.074

[8] P.M. Mortensen, J. Grunwaldt, P.A. Jensen, K.G. Knudsen, A.D. Jensen, A review of catalytic upgrading of bio-oil to engine fuels, Applied Catal. A, Gen. 407 (2011) 1–19.https://doi.org/10.1016/j.apcata.2011.08.046

[9] X. Zhang, Q. Zhang, T. Wang, L. Ma, Y. Yu, L. Chen, Hydrodeoxygenation of lignin-derived phenolic compounds to hydrocarbons over Ni/SiO2-ZrO2 catalysts, Bioresour. Technol. 134 (2013) 73–80.https://doi.org/10.1016/j.biortech.2013.02.039

[10] H. Pucher, N. Schwaiger, R. Feiner, L. Ellmaier, P. Pucher, B. S. Chernevc, M. Siebenhofer, Biofuels from liquid phase pyrolysis oil: a two-step hydrodeoxygenation (HDO) process, Green Chem., 17 (2015) 1291. https://doi.org/10.1039/C4GC01741B

[11] R.N. Olcese, M. Bettahar, D. Petitjean, B. Malaman, F. Giovanella, A. Dufour, Gas-phase hydrodeoxygenation of guaiacol over Fe/SiO2 catalyst, Appl. Catal. B Environ. 115–116 (2012) 63–73.https://doi.org/10.1016/j.apcatb.2011.12.005

[12] J. He, C. Zhao, J.A. Lercher, Impact of solvent for individual steps of phenol hydrodeoxygenation with Pd/C and HZSM-5 as catalysts, J. Catal. 309 (2014) 362–375.https://doi.org/10.1016/j.jcat.2013.09.009

[13] J. Sun, A.M. Karim, H. Zhang, L. Kovarik, X. Shari, A.J. Hensley, J. Mcewen, Y. Wang, Carbon-supported bimetallic Pd–Fe catalysts for vapor-phase hydrodeoxygenation of guaiacol, J. Catal. 306 (2013) 47–57.https://doi.org/10.1016/j.jcat.2013.05.020

[14] M. Saidi, F. Samimi, D. Karimipourfard, T. Nimmanwudipong, B.C. Gates, M.R. Rahimpour, Upgrading of lignin-derived bio-oils by catalytic hydrodeoxygenation, Energy Environ. Sci. 7 (2014) 103–129.https://doi.org/10.1039/C3EE43081B

[15] S. Velu, M.P. Kapoor, S. Inagaki, K. Suzuki, Vapor phase hydrogenation of phenol over palladium supported on mesoporous CeO2 and ZrO2, Appl. Catal. A Gen. 245 (2003) 317–331.https://doi.org/10.1016/S0926-860X(02)00655-5

[16] E. Shin, M.A. Keane, Gas-Phase Hydrogenation/Hydrogenolysis of Phenol over Supported Nickel Catalysts, (2000) 883–

892. https://doi.org/10.1021/ie990643r

[17] C. Newman, X. Zhou, B. Goundie, I.T. Ghampson, R.A. Pollock, Z. Ross, M.C. Wheeler, R.W. Meulenberg, R.N. Austin, B.G. Frederick, Effects of support identity and metal dispersion in supported ruthenium hydrodeoxygenation catalysts, Appl. Catal. A Gen. 477 (2014) 64–74.https://doi.org/10.1016/j.apcata.2014.02.030

[18] V.N. Bui, D. Laurenti, P. Afanasiev, C. Geantet, Hydrodeoxygenation of guaiacol with CoMo catalysts.Part I : Promoting effect of cobalt on HDO selectivity and activity, Applied Catal. B, Environ. 101 (2011) 239–245.https://doi.org/10.1016/j.apcatb.2010.10.025

[19] I.T. Ghampson, C. Sepúlveda, A.B. Dongil, G. Pecchi, R. García, J.L.G. Fierro, N. Escalona, I.T. Ghampson, N. Escalona, Phenol hydrodeoxygenation: Effect of support and Re promoter on the reactivity of Co catalysts, Catal. Sci. Technol. 6 (2016) 7289–7306.https://doi.org/10.1039/C6CY01038E

[20] C. Zhao, J. He, A.A. Lemonidou, X. Li, J.A. Lercher, Aqueous-phase hydrodeoxygenation of bio-derived phenols to cycloalkanes, J. Catal. 280 (2011) 8–16. https://doi.org/10.1016/j.jcat.2011.02.001

[21] A.J.R. Hensley, Y. Wang, J. Mcewen, Phenol deoxygenation mechanisms on Fe (110) and Pd (111), ACS Catal. 5 (2015) 523–536.https://doi.org/10.1021/cs501403w

[22] P.M. De Souza, R.C. Rabelo-Neto, L.E.P. Borges, G. Jacobs, B.H. Davis, T. Sooknoi, D.E. Resasco, F.B. Noronha, Role of keto intermediates in the hydrodeoxygenation of phenol over Pd on oxophilic supports, ACS Catal. 5 (2015).https://doi.org/10.1021/cs501853t

[23] C. A. Teles, R. C. Rabelo-Neto, J. R. de Lima, L. V. Mattos, D. E. Resasco, F. B. Noronha, The Effect of Metal Type on Hydrodeoxygenation of Phenol Over Silica Supported Catalysts, Catal. Letters. 146 (2016) 1848–1857.https://doi.org/10.1007/s10562-016-1815-5

[24] A.R.K. Gollakota, M. Reddy, M.D. Subramanyam, N. Kishore, A Review on the Upgradation Techniques of Pyrolysis Oil, Renew. Sustain. Energy Rev. 58 (2016) 1543–1568.https://doi.org/10.1016/j.rser.2015.12.180

[25] P.M. Mortensen, J. Grunwaldt, P.A. Jensen, A.D. Jensen, Screening of Catalysts for Hydrodeoxygenation of Phenol as a Model Compound for Bio-oil, ACS Catal. 3 (2013) 1774–1785.https://doi.org/10.1021/cs400266e

[26] P.M. Mortensen, J.D. Grunwaldt, P.A. Jensen, A.D. Jensen, Influence on nickel particle size on the hydrodeoxygenation of phenol over Ni/SiO2, Catal. Today. 259 (2016) 277–284.https://doi.org/10.1016/j.cattod.2015.08.022

[27] C. A. Teles, R. C. Rabelo-Neto, G. Jacobs, B. H. Davis, D. E. Resasco, F. B. Noronha, Hydrodeoxygenation of phenol over zirconia supported catalysts . The effect of metal type on reaction mechanism and catalyst deactivation, ChemCatChem 9 (2017) 1-15.https://doi.org/10.1002/cctc.201700047

[28] R.C. Nelson, B. Baek, P. Ruiz, B. Goundie, A. Brooks, M.C. Wheeler, B.G. Frederick, L.C. Grabow, R.N. Austin, Experimental and Theoretical Insights into the Hydrogen-Efficient Direct Hydrodeoxygenation Mechanism of Phenol over Ru/TiO2, ACS Catal. 11 (2015) 6509–6523.https://doi.org/10.1021/acscatal.5b01554

[29] P. Ferreira-Aparicio, B. Bachiller-Baeza, I. Rodriguez-Ramos, A. Guerrero-Ruiz, M. Fernandez-Garcia, Correlation between metal oxidation state and catalytic activity: hydrogenation of crotonaldehyde over Rh catalysts, Catal. Letters. 49 (1997) 163–167.https://doi.org/10.1023/A:1019009422572

[30] B. Coq, F. Figueras, Bimetallic palladium catalysts : influence of the co-metal on the catalyst performance, Journal of Molecular Catalysis A: Chemical 173 (2001) 117–134.https://doi.org/10.1016/S1381-1169(01)00148-0

[31] J.H. Sinfelt, J.L. Carter, D.J.C. Yates, Catalytic hydrogenolysis and dehydrogenation over copper-nickel alloys, J. Catal. 24 (1972) 283–296.https://doi.org/10.1016/0021-9517(72)90072-3

[32] W. Wang, Y. Yang, J. Bao, H. Luo, Characterization and catalytic properties of Ni – Mo – B amorphous catalysts for phenol hydrodeoxygenation, Catal. Commun. 11 (2009) 100–105.https://doi.org/10.1016/j.catcom.2009.09.003

[33] L. Nie, P.M. De Souza, F.B. Noronha, W. An, T. Sooknoi, D.E. Resasco, Selective conversion of m-cresol to toluene over bimetallic Ni–Fe catalysts, Journal Mol. Catal. A, Chem. 389 (2014) 47–55.https://doi.org/10.1016/j.molcata.2013.09.029

[34] T.M. Huynh, U. Armbruster, M.M. Pohl, M. Schneider, J. Radnik, D.L. Hoang, B.M.Q. Phan, D.A. Nguyen, A. Martin, Hydrodeoxygenation of phenol as a model compound for bio-oil on non-noble bimetallic nickel-based catalysts, ChemCatChem. 6 (2014) 1940–1951.https://doi.org/10.1002/cctc.201402011

[35] J. Sun, A.M. Karim, H. Zhang, L. Kovarik, X.S. Li, A.J. Hensley, J.S. McEwen, Y. Wang, Carbon-supported bimetallic Pd-Fe catalysts for vapor-phase hydrodeoxygenation of guaiacol, J. Catal. 306 (2013) 47–57.https://doi.org/10.1016/j.jcat.2013.05.020

[36] Y. Hong, H. Zhang, J. Sun, K.M. Ayman, A.J.R. Hensley, M. Gu, M.H. Engelhard, J.S. McEwen, Y. Wang, Synergistic catalysis between Pd and Fe in gas phase hydrodeoxygenation of m -cresol, ACS Catal. 4 (2014) 3335–3345.https://doi.org/10.1021/cs500578g

[37] P.T.M. Do, A.J. Foster, J. Chen, R.F. Lobo, Bimetallic effects in the hydrodeoxygenation of meta-cresol on γ-Al2O3 supported Pt–Ni and Pt–Co catalysts, Green Chem. 14 (2012) 1388.https://doi.org/10.1039/c2gc16544a

[38] A.M. Robinson, G.A. Ferguson, J.R. Gallagher, S. Cheah, G.T. Beckham, J.A. Schaidle, J.E. Hensley, J.W. Medlin, Enhanced hydrodeoxygenation of m-cresol over bimetallic Pt-Mo catalysts through an oxophilic metal-induced tautomerization pathway, ACS Catal. 6 (2016) 4356–4368.https://doi.org/10.1021/acscatal.6b01131

[39] Z. He, X. Wang, Hydrodeoxygenation of model compounds and catalytic systems for pyrolysis bio-oils upgrading, Catal. Sustain. Energy, 1 (2012) 28–52.https://doi.org/10.2478/cse-2012-0004

[40] C.R. Lee, J.S. Yoon, Y.W. Suh, J.W. Choi, J.M. Ha, D.J. Suh, Y.K. Park, Catalytic roles of metals and supports on hydrodeoxygenation of lignin monomer guaiacol, Catal. Commun. 17 (2012) 54–

58.https://doi.org/10.1016/j.catcom.2011.10.011

[41] P.M. De Souza, R.C. Rabelo-neto, L.E.P. Borges, G. Jacobs, B.H. Davis, D.E. Resasco, F.B. Noronha, Hydrodeoxygenation of phenol over Pd catalysts. Effect of support on reaction mechanism and catalyst deactivation, ACS Catal., 7 (2017) 2058–2073.https://doi.org/10.1021/acscatal.6b02022

[42] P.M. De Souza, R.C. Rabelo-neto, L.E.P. Borges, G. Jacobs, B.H. Davis, U.M. Graham, D.E. Resasco, F.B. Noronha, Effect of Zirconia Morphology on Hydrodeoxygenation of Phenol over Pd/ZrO2, ACS Catal., 5 (2015) 7385–7398.https://doi.org/10.1021/acscatal.5b01501

[43] M. Ziolek, Niobium-containing catalysts-The state of the art, Catal. Today. 78 (2003) 47–64.https://doi.org/10.1016/S0920-5861(02)00340-1

[44] I. Nowak, M. Ziolek, Niobium Compounds : Preparation, Characterization, and Application in Heterogeneous Catalysis, Chem. Rev., 99 (1999) 3603–3624.https://doi.org/10.1021/cr9800208

[45] T. Iizuka, K. Ogasawara, K. Tanabe, Acidic and Catalytic Properties of Niobium Pentaoxide, Bull. Chem. Soc. Jpn., 56 (1983) 2927-2931.https://doi.org/10.1246/bcsj.56.2927

[46] V. Lebarbier, M. Houalla, T. Onfroy, New insights into the development of Bronsted acidity of niobic acid, Catal. Today. 192 (2012) 123–129.https://doi.org/10.1016/j.cattod.2012.02.061

[47] T. Uchijima, SMSI effect in some reducible oxides including niobia, Catal. Today. 28 (1996) 105–117.https://doi.org/10.1016/0920-5861(95)00235-9

[48] C.K. Ronald Brown, Influence of strong metal-support interaction on exchange with deuterium and other reactions of hydrocarbons. Part 1. - Studies with Rh/TiO2 and Rh/SiO2, J. Chem. Soc. Faraday Trans. 91 (1995) 741–748.https://doi.org/10.1039/FT9959100741

[49] Q. Xia, Z. Chen, Y. Shao, X. Gong, H. Wang, X. Liu, S.F. Parker, X. Han, S. Yang, Y. Wang, Direct hydrodeoxygenation of raw woody biomass into liquid alkanes, Nat. Commun. 7 (2016) 11162.https://doi.org/10.1038/ncomms11162

[50] A.M. Barrios, C.A. Teles, P.M. De Souza, R.C. Rabelo-neto, G. Jacobs, B.H. Davis, L.E.P. Borges, F.B. Noronha, Hydrodeoxygenation of phenol over niobia supported Pd catalyst, (2017) 115-124 https://doi.org/10.1016/j.cattod.2017.03.034

[51] A. Trovarelli, Catalytic Properties of Ceria Materials, Catalysis Reviews 38 (2016) 439-520.https://doi.org/10.1080/01614949608006464

[52] J. Mikulova, S. Rossignol, F. Gérardy, D. Mesnard, C. Kappenstein, D. Duprez, Properties of cerium–zirconium mixed oxides partially substituted by neodymium: Comparison with Zr–Ce–Pr–O ternary oxides, Journal of Solid State Chemistry 179 (2006) 2511–2520. https://doi.org/10.1016/j.jssc.2006.04.051

[53] S. Damyanova, B. Pawelec, K. Arishtirova, Study of the surface and redox properties of ceria – zirconia oxides, 337 (2008) 86–96. https://doi.org/10.1016/j.apcata.2007.12.005

[54] S.M. Schimming, O.D. Lamont, M. König, A.K. Rogers, A. D. D'Amico, M.M. Yung, C. Sievers, Hydrodeoxygenation of Guaiacol over Ceria – Zirconia Catalysts, ChemSusChem 8 (2015) 2073–2083.https://doi.org/10.1002/cssc.201500317

[55] Z. Zhang, Y. Wang, J. Lu, M. Wang, M. Li, X. Liu, F. Wang, Conversion of Isobutene and Formaldehyde to Diol Using Praseodymium-doped CeO2 Catalyst, ACS Catal.,6 (2016), 8248–8254.https://doi.org/10.1021/acscatal.6b02134

[56] J.L. Ayastuy, A. Iglesias-González, M.A. Gutiérrez-Ortiz, Synthesis and characterization of low amount tin-doped ceria (CeXSn1-XO2-δ) for catalytic CO oxidation, Chemical Engineering Journal 244 (2014) 372–381.https://doi.org/10.1016/j.cej.2014.01.077

[57] R.D. Bayliss, S.S. Pramana, T. An, F. Wei, C.L. Kloc, A.J.P. White, S.J. Skinner, T.J. White, T. Baikie, Fergusonite-type CeNbO4+δ : Single crystal growth, Symmetry Revision and Conductivity, Journal of Solid State Chemistry 204 (2013) 291–297.https://doi.org/10.1016/j.jssc.2013.06.022

[58] J.G. Thompson, R.L. Withers, F.J. Brink, Modulated Structures in Oxidized Cerium Niobates, Journal of Solid State Chemistry 131 (1999) 122–131.https://doi.org/10.1006/jssc.1998.8096

[59] G. Zhang, W. Wan, P. Long, Q. Li, C. Deng, Z. Yi, Synthesis and characterization of mixed conductor CeNbO4, J. Alloys Compd. 616 (2014) 328–332.https://doi.org/10.1016/j.jallcom.2014.05.229

[60] E. Furimsky, Deactivation of hydroprocessing catalysts, Catal. Today. 52 (1999) 381–495.https://doi.org/10.1016/S0920-5861(99)00096-6

3.CHAPTER III

3.1. Materials and Methods

3.1.1. Formulation of the thermodynamic problem (Chapter 4)

The thermodynamic equilibrium of a closed system with specific temperature (*T*) and pressure (*P*) is achieved when the total Gibbs energy (G) reaches a minimum. For a single gas phase with specified *T* and *P*, the total Gibbs energy depends on the number of moles of the species involved. The goal is to find a set of number of moles that minimizes the total Gibbs energy submitted to restrictions imposed by the mass balance. The relationship between the Gibbs free energy (G) and the temperature, pressure and number of moles (n_i) is given by Eq. 3.1:

$$dG = -SdT + VdP + \sum_{i=1}^{N} \mu_i dn_i \qquad \textbf{3.1}$$

In the Equation 3.1, S is the entropy, V is volume and μ_i is the chemical potential of species i. At equilibrium conditions Eq. 3.2 is valid.

$$dG = \sum_{i=1}^{N} \mu_i dn_i = 0 \qquad \textbf{3.2}$$

In order to calculate n_i that minimize the value of G, two approaches can be adopted: stoichiometric and non-stoichimometric methods [1]. In the stoichiometric method, the system is described by a set of stoichiometrically independent reactions, which are chosen based on the knowledgement of the reaction system. On the other hand, the non-stoichiometric approach calculates the equilibrium composition thorough the direct minimization of the Gibbs free energy for a given set of compounds that are detected on the reaction. The advantages of this method are: (a) it is not necessary a previous selection of the possible chemical equations, (b) no divergence appears during the computation and (c) an accurate estimation of the initial equilibrium composition is not necessary. Therefore, the non-stoichiometric method (Lagrange Multipliers method) was used in this work.

The Lagrange Multipliers method takes into account that although the number of moles of each species *i* (n_i) is not conserved in a closed system, the total number of atoms of each element *k* is constant . The Equation 3.3 is the mass balance of each element (k), where A_k is the total number of atomic mass of the kth element in the system and a_{ik} is the number of atoms of the kth element in each molecule of the chemical species i.

$$\sum_i n_i a_{ik} - A_k = 0; \quad k = 1, 2, ..., w \tag{3.3}$$

If Eq. 3.3 is multiplied by a factor λ_k (the Lagrange multiplier for element *k*), summed over *k* and added to the total Gibbs energy of the system, the function to be minimized (*F*) is obtained (Eq. 3.4).

$$F = G^t + \sum_k \lambda_k \left(\sum_i n_i a_{ik} - A_k \right) \tag{3.4}$$

The minimum of Eq. 3.4 occurs when all its partial derivatives are zero (Eq. 3.5).

$$\left(\frac{\partial F}{\partial n_i} \right)_{T,P,n_j} = \left(\frac{\partial G^t}{\partial n_i} \right)_{T,P,n_j} + \sum_k \lambda_k a_{ik} = 0 \tag{3.5}$$

The first term in the right hand side of Eq. 3.5 is by definition the chemical potential of species *i* (μ_i) (Eq. 3.6).

$$\mu_i = G_i^0 + RT \ln \left(\frac{y_i \hat{\phi}_i P}{f_i^0} \right) \tag{3.6}$$

For reactions occurring in gas phase, since the fugacity of an ideal gas is equivalent to its pressure, than $f_i^0 = P_0$ for each species *i*. The fugacity reflects the non-idealities of the mixture and it is a function of temperature, pressure and composition. After setting to zero the standard-state Gibbs energy of species *i* (G_i^0), then G_i^0 becomes equal to the standard Gibbs-energy change of formation of species *i* (ΔGf_i^0). The general expression that represents the minimization of the total Gibbs energy of a species *i* contained in a system with *N* species may now be written as:

$$\Delta G^0_{f,i} + RT\ln\left(\frac{y_i\hat{\phi}_i P}{P^0}\right) + \sum_k \lambda_k a_{ik} = 0; \quad i = 1, 2, \ldots, N \qquad \textbf{3.7}$$

Then, a system of non-linear algebraic equation must be solved in order to obtain the n_i values at equilibrium. The calculations of thermodynamic equilibrium were carried out using the commercial software Maple ® by the minimization of Gibbs free energy.

Based on the HDO reaction experimental using Pd supported catalysts the following compounds were chosen in the thermodynamic equilibrium calculation for the phenol hydrodeoxygenation [2, 3, 4]: Hydrogen, benzene (C_6H_6), cyclohexanone ($C_6H_{10}O$), cyclohexanol ($C_6H_{12}O$), cyclohexane (C_6H_{12}), biphenyl ($C_{12}H_{10}$), hydroxybiphenyl ($C_{12}H_{10}O$), 2,4-cyclohexadienone (C_6H_6O*), 1,3cyclohexadien-1-ol ($C_6H_8O^{\#}$), 2-cyclohexen-1-one (C_6H_8O) and phenol (C_6H_6O). The simulations to evaluate equilibrium compositions were performed in a reaction temperature range from 473-800 K, hydrogen to phenol ratio (H_2/phenol ratio) from 10 to 100 at atmospheric pressure. For Pd samples, the formation of CH_4 was not observed in any condition of phenol HDO reaction used in previous studies done by our group [2-4]. However, in the presence of more oxophilic metals the formation of CH_4 is favored. Thus, the thermodynamic calculations were also performed adding CH_4 as a product in the studied system, aiming to represent the thermodynamic equilibrium over the surface of others metals, such as, Ru, Ni or Co [5].

As the thermodynamics of phenol HDO reaction in gas phase has never been demonstrated and discussed we apparently do not have enough data to validate this analysis. In a previous work [1], it was demonstrated that the same methodology was validated while estimating the equilibrium composition of the reaction reforming processes, which may ensure that the thermodynamic analysis using this methodology is valid.

3.2. Experimental Analysis

3.2.1. Catalyst Preparation

3.2.1.1. Preparation of bimetallic Pd samples supported on zirconia (Chapter 5)

ZrO_2 support was synthesized by the precipitation method. A solution of 2.0 mol/L zirconyl nitrate (35 wt.% $ZrO(NO_3)_2$ in dilute nitric acid, > 99%, Sigma-Aldrich) was added slowly to a solution of 4.0 mol/L ammonium hydroxide (NH_4OH, Vetec) at room temperature, and kept under vigorous stirring for 30 min. The resulting precipitate was filtered and washed with distilled water until a pH of 7 was reached. Then, the solid was dried in an oven at 383 K for 12 h and calcined in a tubular reactor (ID = 1.9 cm) under dry air flow (0.2 g.mL/min) at 773 K (heating ramp of 5 K/min) for 6 h.

Pd/ZrO_2 catalyst was prepared by incipient wetness impregnation of the support with an aqueous solution of the $Pd(NO_3)_2{\cdot}xH_2O$ (Umicore) (wet point = 0.4 mL/g). After impregnation, the material was dried at 373 K for 12 h and then calcined in air flow of 50mL/min at 673 K for 3 h (2 K/min). The bimetallic catalysts were prepared by incipient wetness co-impregnation of the support with an aqueous solution containing $Pd(NO_3)_2{\cdot}xH_2O$ and the precursors salts of the second metal ($AgNO_3$, $Zn(NO_3)_2{\cdot}6H_2O$, $Cu(NO_3)_2{\cdot}3H_2O$ and $SnCl_2$). Then the samples were calcined following the same procedure previously described for the monometallic catalyst. All the catalysts contained 1 wt.% of Pd and a Me/Pd molar ratio of 0.5. The catalysts were designated as Pd/ZrO_2, $PdAg/ZrO_2$, $PdZn/ZrO_2$, $PdCu/ZrO_2$ and $PdSn/ZrO_2$.

3.2.1.2. Preparation of Pd/ZrO_2 with different Pd loading (Chapter 6)

ZrO_2 was synthesized by the precipitation method as reported for *Chapter 5*. Pd/ZrO_2 catalysts with different Pd loadings (0.5%, 1% and 2%) were prepared by incipient wetness impregnation of the support with an aqueous solution containing $Pd(NO_3)_2$ (Sigma–Aldrich, 10 wt. % in 10 wt. % nitric acid). The drying and calcination procedures were the same as used in the samples used in Chapter 5.

3.2.1.3. Preparation of metallic supported- Nb_2O_5 catalysts (Chapter 7)

Niobic acid (CBMM) was dried and calcined in air stream at 623 K for 2 hours. The studied samples were prepared by incipient wetness impregnation of the support with an aqueous solution of the metals nitrates (Ni, Pd and Rh). All chemicals were purchased from commercial suppliers: phenol (Sigma–Aldrich, 99.5%), $Pd(NO_3)_2$ (Sigma–Aldrich,10 wt. % in 10 wt. % nitric acid, 99.999% trace metals basis), $Ni(NO_3)_2.6H_2O$ (Sigma–Aldrich, 99.999% trace metals basis) and Rhodium(III) nitrate hydrate (~36% rhodium (Rh) basis). After impregnation, the material was dried at 373 K for 12 h and then calcined in air at 623 K for 6 h (5 K/min). The catalysts were designated as 1%Pd/Nb_2O_5, 1%Rh/Nb_2O_5 and 5%wt Ni/Nb_2O_5.

3.2.1.4. Preparation of ceria mixed oxides impregnated with nickel (Chapter 8)

CeO_2 and CeO_2 mixed oxides were synthesized by the precipitation method [6]. Aqueous solutions of cerium (IV) ammonium nitrate (reagent ACS 98.5%) and niobium oxalate (CBMM) were prepared in order to obtain the desired amounts of $Ce_xNb_{1-X}O_2$ (X=1.0, 0.90, 0.80, 0.30). The solutions of ceria and niobium were mixed and precipitated by the addition of an excess of ammonium hydroxide. Finally, the precipitate was washed with distilled water, dried at 353K and calcined at 873 K for 2h. Nickel supported samples were prepared by incipient wetness impregnation of the doped cerium oxides with an aqueous solution of the $Ni(NO_3)_2.6H_2O$ (Vetec 97%). After impregnation, the material was dried at 373 K for 12 h and then calcined in air at 623 K for 6 h (10 K/min). All the catalysts contained 10 wt.% of Ni. The catalysts were designated as Ni/CeO_2, Ni/$Ce_{0.90}Nb_{0.10}O_2$, Ni/ $Ce_{0.80}Nb_{0.20}O_2$ and Ni/$Ce_{0.30}Nb_{0.70}O_2$.

3.2.2. Catalyst Characterization

3.2.3. Dispersive X-Ray Fluorescence (WD-XRF)

The chemical composition of each sample was determined using a Wavelength Dispersive X-Ray Fluorescence Spectrometer (WD-XRF) S8 Tiger, Bruker with a rhodium tube operated at 4 kW. The analyses were performed with the samples (300 mg) in powder form using a semi-quantitative method (QUANT-EXPRES/Bruker).

3.2.4. BET surface área

Brunauer–Emmett–Teller (BET) theory aims to explain the physical adsorption of gas molecules on a solid surface and serves as the basis for an important analysis technique for the measurement of the specific surface area of materials. BET surface areas and pore volumes of the samples were measured using a Micromeritics ASAP 2020 analyzer by nitrogen adsorption at 77 K. The samples were pretreated at 333 K for 12 hours.

3.2.5. Raman Analysis

The Raman spectra were recorded using a LabRam HR-UV800/JobinYvon, equipped with thermal conductivity detector (cooled at 153K with liquid N_2) and excitation source of 632 nm. The calcined samples were analyzed, without any pretreatment.

3.2.6. X-ray powder diffraction (XRD)

The X-ray diffraction technique was used to verify the crystalline phases, to estimate the average crystallite size and lattices parameters of ceria mixed oxides. To determine the average crystallite size of the nickel particles (d), the Scherrer equation 3.8 was used.

$$d(nm) = \frac{0{,}1 * K * \lambda}{\{\beta * \cos(\theta)\}} \qquad \textbf{3.8}$$

Where *K* is a dimensionless shape factor, with a value close to unity.The shape factor has a typical value of about 0.9, but varies with the actual shape of the crystallite;

λ is the X-ray wavelength;

B is the line broadening at half the maximum intensity (FWHM), after subtracting the instrumental line broadening, in radians.

θ is the Bragg angle (in degrees).

The position of a diffraction peak is 'independent' of the atomic positions within the cell and entirely determined by the size and shape of the unit cell of the crystalline phase. Each peak represents a certain lattice plane and can therefore be characterized by a Miller index. In this work the UNITCELL® software was used to estimate ceria´s lattice parameters.

3.2.6.1. XRD analysis of bimetallic Pd samples supported on zirconia (Chapter 5)

X-ray powder diffraction (XRD) patterns were obtained in a Rigaku equipment using CuKα radiation (α = 1.5406 Å). Data were collected over the 2θ range of 10º to 80º using a scan rate of 0.02 ^{o}/step and a scan time of 1 s/step.

3.2.6.2. XRD analysis of Pd/ZrO$_2$ with different Pd loading (Chapter 6)

XRD analysis was performed using Cr Kα radiation (k = 0.22897 nm; 50 kV and 40 mA), between 2θ = 10 and 150°. The Cr Kα radiation was used to avoid fluorescence from iron. The Cr Kα radiation was used to avoid fluorescence from iron. Before the XRD analysis, the samples were reduced at 473 K (1 h) in a H_2 flow (30 mL/min).Then the reduced samples were sealed in a glass capillary in vacuum.

For PdAg/ZrO$_2$ X-ray powder diffraction (XRD) patterns were obtained in a Rigaku equipment using CuKα radiation (α = 1.5406 Å). Data were collected over the 2θ range of 10º to 80º using a scan rate of 0.02 °/step and a scan time of 1 s/step.

3.2.6.3. XRD analysis of metallic supported- Nb$_2$O$_5$ catalysts (Chapter 7)

In situ XRD experiments were carried out in diffractometer equipped with a temperature-controlled. The analyses were performed at the Environmental Molecular Sciences Laboratory facility, Pacific Northwest National Laboratory (Richland, WA, United States). The evolution of the crystalline structure in sample powders was dynamically recorded in a pure H_2 (30 mL/min) environments from 298 to 773K. *In situ* variable temperature XRD experiments were carried out using a Philips X'Pert Multipurpose Diffractometer (PANalytical, Almelo, The Netherlands) equipped with a fixed Cu Kα source and an Anton Paar HTK 1200 high-temperature sample stage. Diffraction data were collected on the sample powders at temperatures between 298 and 773K in 2.75% H_2/N_2 flow (30 mL/min). A scan at room temperature was taken and then again at every 100 degrees until the final temperature of 773 K was reached. The heating rate was 10 K/min. The analysis of diffraction data was carried out using JADE 9.1.5 (Materials Data Inc.) and the database (ICSD).

3.2.6.4. XRD analysis of CeO$_2$ doped impregnated with nickel (Chapter 8)

In situ X-ray diffraction (XRD) analyses were obtained at the XPD beamline at the Brazilian Synchrotron Light Laboratory (LNLS). A wavelength of 1.5498 Å at 8.17 keV was used. Powder samples were placed in a house produced furnace (Arara). The XRD patterns were obtained by a Mythen – 1K detector (Dectris) installed 1 m from the furnace. In the first stage, the calcination process were studied, the samples were heated over helium or air synthetic flow (100 mL/min) from room temperature to 1173 K (10K/min). In second stage, XRD analyses also were performed during the reduction of the calcined oxides. This treatment was done using diluted hydrogen (5%H_2/He), the samples were heated from room temperature to 773 K (10 K/min) and kept at this temperature for 1h using a flow of 100 mL/min of diluted H_2.

3.2.7. Temperature programmed reduction (TPR)

TPR is a technique for the characterization of solid materials and is often used in the field of heterogeneous catalysis to find the most efficient reduction conditions. More details are given by Hurst et al. [7].

3.2.7.1. TPR analysis of bimetallic Pd samples supported on zirconia (Chapter 5) and of CeO_2 mixed oxides impregnated with nickel (Chapter 8)

H_2-TPR was performed in a quartz reactor (Hiden Analytical CatLab PCS) coupled to a mass spectrometer (Hiden Analytical, QGA). The reducing mixture (1.96% H_2 in Ar) was passed through the sample (100 mg) and the temperature was increased from room temperature to 1273K at a heating rate of 10 K/min.

3.2.7.2. TPR analysis of metallic supported- Nb_2O_5 catalysts (Chapter 7)

H_2-TPR was performed in a quartz reactor coupled to an adapted Quantasorb Jr. Prior to a TPR experiment, each sample was pretreated under a flow of He at 373 K for 1h, and cooled to room temperature. The reducing mixture (1.96% H_2 in Ar) was passed through the sample and the temperature was increased to 1273 K at a heating rate of 10 K/min.

3.2.8. Scanning Transmission Electron Microscope (STEM)

3.2.8.1. STEM analysis of bimetallic Pd samples supported on zirconia (Chapter 5)

The determination of Pd particle size by transmission electron microscopy is challenging due to the low contrast between the Pd and ZrO_2 support. STEM analysis of passivated Pd/ZrO_2, PdAg/ZrO_2 and PdSn/ZrO_2 were performed and the chemical mapping of dopants and Pd was recorded. The samples were reduced at 773 K (10 K/min) in flowing H_2 (30 mL/min) for 1h. Then, they were cooled to room temperature and passivated under a 5% O_2 in N_2 mixture (30 mL/min). The samples were analyzed with an aberration corrected Scanning Transmission Electron Microscope (STEM) (JEOL JEM-ARM200F) operated at 200 kV. The instrument is equipped with CEOS GmbH double-hexapole aberration corrector for the probe-forming lens, which allows imaging with ~0.8 nm resolution in scanning transmission electron microscopy (STEM) mode. The images were acquired on an HAADF detector with beam convergence of 27.5 mrad and collection angle of 68-280 mrad.

3.2.8.2. *STEM analysis of Pd/ZrO_2 with different Pd loading and 1% PdAg/ZrO_2 (Chapter 6)*

TEM analysis of passivated 1% PdAg/ZrO_2 and 1% Pd/ZrO_2 were performed and the chemical mapping of Ag and Pd were recorded. The samples were reduced at 473 K (10 K/min) in flowing H_2 (30 mL/min) for 1 h. Then, they were cooled and passivated at oxidative atmosphere (around 2% O_2/N_2; 30 mL/min). The samples were analyzed with aberration corrected Scanning Transmission Electron Microscope (STEM) (JEOL JEM-ARM200F) operated at 200 kV. The instrument is equipped with CEOS GmbH double-hexapole aberration corrector for the probe-forming lens, which allows imaging with ~0.8 nm resolution in scanning transmission electron microscopy (STEM) mode. The presented images were acquired on HAADF detector with beam convergence of 27.5 mrad and collection angle of 68-280 mrad. Elemental analysis was performed using Energy Dispersive Spectroscopy (EDS) with high collection angle SSD (~0.7 srad, JEOL Centurio). The data were acquired and evaluated with NSSThermo Scientific software package. The STEM sample preparation involved mounting powdered samples on copper/nickel grids covered with lacey carbon support films, and then immediately loading them into the STEM airlock to minimize an exposure to atmospheric O_2.

3.2.9. H_2 chemisorption

3.2.9.1. *H_2 chemisorption analysis of bimetallic Pd samples supported on zirconia (Chapter 5)*

The dispersion was determined by H_2 chemisorption, using the dynamic flow method. Prior to adsorption, the sample was reduced *in situ* under pure hydrogen (30 mL/min) at 773 K for 1 h. Then, the sample was cooled to 343 K under He flow (30 mL/min). Then, pulses of 5%H_2 in Ar mixture were injected until saturation was reached, as monitored by a quadrupole mass spectrometer (Balzers, Omnistar). The adsorption was carried out at 343 K in order to avoid formation of the β-Pd hydride phase [14]. Pd dispersion was calculated assuming an H/Pd molar ratio of 1.

3.2.9.2. *H_2 chemisorption analysis of Pd/ZrO_2 with different Pd loading (Chapter 6)*

H_2 chemisorption was measured in an ASAP (Micrometrics) apparatus. The samples were dried at 423 K for 3 h and then reduced at 473 K (10 K/min) in flowing H_2 (30 mL/min).

Following reduction, the samples were evacuated for 1 h at the reduction temperature and cooled to adsorption temperature (343 K) under vacuum. The adsorption stoichiometry of H/$Pd_{surface}$ of 1 was adopted for calculating the number of surface Pd atoms and Pd dispersion (the fraction of surface atoms within all atoms in the particle).

3.2.10. Dehydrogenation of Cyclohexane reaction

In order to investigate the variation of Pd dispersion during the HDO of phenol reaction, the dehydrogenation of cyclohexane reaction was used as an insensitive structure reaction to determine the Pd dispersion of the fresh and used (after HDO of phenol reaction for 24 h TOS) catalysts. This reaction was not carried out with PdCu catalyst because Cu is also active for this reaction. Therefore, the Pd dispersion was determined by a correlation between the rate of cyclohexane dehydrogenation and palladium dispersion of catalysts (Pd/SiO_2, Pd/Al_2O_3 and Pd/ZrO_2) with dispersion measured by CO chemisorptions [8]. Cyclohexane dehydrogenation was performed in a fixed-bed reactor at atmospheric pressure. The fresh samples were first reduced at 773 K for 1 h and the reaction was carried out at 543 K and WHSV = 120 h^{-1}. The reaction mixture was fed into the reactor by bubbling H_2 through a saturator containing cyclohexane at 285 K ($H_2/C_6H_{12} = 13.6$). At these conditions, no mass transfer or equilibrium limitations were observed. The conversions were kept below 10%. For the used catalysts, after HDO of phenol for 24 h, the saturator containing phenol was bypassed and hydrogen was allowed to flow through the catalyst for 30 min at 573 K, which removed hydrocarbons that remained adsorbed on the surface. The reactor was cooled to 543 K under hydrogen. Then, a cyclohexane/H_2 mixture was passed through the reactor. The exit gases were analyzed using an Agilent 7890A/5975C GCMS equipped with a HP-INNOWAX column and a flame-ionization detector (FID).The variation in dispersion after HDO of phenol reaction for 24 h of TOS was calculated according to Eq.3.9, which corresponds to the ratio between the cyclohexane dehydrogenation rate of used and fresh catalysts.

$$DR(\%) = \frac{Cyclo\,hexane\;\;dehydrogenation\;\;\;rate\;\;of\;used\;catalyst}{Cyclo\,hexane\;\;dehydrogenation\;\;\;rate\;\;of\;fresh\,catalyst} * 100 \qquad \textbf{3.9}$$

The calibration curve used was:

$$\text{Pd Dispersion} = 3.56\;10^{4} * \text{Cyclohexane dehydrogenation Rate} + 9.29 \qquad \textbf{3.10}$$

3.2.11. X-ray photoelectron spectroscopy (XPS)

X-ray photoelectron spectroscopy (XPS) is a surface-sensitive quantitative spectroscopic technique that measures the elemental composition at the parts per thousand range, empirical formula, chemical state and electronic state of the elements that exist within a material.

3.2.11.1. *XPS analysis of bimetallic Pd samples supported on zirconia (Chapter 5), Pd/ZrO_2 with different Pd loading (Chapter 6) and metallic supported- Nb_2O_5 catalysts (Chapter 7)*

XPS measurements of both unreduced as well as reduced catalysts were performed at the Environmental Molecular Sciences Laboratory facility, Pacific Northwest National laboratory in a physical Electronics Quantera Scanning X-ray Microprobe. The samples were reduced in situ at the different temperatures (373-773K) under a 5%H_2/Ar mixture inside the side chamber, from which the sample can be transferred to the main spectrometer chamber without any exposure to air. After each treatment, the temperature was cooled to room temperature under 5%H_2/Ar. Then, the system was evacuated and the samples were transferred to the main chamber to proceed with the measurements. This system uses a focused monochromatic Al Kα X-ray (1486.7 eV) source for excitation and a spherical section analyzer. The instrument has a 32 elements multichannel detection system. A 98 W X-ray beam focused to 100 μm diameter was scanned over a 1.2 mm x 0.2 mm rectangle on the sample. The X-ray beam is incident normal to the sample and the photoelectron detector is at 45° off-normal. High energy resolution spectra were collected using a pass-energy of 69.0 eV with a step size of 0.125 eV. For the Ag $3d_{5/2}$ line, these conditions produced a FWHM of 0.91 eV. The binding energy (BE) scale was calibrated using the Cu $2p_{3/2}$ line at 932.62 ± 0.05 eV and Au $4f_{7/2}$ line at 83.96 ± 0.05 eV from known high purity reference foils. The sample experienced variable degrees of charging. Low energy electrons at ~1 eV, 20μA and low energy Ar^+ ions were used to minimize this charging.

3.2.11.2. *XPS analysis of CeO_2 mixed oxides impregnated with nickel (Chapter 8)*

X-ray photoelectron spectroscopy (XPS) analyses of the samples were performed with a hemispherical spectrometer from SPECS (model PHOIBOS150 HSA3500) in operation at the LNLS. The analyses were performed before and after the reduction of the samples. The reduction process was done in situ, the samples were heated from room temperature to 773K and kept at 773K for 1h under a 5%H_2/Ar mixture. This procedure was performed inside the side chamber, from which the sample can be transferred to the main spectrometer chamber without any exposure to air. After reduction treatment, the temperature was cooled to room temperature under 5%H_2/Ar. Then, the system was evacuated and the samples were transferred to the main chamber to proceed with the measurements. This system uses a focused monochromatic Al Kα X-ray (1486.7 eV) source for excitation and a spherical section analyzer. The monochromatic Al Ka source was operated at 10 kV and 10 mA and the spectra were obtained with an analyzer pass energy of 20 eV. The spectra were analyzed using Casa XPS software, version 2.2.99. The binding energies were referenced to the C 1s line at 284.5 eV from the adventitious carbon.

3.2.12. Cyclohexanol dehydration reaction

The oxophilic sites of the reduced catalysts at different temperatures were quantified using the cyclohexanol dehydration reaction, according to the procedure used by de Souza et al. [9]. The reaction was performed in a fixed-bed quartz reactor at atmospheric pressure and 573 K. Prior to the reaction, the fresh catalyst was reduced in situ under pure hydrogen (60 mL/min) at 573 and 773 K for 1 h. The reactant mixture was obtained by flowing He (30 mL/min) through a saturator containing cyclohexanol, which was maintained at 336 K. The reaction products were analyzed by GCMS (Agilent Technologies 7890A/5975C) using an HP-Innowax capillary column and a flame-ionization detector (FID). The dehydration rate was calculated by the sum of cyclohexene, cyclohexane, and benzene yields.

3.2.13. XAS (X-ray absorption spectra) analysis

X-ray absorption spectroscopy (XAS) measures the energy-dependent fine structure of the X-ray absorption coefficient near the absorption edge of a particular element (Ravel2004). The spectrum consists of two parts, the near-edge part XANES (x-ray absorption near-edge structure) which gives chemical information and EXAFS (extended X-ray absorption fine structure) which gives the structural information. The XANES (+/-50 eV relative to the absorption edge) is comprised primarily of multiple scattering and transition-to-empty states in the vicinity of the Fermi level by low energy photoelectrons with relatively long mean free paths. The XANES can provide information on the oxidation state from the size and shift in the edge-transition and on the coordination symmetry of ligands around the excited atom from the shape of the edge transition [10]. For photon energies higher than ~30 eV above the edge, the photoelectron is promoted to a free or continuum state. EXAFS is thus independent of chemical bonding and depends on the atomic arrangement around the absorber. It contains information about the coordination number, interatomic distances and structural and thermal disorder around a particular atomic species [11] [12].

3.2.13.1. *XAS analysis of bimetallic Pd samples supported on zirconia in-situ (Chapter 5)*

H_2-TPR XAFS studies were performed at the Materials Research Collaborative Access Team (MR-CAT) beamline at the Advanced Photon Source, Argonne National Laboratory. A cryogenically cooled Si (1 1 1) monochromator selected the incident energy and a rhodium-coated mirror rejected higher order harmonics of the fundamental beam energy. A stainless steel multi-sample holder (3.0 mm i.d. channels) was used to monitor the *in-situ* reduction of 6 samples during a single TPR run. Approximately 14 mg of each sample was loaded as a self-supporting wafer in each channel. The catalyst to diluent weight was approximately 0.1. The holder was placed in the center of a quartz tube, equipped with gas and thermocouple ports and Kapton windows. The amount of sample used was optimized for the Pd or Ag K edge, considering the absorption by Zr of the support. The quartz tube was placed in a clamshell furnace mounted on the positioning table. Each sample cell was positioned relative to the beam by finely adjusting the position of the table to an accuracy of 20 μm (for repeated scans). Once the sample positions were fine-tuned, the reactor was purged with helium for more than 5 min at 100 ml/min then the reactant gas (4%H_2/He) was flowed through the samples (100 mL/min) and a temperature ramp of ~1K/min was initiated for the furnace. The sample was held at 773 K for 1 h prior to cooling to room temperature. The Pd and Ag K-edge spectra were recorded in transmission mode and a Pd metallic foil spectrum was measured simultaneously with each sample spectrum for energy calibration. X-ray absorption spectra for each sample were collected from 24,100 to 25,300 eV for Pd or 25,280 to 26,100 eV for Ag, with a step size of ~1 eV and acquisition times of 2.3 min per sample. By measuring each sample, in turn, and repeating, this allowed 37 scans to be collected for each sample over an 8.5 h period. The temperature change of the sample from the absorption edge through the end of the scan was around 2 K, while each sample was measured approximately every 13 K.

Data reduction of the EXAFS (Extended X-Ray Absorption Fine Structure) and XANES (X-ray absorption near edge spectra) spectra was carried out using the WinXAS program [13-14]. EXAFS data reduction and fitting were carried out using the catalysts in their final state following TPR and cooling using the WinXAS [13], Atoms[15], FEFF [16], and FEFFIT [17] programs. The k-range used for the fittings was 2.75-12 $Å^{-1}$. Fitting was confined to the first Pd-M (M = Cu, Zn, Pd, Ag, and/or Sn) or Ag-M (M = Pd and/or Ag) metallic coordination shell by applying a Hanning window in the Fourier transform magnitude spectra, and carrying out the back-transform to isolate that shell.

3.2.13.2. XAS analysis of Pd/ZrO$_2$ with different Pd loading (Chapter 6)

X-ray absorption spectra were measured at the Advanced Photon Source, beamline Sector 20 at Argonne National Laboratory (USA) using the Si(111) monochromator. Fresh catalysts were reduced in pure H_2 (30 mL/min) ex situ at 473 K for 1 h and cooled to room temperature. After the reduction, the reactor was isolated and the samples were transferred to a capillary into a glove box that was sealed with wax. To assure that the isolated samples were not contaminated with air during the time, this capillary was also fire sealed. To keep the vacuum inside the capillary during the fire sealing process, the capillary was kept in a liquid N_2 bath. The X-ray absorption spectra were recorded at the Pd K-edge (24350 eV). The raw data were energy-calibrated with Pd foil, background-corrected, normalized and fitted using the ATHENA and ARTHEMIS programs. The k-range used for the fittings was 2.0-12.5 Å^{-1} for Pd. The PdO and the Pd foil spectra were used as references for the linear combination fittings of XANES spectra at the Pd edges. The residual factors (R-factor) of the fits were less than 0.8%, which is an indication that the fitting was good.

3.2.13.3. XAS analysis of metallic supported- Nb$_2$O$_5$ catalysts (Chapter 7)

In-situ H_2-TPR X-ray absorption near edge spectra (XANES) spectra at the Pd K edge (24350 eV), Ni K edge (8333eV), Nb k edge (18986 eV) and Rh K edge (23220 eV) for the samples were collected using the LNLS (Brazilian Synchrotron Light Laboratory - BRAZIL) facility. In the first stage, the spectra were acquired at room temperature in transmission mode with three ionization chambers using a Si(311) double-crystal monochromator under H_2 diluted flow (5% H_2/He) for all the samples. In sequence, the samples were heated until the desired temperatures (573 or 773 K) for 1h (10 K/min). Standard foils of the metals were used for energy calibration.

3.2.13.4. XAS analysis of CeO$_2$ mixed oxides impregnated with nickel (Chapter 8)

In situ X-ray absorption near edge spectroscopy (XANES) measurements at the Ce L3-edge (5723 eV) were performed at the DXAS at the LNLS (Laboratório Nacional de Luz Síncrotron, Campinas, Brazil). DXAS is a dispersive beamline equipped with a curved Si (111) focusing monochromator operating in Bragg mode and the X-ray range varies from 4 to

14 keV focusing the beam at the sample position. The detection system is comprised of 1152 x 1242 (500 x 900) pixel CCD solid-state detector. The samples were analyzed in a pastille placed in a quartz reactor. The reduction process of samples was performed using a diluted hydrogen (5% H_2 balance in He) with a total flow of 100mL/min and a heating rate of the 10 K/min from room temperature to 773K (1h). Athena software packages were used to extract the XANES signal from the measured absorption spectra using standard proceedings. XANES spectra of the reference materials CeO_2 and cerium nitrate were recorded at room temperature.

X-ray absorption spectra (XAS) were acquired in transmission mode at the Nb-K edge (18986 eV) and Ni-K edge (8333 eV) using the XDS and XAFS-2 beamlines at LNLS, respectively. Two monochromators were used as follows: a Si(3 11) crystal for the Nb-K edge and a Si(111) crystal for the Ni-K edges. Intensities were measured using three sequential ionization chambers filled with mixtures of N_2 and Ar at ambient temperature and 1 bar of pressure. Photon energies were calibrated using a thin metal film (Ni or Nb) placed between the second and third ionization chambers. Spectra were collected at the absorption edge for each metal present in a range between 200 eV before and 120 eV after for Nb and 200 eV before and 1000 eV after for Ni dge. The reduction procedure (~ 773 K for 1h) were perfomed for each sample. For EXAFS analysis at Ni-K edge after the reduction, the samples were cooled to ambient temperature under Helium flow (100mL/min). Data reduction of the EXAFS/XANES spectra was carried out using the Arthemis program. EXAFS data reduction and fitting were carried out using the catalysts in their final state following TPR and cooling using the WinXAS [13], Atoms [15], FEFF [16], and FEFFIT [15] programs. The k-range used for the fittings was 2.75-14.16 $Å^{-1}$. Fitting was confined to the first Ni-Ni metallic coordination shell by applying a Hanning window in the Fourier transform magnitude spectra, and carrying out the back-transform to isolate that shell.

3.2.14. HDO reaction in the gas phase

HDO of phenol was carried out in a fixed-bed quartz reactor, operating at atmospheric pressure of H_2. In chapter 4, the reaction was performer at different temperatures (573, 623 and 673 K). Prior to reaction, the Pd and Ru catalysts [24, 23] were reduced in situ under pure hydrogen (60 mL/min) at 573 or 773 K for 1 h, respectively. For the Pd/ZrO_2 and $Pd\text{-}M/ZrO_2$ (M=Ag, Sn, etc) samples presented in chapter 5, the reduction was done in situ under pure hydrogen (60 mL/min) at 773 K for 1 h. For the catalysts presented in chapter 7 ($1\%Pd/Nb_2O_5$, $1\%Pd/Nb_2O_5$ and $5\%Ni/Nb_2O_5$) the reduction was also performed in situ under pure hydrogen flow (60 mL/min) at 573 or 773 K for 1 h. For the samples supported on ceria-niobia, discussed in chapter 8, the sample was reduced in situ under pure hydrogen flow (60 mL/min) at 773 K for 1 h. In the chapters 5, 6, 7 and 8 the reaction was run at 573 K. For all the analysis the catalysts were diluted with inert material (m_{SiC}/m_{catal} = 3.0) to avoid the formation of hot-spots. The reactant mixture (1.6 % of phenol) was obtained by flowing H_2 through the saturator containing the organic compound, which was kept at the specific temperature required to obtain the desired H_2/organic compound molar ratio (about 60). To avoid condensation, all lines were heated at 523 K. The reaction products were analyzed using an Agilent Technologies 7890A/5975C GCMS, using HP-Innowax capillary column and a flame-ionization detector (FID).

In chapters 5 and 8 the catalysts were evaluated at different residence time (W/F) by varying the catalyst amount in the range of 2.5-200 mg. W/F is defined as the ratio of catalyst mass (g) to organic feed mass flow rate (g/h).

In chapters 5, the stability tests were performed during 24 h of time on stream (TOS), using W/F value corresponding to the highest phenol conversion obtained.

The product yield and selectivity for each product were calculated as follows (Eqs. 3.11 and 3.12):

$$yield(\%) = \frac{mol\ of\ product\ produced}{mol\ of\ phenol\ fed} \times 100 \qquad \textbf{3.11}$$

$$Selectivity\ (\%) = \frac{mol\ of\ product\ produced}{mol\ of\ phenol\ consumed} \times 100 \qquad \textbf{3.12}$$

The stability of the catalysts was defined as the ratio between the reaction rate at t_0 = 0.2 h and t_f= 24 h TOS (Eq. (3.13)), assuming that the deactivation rate exhibits a first-order kinetics.

$$DP = \frac{Ln(1-X_{end})}{Ln(1-X_{initial})} \qquad \textbf{3.13}$$

3.2.15. HDO reaction in liquid phase.

Kinetic measurements were carried out in a Parr reactor (Series 4848, 300 mL), using aqueous phenol solutions (0.30 M) at 50 bar of H_2. In a typical experiment, phenol, Pd/ZrO_2 and H_2O were loaded in the reactor, purged three times with H_2 and pressurized to 50 bar of H_2. After the reaction temperature was reached, the stirring (680 rpm) was initiated and the reaction time was recorded from that point. Apparent activation energies were calculated from initial rates measured at 443, 453, 463 and 473 K. After reaction, the reactor was cooled down by ice/water mixture to ambient temperature. Following discharge of the pressure, the reactor was opened and the liquid content was extracted with dichloromethane (DCM) for four times (25 ml per extraction). An aliquot of the DCM solution containing unreacted phenol and products was analyzed by GC/MS using 1,3-dimethoxybenzene as the internal standard. The balance carbon closed around 97%. The catalysts were not previously reduced, according to the procedure validated by Chase et al. [18]. In that work, the authors verified that Pd oxide shell was rapidly reduced at the beginning of the reaction during the heat-up to 473 K. This was also shown using XAS experiments under similar reactions conditions used in the present work.

Reference

[1] K.A. Resende, C.N. Ávila-Neto, R.C. Rabelo-Neto, F.B. Noronha, C.E. Hori, Thermodynamic analys
reaction routes of steam reforming of bio-oil aqueous fraction, Renew. Energy. 80 (2015) 166–176.
https://doi.org/10.1016/j.renene.2015.01.057

[2] C.A. Teles, R.C. Rabelo-neto, G. Jacobs, B.H. Davis, D.E. Resasco, Hydrodeoxygenation of phenol c
zirconia supported catalysts . The effect of metal type on reaction mechanism and catalyst deactivation,
ChemCatChem 9 (2017) 1-15. https://doi.org/10.1002/cctc.201700047

[3] P.M. de Souza, R.C. Rabelo-neto, L.E.P. Borges, G. Jacobs, B.H. Davis, T. Sooknoi, D.E. Resasco, F
Noronha, Role of Keto Intermediates in the Hydrodeoxygenation of Phenol over Pd on Oxophilic Suppo
Catal., 5 (2015) 1318–1329. https://doi.org/10.1021/cs501853t

[4] P.M. De Souza, R.C. Rabelo-neto, L.E.P. Borges, G. Jacobs, B.H. Davis, D.E. Resasco, F.B. Noronh
Hydrodeoxygenation of phenol over Pd catalysts . Effect of support on reaction mechanism and catalyst
deactivation, ACS Catal., 7 (2017) 2058–2073. https://doi.org/10.1021/acscatal.6b02022

[5] C. A. Teles, R. C. Rabelo-Neto, J. R. de Lima, L. V. Mattos, D. E. Resasco, F. B. Noronha, The Effec
Metal Type on Hydrodeoxygenation of Phenol Over Silica Supported Catalysts, Catal. Letters. 146 (201
1857. https://doi.org/10.1007/s10562-016-1815-5

[6] C.E. Hori, H. Permana, K.Y.S. Ng, A. Brenner, K. More, K.M. Rahmoeller, D. Belton, Thermal stabi
oxygen storage properties in a mixed CeO2-ZrO2 system, Appl. Catal. B-Environmental. 16 (1998) 105-
https://doi.org/10.1016/S0926-3373(97)00060-X

[7] N.W. Hurst, S.J. Gentry, B.D. Mcnicol, Temperature Programmed Reduction, Catalysis Reviews : Sc
and Engineering Temperature Programmed Reduction, 24 (1982) 233-309.
https://doi.org/10.1080/03602458208079654

[8] L.S.F. Feio, C.E. Hori, S. Damyanova, F.B. Noronha, W.H. Cassinelli, The effect of ceria content on
properties of Pd/CeO2/Al2O3 catalysts for steam reforming of methane, 316 (2007) 107–116.
https://doi.org/10.1016/j.apcata.2006.09.032

[9] P.M. De Souza, R.C. Rabelo-neto, L.E.P. Borges, G. Jacobs, B.H. Davis, U.M. Graham, D.E. Resasc
Noronha, Effect of Zirconia Morphology on Hydrodeoxygenation of Phenol over Pd/ZrO2, ACS Catal. 5
7385–7398. https://doi.org/10.1021/acscatal.5b01501

[10] S. Mukerjee, S. Srinivasan, M.P. Soriaga, J. Mcbreen, Role of Structural and Electronic Properties o
Pt Alloys on Electrocatalysis of Oxygen Reduction, J. Electrochem. Soc.,142 (1995).
https://doi.org/10.1149/1.2048590

[11] D.E. Sayerst, E.A. Sterntf, F. Lytle, New Technique for Investigating Noncrystalline Structures: Fou
Analysis of the Extended X-Ray- Absorption Fine Structure, Physical Review Letters, 2 (1971) 1204.
https://doi.org/10.1103/PhysRevLett.27.1204

[12] S.I. Zabinsky, J.J. Rehr, A. Ankudinov, R.C. Albers, M.J. Eller, Multiple Scattering Calculations of
Absorption Spectra, (1994) 1–43. https://doi.org/10.1103/PhysRevB.52.2995

[13] Ressler, T. WinXAS: A program for X-ray absorption spectroscopy data analysis under MS-Windo
Synchrotron Rad. 5 (1998) 118–22. https://doi.org/10.1107/S0909049597019298

[14] Jacobs, G.; Ji, Y.; Davis, B.H.; Cronauer, D.; Kropf, A.J.; Marshall, C.L. Fischer-Tropsch synthesis:
Temperature programmed EXAFS/XANES investigation of the influence of support type, cobalt loading
noble metal promoter addition to the reduction behavior of cobalt oxide particles. Appl. Catal. A 333 (20
177–191. https://doi.org/10.1016/j.apcata.2007.07.027

[15] Ravel, B. Atoms: crystallography for the X-ray absorption spectroscopist. J. Synchrotron Rad. 8 (20
316. https://doi.org/10.1107/S090904950001493X

[16] Rehr, J. J.; de Leon, J. M.; Zabinsky, S. I.; Albers, R. C. Theoretical x-ray absorption fine structure
standards. J. Am. Chem. Soc. 113 (1991) 5135–5140. https://doi.org/10.1021/ja00014a001

[17] Ravel, B.; Newville, M. ATHENA, ARTEMIS, HEPHAESTUS: Data analysis for X-ray absorption
spectroscopy using IFEFFIT. J. Synchrotron Rad. 12 (2005) 537–541.
https://doi.org/10.1107/S0909049505012719

[18] Z.A. Chase, J.L. Fulton, D.M. Camaioni, D. Mei, M. Balasubramanian, V. Pham, C. Zhao, R.S. Wel
Wang, J.A. Lercher, State of Supported Pd during Catalysis in Water, J. Phys. Chem. C 117 (2013)
17603−17612. https://doi.org/10.1021/jp404772p

4.CHAPTER IV

4.1. Thermodynamic Analysis of the hydrodeoxygenation reaction of phenol in gas phase.

ABSTRACT –The conversion of biomass into bio-oil through fast pyrolysis followed by its upgrading via hydrodeoxygenation (HDO) is considered a potential route for the production of renewable fuels. The catalytic upgrading of bio-oil is a complex reaction network involving different reactions such as decarbonylation, decarboxylation, hydrocracking, hydrodeoxygenation, hydrogenation and polymerization. Since the upgrading of the phenolic compounds present in bio oil is a vital step to its viabilization as an energy alternative, it is interesting to perform a thermodynamic study in order to determine the most favorable operational conditions for this process. It is also important to determine the thermodynamic limits for the mole fractions of each component. In this study phenol was used as model compound to represent bio-oil. Initially, we conducted the activity test of the phenol HDO reaction at different temperatures using 2%Pd/ZrO_2 and 5%Ru/ZrO_2 as catalysts. In sequence, the equilibrium mole fractions of the gaseous products in dry basis were calculated using the Lagrange multipliers method. These data were obtained at different temperatures (400-800K) and for various H_2/phenol ratios (10-100). During the thermodynamic analysis, when CH_4 was considered as a product, only it was observed in equilibrium conditions. For the study without CH_4, the best operationalconditions to perform the phenol HDO reaction are at intermediate temperatures (≤600K) and with high H_2/phenol ratio.

Keywords: Equilibrium, hydrodeoxygenation, gas phase, phenol, H_2, Pd.

4.2. Introduction

The conversion of biomass to bio-oil is a promising route to produce high-energy density fuels [1], which may be processed through the fast pyrolysis or liquefaction of biomass at fixed conditions (temperature > 700 K) [2,3]. The high oxygen content in pyrolysis oil leads to undesirable oil properties, such as low energy density and thermal and chemical instability. Thus, the upgrading of bio-oil by hydrodeoxygenation (HDO) is considered a very important step to the final production of renewable fuels, since this process provides the elimination of oxygen from biomass-derived feed stocks through the water production [1].

The catalytic upgrading of bio-oil is a complex reaction network involving different reactions such as decarboxylation, hydrocracking, hydrodeoxygenation, hydrogenation and polymerization [4].The average composition of pyrolysis oils is 50–65 wt% organic components, that includes organic acids, aldehydes, ketones, furans, phenolic compounds, guaiacols, syringols and sugar based compounds, 15–30 wt% water and 20 wt% colloidal lignin fraction [5,6]. The phenolic content are a major part of the lignin fraction, which may reach 30% of this fraction [6–7]. Thus, due to the complex composition of bio-oil, a significant number of studies have reported the use of model molecules to elucidate the HDO reaction mechanism [5-7]. These compounds are chosen to represent different fractions of biomass such as sugars and sugar alcohols (cellulose and hemi-cellulose) and phenolic compounds such as cresols, guaiacol, phenol (lignin fraction of biomass) [5].

There are several groups that investigated HDO reactions aiming the upgrade of bio-oil. Three routes can be considered for HDO reaction: (i) hydrogenation (HYD) (ii) direct deoxygenation route (DDO) and (iii) tautomerization [9-11]. Mortensenet al.[11] studied different catalysts in the phenol HDO reaction and suggested a mechanism for the HDO of phenol over nickel catalysts supported on ZrO_2. According to them the activation of phenol on the oxide can take place through heterolytic dissociation of the O-H bond on the oxide, which behaves like Lewis acid site. The hydrogen from the phenol is adsorbed on an oxygen site in the oxide surface layer and a metal vacancy site stabilizes the phenoxide ion. The phenoxide will interact with a nickel crystallite where hydrogen has been adsorbed, thereby facilitating the saturation of the double bounds and producing cyclohexanone. Sun et al. [13] studied the vapor-phase hydrodeoxygenation (HDO) of guaiacol (GUA). The reaction pathways for guaiacol HDO (based on the major products) are highly dependent on the type of catalyst. In most cases, phenol was the major intermediate formed through either demethylation of guaiacol followed by HDO of catechol or demethoxylation of guaiacol with the latter being the major pathway on Fe, Cu, and PdFe catalysts. Phenol conversion preceded in different reaction pathways depending on the metal and reaction temperatures. Another interesting study was presented by Nieet al. [14], which investigated the catalytic conversion of m-cresol in the presence of H_2 on SiO_2-supported Ni, Fe ,and bimetallic Ni–Fe catalysts at 573 K and atmospheric pressure. The authors proposed at least two parallel pathways: (i) One is the direct hydrogenation of the aromatic ring, which could be dehydrated and then dehydrogenated to the deoxygenated product (Toluene); (ii) a second (indirect) path where m-cresol can tautomerize to a highly unstable methyl cyclohexadienone or cyclohexanol. Therefore, phenol is an important intermediated in the HDO reaction of the different model compounds.

Thermodynamic analysis has been used extensively used in the literature to help to optimize operational conditions of different processes: (i) reforming of bio-oil compounds aiming the production of hydrogen [15,16]; (ii) gas-phase hydrogenation of aromatics [17]; (iii) glycerol [18,19] (iv) methanation reactions [20] (v) upgrading of syngas [21] (vi) supercritical water gasification of different compounds [22]. In general, thermodynamic analyses are done using model molecules [15-19]. In the literature there are very few thermodynamic studies of HDO reactions. Shin et al. [17] studied the gas-phase hydrogenation/hydrogenolysis alcoholic phenol solutions between 423 and 573 K using a Y zeolite-supported nickel catalyst (2.2% w/w Ni) and Ni/SiO_2 catalysts (1.5-20.3% w/w Ni). The thermodynamic limitations of the hydrogenation/hydrogenolysis reactions involved in the process were considered by estimating the equilibrium constants using the NIST database at 498 K. According to them the calculations indicate that the standard free energies of reaction are negative for each hydrogenolysis/hydrogenation step with the exception of the partial hydrogenation of benzene to cyclohexene. All hydrogenolysis and the benzene to cyclohexane steps can be considered to be irreversible while the stepwise hydrogenation of phenol may be governed by equilibrium.

To our knowledge there is no study in the literature dealing with the thermodynamic analysis of the gas phase phenol HDO reaction.Thus, the objective of this work is to analyze the thermodynamics of this reaction, to understand the effect of operating variables such as H_2 to phenol ratio and temperature on the product distribution verified at equilibrium conditions. The thermodynamic analyses are then related to experimental tests of gas phase phenol HDO over $5\%Ru/ZrO_2$ and $2\%Pd/ZrO_2$ catalyst.

4.3. Results and Discussion

In general, three routes can be considered for HDO reaction: (i) hydrogenation (HYD) (ii) direct deoxygenation route (DDO) and (iii) tautomerization. Recently, our group have been intensely investigated the gas phase HDO reaction of phenol [23-25]. De Souza et al. [23] tested the performance of Pd catalysts supported on SiO_2, Al_2O_3 and ZrO_2 for HDO of phenol in the followed operational conditions: reaction temperature = 573 K, P = 1 atm and H_2/phenol molar ratio = 60. The possible pathway proposed by the authors over Pd catalysts is the phenol tautomerization to 2,4-cyclohexadienone intermediate. In general, they reported that Pd supported on ZrO_2 favors the formation of benzene though dehydration of 2,4 - cyclohexadienol, while Pd on SiO_2 and Al_2O_3 showed a high selective to hydrogenated (cyclohexanone and cyclohexanol) products. Teles et al. [24] investigated different metals in the HDO reaction using operational conditions similar to the ones used by de Souza et al. [23]. A neutral support (SiO_2) was chosen to better understand the metal effect in this reaction. According to the authors more oxophilic metals, such as, Ru, Co and Ni favor the direct dehydroxylation of phenol followed by hydrogenolysis, which leads the formation of benzene and hydrocarbons. On the other hand Pt, Pd and Rh promote mainly phenol tautomerized to hydrogenated products, such as, cyclohexanone and cyclohexanol. The HDO reaction pathways over supported metal catalysts proposed by de Teles et al. [24] are present in Figure 4.1.

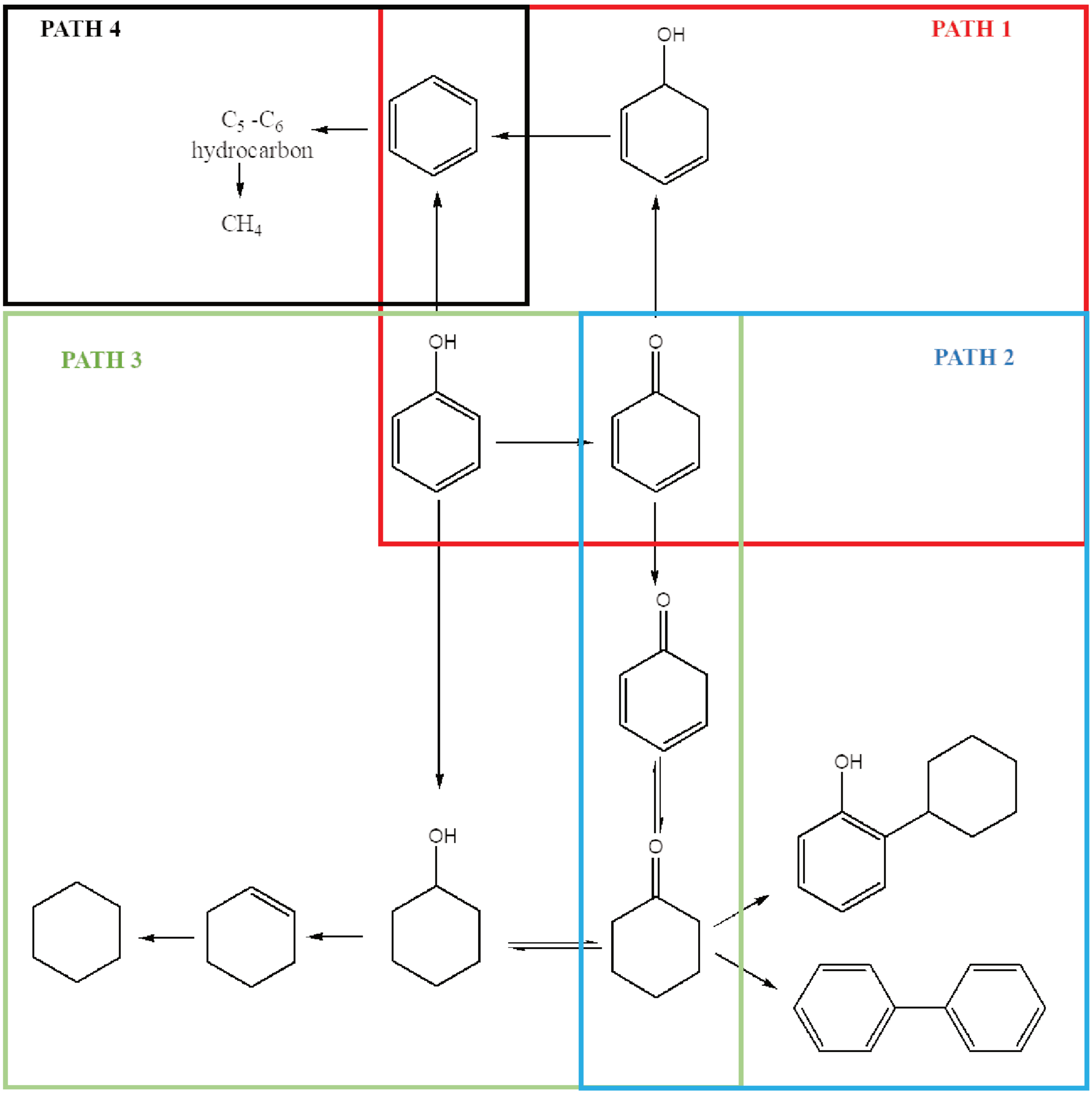

Figure 4-1. HDO reaction pathway over supported catalysts proposed by Teles et al. [24].

Based on the reaction mechanism previous studies [23-25], the system of linearly independent reactions represented by reactions R1-R16 is proposed to represent the thermodynamic equilibrium of phenol HDO (Table 4.1). The possibility of thermodynamic limitations was considered by estimating the equilibrium constants using the NIST database. The thermodynamically calculations indicate that the standard free energies of reaction are negative for each hydrogenolysis/hydrogenation, as reported by Shin et al. [17].

The mechanism proposed by Teles et al. [24] for phenol HDO reaction in the gas phase was divided in 4 paths as shown in Figure 4.1 and the natural logarithms of the equilibrium constants of these reactions (R1-R16) as a function of temperature were evaluated. Similar studied was performed by Liu et al. [27] to evaluate the five possible pyrolytic pathway of guaiacol.

Table 4-1.Standard Gibbs free energies of reactions considered in the mechanism of phenol HDO mechanism [23-25].

	Reaction	**ΔG^0_{298K} (kJ/mol)**
(R1)	$C_6H_6O+H_2\rightarrow C_6H_6+H_2O$	**-82.52**
(R2)	$C_6H_6O +3H_2\rightarrow C_6H_{12}O$	**-79.84**
(R3)	$C_6H_{12}O \rightarrow C_6H_{10} +H_2O$	**-62.60**
(R4)	$C_6H_{12}O+H_2\rightarrow C_6H_{12} +H_2O$	**-92.61**
(R5)	$C_6H_{10}+H_2\rightarrow C_6H_{12}$	**-30.00**
(R6)	$C_6H_6O\rightarrow C_6H_6O^*$	**2.09**
(R7)	$C_6H_6O^*+H_2\rightarrow C_6H_8O^\#$	**-21.96**
(R8)	$C_6H_8O^\#\rightarrow C_6H_6+H_2O$	**-62.63**
(R9)	$C_6H_6O^\#+H_2\rightarrow C_6H_8O$	**-29.99**
(R10)	$C_6H_8O+H_2\rightarrow C_6H_{10}O$	**-29.97**
(R11)	$C_6H_{10}O+H_2\rightarrow C_6H_{12}O$	**-203.67**
(R12)	$2C_6H_{10}O\rightarrow C_{12}H_{10}+2H_2O+3H_2$	**-26.21**
(R13)	$2C_6H_{10}O\rightarrow C_{12}H_{10}O+H_2O+4H_2$	**108.79**
(R14)	$C_6H_6 + 4H_2\rightarrow C_6H_{14}$	**-537.08**
(R15)	$C_6H_{14} +5H_2\rightarrow 6CH_4$	**110.20**
(R16)	$C_6H_6 + 9H_2\rightarrow 6CH_4$	**-426.90**

*2,4-cyclohexadienone ($C_6H_6O^*$); 1,3cyclohexadien-1-ol ($C_6H_8O^\#$)

To estimate the most favorable reactions involved in the phenol HDO process, some experimental reactions were performed at selected conditions using 2%Pd/ZrO_2 and 5%Ru/ZrO_2.

4.3.1. 5%Ru/ZrO_2

The molar fractions obtained during the experimental phenol HDO reaction are shown in Table 4.2. For this catalyst, phenol conversions ranged from 14 to 99% between 473.15 and 673.15 K. 5%Ru/ZrO_2 promotes the formation of cyclohexanone, benzene, C_5-C_6 hydrocarbons and CH_4 as the main products. At low temperature (473 K), the catalyst presented low conversions, with no CH_4 formation. As the temperature is raised, phenol conversion and methane formation increased and reached almost 100% at 673.15 K. Based on the data obtained during the experiments with phenol HDO reaction using Ru supported catalysts and in the HDO reaction pathway reported by Teles [24], the following compounds were chosen in the thermodynamic equilibrium calculation for the phenol hydrodeoxygenation : Hydrogen, benzene (C_6H_6), cyclohexanone ($C_6H_{10}O$), cyclohexanol ($C_6H_{12}O$), cyclohexane (C_6H_{12}), biphenyl ($C_{12}H_{10}$), hydroxybiphenyl ($C_{12}H_{10}O$), 2,4-cyclohexadienone ($C_6H_6O^*$), 1,3cyclohexadien-1-ol ($C_6H_8O^{\#}$), 2-cyclohexen-1-one (C_6H_8O), methane (CH_4) and phenol (C_6H_6O). The reaction temperature range was 473-673 K and the hydrogen to phenol ratio (H_2/phenol ratio) equals 60 at atmospheric pressure were applied for the thermodynamic equilibrium calculation. At these conditions, the thermodynamic analysis predicted 100% conversion of phenol for this temperature range. The molar fractions obtained during the thermodynamic analysis results also are shown in Table 4.2. The thermodynamic equilibrium calculations indicated only the formation of CH_4, which was kind of expected since this is the most stable molecule considered in this system. At 673.15K the experimental data showed only the formation of methane and a full conversion of phenol, as indicated by the equilibrium calculations.

Table 4-2. Molar fractions obtained experimentally for phenol HDO reaction compared with the thermodynamic analysis results considering CH_4 as a product.

Reaction 5%Ru/ ZrO_2 (W/F= 0.48 h)							
T [K]	**Benzene**	**Cyclohexanone**	**Cyclohexanol**	**CH_4**	**C_5-C_6 Hydrocarbons**	**Deoxygenated**	**Oxygenated**
473.15	11.7	23.7	63.1	0	0.1	0	0
573.15	35.2	3.1	0.1	43.1	15.4	0.3	2.8
673.15	0	0	0	100	0	0	0

Thermodynamic Analysis with CH_4							
T [K]	**Benzene**	**Cyclohexanone**	**Cyclohexanol**	**CH_4**	**C_5-C_6 Hydrocarbons**	**Deoxygenated**	**Oxygenated**
473.15-673.15	0	0	0	100	0	0	0

Table 4.3 shows the natural logarithms of the equilibrium constants at 473.15, 573.15 and 673.15 K of the some reactions involved in the HDO phenol process (R14-R16. According to these data, CH_4 formation is more thermodynamically favored through the hydrogenation of benzene to C_6 hydrocarbon (R14) and in sequence the hydrogenation of this hydrocarbon to methane (R15) than through the direct breaking of the aromatic ring to methane (R16) [26].

Table 4-3. Natural logarithms of the equilibrium constants (Kj) at 473-673 K for R14-R16.

	473.15 (K)	**573.15 (K)**	**673.15 (K)**
R14	173.80831	160.54196	150.97316
R15	-82.43960	-94.05015	-102.32986
R16	-91.36870	-66.49181	-48.64330

4.3.2. 2%Pd/ZrO_2

As performed with 5%Ru/ZrO_2, the most favorable reactions involved in the phenol HDO process were estimated experimentally using 2%Pd/ZrO_2. The molar fractions obtained during the experimental phenol HDO reaction compared with the thermodynamic analysis results are shown in Table 4.4. At 473 K, the catalysts showed the highest molar fraction of cyclohexanone and benzene. In addition, small amounts of cyclohexanol, cyclohexane, oxygenated and deoxygenated compounds were also observed. The selectivity of benzene increased for higher temperatures, while the amount of cyclohexanone and cyclohexanol decreased. Only at 673.15K was observed 100% of selective for benzene and a full conversion of phenol.

De Souza et al. [25] showed that Pd supported on an oxophilic support such as ZrO_2 favored the selectivity towards benzene, reducing the formation of ring-hydrogenated products, cyclohexanone and cyclohexanol, which were expected thermodynamically. For Pd samples, the formation of CH_4 was not observed in any condition of the phenol HDO reaction previous studied by our group [23-25] and also in the reactions conditions reported in this work. However in the presence of more oxophilic metals (Ru), the formation of CH_4 was favored. Thus, the thermodynamic calculations were also performed without CH_4 as a product in the studied system, aiming to represent the thermodynamic equilibrium over the surface of less oxophilic metals [24]. These thermodynamic equilibrium calculations showed complete phenol conversion for all temperature range and are perfectly in line with the HDO tests at 673.15K, demonstrating that the Pd catalyst is very active in the HDO and it can reach the thermodynamic equilibrium composition at some given reaction conditions.

Table 4-4. Molar fractions obtained experimentally for phenol HDO reaction compared with the thermodynamic analysis results without CH_4.

Reaction 2%Pd/ZrO_2 (W/F= 0.054 h)						
T [K]	**Cyclohexane**	**Benzene**	**Cyclohexanone**	**Cyclohexanol**	**Deoxygenated**	**Oxygenated**
473.15	0.5	2.9	67.6	29.9	0	0
573.15	0.2	56.5	38.1	2.6	2.2	0.4
623.15	0.1	96.3	1.2	0	1.9	0.7
673.15	0	99	0	0	1.1	0
Thermodynamic Analysis						
T [K]	**Cyclohexane**	**Benzene**	**Cyclohexanone**	**Cyclohexanol**	**Deoxygenated**	**Oxygenated**
473.15	99	1	0	0	0	0
573.15	4	96	0	0	0	0
623.15	1	99	0	0	0	0
673.15	0	100	0	0	0	0

In order to correlate better the experimental data with thermodynamic results, Table 4.5 shows the natural logarithms of the equilibrium constants at 473.15, 573.15, 623.15 and 673.15 K of the reactions involved in the HDO phenol process. According to these data, benzene formation is more thermodynamically favored through the dehydration of 1,3 cyclohexadien-1-ol (C_6H_8O) (R8) than through the direct deoxygenation reaction (R1). At 473.15 K and 573.15K the experimental data showed high amounts of cyclohexanone and cyclohexanol, which was not indicated by the thermodynamic analysis. Therefore, the experimental reaction is far from equilibrium limitations, which indicates that catalysts evaluation should be carried out below this temperature.

Table 4-5. The natural logarithms of the equilibrium constants (Kj) at 573.15, 623.15 and 673.15 K for the reactions involved in the HDO phenol process.

	473.15(K)	573.15 (K)	623.15 (K)	673.15 (K)
R1	17.20345	12.31841	10.44543	8.840804
R2	3.15000	-5.77192	-9.19452	-12.1218
R3	24.82797	24.69497	24.6341	24.57378
R4	18.94686	13.34889	11.19792	9.353193
R5	-5.88110	-11.3461	-13.4362	-15.2206
R6	3.26667	4.421447	4.812032	5.108689
R7	-3.07209	-6.65202	-8.01833	-9.18566
R8	17.00887	14.54898	13.65173	12.91778
R9	-3.36577	-8.06029	-9.86283	-11.4088
R10	2.857384	0.059944	-0.95937	-1.78923
R11	8.31038	-11.0853	-17.8314	-23.2054
R12	17.36873	25.81693	29.01424	31.71798
R13	6.38444	21.99677	27.94617	32.99259

According to the natural logarithms of the equilibrium constants, cyclohexanone may be produced by reaction R10, while cyclohexanol probably is generated by reaction R2 instead of R11, since R2 has a higher equilibrium constant. At the temperature range studied (473-673K), the experimental data showed the formation of deoxygenated and oxygenated products when a lower temperature was used.

4.3.3. Equilibrium constants of the reactions involved in phenol HDO.

4.3.3.1. Path 1

Fig. 4.2 shows the natural logarithms of the equilibrium constants as a function of temperature of the tautomerization-hydrogenation-dehydration mechanism, which may be represented by the reactions R6, R7 and R8.The natural logarithms of the equilibrium constants of direct HDO of phenol to benzene (R1) were also plotted in the same graph, for reference. The direct HDO of phenol yielding benzene and H_2O (R1) has a similar equilibrium constant than the dehydration of 1,3cyclohexadien-1-ol (C_6H_8O) (R8) at lower temperatures. As the temperature increases, reaction R1 is disfavored. The same effect was observed for the hydrogenation of the 2,4-cyclohexadienone (R7) and dehydration of 1,3cyclohexadien-1-ol (C_6H_8O)(R8), although to a smaller extend. The tautomerization reaction also did not suffer a strong influence of the temperature (R6).

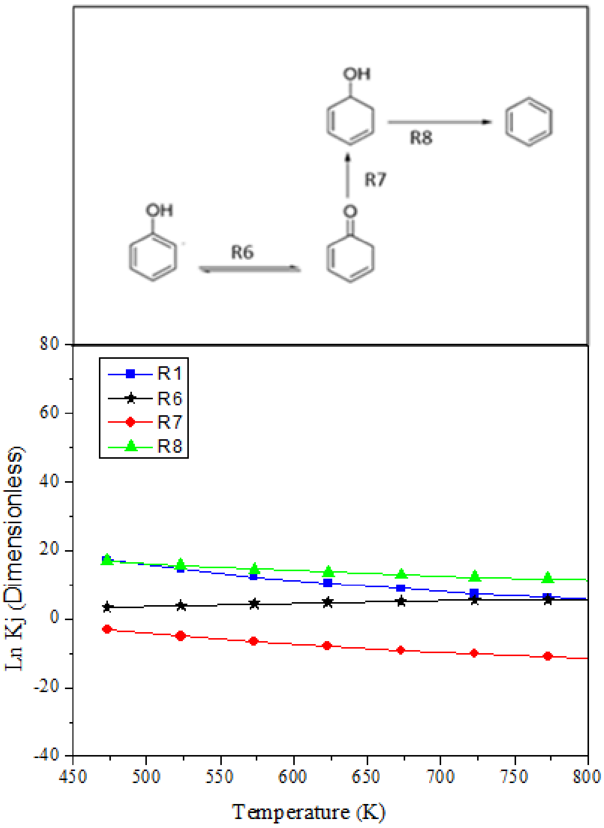

Figure 4-2. Natural logarithms of the equilibrium constants (Kj) as a function of temperature of the tautomerization-hydrogenation-dehydration mechanism reactions.

4.3.3.2. Path 2

Path 2 represents the hydrogenation of phenol to cyclohexanone ($C_6H_{10}O$) followed by the formation of biphenyl ($C_{12}H_{10}$) or hydroxybiphenyl ($C_{12}H_{10}O$). The natural logarithms of the equilibrium constants as a function of temperature of these reactions (R6, R9, R10, R12 and R13) are present in Fig. 4.3. As previous shown, the equilibrium of the tautomerization of phenol was not strongly affected by the temperature (R6). The hydrogenation of 2,4-cyclohexadienone to 2-cyclohexen-1-one(C_6H_8O)(R9) and the hydrogenation of 2-cyclohexen-1-one to cyclohexanone ($C_6H_{10}O$) (R10) are both disfavored when the system is heated.

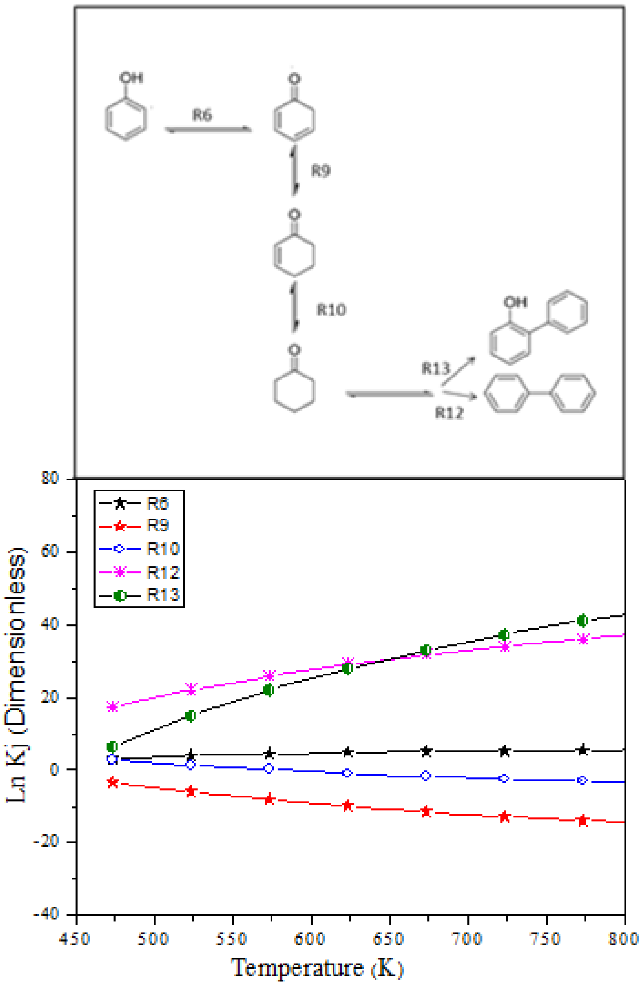

Figure 4-3. The natural logarithms of the equilibrium constants (Kj) as a function of temperature. Hydrogenation of phenol to cyclohexanone ($C_6H_{10}O$) followed by the formation of biphenyl ($C_{12}H_{10}$) or hydroxybiphenyl ($C_{12}H_{10}O$).

The formation of C12 hydrocarbons is highly favored by the temperature [28]. The formation of hydroxybiphenyl ($C_{12}H_{10}O$) is more favorable than the reaction related to biphenyl($C_{12}H_{10}$) at lower temperature. However, the polymerization to biphenyl (R13) is preferred at higher temperatures than reaction R12. In general, both reactions may be favored by the high stability and symmetry of the final product, as pointed by Furimsky [29].

4.3.3.3. Path 3

The hydrogenation of phenol to cyclohexanone ($C_6H_{10}O$) followed by the formation of cyclohexanol($C_6H_{10}O$), cyclohexene (C_6H_{10}), and cyclohexane (C_6H_{12}) are present in the Fig. 4.4 The natural logarithms of the equilibrium constants (Kj) as a function of temperature of the reactions R6, R9, R10, R11, R3, R2 and R5 are also shown in the same figure. In general, reactions R9, R5, R2 and R11 are disfavored by the temperature. The hydrogenation of cyclohexanone ($C_6H_{10}O$) to cyclohexanol ($C_6H_{12}O$) (R11) showed the smallest equilibrium constant, which indicates that the formation of cyclohexanol is more favored by the direct hydrogenation of phenol (R2) [17].

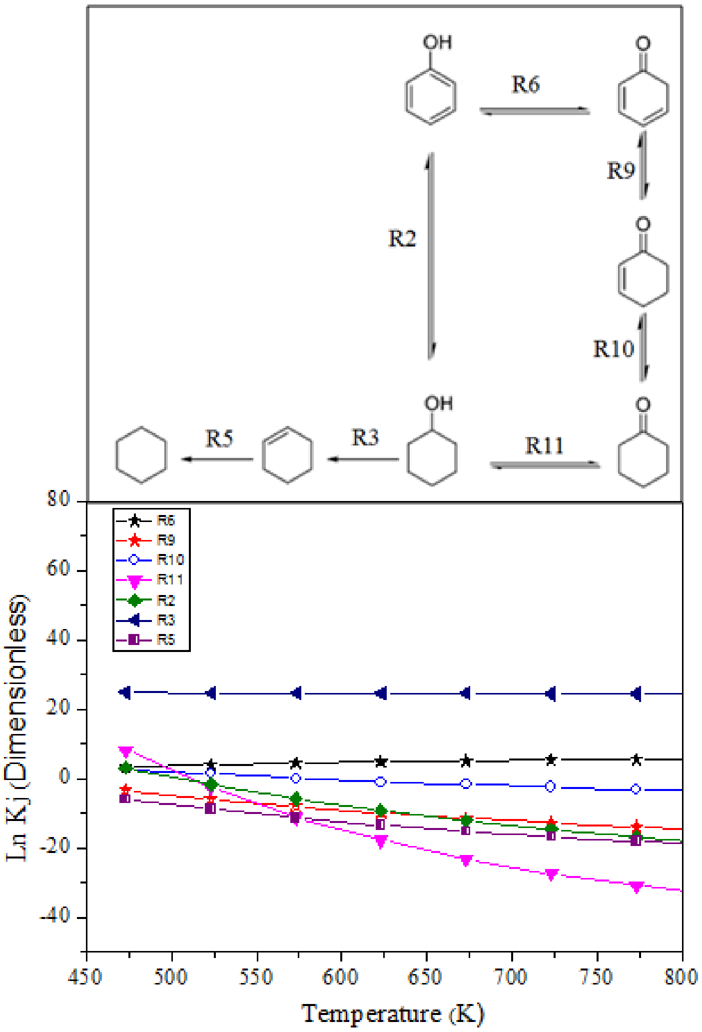

Figure 4-4. The natural logarithms of the equilibrium constants (Kj) as a function of temperature of R6, R9, R10, R11, R2, R3 and R5.

4.3.3.4. Path 4

The direct deoxygenation route of phenol to benzene (C_6H_6) and the decompositionof benzene to hydrocarbons (C_6H_{14} and methane) are presented in the Fig. 4.5. The natural logarithms of the equilibrium constants (Kj) as a function of temperature of reactions R1, R14, R15 and R16 are also shown in the same figure. In general, the reaction R1 is disfavored by the temperature, while R14, R15 and R16 are favored by the temperature. In this situation, the formation of CH_4 or other hydrocarbons are more favored than the DDO reaction (R1). Tan et al. [27] in HDO of m –cresol reported that the hydrogenolysis reaction proceeds by cleaving C-C bonds to form CxHy and CH_x species.

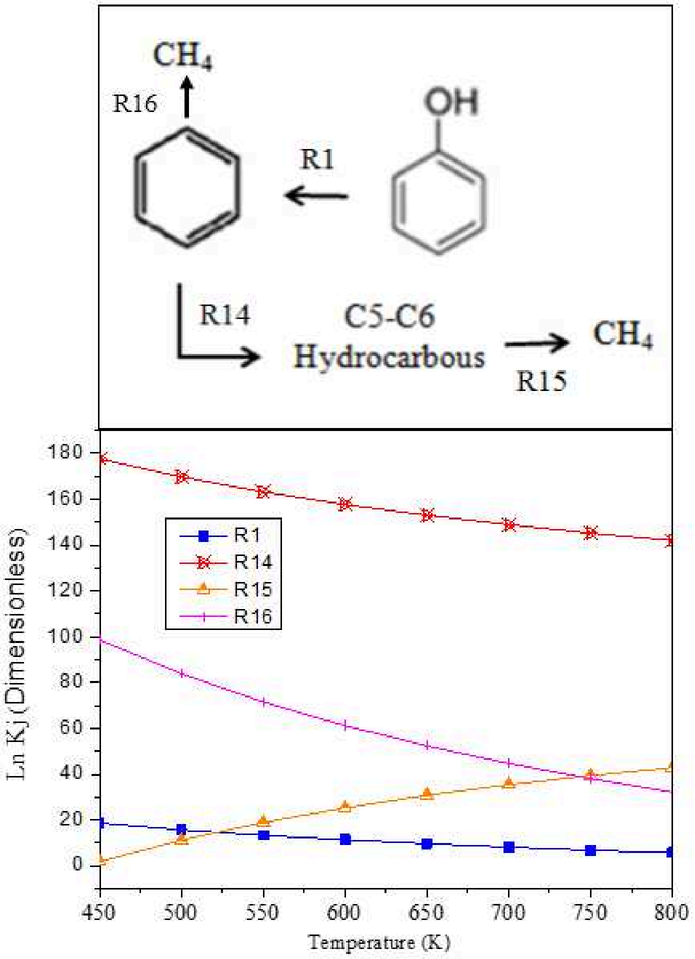

Figure 4-5. The natural logarithms of the equilibrium constants (Kj) as a function of temperature of R1, R14 and R15.

4.3.4. Thermodynamic Analysis: equilibrium compositions of phenol HDO in the gas phase without CH_4

Equilibrium compositions of phenol HDO were calculated at atmospheric pressure using as parameters the reactor temperature (473-800 K), and the H_2/phenol ratio 10 to 100 with and without CH_4. When CH_4 was added to the system, the system converges to the formation of this molecule, independently of the conditions used. However, as reported before, Pd samples do not favor the formation of CH_4, thus the thermodynamic calculations were performed also without this molecule to evaluate the equilibrium at these conditions.

For the thermodynamic calculations without methane, regardless of the H_2/Phenol ratio employed, phenol is fully converted at all temperatures. In general, the system did not show the formation of cyclohexane, cyclohexanol, cyclohexanone, 1,3cyclohexadien-1-ol,hydroxybiphenyland 2-cyclohexen-1-one. Neri et al. [30] showed the influence of the reaction temperature on the activity of Pd/Al_2O_3 in the gas-phase hydrogenation of phenol to cyclohexanone. In the range of temperature studied by them, chemical equilibrium is shifted completely towards the reaction products, therefore the decrease in the catalytic activity was not attributed to thermodynamic limitations.

As the temperature increases, the conversion reaches a maximum and then decreases. However, the drop in phenol conversion was not attributed to thermodynamic limitations. According to the authors the decrease of catalytic activity at higher temperature was attributed to a decrease of the fraction of surface covered by the reactants.

4.3.4.1. Effect of temperature

The equilibrium mixture formed from HDO reaction of phenol consists of benzene, a small amount of cyclohexane, 2,4-cyclohexadienone and hydroxybiphenyl (deoxygenated compounds). Fig. 4.6 presents the equilibrium mole fractions of the gaseous products in dry and H_2 free basis as a function of temperature. At low temperatures phenol seems to be fully hydrogenated to cyclohexane. Benzene appears as a product of the HDO reaction when the temperature rises. According to the equilibrium constants, reaction R5, related to the generation of cyclohexane, is slightly disfavored by temperature. Itoh and Xu [31] presented a thermodynamic study of the hydrogenation reaction of phenol to cyclohexanone and then to cyclohexanol at 423-573K temperature range. According to the authors as the temperature decreases, hydrogenation reaction takes place. Similar result was observed in this work, however in the studied system, phenol is hydrogenated to cycloehexane.

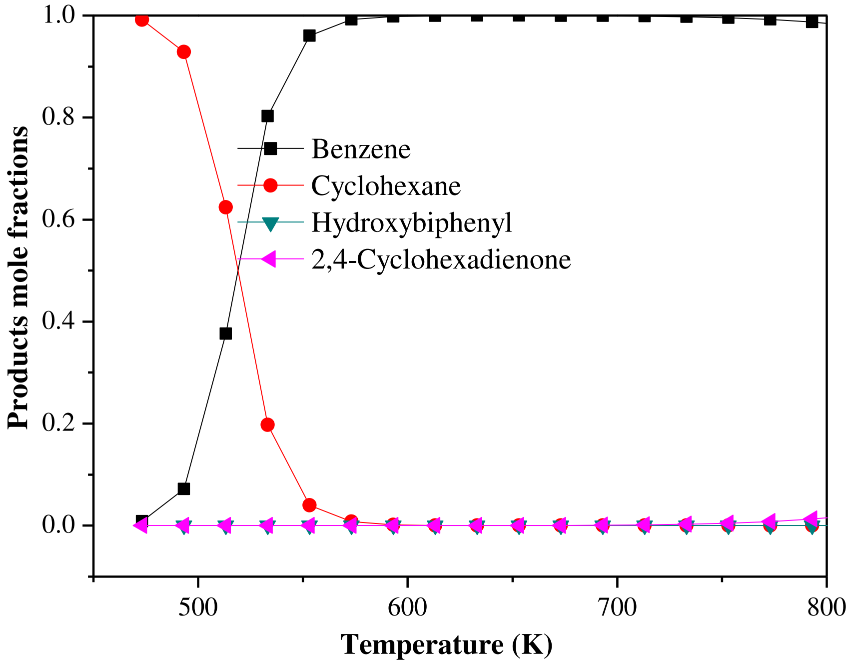

Figure 4-6. HDO reaction of phenol-effect of temperature on equilibrium product composition, at H_2/phenol=60.

4.3.4.2. Effect of H_2 to phenol ratio

H_2 to phenol ratio plays an important role in the HDO reaction. The effect of this parameter is complicated by the fact that its influence depends on the temperature. Fig. 4.7(a)–(c) depicts the mole fraction of the main gaseous products as a function of the H_2/phenol ratio and the temperature. Figure 4.8 shows the 3D profiles. Figure 4.7a shows benzene molar fraction as a function of temperature and H_2/phenol ratio. In general, the increase of H_2 concentration in the feed favored the formation of benzene. The shape of the curves observed in Figure 4.7a for benzene formation does not vary with temperature. Benzene production has a maximum around 550-750K under any H_2/phenol ratio. Benzene molar fraction starts to decrease at high temperatures and the temperature at which this decrease starts strongly depends on the H_2/Phenol ratio. Fig. 4.7b shows the cyclohexane molar fractions variations as a function of the H_2/phenol ratio and the temperature, respectively. At 473 K, the molar fraction cyclohexane molar fraction is around 33%. For temperatures higher than 573 K the equilibrium molar fractions of cyclohexane are very small. Fig. 4.7c shows that regardless of H_2/Phenol ratio, the production of 2,4-cyclohexadienone is favored at higher temperatures. The natural logarithms of the equilibrium constants showed that the reaction related to the 2,4-cyclohexadienone formation (R6) is not very affected by the temperature. However the reactions related to benzene (R1 and R8) and cyclohexane (R5) suffered a slightly decreased in the natural logarithms of the equilibrium constant, which may disfavor the formation of these products.

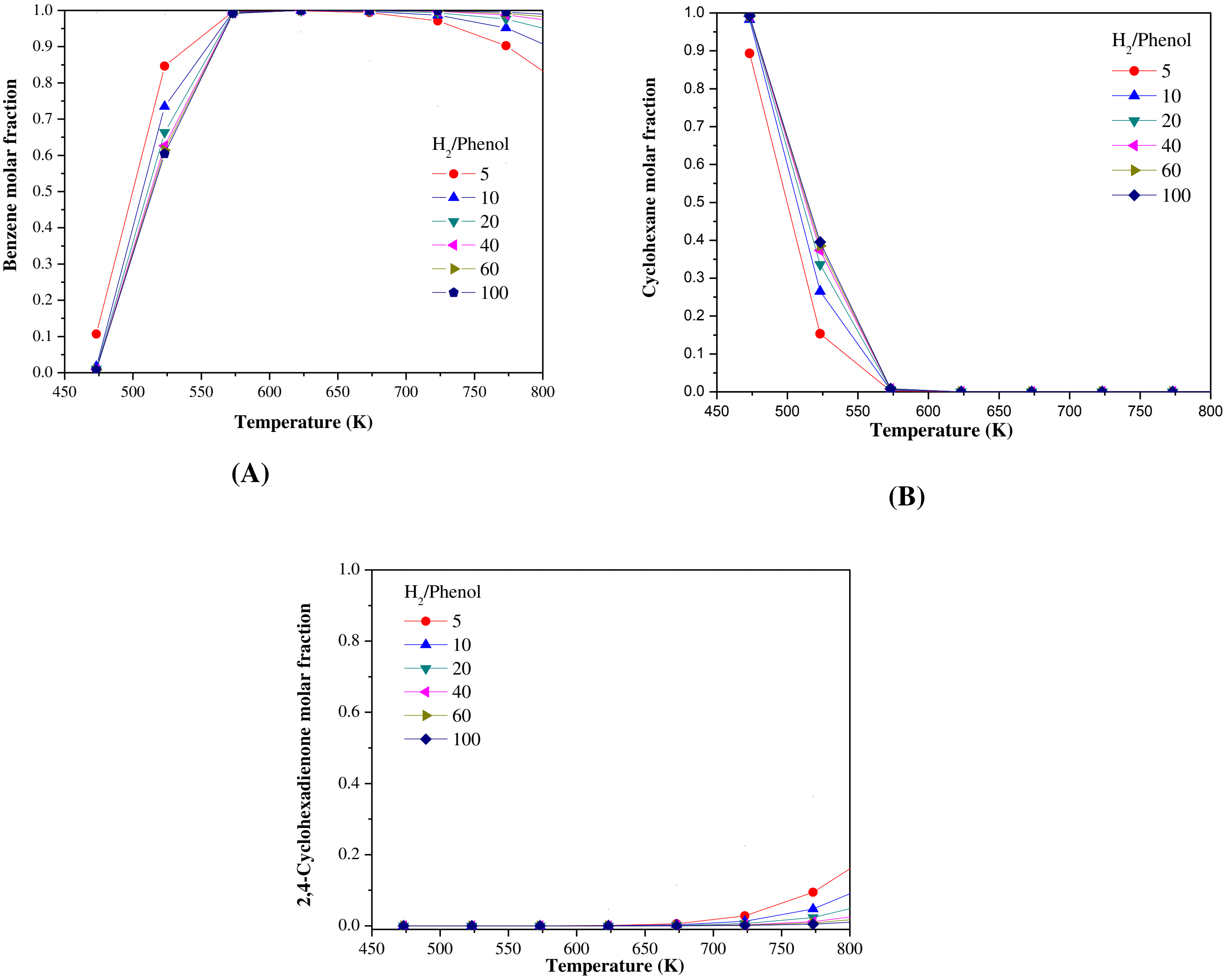

(A)

(B)

(c)

Figure 4-7. Distribution of products in dry basis (free of H_2) for the chemical equilibrium of HDO of phenol at atmospheric pressure.(A)Benzene, (B) Cyclohexane and (C) 2,4-Cyclohexadienone.

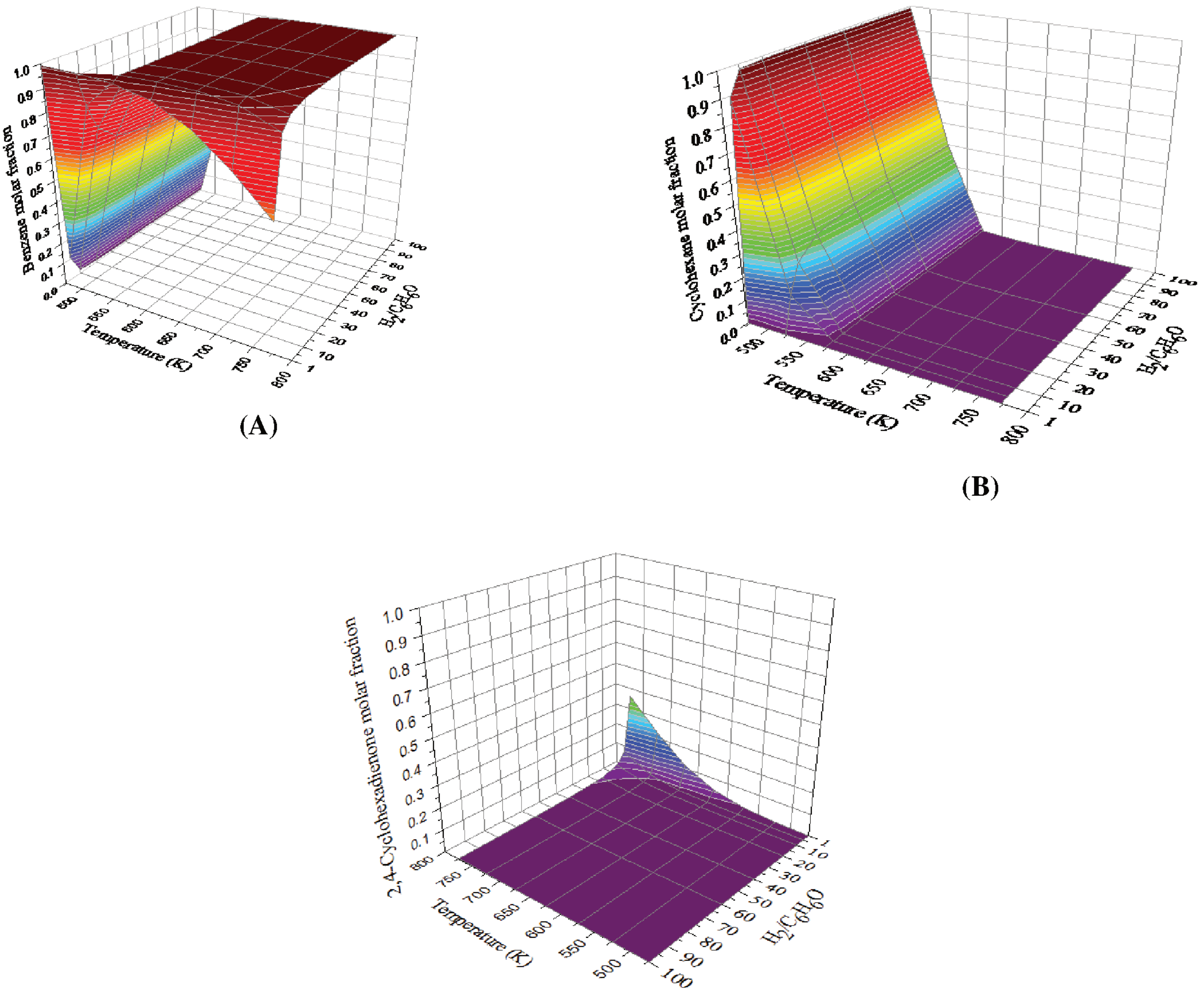

(A)

(B)

(C)

Figure 4-8. 3D Distribution of products in dry basis (free of H_2) for the chemical equilibrium of HDO of phenol at atmospheric pressure.(A)Benzene, (B) Cyclohexane and (C) 2,4-Cyclohexadienone.

4.4. Conclusions

The application of the Lagrange Multipliers method was efficient to calculate the equilibrium mole fractions of phenol HDO reaction. When CH_4 was added to the thermodynamic analysis, this was the only product observed, which represents the equilibrium behavior of phenol HDO reaction over more oxofilic metals. For Pd samples, methane was not observed as a product during catalytic tests. Therefore, this species was not added to the study. In this case, the thermodynamic calculations showed that a high ratio of H_2 to phenol contributed to a greater selectivity for benzene and reduced the hydroxybiphenyl presence in the system. Also, the thermodynamic data indicated full conversion of phenol in all temperature range studied. In general, the best operating temperature to perform the studied reaction is around 600 K and H_2/phenol around 60. The experimental activity tests data of the phenol HDO reaction showed the formation of the following products: cyclohexane, benzene, cyclohexanone, cyclohexanol, deoxygenated and oxygenated compounds. Among these products only benzene and cyclohexane appeared in the thermodynamic analysis at the same temperature range and H_2/phenol ratio. The thermodynamic calculations of the reaction mechanism proposed in the literature and the experimental activity test data performance were efficient to explain the reactions involved in this complex reaction network.

Acknowledgements

The authors would like to acknowledge the financial support of CNPq, Fapemig and CAPES.

Reference

[1] N. Li, G.W. Huber, Aqueous-phase hydrodeoxygenation of sorbitol with Pt/SiO2–Al2O3: Identificati
of reaction intermediates, Journal of Catalysis. 270 (2010) 48–59.https://doi.org/10.1016/j.jcat.2009.12.00

[2] A. Gutierrez, R.K. Kaila, M.L. Honkela, R. Slioor, A.O.I. Krause, Hydrodeoxygenation of guaiacol
noble metal catalysts, CatalysisToday. 147 (2009) 239–246.https://doi.org/10.1016/j.cattod.2008.10.037

[3] C. Zhao, J. He, A.A. Lemonidou, X. Li, J.A. Lercher, Aqueous-phase hydrodeoxygenation of bi
derived phenols to cycloalkanes,Journal of Catalysis 280. (2011) 8–
.https://doi.org/10.1016/j.jcat.2011.02.001

[4] P.M. Mortensen, J. Grunwaldt, P.A. Jensen, K.G. Knudsen, A.D. Jensen, A review of cataly
upgrading of bio-oil to engine fuels, Applied Catalysis A : General, 407 (2011)
19.https://doi.org/10.1016/j.apcata.2011.08.046

[5] A. V Bridgwater, Review of fast pyrolysis of biomass and product upgrading, Biomass and Bioenerg
38 (2011) 68–94.https://doi.org/10.1016/j.biombioe.2011.01.048

[6] E. Furimsky, Catalytic hydrodeoxygenation, Applied Catalysis A: General, 199 (2000) 14
190.https://doi.org/10.1016/S0926-860X(99)00555-4

[7] T. V. Choudhary, C. B. Phillips, Renewable fuels via catalytic hydrodeoxygenation, Appl. Catal.
Gen., 397 (2011) 1–12.https://doi.org/10.1016/j.apcata.2011.02.025

[8] H.Y. Zhao, D. Li, P. Bui, S.T. Oyama, Hydrodeoxygenation of guaiacol as model compound f
pyrolysis oil on transition metal phosphide hydroprocessing catalysts, Applied Catalysis A: General, 3
(2011) 305–310.https://doi.org/10.1016/j.apcata.2010.07.039

[9] V. N. Bui, D. Laurenti, P. Afanasiev, C. Geantet, Hydrodeoxygenation of guaiacol with CoMo catalys
Part I: Promoting effect of cobalt on HDO selectivity and activity, Applied Catalysis B: Environmental, 1
(2011) 239–245.https://doi.org/10.1016/j.apcatb.2010.10.025

[10] A. J. R. Hensley, Y. Wang, J. McEwen, Phenol Deoxygenation Mechanisms on Fe(110) and Pd(11
ACS Catal., 5 (2015) 523−536.https://doi.org/10.1021/cs501403w

[11] P. M. Mortensen, J. Grunwaldt, P. A. Jensen, A. D. Jensen, Screening of Catalysts f
Hydrodeoxygenation of Phenol as a Model Compound for Bio-oil, ACS Catal., 3 (2013) 1774–17

https://doi.org/10.1021/cs400266e

[12] I. T. Ghampson, C. Sepúlveda, A. B. Dongil, G. Pecchi, R. García, J. L. G. Fierro, N. Escalona, Phen hydrodeoxygenation: effect of support and Re promoter on the reactivity of Co catalysts, Catal. S Technol., 6 (2016), 7289.https://doi.org/10.1039/C6CY01038E

[13] J. Sun, A. M. Karim, H. Zhang, L. Kovarik, X. S. Li, A. J. Hensley, J. McEwen, Y. Wang, Carbo supported bimetallic Pd–Fe catalysts for vapor-phase hydrodeoxygenation of guaiacol, Journal of Catalys 306 (2013) 47–57.https://doi.org/10.1016/j.jcat.2013.05.020

[14] L. Nie, D. E. Resasco, Kinetics and mechanism of m-cresol hydrodeoxygenation on a Pt/SiO2 cataly Journal of Catalysis 317 (2014) 22–29.https://doi.org/10.1016/j.jcat.2014.05.024

[15] K.A. Resende, C.N. Avila-Neto, R.C. Rabelo-Neto, F.B. Noronha, C.E. Hori, Thermodynamic analy and reaction routes of steam reforming of bio-oil aqueous fraction, Renewable Energy 80 (2015) 166 176.https://doi.org/10.1016/j.renene.2015.01.057

[16] E. C. Vagia, A. A. Lemonidou, Thermodynamic analysis of hydrogen production via autothermal stea reforming of selected components of aqueous bio-oil fraction, International journal of hydrogen energy, (2008) 2489– 2500.https://doi.org/10.1016/j.ijhydene.2008.02.057

[17] E. Shin, M. A. Keane, Gas-Phase Hydrogenation/Hydrogenolysis of Phenol over Supported Nick Catalysts, Ind. Eng. Chem. Res., 39 (2000), 883-892.https://doi.org/10.1021/ie990643r

[18] S. Adhikari, S. Fernando, S. R. Gwaltney, S.D. F. To, R. M. Bricka, P. H. Steele, A. Haryant Athermodynamic analysis of hydrogen production by steam reforming of glycerol, International Journal Hydrogen Energy, 32 (2007) 2875 – 2880.https://doi.org/10.1016/j.ijhydene.2007.03.023

[19] H. Wang, X. Wang, M. Li, S. Li, S. Wang, X. Ma, Thermodynamic analysis of hydrogen producti from glycerol autothermal reforming, International Journal of hydrogen energy, 34 (2009) 568 5690.https://doi.org/10.1016/j.ijhydene.2009.05.118

[20] J. Gao, Y. Wang, Y. Ping, D. Hu, G. Xu, F. Gu, F. Su, A thermodynamic analysis of methanation reactions of carbon oxides for the production of synthetic natural gas, RSC Advances, 2 (2012), 2358–2368.https://doi.org/10.1039/c2ra00632d.

[22] F.A.P. Voll, C.C.R.S. Rossi, C. Silva, R. Guirardello, R.O.M.A. Souza, V.F. Cabral, L. Cardozo-Filho, Thermodynamic analysis of supercritical water gasification of methanol, ethanol, glycerol, glucose and cellulose, International Journal of hydrogen energy 34 (2009) 9737-9744. https://doi.org/10.1016/j.ijhydene.2009.10.017

[23] P.M. de Souza, R. C. Rabelo-Neto, L. E. P. Borges, G. Jacobs, B. H. Davis, T. Sooknoi,D. E. Resasco, F. B. Noronha, Role of Keto Intermediates in the Hydrodeoxygenation of Phenol over Pd on Oxophilic Supports, ACS Catal. 5 (2015), 1318−1329. https://doi.org/10.1021/cs501853t

[24] C. A. Teles, R. C. Rabelo-Neto, J. R. de Lima, L. V. Mattos, D. E. Resasco, F. B. Noronha, The Effe of Metal Type on Hydrodeoxygenation of Phenol Over Silica Supported Catalysts, CatalLett 146 (201 1848–1857. https://doi.org/10.1007/s10562-016-1815-5

[25] P. M. de Souza, R. C. Rabelo-Neto, L. E. P. Borges, G. Jacobs, B. H. Davis, U. M. Graham,D. Resasco, F. B. Noronha, Effect of Zirconia Morphology on Hydrodeoxygenation of Phenol over Pd/ZrO ACS Catal. 5 (2015), 7385−7398. https://doi.org/10.1021/acscatal.5b01501

[26] Q. Tan, G. Wang, L. Nie, A. Dinse, C. Buda, J. Shabaker, D. E. Resasco, Different Produ Distributions and Mechanistic Aspects of the Hydrodeoxygenation of m-Cresol over Platinum a Ruthenium Catalysts, ACS Catal.5 (2015) 6271–6283. https://doi.org/10.1021/acscatal.5b00765

[27] C. Liu, Y. Zhang, X. Huang, Study of guaiacol pyrolysis mechanism based on density function theor Fuel Processing Technology 123 (2014) 159–165. https://doi.org/10.1016/j.fuproc.2014.01.002

[28] S. Stein, On the High Temperature Chemical Equilibria of Polycyclic Aromatic Hydrocarbons, J. Phy Chem.82(1978) 566–571. https://doi.org/10.1021/j100494a600

[29] E. Furimsky, Catalytic hydrodeoxygenation, Applied Catalysis A: General 199 (2000) 147–1 https://doi.org/10.1016/S0926-860X(99)00555-4

[30] G. Neri, A.M. Visco, A. Donate, C. Milone, M. Malentacchi, G. Gubitosa, Hydrogenation of phenol cyclohexanone over palladium and alkali-doped palladium catalysts, Applied Catalysis A: General 1 (1994) 49-59. https://doi.org/10.1016/0926-860X(94)80104-5

[31] N. Itoh and W.C. Xu, Selective hydrogenation of phenol to cyclohexanone using palladium-bas membranes as catalystsApplied Catalysis A: General, 107 (1993) 83-100. https://doi.org/10.1016/092 860X(93)85117-8

5.CHAPTER V

5.1. Hydrodeoxygenation of phenol over zirconia supported Pd bimetallic catalysts. The effect of second metal on catalyst performance

ABSTRACT- This work investigated the effect of the addition of a second metal (Cu, Ag, Zn, Sn) on the performance of Pd/ZrO_2 catalyst for HDO of phenol at 573 K in the gas phase. The incorporation of dopants resulted in the formation of Pd–X (Cu, Ag, Zn) alloys, which reduced the reaction rate for HDO and increased the selectivity to hydrogenation products (cyclohexanone and cyclohexanol). The lower activity of the bimetallic catalysts was probably due to the segregation of the second metal on the surface of the Pd particle. For $PdSn/ZrO_2$, alloying was also observed but tin oxide was still present on the surface after reduction at 773 K. For Pd and $PdSn/ZrO_2$, the oxophilic sites represented by Zr and Sn cations promotes the hydrogenation of the carbonyl group of the keto-tautomer intermediate formed, producing benzene as the main product. All catalysts significantly deactivated during the reaction but the deactivation degree depended on the type of the metal. Pd/ZrO_2 and $PdZn/ZrO_2$ and $PdAg/ZrO_2$ exhibited approximately the same deactivation degree. However, the loss of activity was less pronounced for $PdSn/ZrO_2$ catalyst, which was related to the presence of Sn^{n+} species. Pd dispersion significantly decreased during the reaction, indicating that the sintering of Pd particles is one of the causes for catalyst deactivation.

Keywords: phenol; bio-oil; hydrodeoxygenation; stability; bimetallic catalysts; oxophilic sites.

5.2. Introduction

The lignocellulosic biomass may be converted into biofuels by different technologies [1,2]. The conversion of biomass into bio-oil through fast pyrolysis followed by its upgrading by hydrodeoxygenation (HDO) is considered a potential route for the production of renewable fuels [3]. The bio-oil produced is composed of a very complex mixture of oxygenated compounds with high water content. The presence of highly reactive oxygenated compounds renders the bio-oil unstable during storage. Therefore, bio-oil must be upgraded to be feasible as a transportation fuel [4,5].

Due to the complex composition of bio-oil, a significant number of studies reported the use of model molecules to elucidate the HDO reaction mechanism [5-7]. Those compounds are chosen to represent different fractions of biomass such as sugars and sugar alcohols (cellulose and hemi-cellulose), as well as phenolic compounds such as cresols, guaiacol, and phenol (i.e., the lignin fraction of biomass) [5].

Different catalysts have been reported for HDO reactions of several molecules [4-7]. Despite of all the research efforts, the development of an appropriate catalyst for HDO reaction is still an issue. The optimal catalyst for bio-oil upgrading should exhibit high activity for deoxygenation and stability under reaction conditions [6].

Currently the greatest challenge in developing new catalysts for the HDO reaction is improving the stability. Catalyst deactivation is generally attributed to the deposition of carbonaceous species on the catalyst surface or sintering of the metallic particles [3]. Therefore, understanding of the catalyst deactivation mechanisms for HDO of bio-oils is needed to design efficient catalysts. However, the number of studies dedicated to catalyst deactivation during HDO reaction is scarce. The HDO reaction requires a metallic site for hydrogenation/dehydrogenation as well as a support that adsorbs the oxy compound and promotes alkylation and polymerization reactions. Therefore, control of the metal particle size and the selection of the support with appropriate acidic properties may inhibit catalyst deactivation.

The addition of a second metal may induce changes in both catalytic and adsorptive properties. The dilution or the coverage of a fraction of the surface of the host metal (i.e., geometric effects) induces a decrease in the size of the ensemble, and this inhibits the formation of carbon. Furthermore, it may also suppress metal particle sintering. Therefore, the addition of a second metal induces changes in selectivity, affecting more severely reactions involving C-C bond scission, which could lead to carbon deposition.

There are only few studies regarding bimetallic catalysts for the HDO reaction [8-10]. Sun et al. [8] investigated the performance of carbon supported metal catalysts (Cu, Fe, Pd, Pt, PdFe and Ru) for HDO of guaiacol. Cyclohexanone (ONE), cyclohexanol (OL) and C_1 gas products were the main compounds formed over precious metal catalysts. On the other hand, PdFe/C catalyst exhibited higher activity to deoxygenated products (benzene/toluene) than the monometallic catalysts. DFT calculations demonstrated the preferential adsorption and activation of phenol on unreduced Fe, which likely inhibits the hydrogenation of the ring on Pd. Our group studied the selective conversion of m-cresol to toluene over bimetallic silica supported Ni-Fe catalysts [10]. For Ni/SiO_2, DFT calculations demonstrated[10] that the aromatic compound adsorbs parallel to the surface of the metal, favoring the hydrogenation of the ring and the formation of 3-methyl-cyclohexanol and 3-methyl-cyclohexanone. For the bimetallic catalyst, the presence of an oxophilic metal, such as the unreduced Fe species present in the Ni-Fe/SiO_2 catalysts enhances the interaction with the carbonyl group. In the case of Ni-Fe [10], the DFT study shows both repulsion between the phenyl ring and the catalyst surface and a stronger interaction between the oxygen atoms in m-cresol and the catalyst surface, promoting the oxygen removal reaction pathway. In spite of few works dealing with the selectivity of bimetallic catalysts for HDO reactions, there are no studies about their deactivation.

The support also plays an important role for HDO. De Souza et al. [11-13] studied the effect of the type of support (SiO_2, Al_2O_3, TiO_2, ZrO_2, CeO_2 and $CeZrO_2$) on the performance of Pd-based catalysts for the hydrodeoxygenation of phenol at 573 K. Benzene was the major product over Pd/TiO_2 and Pd/ZrO_2 whereas Pd/SiO_2, Pd/Al_2O_3, Pd/CeO_2 and Pd/$CeZrO_2$ produced mainly cyclohexanone. For Pd/ZrO_2, the oxophilic sites represented by incompletely coordinated Zr^{4+} cations near the perimeter of the metal particles favor the interaction of the oxygen of the carbonyl group in the phenol tautomer intermediate with the catalyst surface. Then, the carbonyl group is preferentially hydrogenated on the metal particles at the metal-support interface, leading to the formation of benzene. Then, oxophilic supports such as zirconia promote the production of deoxygenated products during the HDO reaction.

Therefore, the present study investigated the HDO of phenol in gas phase over bimetallic Pd catalysts (PdAg, PdZn, PdCu and PdSn) supported on ZrO_2. These elements were selected based on the literature that reports the formation of an alloy with Pd. The effect of the addition of a second metal on the catalyst activity, selectivity to deoxygenated products and stability during HDO of phenol was examined. The formation of Pd alloy with the reduction temperature was studied by in situ X-ray photoelectron spectroscopy (XPS) and X-ray absorption spectroscopy (XAS) experiments [13-19].

5.3. Results and Discussion

5.3.1. Catalyst Characterization

Table 5.1 shows the Pd loadings and dopant/metal molar ratios of the catalysts. Pd content was close to the nominal value (1 wt.%) for all samples. The samples exhibited a dopant/Pd molar ratio around the expected value (0.50), except for PdSn/ZrO_2 that was slightly lower (0.30). Table 5.1 also presents the textural properties of the catalysts. All samples showed similar specific surface areas (73 – 79m^2 g^{-1}), which are close to the surface area of the support (82 m^2/g). The total pore volumes (0.28 - 0.30 cm^{3}g^{-1}) were also very similar for all the catalysts. The addition of small amount of Pd and the other metals did not change the specific surface area and pore volume of the samples.

Table 5-1. BET surface area, pore volume, pore size, Pd and dopant content of the samples and Pd dispersion determined by H_2 chemisorption and by cyclohexane dehydrogenation.

Samples	**Pd (wt%)**	**Dopant/Pd**[a]	**BET area (m^2 g^{-1})**	**Pore Volume (cm^3 g^{-1})**	**Dispersion**[b] **(%)**	**Dispersion**[c] **(%)**
Pd/ZrO_2	1.02	-	77	0.30	35	38
PdAg/ZrO_2	0.98	0.49	73	0.29	11	9
PdCu/ZrO_2	0.97	0.55	79	0.30	6	-
PdSn/ZrO_2	0.97	0.30	79	0.28	9	10
PdZn/ZrO_2	1.00	0.55	76	0.29	4	5

[a] Molar ratio
[b] Measured by hydrogen chemisorption.
[c] Measured by cyclohexane dehydrogenation reaction

X-ray diffraction patterns of the calcined samples are compared in Figure S1 (Appendix I). The diffractograms of all samples showed lines characteristic of a mixture of monoclinic (JCPDS 37-1484) and tetragonal (JCPDS 17-0923) ZrO_2 phases. The proportion of each phase was calculated taking into account the procedure proposed by

Khaodee et al. [20]. The monoclinic is the dominant phase for all catalysts, varying from 82 - 88%. The lines characteristic of palladium and transition metals oxides were not detected. This is likely due to the low content of these metals.

Pd dispersion of fresh catalysts measured by H_2 chemisorption and cyclohexane dehydrogenation reaction are also reported in Table 5.1. The results obtained by both techniques were quite close, revealing that the cyclohexane dehydrogenation reaction can be used for the determination of metal dispersion. Furthermore, these techniques showed a decrease in Pd dispersion when the second metal was added. Considering that H_2 chemisorption occurs only on Pd surface, these results might be explained by one or more of the following reasons [21]: (i) sintering of Pd particles by the addition of second metal; (ii) the formation of an alloy between Pd-second metal, which may modify the adsorption properties of Pd atoms; (iii) the second metal partially covers the surface of Pd particle (ensemble effect).

In order to investigate the effect of the addition of a second element on the metal particle size, STEM analysis was carried out. The STEM images of the Pd/ZrO_2 catalyst are shown in Figure S2 (Appendix I). Due to the low Pd content and the poor contrast between Pd and ZrO_2, it is difficult to distinguish between the Pd particles and the individual ZrO_2 crystallites in the STEM image shown in Figure S2. Therefore, the size distribution analysis was not performed. Only few Pd particles were found with 2.5 nm. The same problem happens with PdAg/ZrO_2 and PdSn/ZrO_2 catalysts but the few particles observed have approximately the same size (2.5 nm) compared to that of the monometallic catalyst. Therefore, sintering of Pd particles due to the addition of the second element on the bimetallic catalysts could be ruled out.

These results are not in agreement with the metal dispersion determined by H_2 chemisorption as well as cyclohexane dehydrogenation reaction, which estimated larger metal particles for the bimetallic catalysts. As the chemisorption and the probe reaction are indirect measurements of dispersion, this decrease is likely due to the alloy formation or the coverage of the Pd surface by the second metal.

The formation of an alloy between Pd-second metal was studied by TPR, in situ EXAFS, in situ XPS and the results obtained will be discussed next.

5.3.1.1. Effect of the second metal on Pd reduction and alloy formation.

Figure 5.1 shows the TPR profiles obtained for zirconia-supported catalysts. For Pd/ZrO_2, the reduction profile exhibits one peak at 430 K and a shoulder at around

500K. The hydrogen consumption at this low temperature region is attributed to the reduction of palladium oxide with different particles sizes [22]. There is also a hydrogen uptake at high temperature (650 – 750 K). The hydrogen uptake obtained in the low temperature region corresponds exactly to the complete reduction of PdO (Table 5.2). Therefore, the H_2 consumption at high temperature could be attributed to the reduction of zirconia support. The XANES spectra at the Zr K-edge of Pd/ZrO_2 catalysts after reduction at different temperatures showed that Zr^{4+} was partially reduced to Zr^{3+}, which is in agreement with the result of our TPR profile [13].

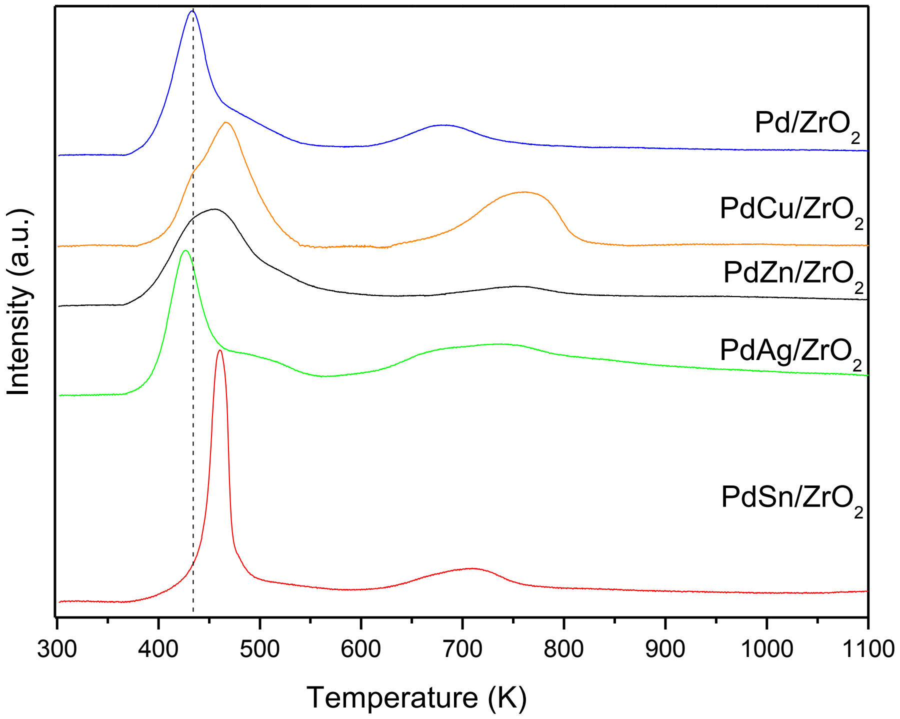

Figure 5-1. TPR profiles of Pd and bimetallic supported on zirconia catalysts.

Table 5-2. H_2 consumption related to the 1st and 2nd peaks in the TPR profile and the degree of PdO reduction (DRPR).

Samples	H_2 observed consumption in the 1^{st}Peak (mol g^{-1})x 10^5	H_2 observed consumption in the 2^{nd}Peak (mol g-1) x 10^5	Total consumption x 10^5	Expected Consumption of dopant (mol/g) x 10^5	Expected total consumption (mol/g) x 10^5**	PdO degree of reduction 1^{st} peak (%)	Total reduction degree(%) (dopant +Pd)
Pd/ZrO_2	4.74	2.76	7.50	-	4.72	100	159
$PdAg/ZrO_2$	4.84	7.41	12.2	2.27	6.99	103	175
$PdCu/ZrO_2$	5.27	3.41	8.68	4.33	9.04	112	96
$PdSn/ZrO_2$	7.10	4.46	11.6	2.53	7.24	151	160
$PdZn/ZrO_2$	4.46	3.63	8.09	4.21	8.92	95	91

*Expected H_2 consumption for total reduction of PdO ($4.71 x 10^{-5} mol g^{-1}$)

** Expected H_2 consumption considering total reduction of SnO_2, CuO, Ag_2O and ZnO.

TPR profiles of bimetallic catalysts are similar to that of Pd/ZrO_2, with the main reduction peak around 400-550K and a second peak at high temperature. An additional peak relative to the dopant metal reduction did not appear in any of the bimetallic profiles. In general, this result may be attributed to the formation of an alloy. Fox et al. [23] also observed that the reduction occurred in a single broad peak for $PdCu/CeO_2$ bimetallic catalyst. Karski et al. [22] reported similar results for the following bimetallic systems: 5%Pd–1%Ag/SiO_2, 5%Pd–3%Ag/SiO_2 ad 5%Pd–5% Ag/SiO_2. According to them, this corresponds to the reduction of a Pd_xAg_yO mixed oxide formed during the calcination with oxygen. Vicente et al. [14] showed that PdO is completely reduced around 373 K for 1%Pd/SiO_2. The TPR profile of Pd-Sn/SiO_2 (1%Pd-1-2%Sn) bimetallic catalysts exhibited the reduction of Sn species in contact with Pd, which may be an indication of alloy formation. In our work, hydrogen consumption observed between 400-550K corresponds to the complete reduction of PdO for $PdAg/ZrO_2$, $PdCu/ZrO_2$ and $PdZn/ZrO_2$, indicating that only Pd oxide is reduced in the low temperature region (Table 2). Ag_2O, CuO and ZnO were completely reduced in the high temperature region. For $PdSn/ZrO_2$, the hydrogen uptake in the first peak is higher than that expected for the reduction of PdO, which suggests that Sn oxide is also reduced in this region. The higher total hydrogen consumption observed for Pd/ZrO_2, $PdAg/ZrO_2$ and $PdSn/ZrO_2$ indicates that ZrO_2 is also partially reduced at this temperature, as reported by de Souza et al. [13]. TPR-XANES spectra as a function of temperature are shown in Figure 5.2 and snapshots of XANES spectra at the initial, intermediate, and final stages of reduction are provided in Figure 5.3.

The temperatures to achieve 50% of PdO reduction were as follows for the various catalysts according to edge energy: Pd K-edge: Pd (372 K); Pd-Cu (370 K); Pd-Zn (346 K); Pd-Ag (360 K); Pd-Sn (374 K). Thus, significant promoting effects on reduction were observed by adding Zn or Ag to the Pd particles. The slightly lower temperature of Ag compared to Pd in the Pd-Ag catalyst suggests that nucleation of reduced metal centers in the Pd-Ag catalyst occurred at Ag atoms. Once the Ag^0 centers were formed, Pd was rapidly reduced (temperature difference at 50% metal reduction for Ag and Pd are within 1.3K). Then, a significant fraction of Ag is likely in intimate contact with Pd, and quite possibly at the atomic level (e.g., alloy formation). This effect can be clearly observed in Figure 5.3.

The evolution of the Pd species during reduction calculated by the linear combination of Pd K-edge XANES spectra is shown in Figure 5.4. The initial spectrum of the oxidized catalyst and the final spectrum of the reduced catalyst were used as references for the linear combination fittings. The calcined samples contain PdO and the reduction to Pd^0 begins at around 333 K for all samples. The temperature to achieve 90% as metallic Pd was 418 K for Pd; 419 K for Pd-Cu; 372 K for Pd-Zn; 394 K for Pd-Ag; and 404 K for Pd-Sn, while the temperature was 385 K to achieve 90% as metallic Ag for the Pd-Ag catalyst.

TPR-EXAFS spectra as a function of temperature are shown in Figure 5.5. Snapshots of EXAFS spectra at the initial, intermediate, and final stages of reduction are provided in Figure 5.6. In agreement with the TPR-XANES results, the initial spectra (Figure 5.5, spectrum at room temp) are dominated by the Pd-O bond. The EXAFS spectra following reduction at ~773 K for Pd, Pd-Ag, and Pd-Sn catalysts are dominated by a single peak located between 2 and 3 angstroms in the phase-uncorrected Fourier transform magnitude spectra, which can be assigned to the first Pd-Pd shell [24]. On the other hand, the EXAFS spectra of Pd-Cu and Pd-Zn catalysts show two peaks, one located close to 2 angstroms and the second peak, though smaller in magnitude as compared to Pd, Pd-Ag, and Pd-Sn catalysts, situated between 2 and 3 angstroms. XRD studies indicate that doping of Cu [25] or Zn [26] to Pd should lead to a decrease in the lattice spacing, while doping of Ag [27] or Sn [28] should lead to a slight increase in lattice spacing.

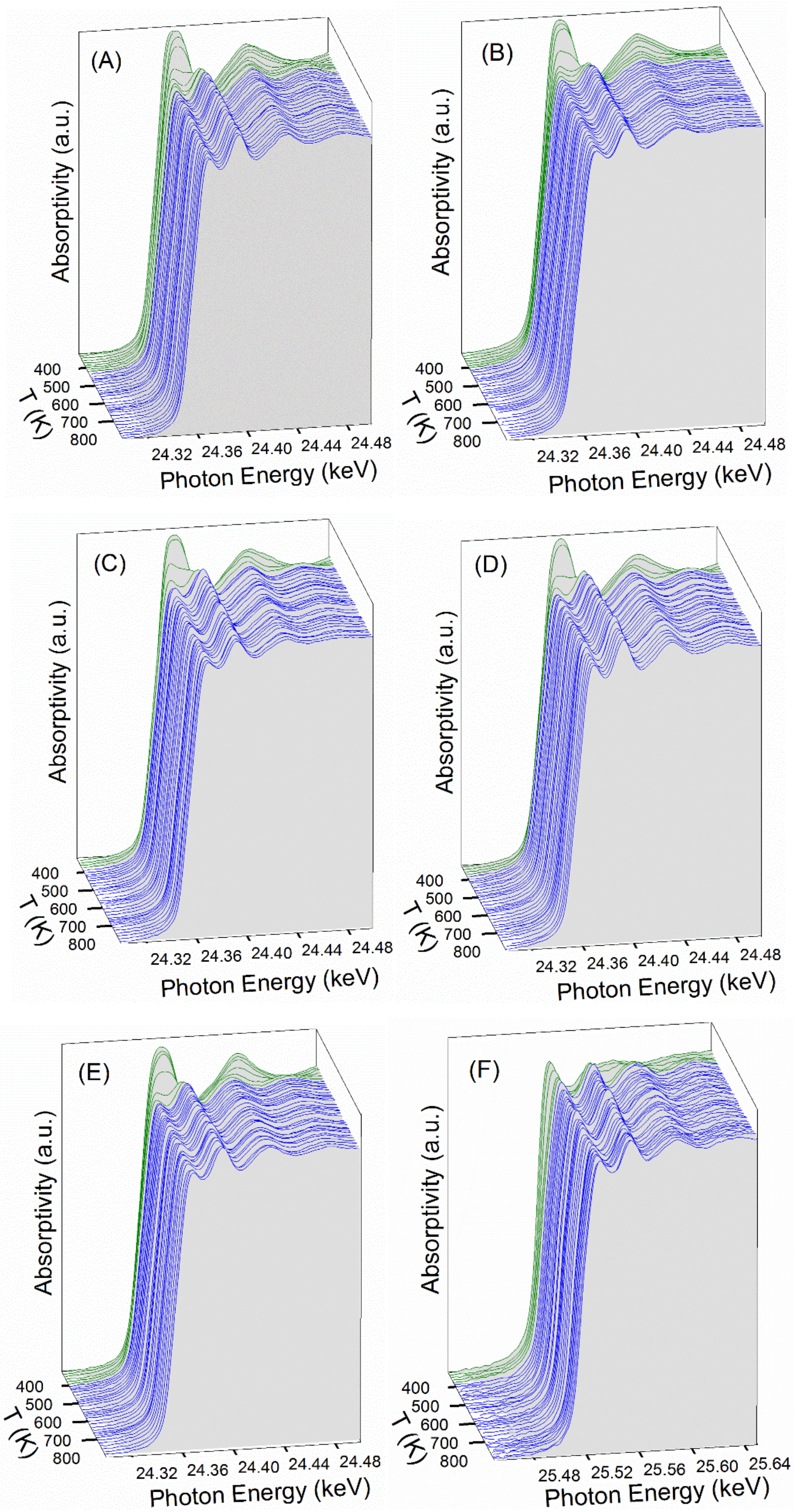

Figure 5-2. Hydrogen TPR-XANES profiles at the Pd K-edge of (A) Pd, (B) Pd-Cu, (C) Pd-Zn, (D) Pd-Ag, and (E) Pd-Sn catalysts as a function of temperature.

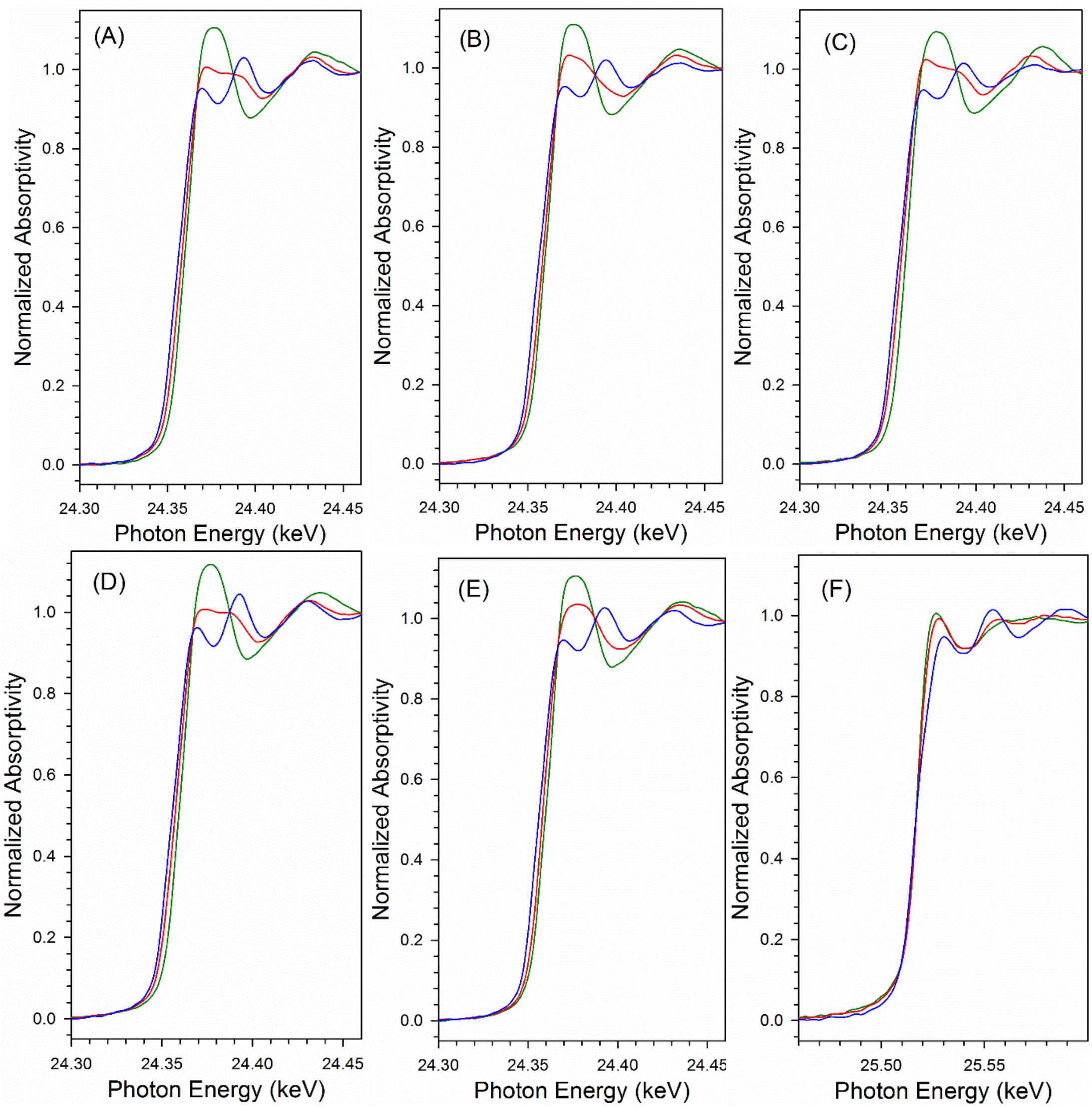

Figure 5-3. Snapshots of XANES profiles at the Pd K-edge at (green line) ~331 K; (red line) partial reduction; and (blue line) ~773 K complete reduction of (A) Pd; (B) PdCu; (C) PdZn; (D) PdAg; and (E) PdSn catalysts, and at the Au K-edge of (F) PdAg catalyst.

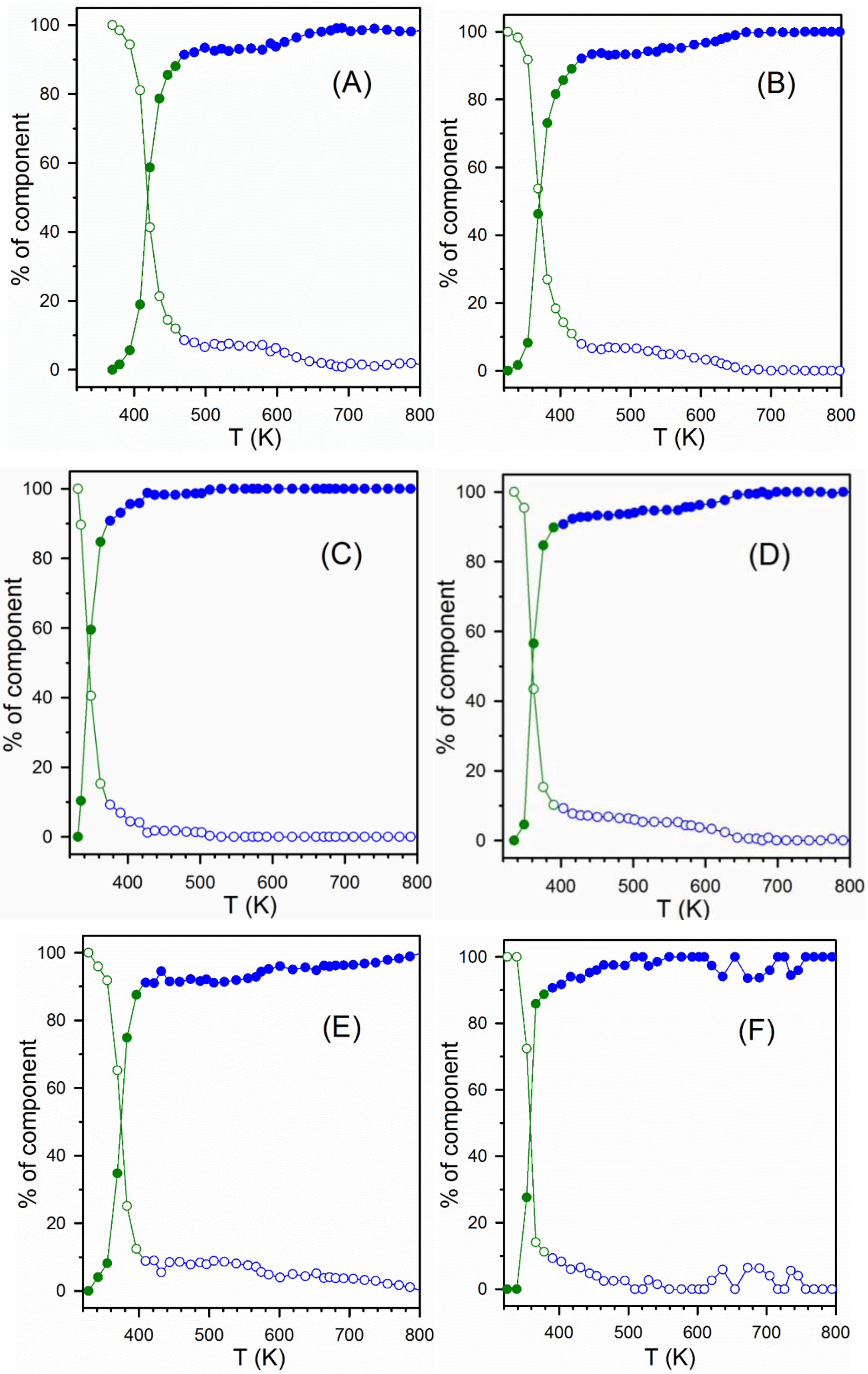

Figure 5-4. Linear combination fittings of TPR-XANES profiles at the Pd K-edge of (A) Pd, (B) Pd-Cu, (C) Pd-Zn, (D) Pd-Ag, and (E) Pd-Sn catalysts, and (F) at the Ag K-edge of Pd-Ag. (Green) % metallic < 90%; (Blue) % metallic greater than or equal to 90%.

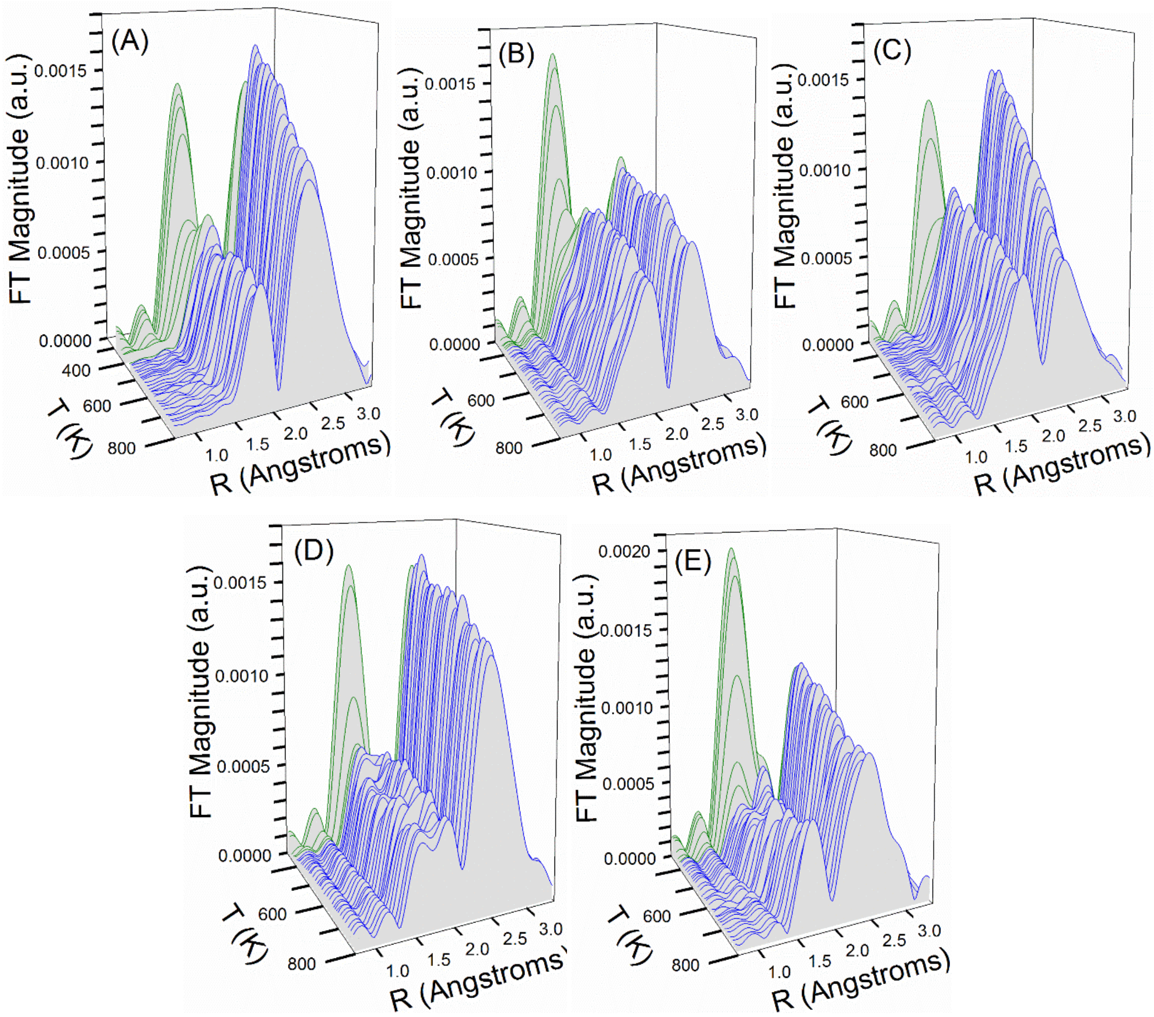

Figure 5-5. Hydrogen TPR-EXAFS k1-weighted Fourier transform magnitude spectra at the Pd K-edge of (A) Pd, (B) Pd-Cu, (C) Pd-Zn, (D) Pd-Ag, and (E) Pd-Sn.

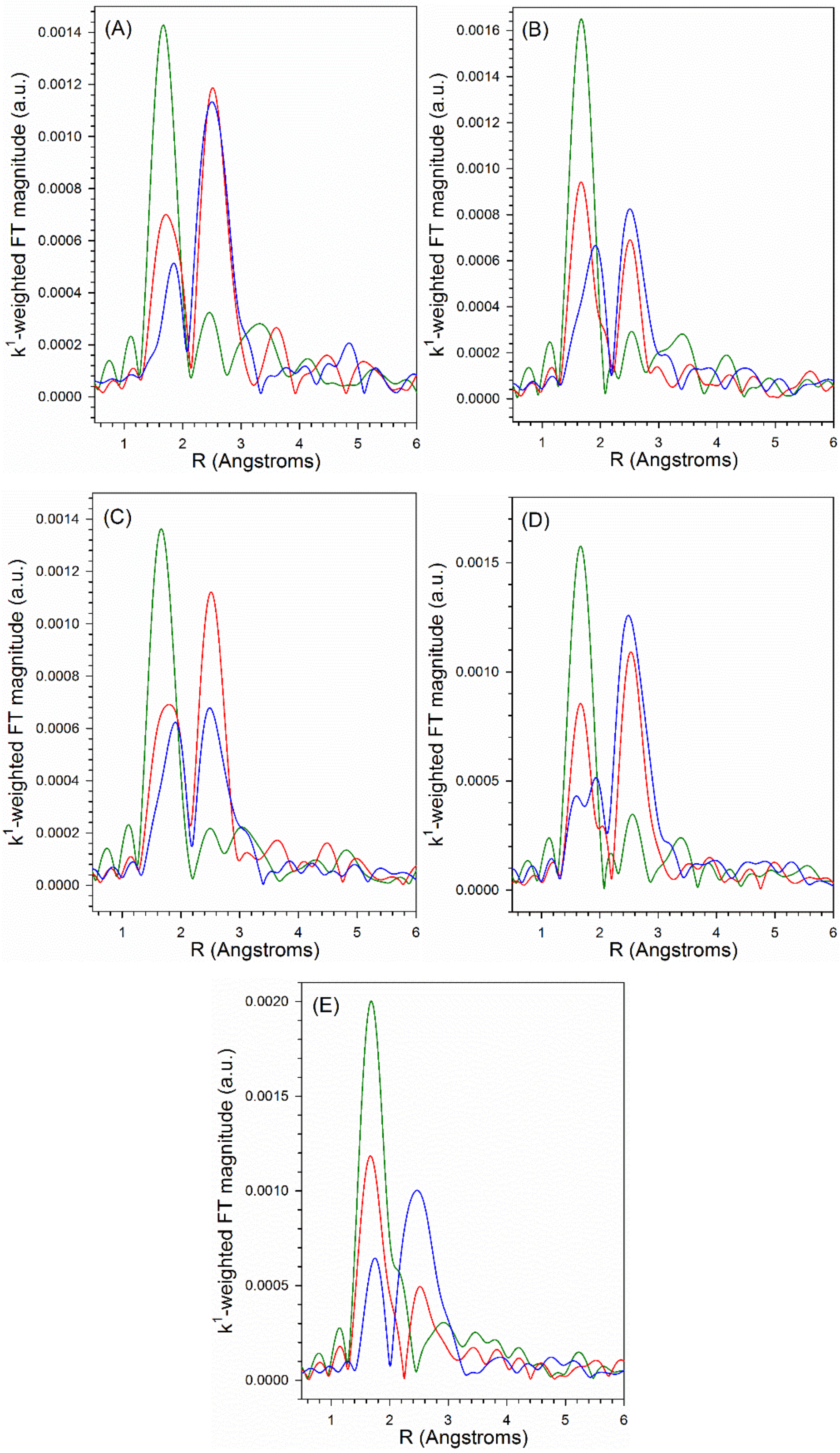

Figure 5-6. Snapshots of EXAFS profiles at the Pd K-edge at (green line) ~58°C; (red line) partial reduction; and (blue line) ~500°C complete reduction of (A) Pd; (B) PdCu; (C) PdZn; (D) PdAg; and (E) PdSn catalysts.

The raw $\chi(k)$ spectra presented in Figure 5.7 reveal that there are only slight differences in the spectra of Pd-Ag (Figure 5.7g) and Pd-Sn (Figure 5.7p) compared to the Pd alone catalyst (Figure 5.7d). There is a sharpening of the fifth maxima and an increase in the sixth minima. The result shows subtle differences in higher shells (~5 angstroms) in the Fourier transform magnitude spectra. Thus, the results are suggestive of alloying of Pd-Ag and Pd-Sn, but not conclusive. With doping of Cu or Zn, however, the results are more conclusive. The oscillations are significantly attenuated due to interference phenomena in the raw $\chi(k)$ spectra of Pd-Cu (Figure 5.7m) and Pd-Zn (Figure 5.7s) catalysts as compared to Pd alone (Figure 5.7d). In addition, two clearly defined peaks emerge in the FT magnitude spectra of Pd-Cu (Figure 5.7o) and Pd-Zn (Figure 5.7u) catalysts as compared to Pd alone (Figure 5.7f), consistent with the presence of both Pd-Pd and Pd-Cu or Pd-Zn in the first coordination sphere.

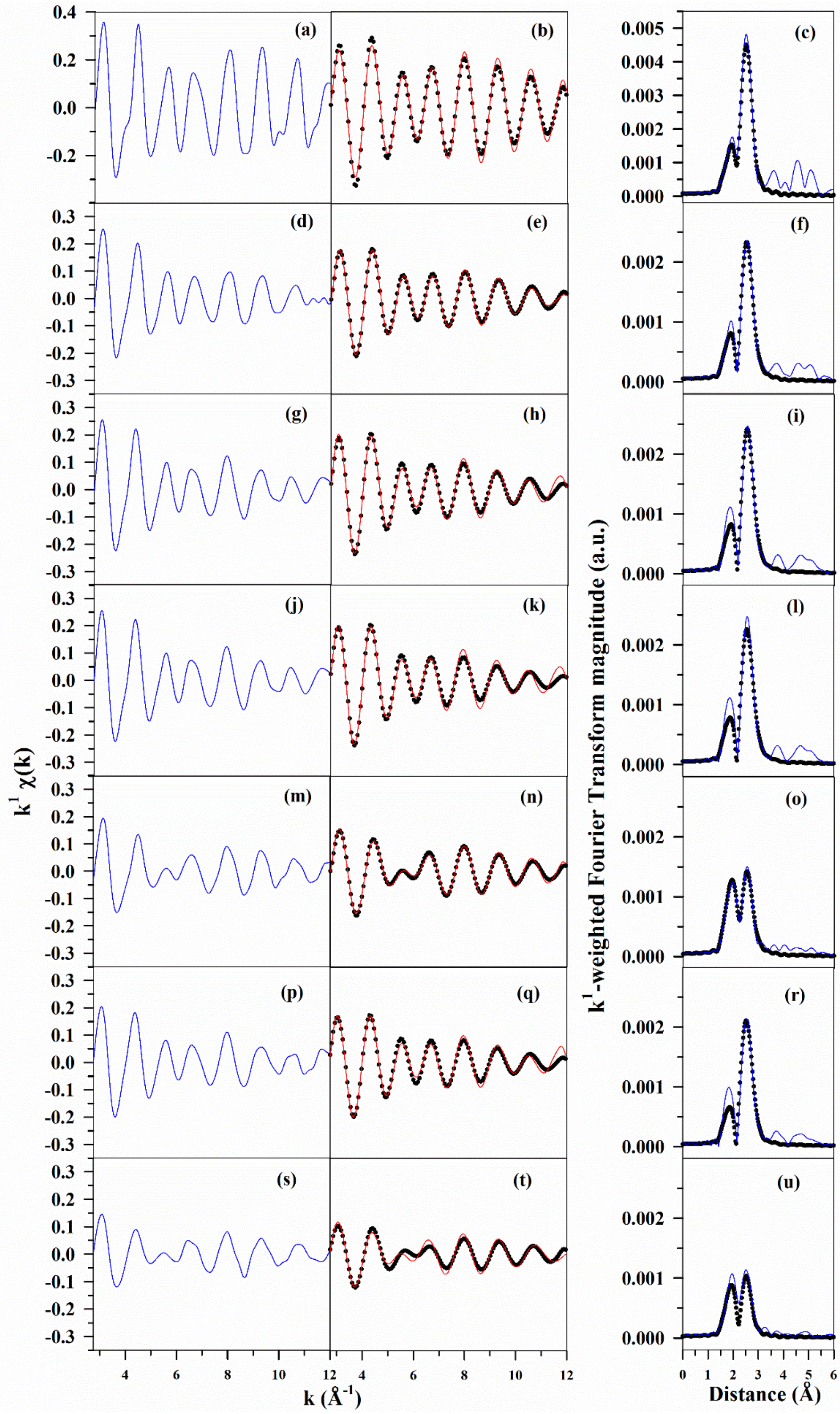

Figure 5-7. (left) (blue line) raw k1-weighted χ(k) spectra; (middle) (solid red line) filtered and (filled circles) fitted k1-weighted χ(k) spectra; and (right) (solid blue line) raw and (filled circles) fitted k1-weighted Fourier Transform magnitude spectra of (a-c) Pd^0 foil and (d-f) Pd, (g-i) Pd-Ag (separate fitting), (j-l) Pd-Ag (combination fitting), (m-o) Pd-Cu, (p-r) Pd-Sn, and (s-u) Pd-Zn catalysts. Fittings were conducted over the first Pd–M(M = Pd and/or Ag, Cu, Sn, Zn) coordination shell.

EXAFS fitting parameters of all catalysts, as well as that of the Pd foil reference are given in Table 3. For the case of the Pd-Ag catalyst, two different fittings were conducted; a fitting where data were treated separately at the Pd and Ag K-edges, and a fitting whereby some shared parameters were utilized in the fitting (e.g., Pd-Ag distance). The coordination number of the first Pd–Pd shell for Pd/ZrO_2 determined by curve-fitting was 8.6 (Pd–Pd distance, 2.733Å). The bimetallic samples showed total coordination numbers slightly higher than that of the monometallic catalyst, except for PdZn (PdAg (9.5); PdCu (10.0); PdSn (9.2); and PdZn (6.3)). The average coordination number is the EXAFS parameter related to the size and shape of the metal particles and then, it can be used to provide a rough estimate of the particle size using the analysis of Jentys [29]. Assuming a fcc crystal structure, spherical cluster morphology, and similar atomic radii relative to Pt (e.g., Cu – 135 pm, Zn – 135 pm, Sn – 145 pm, Pd – 140 pm, Pt – 135 pm, Ag – 160 pm), the results suggest that Pd/ZrO_2 catalyst had a cluster size of 1.8 ± 0.3 nm, while the PdAg, PdCu, and PdSn bimetallic catalysts exhibited slightly larger sizes (2.8 ± 0.9 nm, 3.3 ± 1.0 nm, 2.4 ± 0.9 nm), and the PdZn catalyst had a slightly smaller size (1.0 ± 0.4 nm).

Moreover, the local atomic concentration of palladium in the bimetallic catalysts was calculated by the $N_1/(N_1+N_2)$ ratio: PdAg (67%); PdCu (67%); PdSn (77%); and PdZn (68%). The results obtained indicate that the first shell around Pd atoms is close to the chemical composition expected for the bimetallic catalysts. For Pd-Cu and Pd-Zn catalysts, the fitting parameters floated to distances consistent with virtually complete alloying, since these samples showed a shorter Pd bond distance (Pd-Cu- 2.701 Å; Pd-Zn-2.681 Å versus 2.733 Å for the monometallic sample). Similar results were observed by Fox et al. [23] in an EXAFS analysis of 30% Cu–1% Pd/CeO_2 and 30% Cu–1% Pd/Al_2O_3 and it was associated with alloy formation. The r-factor for the Pd (0.0022) and PdCu fitting were excellent (0.0045), while that of PdZn was good (0.018). For both PdAg (separate fitting) and PdSn, an attempt to fit the data without constraints led to nonsensical values, where Pd-M (M=Ag and Sn) distances were significantly shorter than Pd-Pd distances. The r-factors for the separate fittings of PdAg and PdSn were excellent (0.0026) and good (0.012), respectively. In those cases, constrained fittings were made where Pd and Ag or Sn were partitioned according to their molar ratio in the first coordination shell. In that case, the results were consistent with alloy formation, but do not prove alloy formation.

Table 5-3. Results of EXAFS fitting parameters for references acquired near the Pd K-edge. The fitting ranges were Δk = 2.75 – 12.0 Å-1 and ΔR = 1.5 – 3.0 Å. $S_0^2 = 0.9$.

Sample	**N_1 Pd-Pd**	**R Pd-Pd (Å)**	**N_2 Pd-M***	**R Pd-M* (Å)**	**e_0 (eV)**	**σ^2 (Å^2)**	**r-factor**
Pd^{0}foil	**12 (set)**	2.739 (0.0078)	-	-	-1.69 (0.53)	0.00635 (0.00061)	0.014
Pd/ZrO$_2$	8.6 (0.30)	2.733 (0.0048)	-	-	-1.67 (0.28)	0.00951 (0.00064)	0.0022
PdAg/ZrO$_2$ separatefitting**	6.4 (0.46)	2.727 (0.010)	3.1 (0.23)	2.798 (0.011)	-2.37 (0.58)	0.00913 (0.0014)	0.0080
PdAg/ZrO$_2$ combinedfitting	6.8 (2.8)	2.724 (0.018)	3.3 (2.3)	2.794 (0.018)	-2.65 (0.52)	0.0105 (0.0015)	0.012
PdCu/ZrO$_2$	6.7 (0.35)	2.701 (0.0070)	3.3 (0.36)	2.604 (0.0067)	-3.29 (0.47)	0.0102 (0.00091)	0.0045
PdSn/ZrO$_2$**	7.1 (0.63)	2.723 (0.012)	2.1 (0.19)	2.765 (0.013)	-1.87 (0.71)	0.0103 (0.0017)	0.012
PdZn/ZrO$_2$	4.3 (0.71)	2.683 (0.026)	2.0 (0.67)	2.615 (0.024)	-4.94 (1.33)	0.00787 (0.0038)	0.018

Sample	**N Ag-Ag**	**R Ag-Ag (Å)**	**N Ag-Pd**	**R Ag-Pd (Å)**	**e_0 (eV)**	**σ^2 (Å^2)**	**r-factor**
PdAg/ZrO$_2$ separatefitting**	2.9 (0.14)	2.818 (0.0077)	5.9 (0.28)	2.749 (0.0075)	-0.867 (0.380)	0.0128 (0.0011)	0.0026
PdAg/ZrO$_2$ combinedfitting	0.0 (1.4)	2.864 (0.019)	7.8 (1.3)	2.794 (0.018)	-2.65 (0.52)	0.0105 (0.0015)	0.012

* where M = Ag, Cu, Sn, or Zn.

** where M (Ag or Sn) and Pd were partitioned according to the molar ratio in the first coordination shell.

Pd and Ag have a similar backscattering amplitude and phase effects on the photoelectron wave, which makes it hard to distinguish the parameters between these two elements. However, the near-neighbor distances of Pd and Ag are quite different: Pd-Pd (2.75 Å) and Ag-Ag (2.88 Å) [30]. Thus, to better evaluate alloy formation in Pd-Ag systems some authors conducted EXAFS analysis at both metal edges [31]. TPR-EXAFS spectra and the EXAFS profiles at different points of the reduction process for Ag K-edge data corresponding to the Pd-Ag catalyst are provided in Figure S3 (Appendix I).The EXAFS spectrum at room temperature shows a distinct peak for Ag-O coordination, while following reduction, a significant asymmetric peak is formed between 2 and 3 angstroms consistent with Ag-M coordination, where M is Ag and/or Pd. EXAFS fittings at the Ag K-edge are shown in Fig. S4 (Ag K-edge), while the EXAFS fittings in the Pd K-edge are shown in Fig. 5.7. The fitting parameters are presented in Table 5.3. For Pd-Ag catalyst, two different fittings were conducted, a fitting where data were treated separately at the Pd and Ag K-edges, and a fitting whereby some shared parameters were utilized in the fitting (e.g., Pd-Ag distance). After this modification, the obtained results were consistent with alloy formation, but are not conclusive. With the combination fitting for PdAg, the results suggest that Ag is, for the most part, surrounded by Pd, while Pd is surrounded by both Pd and Ag in the first coordination shell, with the ratio being consistent with alloy formation. The r-factors for the PdAg combination fitting was also good (0.012).

XPS experiments were carried out at different reduction temperatures in order to follow the evolution of the surface composition (Figure 5.8). Figures 5.8a and 5.8b shows the Zr 3p and Zr3d spectra, respectively. All catalysts exhibited a spin–orbit doublet of the Zr3d core level into $3d_{5/2}$ and $3d_{3/2}$ levels with an energy gap of 2.4 eV between them (Figure 5.8d) as well as a doublet of the Zr 3p core level representing $3p_{1/2}$ and $3p_{3/2}$. This suggests the existence of ZrO_2-like species according to previous data in the literature [32]. The analysis of the Pd 3d spectra is rather complicated due to the overlapping with the more intense Zr 3p doublet [32-34], which hinders the identification of metallic palladium. The Pd 3d spectrum of the calcined Pd/ZrO_2 sample displays a shoulder at around 338.0 eV that corresponds to the binding energy (B.E.) of $Pd3d_{5/2}$ of PdO_2 [35]. However, the data treatment of the spectrum by subtraction of the Zr 3p spectra of the support in order to obtain the Pd 3d spectrum was not carried out due to the low signal-to-noise ratio. The same problem was reported by Faticanti et al. [32] for the XPS analyses of Pd/ZrO_2 catalysts containing 0.9 and 1.1

wt.% Pd. The reduction at 373 K led to the disappearance of this peak and the appearance of a shoulder corresponding to the B.E. of Pd3d$_{3/2}$, indicating that PdO was reduced to Pd^0. After reduction at 773 K, the samples were submitted to an oxidative atmosphere (pure O_2) at room temperature, but the Pd^0 particles were stable against re-oxidation.

The Cu 2p spectra of PdCu/$ZrO_2$are shown in Figure 5.8f. The calcined sample exhibits a peak around 934.8 eV, which is characteristic of Cu^{2+} species in CuO [36]. After reduction at 373K, a rather asymmetric peak is observed, with a shoulder at 934.8 eV, indicating that partial reduction of CuO takes place. Further increasing to 473K produces a peak around 931.9eV, which is assigned to Cu^0 [23]. This result suggests that copper was completely reduced at this temperature [36]. Increasing the reduction temperature to 773K decreased the intensity of this band that is likely due to Cu^0 sintering. According to the literature, the Cu 2p peak related to Cu^0 in this work is shifted towards lower BE around 0.9 eV [23]. Fox et al. [23] observed that for CuPd/CeO_2 bimetallic catalysts the Cu 2p$_{3/2}$ and Cu2p$_{1/2}$ peaks were located at 932.0 and 951.6 eV, respectively, which were shifted by 0.4–0.6 eV compared to the monometallic Cu/CeO_2 catalyst. These results may be an indication of the existence of a PdCu alloy.

For PdAg/ZrO_2 (Figure 5.8h), the spectrum for the calcined sample exhibited a band around 368.6 eV. After reduction at 373 K, this band moved to 367.6 eV and remained unchanged during heating up to 773 K. According to the literature, the binding energy of Ag$^+$ in Ag_2O is around 367.8 eV, while the value around 368.2 eV indicates the presence of metallic Ag [37]. Therefore, this result revealed the presence of Ag^0 on the PdAg/ZrO_2 calcined sample. The B.E. of Ag3d$_{5/2}$ observed for the reduced sample was shifted -0.6 eV in comparison to the binding energy of Ag^0, which suggests the formation of a Pd-Ag alloy. The core level shifts relative to pure Pd and Ag depend on changes in the bulk charge around an atomic site. According to Lamb et al. [38] the partial charge transfer from Ag to Pd during the reduction treatment can result in a decrease in the binding energy of Ag.

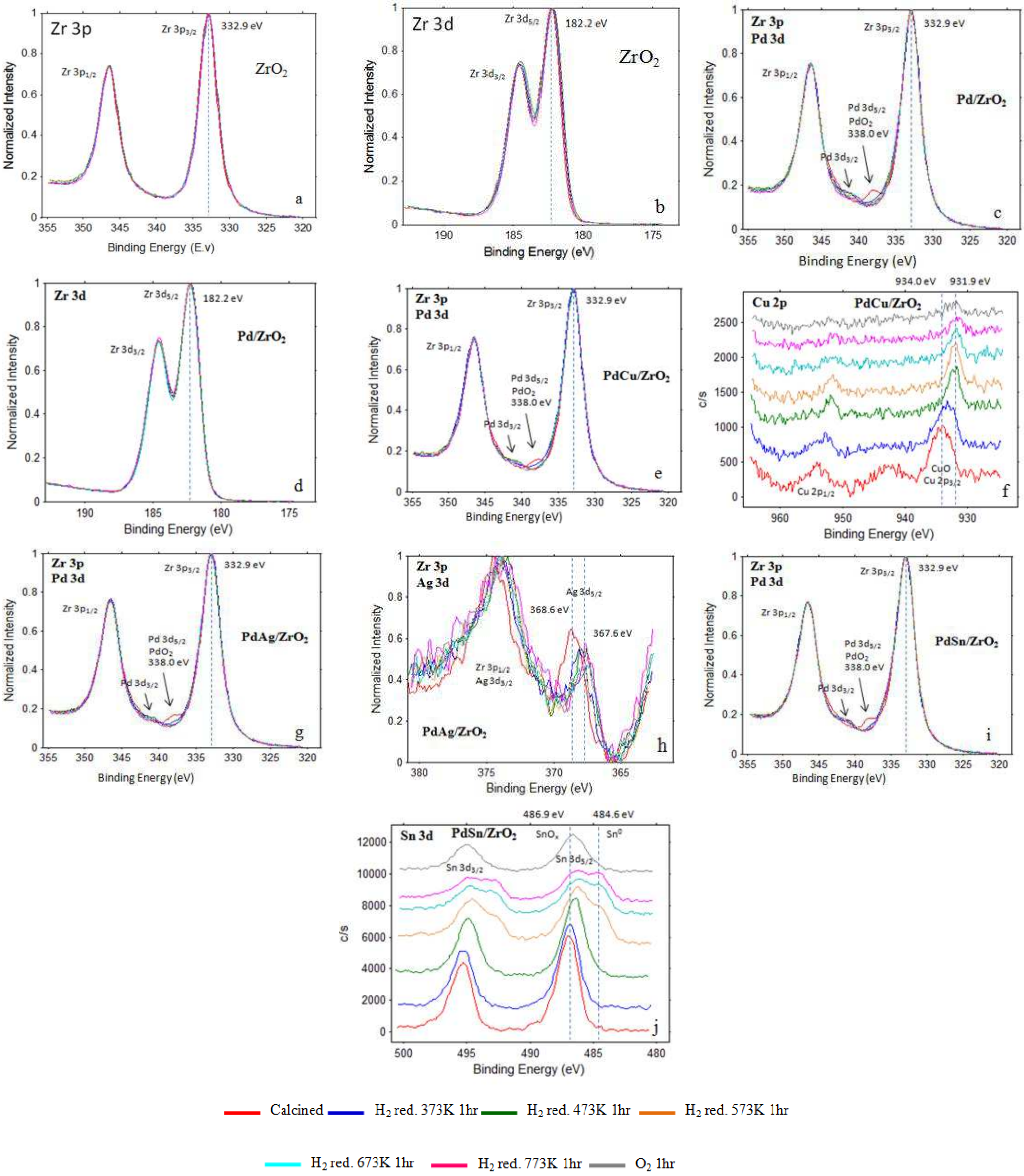

Figure 5-8. XP spectra of the Pd/ZrO$_2$ and PdMe/ZrO$_2$ catalysts (Me=Ag, Cu and Sn).

Figure 5.8j displays the Sn 3d spectra of $PdSn/ZrO_2$ catalyst. The spectrum of the calcined sample showed two peaks at 486.8 eV and 495.3 eV attributed to the Sn $3d_{5/2}$ and $3d_{3/2}$ core levels respectively. According to the literature [14,39,40], these peaks correspond to the presence of oxidized Sn. However, it is not possible to distinguish between Sn^{2+} and/or Sn^{4+}oxidation states through XPS analysis [14,41]. According to Nishiiyama et al. [41], the spectra of SnO_2 powder and Sn foil showed peaks at 486.9 and 484.8 eV, respectively, which were assigned to Sn^{2+} and/or Sn^{4+}species and Sn^0. The spectrum remained unchanged after reduction at 373K. The treatment at 473K under H_2 slightly shifted the bands to lower binding energies, indicating that tin oxide is partially reduced to species with lower valence. The increase in the reduction temperature to 573 K led to the appearance of a shoulder at 484.6 eV, which suggests that metallic tin was formed. This result is in agreement with the TPR experiment that also revealed the reduction of tin oxide around this temperature. The spectrum obtained after reduction at 773K still contains the peaks characteristic of SnO and Sn^0, which reveals that tin remains partially oxidized on the surface at this temperature.

In general, palladium is known to form an homogenous solid solution at all compositions with different metals, such as Ag [42,43], and Cu [44,45]. Fernández-García et al. [46] studied the reduction of three Pd-Cu/KL-zeolite bimetallic catalysts with different Pd:Cu atomic ratios. This study was performed using XANES and infrared spectroscopy of adsorbed CO as a probe molecule. The authors observed the formation of Pd-Cu alloys, with electronic perturbation of both components over the full range of compositions. According to them, the alloy particles did not exhibit significant Cu segregation on the surface. Venezia et al. [47] studied the structure of supported Pd-Ag and Pd-Cu catalysts. The samples were characterized by XPS and XRD. In general, the systems showed different behaviors; For Pd-Cu, it was observed a mixture of monometallic and alloyed particles, while silver segregation to the surface was observed with no evidence of alloy formation for Pd-Ag. Cárdenas et al. [48] used chemisorption technique to investigate the Pd_nSn_m alloys in PdSn supported samples. For the samples supported on Al_2O_3 a relatively small amount of Sn alloying with Pd was observed. However, Sn apparently tends to cover the Pd particles on the silica supported catalysts. Vicente et al. [14] confirmed the existence Pd–Sn bimetallic interactions for $PdSn/SiO_2$. According to them, the quantity of Sn^0 species suggested the formation of a Pd_3Sn alloy for samples reduced above 573K. The formation of PdZn alloy has also been reported in the literature [49,50]. The bulk PdZn alloy was formed by the spill-over of atomic hydrogen from the Pd metal to the ZnO, leading to facile reduction of the ZnO and migration of Zn to the metallic surface [51]. It is important to note that it was not possible to determine the surface composition of the samples by XPS analysis. The Pd 3d signal derived from spectra subtraction had a too low signal-to-noise ratio to lead to unambiguous results.

5.3.2. HDO of phenol

The phenol conversion and product yield for HDO of phenol at 573 K over all catalysts as a function of W/F are shown in Figure 5.9.

The zirconia support was also tested and it was inactive under the reaction conditions used. Pd/ZrO_2 catalyst was much more active than all bimetallic catalysts. The addition of metal dopant decreased the phenol conversion, which agrees very well with the decrease in H_2 chemisorption and reaction rate of cyclohexane dehydrogenation reaction. The product distributions showed a remarkable dependence on the type of the second metal. For Pd/ZrO_2 catalyst, benzene was the dominant product for W/F > 0.1 h, with the formation of cyclohexanone (ONE) and traces amounts of C_{12} hydrocarbons (biphenyl, cyclohexylbenzene) and C_{12} oxygenated compounds (2-phenylphenol, 2-cyclohexylphenol, 2-cyclohexylcyclohexan-1-one). de Souza et al. [13] showed that the formation of these bicyclic compounds during the HDO of phenol comes from the alkylation of phenolic and aromatic rings by saturated alcohols, which is catalyzed by Lewis acid sites.

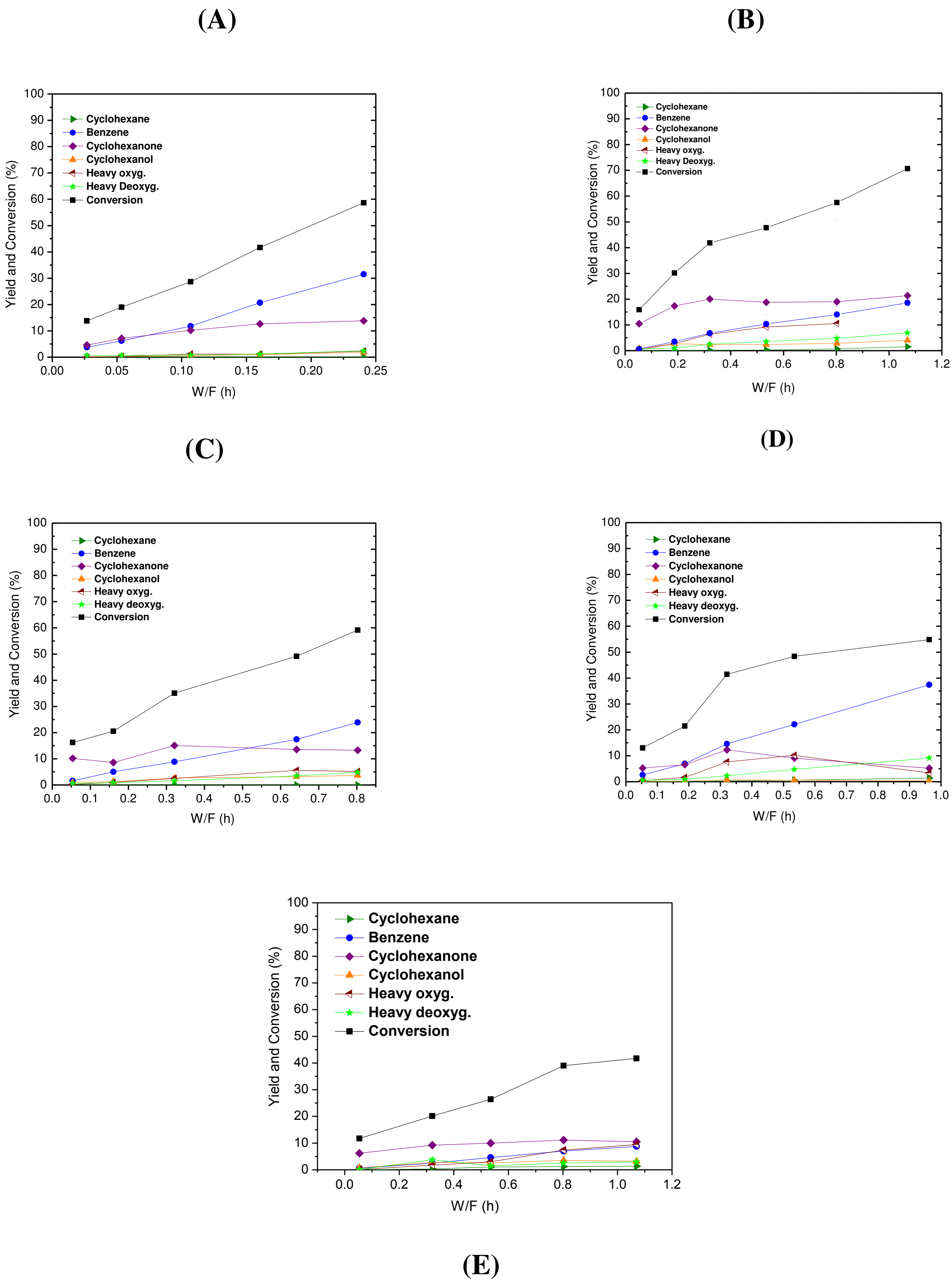

Figure 5-9. Phenol conversion and yield of products as a function of W/F over: (A) Pd/ZrO_2; (B) $PdAg/ZrO_2$; (C) $PdCu/ZrO_2$; (D) $PdSn/ZrO_2$; (E) $PdZn/ZrO_2$. Reaction conditions: T = 573 K, P = 1 atm, and H2/phenol molar ratio =60.

PdCu/ZrO_2 catalyst showed a product distribution similar to that observed for Pd/ZrO_2. However, significant formation of benzene was achieved only at higher W/F (> 0.5 h). Cyclohexanone was the main product over PdZn/ZrO_2 catalyst. The other products formed were benzene and C_{12} oxygenated compounds, with small amounts of OL. The addition of Ag to Pd promoted the formation of cyclohexanone, decreasing the production of benzene. Furthermore, a higher formation of C_{12} hydrocarbons and C_{12} oxygenated compounds was also observed. PdSn/ZrO_2 catalyst exhibited similar product distribution of the monometallic catalyst, with higher formation of C_{12} oxygenated compounds.

Figure S5 (Appendix I) displays the selectivity as a function of conversion. For all catalysts, increasing the phenol conversion rises the selectivity to benzene and bicyclic compounds, whereas the formation of cyclohexanone decreases.

The reaction rate of HDO of phenol was calculated and the selectivity of all catalysts was compared at low phenol conversion (around 13%), as shown in Table 5.4. The monometallic catalyst showed the highest reaction rate that followed the order: Pd > PdAg ≈ PdCu > PdSn > PdZn. This was the same order observed for the metal dispersion reported in Table 1, which suggests that Pd particles are covered by the metal dopant or the Pd-alloy has a lower activity. Pd/ZrO_2 exhibited the highest selectivity to benzene followed by PdSn, while the addition of Ag, Cu and Zn favors the formation of cyclohexanone and cyclohexanol. These results indicate that the type of metal dopant significantly impacts the adsorptive and catalytic properties of Pd particles, which is likely due to the formation of Pd-based alloys.

5.3.2.1. The effect of the second metal on the reaction pathways for HDO of phenol

Different catalysts have been studied for HDO of phenolic compounds such as phenol or cresol, including supported noble metals (Pd, Pt, Rh, Ru) [6,9,11,52-58] supported base metals (Ni,Co,Fe,Cu) [3,5,6,59-63] and bimetallic catalysts [10,8]. However, studies comparing the performance of a series of catalysts with different metals are scarce and only few were carried out in gas phase but in these cases, the HDO of m-cresol was investigated [10].

Table 5-4. Conversion, selectivity and reaction rate for HDO of phenol at 573 K and atmospheric pressure.

Samples	**Conversion** (%)	**Selectivity (%)**					**Reaction Rate** ($mol_{phenol}.min^{-1} g_{cat}^{-1}$)
		Benzene	**OL**	**ONE**	**C_{12}Oxigenated**	**C_{12}Hydrocarbon**	
Pd/ZrO_2	9.09	41.29	1.58	50.34	0.0	6.78	0.086
PdAg/ZrO_2	12.99	4.97	6.32	80.70	2.68	5.34	0.049
PdCu/ZrO_2	13.54	11.79	7.15	74.91	1.68	4.46	0.050
PdSn/ZrO_2	8.91	29.29	1.28	58.96	4.03	6.43	0.040
PdZn/ZrO_2	7.74	7.51	9.57	80.36	1.24	1.32	0.036

Comprehensive studies were performed about the HDO of m-cresol in gas phase at 573 K over different silica supported catalysts (Pd, Pt, Ru, Ni, Fe, NiFe) [64-65]. Hydrogenation products (3-methylcyclohexanone and 3-methylcyclohexanol) were the main products formed over Pt/SiO_2, Pd/SiO_2 and Ni/SiO_2 catalysts, whereas toluene was the dominant product on Fe and Ni–Fe bimetallic catalysts. Ru/SiO_2 catalyst showed significant formation of toluene as well as CH_4 and C_2-C_6 hydrocarbons. For the bimetallic catalyst, the presence of an oxophilic metal, such as the unreduced Fe species promoted the hydrogenation of the carbonyl group of the tautomer intermediate, producing toluene.

Sun et al. [8] investigated the performance of different supported metal catalysts (Cu/C, Fe/C, Pd/C, Pt/C, PdFe/C, and Ru/C) for the vapor phase hydrodeoxygenation of guaiacol at 523-723K temperature range. For all the samples, phenol was the major intermediate product. For the noble metals, the main reaction pathway was the saturation of the aromatic ring, which leads to the formation of cyclohexanone and cyclohexanol. The base metals showed lower activity than the noble metal catalysts, however they favored the formation of ring-saturated or ring-opening products. The bimetallic PdFe/C catalyst showed the highest HDO activity and selectivity to deoxygenated products.

In the present work, Pd/ZrO_2 catalyst exhibited the highest selectivity to benzene. The high selectivity to deoxygenated products of zirconia supported catalysts has been attributed to the presence of oxophilic sites represented by incompletely coordinated Zr^{4+} and Zr^{3+}cations near the perimeter of the metal particles [11]. These oxophilic sites favor the interaction of the oxygen of the carbonyl group in phenol tautomer intermediate with the metal particle. Then, the carbonyl group is preferentially hydrogenated on the metal particles at the metal-support interface, leading to the formation of benzene after the facile dehydration of the reactive intermediate. However, the addition of a second metal significantly affected product distribution for HDO of phenol over Pd/ZrO_2 catalyst. The following order of selectivity to cyclohexanone and cyclohexanol was observed: Pd (52%) < PdSn (60%) < PdCu (82%) < PdAg (87%) ≈ PdZn (90%). Considering the reaction mechanism based on the tautomerization, Ag, Cu and Zn dopants seem to promote the hydrogenation of the ring, producing preferentially cyclohexanone and cyclohexanol. Sn exhibits an intermediate behavior, more close to the monometallic Pd catalyst, which favored the formation of benzene likely due to the hydrogenation of the carbonyl group. Therefore, the hydrogenation capacity of Pd was enhanced in the presence of Ag, Cu and Zn dopants, suggesting that adsorptive and catalytic properties of Pd were modified. In our work, in situ EXAFS and XPS provided evidence for the formation of Pd alloy with the second element for all these samples (Ag,Cu and Zn), which could be responsible for the increase in the hydrogenation capacity observed.

Iwasa et al. [66] studied the hydrogenation of crotonaldehyde over supported Pd catalysts in gas phase. The authors showed that alloying of Pd with Zn improves the activity for hydrogenation of crotonaldehyde to crotyl alcohol. According to the authors, the selectivity to unsaturated alcohol is improved when the Pd is alloyed with another more electropositive metal, which increases the electron density of the Pd and favors the hydrogenation of the C=O. Sitthisa et al. [67] reported that the incorporation of Cu to Pd/SiO_2 catalyst results in the formation of PdCu alloys, which exhibited an electronic structure different from that of pure Pd. This electronic change affects the product distribution of the hydrogenation of furfural and 2-methylpentanal. The overall activity and the decarbonylation selectivity for both reactions decreased on PdCu catalysts, while the selectivity to hydrogenation and etherification increased.

Therefore, in this work, the interaction of the oxygen of the carbonyl group from the phenol tautomer intermediate with the Pd surface is likely weakened, favoring the hydrogenation of the ring due to the Pd alloying with Ag, Cu, and Zn dopants.

However, PdSn/ZrO_2 catalyst showed a higher formation of benzene than the other bimetallic catalysts. In fact, XPS analysis of PdSn sample revealed the presence of unalloyed Sn that remained as tin oxide on the surface even after reduction at high temperature. For the PdSn/ZrO_2 catalyst, tin oxide promoting the formation of benzene (Table 5.4). Once Sn^{n+} is located at or near the hydrogenation active metal particles, it favors the adsorption of the reagent through its carbonyl group, which increases the hydrogenation probability of the C=O double bond. The same result was reported by Nie et al. [10] for a NiFe/SiO_2 catalyst where the unreduced Fe species promoted the hydrogenation of the carbonyl group. The presence of unreduced iron promoted the hydrogenation of carbonyl group. Vicente et al. [14] studied influence of the structural properties of the PdSn/SiO_2 catalysts on citral hydrogenation reaction. According to them, the addition of Sn considerably increases the selectivity toward the unsaturated alcohol. These results were attributed to the formation of the Pd_3Sn intermetallic phase.

Regardless of the type of the dopant, C_{12} hydrocarbons (biphenyl, cyclohexylbenzene) and C_{12} oxygenated compounds (2-phenylphenol, 2-cyclohexylphenol, 2-cyclohexylcyclohexan-1-one) were also observed. These bicyclic hydrocarbons have been observed during the conversion of HDO of phenol over Pd/Al_2O_3, whereas only trace amounts of these compounds were detected over Pd/ZrO_2 [11]. Bicyclic products are formed by the alkylation of phenolic and aromatic rings by cyclohexanone. Alkylation is catalyzed by acid sites such as Lewis acid sites present on the supports. Therefore, the formation of bicyclic oxygenated compounds on the Pd-Me/ZrO_2 catalysts is likely due to the presence of Lewis acid sites present on zirconia.

The variation of product distribution could also be attributed to the changes in ensemble size. In this work, Pd dispersion significantly decreased when the metal dopant was added (Table 5.1). De Souza et al. [11] studied the effect of Pd particle size on the product distribution for HDO of phenol over Pd/ZrO_2 catalysts, which had different Pd dispersions. Both catalysts exhibited similar selectivities indicating that metal dispersion does not significantly affect the product distribution for HDO of phenol reaction.

5.3.3. Stability tests

Phenol conversion and product distributions as a function of TOS (24h) for all catalysts are shown in Figure 5.10.

Pd/ZrO_2, $PdCu/ZrO_2$, $PdSn/ZrO_2$ and $PdAg/ZrO_2$ showed similar initial conversion (60%), while $PdZn/ZrO_2$ had lower initial conversion (40%) (Figure 5.10a). All catalysts deactivated mainly during the first 6 h of TOS but the deactivation degree depended on the type of the metal. The stability of the catalysts defined by Eq. (4) was calculated and the results are listed in Table 5.5 (deactivation parameter – DP). Pd/ZrO_2 and $PdZn/ZrO_2$ and $PdAg/ZrO_2$ exhibited approximately the same deactivation degree. These results demonstrate that the addition of these dopants did not decreased catalyst deactivation during HDO of phenol. Therefore, the Pd-alloying with Ag, Zn and Cu did not have a positive effect on catalyst stability. However, the loss in activity was less pronounced for $PdSn/ZrO_2$ catalyst.

There were also changes in the product distribution along the reaction (Figure 5.10 b-f). Selectivity to ONE and benzene remained approximately constant during 24 h for all catalysts. However, the selectivity to C_{12} oxygenated compounds (2-phenylphenol, 2-cyclohexylphenol, 2-cyclohexylcyclohexan-1-one) significantly increased whereas the C_{12} hydrocarbons (biphenyl, cyclohexylbenzene) were no longer detected after 6h of TOS.

Table 5-5. Deactivation parameters (DP) of the studied samples.

Samples	$X_{initial}$	X_{final}	DP
Pd/ZrO_2	0.62	0.30	0.37
$PdAg/ZrO_2$	0.62	0.28	0.34
$PdCu/ZrO_2$	0.57	0.22	0.29
$PdSn/ZrO_2$	0.60	0.36	0.49
$PdZn/ZrO_2$	0.39	0.16	0.35

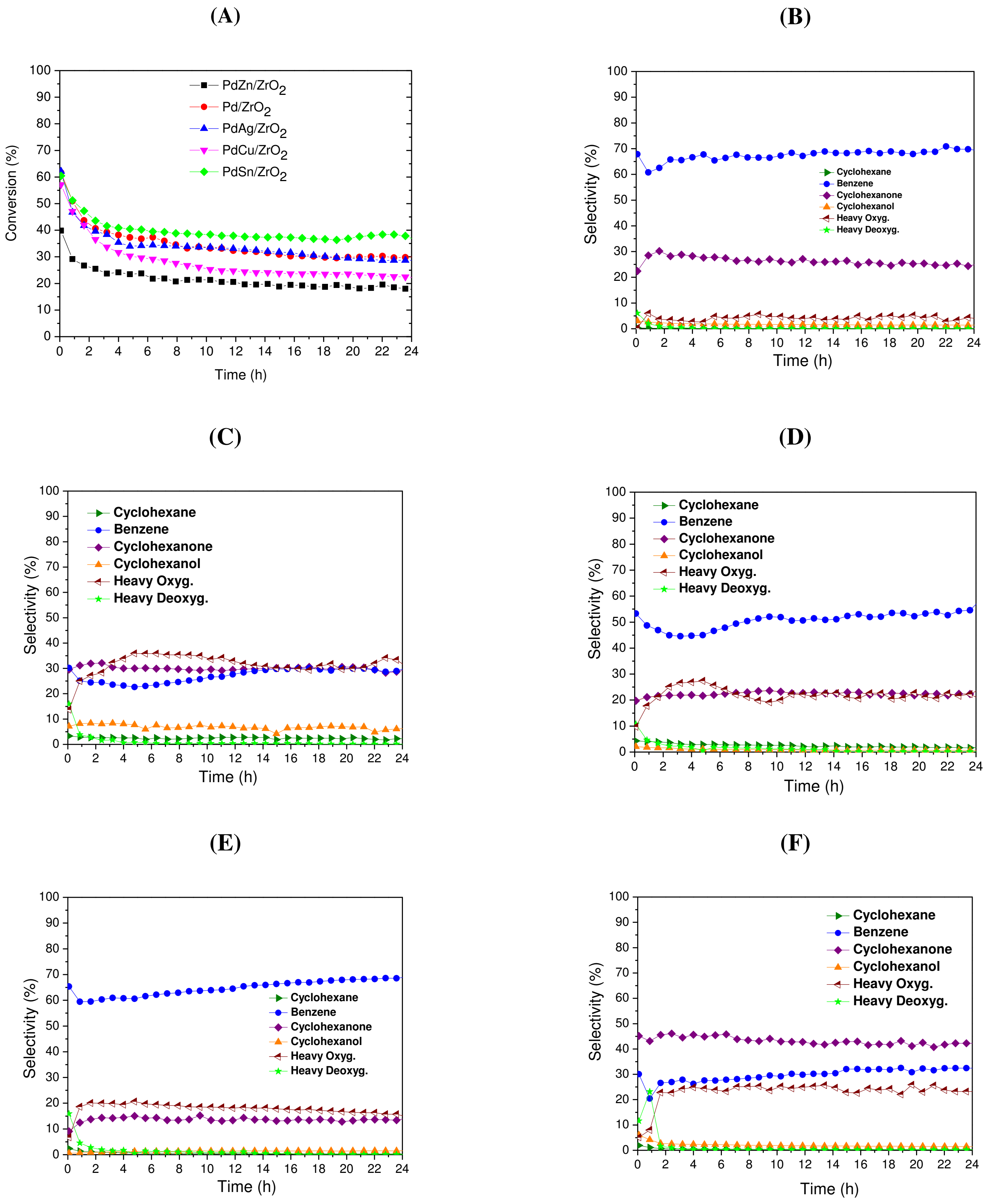

Figure 5-10. Conversion of phenol (A) and selectivity to products as a function of TOS for: (B) Pd/ZrO$_2$ (W/F = 0.320 h-1); (C) PdAg/ZrO$_2$ (W/F = 0.963 h-1); (D) PdCu/ ZrO$_2$ (W/F = 0.963 h-1); (E) PdSn/ZrO$_2$ (W/F = 0.963 h-1); (F) PdZn/ZrO$_2$ (W/F = 1.069 h-1). Reaction conditions: T = 573 K, P = 1 atm, and H_2/phenol molar ratio =60.

Catalyst deactivation is one of the main challenges of HDO reactions. Catalyst deactivation during HDO of phenol could be due to the sintering of the metallic particles, changes in the density of acid sites or the deposition of carbonaceous species on the catalyst surface [3].

In order to investigate the main causes of deactivation of Pd-dopant/ZrO_2, the spent catalysts were characterized by Raman spectroscopy and cyclohexane dehydrogenation reaction. The Raman spectra of the used catalysts did not show bands characteristic of carbon materials in the range of 1200 - 1800 cm^{-1}. This result indicates that the deactivation of Pd catalysts was likely not caused by the coverage of Pd particles or acid sites by carbonaceous deposits.

The comparison between the rates of the cyclohexane dehydrogenation reaction before and after HDO of phenol was used to provide information about changes in Pd particle size during HDO reaction. Table 5.6 lists the Pd dispersion of the fresh and used catalysts after 24 h of TOS. This reaction was not carried out with PdCu catalyst because Cu is also active for this reaction. Pd dispersion significantly decreased during the reaction, indicating that the sintering of Pd particles is one of the causes for catalyst deactivation. The undoped Pd catalyst exhibited the highest decrease in the ratio of the reaction rate of cyclohexane dehydrogenation of the used and fresh catalyst (DR), whereas the lowest decrease was observed for PdSn/ZrO_2 catalyst. These results are in agreement with deactivation observed during HDO of phenol reaction (Table 5), confirming that Pd sintering is the main cause of catalyst deactivation. Furthermore, the addition of dopants (Ag, Zn) to Pd/ZrO_2 did not improve the resistance of Pd to sintering and then, the catalysts still deactivated in spite of the formation of a Pd-alloy.

Changes in the density of acid sites of the support may also contribute to catalyst deactivation. However, in our work, all samples use the same support and then, it is expected that the changes in the density of acid sites will affect all the samples in a similar way and could not explain the differences in deactivation observed among the catalysts.

Recently, de Souza et al. [12] investigated the mechanism of deactivation of Pd-based catalysts for HDO of phenol. All catalysts deactivated during the reaction but the deactivation degree depended on the support. Pd/ZrO_2 catalyst showed a strong deactivation during the reaction. The DRIFTS experiments revealed that there was a significant buildup of intermediate species on the surface during the reaction. This result was attributed to the loss of the metal-support interface due to the growth of Pd particles that affects the ability of the adsorbed species to turnover, leading to an accumulation of phenoxy species during reaction.

Table 5-6. Reaction rate of cyclohexane dehydrogenation reaction and calculated dispersion by dehydrogenation of cyclohexane before and after HDO of phenol reaction.

Samples	**Fresh catalyst**		**Used catalyst**		**DR(%)**
	Reaction rate*	**Dispersion (%)**	**Reaction rate***	**Dispersion (%)**	
Pd/ZrO$_2$	7.78E-04	38	1.23E-04	7	15.81
PdCu/ZrO$_2$	7.02E-04	-	1.57E-05	-	-
PdAg/ZrO$_2$	1.84E-04	9	1.57E-05	1	8.53
PdSn/ZrO$_2$	2.10E-04	10	1.26E-05	1	6.0
PdZn/ZrO$_2$	9.32E-05	5	1.28E-05	1	13.73

*mol cyclohexane/ (g_{Pd}.min)

Therefore, metal sintering is likely the main cause of the deactivation of zirconia supported bimetallic catalysts of the present work, which can be related to the re oxidation of the Pd [68]. Among the samples, PdSn/ZrO$_2$ showed a deactivation ratio lower than the others, however it had a similar metal sintering level. The higher stability observed for this sample may be related to the presence of Sn oxide on its surface as revealed by XPS analysis. Sn^{n+} species are oxophilic sites that favors the adsorption of the keto-tautomer of phenol through its carbonyl group and promotes the hydrogenation of the C=O bond. These sites turn over the oxygenate intermediates, decreasing their accumulation on the surface and reducing catalyst deactivation.

5.4. Conclusions

This work studied the performance of zirconia supported bimetallic catalysts for HDO of phenol reaction. Pd/ZrO$_2$ catalyst exhibited the highest activity and selectivity to benzene. This has been attributed to the presence of oxophilic sites represented by Zr^{4+}and Zr^{3+}cations near the perimeter of the metal particles, which favors the interaction of the oxygen from the carbonyl group of phenol tautomer intermediate with the metal particle. Then, the carbonyl group is preferentially hydrogenated on the metal particles at the metal-support interface, leading to the formation of benzene after the facile dehydration of the reactive intermediate.

The addition of a second metal significantly affected activity and product distribution for HDO of phenol over Pd/ZrO_2 catalyst. All bimetallic catalysts exhibited lower reaction rates for HDO of phenol compared to the monometallic one. H_2 chemisorption and the reaction of dehydrogenation of cyclohexane demonstrated that the loss in activity was due to the surface segregation of the second metal. Considering the reaction mechanism based on the tautomerization, Ag, Cu and Zn dopants seem to promote the hydrogenation of the ring, producing preferentially cyclohexanone and cyclohexanol. Sn exhibits an intermediate behavior, more close to that of the monometallic Pd catalyst, with a higher formation of benzene, which is likely due to the hydrogenation of the carbonyl group.

Therefore, the hydrogenation capacity of Pd was enhanced in the presence of Ag, Cu and Zn dopants, suggesting that adsorptive and catalytic properties of Pd were modified. In situ EXAFS, STEM and XPS provided evidence for the formation of Pd alloy with the second element for all these samples, which could be responsible for the increase in the hydrogenation capacity observed.

XPS analysis of PdSn sample revealed the presence of unalloyed Sn that remained as tin oxide on the surface even after reduction at high temperature. For the PdSn/ZrO_2 catalyst, tin oxide should exhibit an oxophilicity similar to Zr^{4+} cations, promoting the formation of benzene. Once Sn^{n+} is located at or near the metal particles, it favors the adsorption of the keto-tautomer of phenol through its carbonyl group, which increases hydrogenation of the C=O bond.

All catalysts deactivated mainly during the first 6 h of TOS. Pd/ZrO_2 and PdZn/ZrO_2 and PdAg/ZrO_2 exhibited approximately the same deactivation degree. However, the loss of activity was less pronounced for PdSn/ZrO_2 catalyst. The Raman spectra of the used catalysts did not show bands characteristic of carbon materials in the range of 1200 - 1800 cm^{-1}. The comparison between the rates of the cyclohexane dehydrogenation reaction before and after HDO of phenol was used to provide information about changes in Pd particle size during HDO reaction. Pd dispersion significantly decreased during the reaction, indicating that the sintering of Pd particles is one of the causes for catalyst deactivation.

Acknowledgments

The authors thank CAPES (Coordenação de Aperfeiçoamento de Pessoal de Ensino Superior) and CNPq (Conselho Nacional de Desenvolvimento Científico e Tecnológico) for supporting this research and the scholarship received. The XPS and TEM analyses were performed by Drs. Mark Engelhard and Libor Kovarik, respectively, using resources at EMSL, a DOE Office of Science User Facility sponsored by the Office of Biological and Environmental Research and located at Pacific Northwest National Laboratory. The work carried out at the CAER was supported in part by funding from the Commonwealth of Kentucky. Argonne's research was supported in part by the U.S. Department of Energy (DOE), Office of Fossil Energy, National Energy Technology Laboratory (NETL). The use of the Advanced Photon Source was supported by the U.S. Department of Energy, Office of Science, Office of Basic Energy Sciences, under Contract No. DE-AC02-06CH11357. MRCAT operations are supported by the Department of Energy and the MRCAT member institutions.

Reference

[1] Huber, G.W.; Dumesic, J.A. An overview of aqueous-phase catalytic processes for production of hydrogen and alkanes in a biorefinery. Catal. Today 2006, 111, 119–132.https://doi.org/10.1016/j.cattod.2005.10.010

[2] Bridgwater, A.V. Catalysis in thermal biomass conversion. Appl. Catal. A 1994, 116, 5-47.https://doi.org/10.1016/0926-860X(94)80278-5

[3] Mortensen, P. M.; Grunwaldt, J. D.; Jensen, P. A.; Jensen, A. D. Screening of Catalysts for Hydrodeoxygenation of Phenol as Model Compound for Bio-oil. ACS Catal. 2013, 3, 1774–1785.https://doi.org/10.1021/cs400266e

[4] Bridgwater, A. V. Review of fast pyrolysis of biomass and product upgrading. Biomass and Bioenergy 2012, 38, 68–94.https://doi.org/10.1016/j.biombioe.2011.01.048

[5] Furimsky, E. Catalytic hydrodeoxygenation. Appl. Catal. A Gen 2000, 199, 147–190.https://doi.org/10.1016/S0926-860X(99)00555-4

[6] Choudhary, T. V.; Phillips, C.B. Renewable fuels via catalytic hydrodeoxygenation. Appl. Catal. A 2011, 397, 1–12.https://doi.org/10.1016/j.apcata.2011.02.025

[7] Graça, I.; Lopes, J.M.; Cerqueira, H.S.; Ribeiro, M.F. Bio-oils upgrading for second generation biofuels. Ind. Eng. Chem. Res. 2013, 52, 275–287.https://doi.org/10.1021/ie301714x

[8] Sun, J.; Karim, A.M.; Zhang, H.; Kovarik, L.; Li, X.S.; Hensley, A.J.; McEwen, J.S.; Wang, Y. Carbon-supported bimetallic Pd-Fe catalysts for vapor-phase hydrodeoxygenation of guaiacol. J. Catal. 2013, 306, 47–57.https://doi.org/10.1016/j.jcat.2013.05.020

[9] Hong, Y.; Zhang, H.; Sun, J.; Ayman, K. M.; Hensley, A. J. R.; Gu, M.; Engelhard, M. H.; McEwen, J. S.; Wang, Y. Synergistic catalysis between Pd and Fe in gas phase hydrodeoxygenation of m-cresol. ACS Catal. 2014, 4, 3335–3345.https://doi.org/10.1021/cs500578g

[10] Nie, L.; De Souza, P.M.; Noronha, F.B.; An W.; Sooknoi, T.; Resasco, D.E. Selective conversion of m-cresol to toluene over bimetallic Ni-Fe catalysts. J. Mol. Catal. A Chem. 2014, 388, 47–55.https://doi.org/10.1016/j.molcata.2013.09.029

[11] de Souza, P.M.; Rabelo-Neto, R.C.; Borges, L. E. P.; Jacobs, G.; Davis, B. H.; Sooknoi, T.; Resasco,

D. E.; Noronha, F. B. Role of keto intermediates in the hydrodeoxygenation of phenol over Pd on oxophilic supports, ACS Catal. 2015, 5, 1318–1329. https://doi.org/10.1021/cs501853t

[12] de Souza, P. M.; Rabelo-Neto, R. C.; Borges, L. E. P.; Jacobs, G.; Davis, B. H.; Resasco, D. E.; Noronha, F. B., Hydrodeoxygenation of phenol over Pd catalysts. Effect of support on reaction mechanism and catalyst deactivation, ACS Catal. 2017, doi:10.1021/acscatal.6b02022. https://doi.org/10.1021/acscatal.6b02022

[13] de Souza, P. M.; Rabelo-Neto, R. C.; Borges, L. E. P.; Jacobs, G.; Davis, B. H.; Graham, U. M.; Resasco, D. E.; Noronha, F. B. Effect of Zirconia Morphology on Hydrodeoxygenation of Phenol over Pd/ZrO2. ACS Catal. 2015, 5, 7385−7398. https://doi.org/10.1021/acscatal.5b01501

[14] Vicente, A.; Lafaye, G.; Especel, C.; Marécot, P.; Williams, C. T. The relationship between the structural properties of bimetallic Pd-Sn/SiO2 catalysts and their performance for selective citral hydrogenation. J. Catal. 2011, 283, 133–142. https://doi.org/10.1016/j.jcat.2011.07.010

[15] Ressler, T. WinXAS: A program for X-ray absorption spectroscopy data analysis under MS-Windows. J. Synchrotron Rad. 1998, 5, 118–22. https://doi.org/10.1107/S0909049597019298

[16] Jacobs, G.; Ji, Y.; Davis, B.H.; Cronauer, D.; Kropf, A.J.; Marshall, C.L. Fischer-Tropsch synthesis: Temperature programmed EXAFS/XANES investigation of the influence of support type, cobalt loading, and noble metal promoter addition to the reduction behavior of cobalt oxide particles. Appl. Catal. A 2007, 333, 177–191.https://doi.org/10.1016/j.apcata.2007.07.027

[17] Ravel, B. Atoms: crystallography for the X-ray absorption spectroscopist. J. Synchrotron Rad. 2001, 8, 314-316. https://doi.org/10.1107/S090904950001493X

[18] Rehr, J. J.; de Leon, J. M.; Zabinsky, S. I.; Albers, R. C. Theoretical x-ray absorption fine structure standards. J. Am. Chem. Soc. 1991, 113, 5135−5140. https://doi.org/10.1021/ja00014a001

[19] Ravel, B.; Newville, M. ATHENA, ARTEMIS, HEPHAESTUS: Data analysis for X-ray absorption spectroscopy using IFEFFIT. J. Synchrotron Rad. 2005, 12, 537–541.https://doi.org/10.1107/S0909049505012719

[20] Khaodee, W.; Jongsomjit, B.; Assabumrungrat, S.; Praserthdam, P.; Goto, S. Investigation of isosynthesis via CO hydrogenation over ZrO2 and CeO2 catalysts: Effects of crystallite size, phase composition and acid-base sites, Catal. Commun. 2007, 8, 548–556.https://doi.org/10.1016/j.catcom.2006.08.001

[21] Coq, B.; Figueras, F. Bimetallic palladium catalysts : Influence of the co-metal on the catalyst performance. J. Mol. Catal. A 2001, 173, 117–134.https://doi.org/10.1016/S1381-1169(01)00148-0

[22] Karski, S.; Wito, I.; Rogowski, J.; Gołuchowska, J. Interaction between Pd and Ag on the surface of silica. J. Mol. Catal. A 2005, 240, 155–163.https://doi.org/10.1016/j.molcata.2005.06.053

[23] Fox, E. B.; Velu, S.; Engelhard, M. H.; Chin, Y.; Miller, J.T.; Kropf, J.; Song, C. Characterization of CeO2-supported Cu–Pd bimetallic catalyst for the oxygen-assisted water – gas shift reaction. J. Catal. 2008, 260, 358–370.https://doi.org/10.1016/j.jcat.2008.08.018

[24] Jacobs, G.; Ma, W.; Gao, P. Fischer – Tropsch Synthesis : Differences Observed in Local Atomic Structure and Selectivity with Pd Compared to Typical Promoters (Pt, Re, Ru) of Co/Al2O3 Catalysts. Top. Catal. 2012, 55, 811–817.https://doi.org/10.1007/s11244-012-9856-5

[25] Lesiak, M.; Binczarski, M.; Karski, S.; Maniukiewicz, W.; Rogowski, J.; Szubiakiewicz, E.; Berlowska, J.; Dziugan, P.; Witońska, I. Hydrogenation of furfural over Pd-Cu/Al2O3 catalysts. The role of interaction between palladium and copper on determining catalytic properties. J. Mol. Catal. A 2014, 395, 337–348.https://doi.org/10.1016/j.molcata.2014.08.041

[26] Okhlopkova, L. B.; Kerzhentsev, M. A. Palladium – zinc catalysts on mesoporous titania prepared by colloid synthesis . II . Synthesis and characterization of PdZn/TiO2 coating on inner surface of fused silica capillary. J. Nanopart. Res. 2012, 14, 1088-1103.https://doi.org/10.1007/s11051-012-1088-x

[27] Fort, D.; Farr, J. P. G.; Harris, I. R. A comparison of palladium-silver and palladium-yttrium alloys as hydrogen separation membranes. J. Less-Common Met. 1975, 39, 293-308.https://doi.org/10.1016/0022-5088(75)90204-0

[28] Harris, I.R.; Cordey-Hayes, M. A Study of some Palladium-Tin, Silver-Tin and Palladium-Silver-Tin Alloys, J. Less Common Met. 1968, 6, 223–232.https://doi.org/10.1016/0022-5088(68)90018-0

[29] Jentys, A. Estimation of mean size and shape of small metal particles by EXAFS. Phys. Chem. Chem. Phys. 1999, 1, 4059-4063.https://doi.org/10.1039/a904654b

[30] Lahiri, D.; Bunker, B.; Mishra, B.; Zhang, Z.; Meisel, D.; Doudna, C. M.; Bertino, M.F.; Blum, F.D.; Tokuhiro, A.T.; Chattopadhyay, S.; Shibata, T.; Terry, J. Bimetallic Pt – Ag and Pd – Ag nanoparticles. J. Appl. Phys. 2005, 97, 094304.https://doi.org/10.1063/1.1888043

[31] Huang, W.; Pyrz, W.; Lobo, R. F.; Chen, J. G. Selective hydrogenation of acetylene in the presence of ethylene on K+ -β-zeolite supported Pd and PdAg catalysts. Appl. Catal. A 2007, 333, 254–263.https://doi.org/10.1016/j.apcata.2007.09.017

[32]Faticanti, M.; Cioffi, N.; De Rossi, S.; Ditaranto, N.; Porta, P.; Sabbatini, L.; Bleve-Zacheo, T. Pd supported on tetragonal zirconia: Electrosynthesis, characterization and catalytic activity toward CO oxidation and CH4 combustion, Appl. Catal. B 2005, 60, 73–82.https://doi.org/10.1016/j.apcatb.2005.02.022

[33] Kapoor, M.P.; Ichihashi, Y.; Shen, W.; Matsumura, Y. Catalytic activity of palladium supported on mesoporous zirconium oxide in low-temperature methanol decomposition. Catal. Lett. 2001, 76, 139–142.https://doi.org/10.1023/A:1012249529720

[34]Matsumura, Y.; Okumura, M.; Usami, Y.; Kagawa, K.; Yamashita, H.; Anpo, M.; Haruta, M. Low-temperature decomposition of methanol to carbon monoxide and hydrogen with low activation energy over Pd/ZrO2 catalyst. Catal. Lett. 1997, 44, 189-191.https://doi.org/10.1023/A:1018918301790

[35] Cioffi, N.; Faticanti, M.; Ditaranto, N.; De Rossi, S.; Traversa, L.; Monopoli, A.; Nacci, A.; Torsi, L.; Sabbatini, L. Analytical Characterization of Pd/ZrO2 Composite Nanoparticles Employed in Heterogeneous Catalysis. Current Nanoscience 2007, 3, 121-127.https://doi.org/10.2174/157341307780619288

[36] Barrabés, N.; Just, J.; Dafinov, A.; Medina, F.; Fierro, J. L. G.; Sueiras, J. E.; Salagre, P.; Cesteros, Y. Catalytic reduction of nitrate on Pt-Cu and Pd-Cu on active carbon using continuous reactor: The effect of copper nanoparticles. Appl. Catal. B 2006, 62, 77–85.https://doi.org/10.1016/j.apcatb.2005.06.015

[37] Pachulski, A.; Schödel, R.; Claus, P. Performance and regeneration studies of Pd–Ag/Al2O3 catalysts for the selective hydrogenation of acetylene. Appl. Catal. A 2011, 400, 14–24.https://doi.org/10.1016/j.apcata.2011.03.019

[38] Lamb, R.N.; Ngamsom, B.; Trimm, D. L.; Gong, B.; Silveston, P. L.; Praserthdam, P. Surface characterisation of Pd–Ag/Al2O3 catalysts for acetylene hydrogenation using an improved XPS procedure. Appl. Catal. A 2004, 268, 43–50.https://doi.org/10.1016/j.apcata.2004.03.041

[39] Neri, G.; Milone, C.; Galvagno, S.; Pijpers A. P. J.; Schwank J. Characterization of Pt-Sn / carbon hydrogenation catalysts, Appl. Catal. A 2002, 227, 105–115.https://doi.org/10.1016/S0926-860X(01)00927-9

[40] Aguirre, M.C.; Reyes, P.; Oportus, M.; Melián-cabrera, I.; Fierro J. L. G. Liquid phase hydrogenation of crotonaldehyde over bimetallic Rh-Sn/SiO2 catalysts Effect of the Sn/Rh ratio. Appl. Catal. A 2002, 233, 183–196.https://doi.org/10.1016/S0926-860X(02)00141-2

[41] Nishiyama, S.; Hara, T.; Tsuruya, S.; Masai, M. Infrared Spectroscopy Study of Aldehydes Adsorbed on Rh-Sn Bimetallic Systems: Selective Activation of Aldehydes by Tin. J. Phys. Chem. B 1999, 103, 4431-4439.https://doi.org/10.1021/jp984553w

[42] Kuijers, F. J.; Ponec, V. The Surface composition of Pd-Ag Alloy. J. Catal. 1979, 60, 100-109. https://doi.org/10.1016/0021-9517(79)90072-1

[43] Karakaya, I.; Thompson, W.T. The Ag-Pd (Silver-Palladium) System. Bulletin of Alloy Phase Diagrams 1988, 9, 237–243.https://doi.org/10.1007/BF02881271

[44] Subramanlan, P.R.; Laughlin, D.E. Cu-Pd (Copper-Palladium). J. Phase Equilibria 1991, 12, 2

[45] Batista, J.; Pintar, A.; Mandrino, D.; Jenko, M.; Martin, V. XPS and TPR examinations of γ-alumina-supported Pd-Cu catalysts. Appl. Catal. A 2001, 206, 113–124.https://doi.org/10.1016/S0926-860X(00)00589-5

[46] Fernández-García, M.; Anderson, J. A.; Haller, G. L. Alloy Formation and Stability in Pd - Cu Bimetallic Catalysts. J. Phys. Chem. 1996, 100, 16247–16254.https://doi.org/10.1021/jp9608133

[47] Venezia, A. M.; Liotta, L. F.; Deganello, G.; Schay, Z.; Guczi, L. Characterization of Pumice-Supported Ag – Pd and Cu – Pd Bimetallic Catalysts by X-Ray Photoelectron Spectroscopy and X-Ray Diffraction, J. Catal. 1999, 182, 449–455.https://doi.org/10.1006/jcat.1998.2343

[48] Cárdenas, G.; Oliva, R.; Reyes, P.; Rivas, B.L. Synthesis and properties of PdSn/Al2O3 and PdSn/SiO2 prepared by solvated metal atom dispersed method. J. Mol. Catal. 2003, 191, 75–86. https://doi.org/10.1016/S1381-1169(02)00333-3

[49] Conant, T.; Karim, A.M.; Lebarbier, V.; Wang, Y.; Girgsdies, F.; Schlögl, R.; Datye, A. Stability of bimetallic Pd-Zn catalysts for the steam reforming of methanol. J. Catal. 2008, 257, 64–70.https://doi.org/10.1016/j.jcat.2008.04.018

[50] Iwasa, N.; Mayanagi, T.; Masuda, S.; Takezawa, N. Steam reforming of methanol over Pd-Zn catalysts. React. Kinet. Catal. Lett. 2000, 69, 355-360.https://doi.org/10.1023/A:1005668404401

[51] Suwa, Y.; Ito, S.; Kameoka, S.; Tomishige, K.; Kunimori, K. Comparative study between Zn – Pd/C and Pd/ZnO catalysts for steam reforming of methanol. Appl. Catal. A 2004, 267, 9–16. https://doi.org/10.1016/j.apcata.2004.02.016

[52]Echeandia, S.; Pawelec, B.; Barrio, V.L.; Arias, P.L.; Cambra, J.F.; Loricera, C.V.; Fierro, J.L.G. Enhancement of phenol hydrodeoxygenation over Pd catalysts supported on mixed HY zeolite and Al2O3. An approach to O-removal from bio-oils, Fuel 2014, 117, 1061–1073.https://doi.org/10.1016/j.fuel.2013.10.011

[53] Zhao, C.; He, J.; Lemonidou, A. A.; Li X.; Lercher, J. A. Aqueous-phase hydrodeoxygenation of bio-derived phenols to cycloalkanes, J. Catal. 2011, 280, 8-16.https://doi.org/10.1016/j.jcat.2011.02.001

[54] Horácek, J.; St'ávová, G.; Kelbichová, V.; Kubicka, D. Zeolite-Beta-supported platinum catalysts for hydrogenation/hydrodeoxygenation of pyrolysis oil model compounds, Catal. Today 2013, 204, 38–45.https://doi.org/10.1016/j.cattod.2012.08.015

[55]Newman, C.; Zhou, X.; Goundie, B.; Ghampson, I. T.; Pollock, R. A.; Ross, Z.; Wheeler, M.C.; Meulenberg, R.; Austin, R.N.; Frederick, B.G. Effects of support identity and metal dispersion in supported ruthenium hydrodeoxygenation catalysts. Appl. Catal. A 2014, 477, 64-74. https://doi.org/10.1016/j.apcata.2014.02.030

[56] Do, P. T. M.; Foster, A. J.; Chen, J.; Lobo, R. F. Bimetallic effects in the hydrodeoxygenation of meta-cresol on γ-Al2O3 supported Pt–Ni and Pt–Co catalysts. Green Chem. 2012, 14, 1388-1397.https://doi.org/10.1039/c2gc16544a

[57] Wan, H.; Chaudhari, R.V.; Subramaniam, B. Catalytic Hydroprocessing of p-Cresol: Metal, Solvent and MassTransfer Effects. Top. Catal. 2012, 55, 129–139.https://doi.org/10.1007/s11244-012-9782-6

[58] Zhu, X.; Nie, L.; Lobban, L. L.; Mallinson, R. G.; Resasco, D. E. Efficient Conversion of m Cresol to Aromatics on a Bifunctional Pt/ HBeta Catalyst. Energy Fuels 2014, 28, 4104-4111.https://doi.org/10.1021/ef500768r

[59] Shin, E.J.; Keane, M.A. Gas-Phase Hydrogenation/Hydrogenolysis of Phenol over Supported Nickel Catalysts. Ind. Eng. Chem. Res. 2000, 39, 883-892.https://doi.org/10.1021/ie990643r

[60] Zhao, C.; Camaioni, D. M.; Lercher, J. A.; Selective catalytic hydroalkylation and deoxygenation of substituted phenols to bicycloalkanes. J. Catal. 2012, 288, 92-103.https://doi.org/10.1016/j.jcat.2012.01.005

[61] Zhang, X.; Wang, T.; Ma, L.; Zhang, Q.; Huang, X.; Yu, Y. Production of cyclohexane from lignin degradation compounds over Ni/ZrO2–SiO2 catalysts. Appl. Energy 2013, 112, 533–538.https://doi.org/10.1016/j.apenergy.2013.04.077

[62] Guvenatam, B.; Kurşun, O.; Heeres, E. H. J.; Pidko, E. A.; Hensen, E. J. M. Hydrodeoxygenation of mono- and dimeric lignin model compounds on noble metal catalysts, Catal. Today 2013, 233, 83-91.https://doi.org/10.1016/j.cattod.2013.12.011

[63] Teles, C. A.; Rabelo-Neto, R. C.; de Lima, J. R.; Mattos, L. V.; Resasco, D. E.; Noronha, F. B. Bio-oil, The Effect of Metal Type on Hydrodeoxygenation of Phenol Over Silica Supported catalysts. Catal. Lett. 2016, 146, 1848–1857.https://doi.org/10.1007/s10562-016-1815-5

[64]Tan, Q.; Wang, G.; Nie, L., Dinse, A.;Buda, C.; Shabaker, J.; Resasco, D. E.Different Product Distributions and Mechanistic Aspects of the Hydrodeoxygenation of m-Cresol over Platinum and Ruthenium Catalysts, ACS Catal. 2015, 5, 6271–6283.https://doi.org/10.1021/acscatal.5b00765

[65] De Souza, P.M.; Nie, L.; Borges, L. E. P.; Noronha F.B.; Resasco, D.E. Role of oxophilic supports in the selective hydrodeoxygenation of m-cresol on Pd catalysts. Catal. Lett. 2014, 144, 2005–2011.https://doi.org/10.1007/s10562-014-1337-y

[66] Iwasa, N.; Takizawa, M.; Arai, M.Palladium-based alloy and monometallic catalysts for gas phase hydrogenation of crotonaldehyde: effects of alloying and alloy crystallite size, Appl. Catal. A 2005, 283, 255–263.https://doi.org/10.1016/j.apcata.2005.01.015

[67] Sitthisa, S.; Pham, T.; Prasomsri, T.; Sooknoi, T.; Mallinson, R.G.; Resasco, D.E. Conversion of furfural and 2-methylpentanal on Pd/SiO2 and Pd–Cu/SiO2 catalysts. Catal. Lett. 2011, 280, 17–27.https://doi.org/10.1016/j.jcat.2011.02.006

[68] Lyubovsky, M., Pfefferle, L. Complete methane oxidation over Pd catalyst supported on a-alumina. Influence of temperature and oxygen pressure on the catalyst activity, Catalysis Today 1999, 47, 29-44.https://doi.org/10.1016/S0920-5861(98)00281-8

6.CHAPTER VI

6.1. Aqueous phase hydrogenation of phenol catalyzed by Pd and PdAg on ZrO_2

ABSTRACT- The impact of particle size of ZrO_2-supported Pd and of alloying with Ag was explored for hydrogenation of phenol in aqueous phase. Kinetic assessments were performed in a batch reactor, on monometallic Pd/ZrO_2 samples with different Pd loadings (0.5%, 1% and 2%), as well as on a 1% Pd 0.5%Ag/ZrO_2 sample. The catalytic activity normalized to accessible Pd (turnover frequency, TOF) increased with the particle size of Pd. Reaction orders in phenol and H_2 and lower activation energies suggest that smaller particles bind the reacting substrates more strongly, leading to higher surface coverages by phenol. However, surprisingly, smaller Pd particles exhibited lower TOFs. The lower activity of the small Pd particles is attributed to lower activation entropies for the strongly bound species. The presence of Ag increased the catalyst activity by decreasing the apparent energy of activation and increasing the coverages of phenol and H_2, without negatively affecting the activation entropy.

6.2. Introduction

One of the technologies used for bio-oil upgrading is catalytic hydrotreatment, which involves a multitude of reactions [1]. Upgrading bio-oil by hydrodeoxygenation (HDO) is a potential route for production of renewable fuels, since this process eliminates oxygen and stabilizes the product [2-4]. Bio-oil obtained from biomass pyrolysis is a complex mixture of reactive compounds; phenolic compounds represent the major part of the lignin fraction of the bio-oil [4], leading to their frequent use as model compounds [3,5-11]. Thus, exploring hydrogenation reactions of phenolic compounds in aqueous phase provides insight into the more complex real feeds, which are converted at relatively low temperatures in the presence of significant concentrations of water.

Without adding an appropriate source of sulfur, the traditional hydrotreating catalysts (e.g., sulfided CoMo/Al_2O_3) are not suitable for processing nearly sulfur-free feedstocks such as bio-oils. Thus, various noble and base metals and their combinations have been extensively investigated for HDO of phenolics [5-7,12-17]. In a study using carbon-supported noble metal catalysts for hydrotreating beech bio-oil in a batch reactor [2], Wildschut et al. concluded that Ru/C and Pd/C were good candidates for the process, with higher degrees of deoxygenation. Mortensen *et al.* [17] performed a catalyst screening study for HDO of neat phenol liquid in a batch reactor; they reported that the apparent activity for Ni-based catalysts, using the yield of cyclohexane as a measure, decreased in the sequence $Ni/ZrO_2 > Ni/Al_2O_3 > Ni/SiO_2 >> Ni/C$ (with similar Ni crystallite sizes). Importantly, this trend was mainly caused by the difference in catalytic rates of phenol hydrogenation in the whole HDO sequence. Similarly, de Souza et al. found that Pd/ZrO_2 catalyst was much more active than SiO_2- and Al_2O_3-supported Pd catalysts for phenol HDO in vapor phase [18]. Regarding the fact that ZrO_2 was often among the best supports, it was suggested that phenol adsorbs on coordinatively unsaturated metal sites at the oxide surface (i.e., Zr^{4+} or Zr^{3+} cations), which stabilizes the phenoxide ion that interacts with Ni or Pd atoms near the metal-support perimeter and facilitates the hydrogenation of the aromatic ring (producing cyclohexanone/-ol) or the carbonyl group in a phenol tautomer (producing 2,4-cyclohexadienol/benzene) [17,18]. When tested for hydrotreament of fast pyrolysis oil, Pd/ZrO_2 showed the highest activity, while Rh/ZrO_2 gave a product oil with the lowest tendency for coking [19]. A recent review summarizes advances in the understanding of the HDO chemistry of bio-oils and their model compounds, mainly on noble metal catalysts [3].

As the addition of a second metal is often found to induce variations in the local coordination environment, leading to synergistic effects on both catalytic and adsorptive properties [20], the bimetallic strategy has been widely exploited for HDO reactions. For example, addition of Cu improved the activity of Ni-based catalysts for HDO of guaiacol in dodecane [21]. Similarly, PdFe/C exhibited a substantially enhanced HDO activity compared to Fe/C in the vapor phase conversion of guaiacol, while maintaining the high selectivity to HDO products without ring saturation or ring opening [12]. In some cases, selectivity patterns can be drastically altered. As an example, in the HDO of *m*-cresol in gas phase, the monometallic Ni catalyst preferentially interacted with the aromatic ring promoting its hydrogenation, inhibiting the formation of toluene; in contrast, using Ni-Fe, the hydrogenation of a keto-tautomeric intermediate was greatly enhanced, resulting in a cyclohexadienol intermediate that was readily dehydrated to toluene [22]. In this respect, silver and other Group IB metals are common modifiers for Pd catalysts in selective hydrogenation of acetylene [23] and hexadienes [24]. Although widely used, the nature of the Pd-Ag bimetallic particles and the specific impact of Ag on Pd-catalyzed hydrogenation and hydrodeoxygenation are yet to be fully understood, especially in aqueous phase.

The impact of the metal particle size on catalytic activity, another important aspect for metal catalysis in general, has been controversially discussed for HDO reactions. For example, Echeandia *et al.* showed that the highest activity per surface Pd atom in gas-phase HDO of phenol was obtained on the HY zeolite-supported Pd catalyst with the highest Pd dispersion [25]. In contrast, an increase in the pseudo-first-order rate constant with increasing Ni particle size was observed in gas-phase hydrogenation/hydrogenolysis of phenol on Ni/SiO_2 in alcoholic solutions [26]. In some cases, the turnover frequency (TOF) for gas-phase phenol hydrogenation was found to hardly change when varying the metal particle size in supported Pd catalysts [27-29]. In a more recent study, Mortensen et al. investigated HDO of liquid phenol over SiO_2-supported Ni nanoparticles of different sizes (5–22 nm) in a batch reactor [30]. Phenol hydrogenation (to cyclohexanol) and cyclohexanol deoxygenation (to cyclohexane) were found to exhibit different dependencies on Ni particle size. Specifically, the TOF of hydrogenation increased by nearly two orders of magnitude, while the TOF of cyclohexanol deoxygenation decreased by a factor of 20, when the average Ni particle size increased from 5 to 22 nm.

However, there is scant information on the metal particle size effect on metal-catalyzed hydrogenation reactions of phenolics in aqueous phase. In the absence of acidic or oxophilic functions, or when the reaction conditions do not allow hydrogenolysis and acid-catalyzed reactions to occur, hydrogenation - without oxygen removal - is the predominant reaction of phenolics on metal catalysts. Hydrogenation is also the first step in a bi-functional (metal-acid) catalysis scheme for upgrading phenolics [6]. Understanding the impact of particle size and alloying on the catalytic rates of aqueous phase hydrogenation is, therefore, essential for the overall HDO chemistry of phenols. However, previous knowledge gained from extensive studies of phenolics hydrogenation in gas phase or neat liquid form may not be applicable in aqueous phase, as water could modify the electronic structure of the metal surface and might directly participate in surface reactions by providing proton transfer and exchange pathways [31-33].

In view of the knowledge gap identified above, this work aims to investigate the effects of Pd particle size and of the formation of Pd-Ag bimetallic particles on the activity and selectivity in aqueous phase hydrogenation of phenol, using ZrO_2 as the support. Physicochemical characterizations are combined with kinetic measurements to develop an atomistic and molecular description of the occurring catalyzed processes and the state of the catalysts.

6.3. Results and discussion

6.3.1. Pd/ZrO_2 with different Pd particle sizes

Table 6.1 compiles Pd content, BET surface area, pore volume, and Pd dispersion for Pd/ZrO_2 samples. All catalysts showed a similar BET surface area of approximately 70 m^2 g^{-1}. The Pd dispersions varied significantly with the Pd loading from 86% for 0.5%Pd/ZrO_2 to 8% for 2% Pd/ZrO_2.

Table 6-1. Physicochemical properties, Pd loadings and dispersions of the Pd/ZrO_2 samples.

	Pd Loading (%)[a]	**Ag Loading (%)[a]**	**BET surface area (m^2 g^{-1})**	**Pore volume (cm^3 g^{-1})**	**Pd dispersion**
0.5% Pd/ZrO_2	0.38	-	69	0.16	0.86
1% Pd/ZrO_2	1.02	-	75	0.30	0.35
2% Pd/ZrO_2	1.81	-	68	0.15	0.08
1% $PdAg/ZrO_2$	0.98	0.49	73	0.29	0.11

[a]Measured by XRF

XRD patterns of all Pd/ZrO_2 samples (pre-reduced, and maintained in a reduced state in a sealed capillary) are presented in Fig. 1SI (Appendix II). The diffractograms showed peaks characteristic of a mixture of monoclinic and tetragonal ZrO_2 phase [34]. The monoclinic phase dominated (86 ± 1 %, determined according to Khaodee *et al.* [35]). It was not possible to detect diffraction lines of metallic Pd.

The Pd K-edge EXAFS for the various catalysts reduced ex situ at 473 K strongly vary with Pd loading. The Fourier transforms of the $k^2\chi$ data are compiled in Fig. 6.1. 0.5% Pd/ZrO_2 shows a peak at 1.53 Å attributed to a Pd–O contribution and a peak around 2.75 Å attributed to a Pd-Pd contribution. The two samples with higher Pd loadings showed a more intense peak around 2.4 Å, indicating a higher degree of reduction (Fig. 6.1) in agreement with Ali et al. [36]. Using a linear combination of the Pd metal and PdO, the oxidized fractions were quantified (Table 6.2). The 0.5% Pd/ZrO_2 sample consists of 77.9% Pd metal after the reduction treatment, while the other samples have approximately 90% of Pd^0. It is hypothesized that the Pd oxide species are located at the metal-support-interface as the XPS results showed complete reduction at the surface.

Table 6-2. Linear combination fitting of the studied samples.

Samples	R-factor	PdO (%)	Pd^0(%)
0.5%Pd/ZrO_2	0.00841	22.1	77.9
1%Pd/ZrO_2	0.00057	9.9	90.1
2%Pd/ZrO_2	0.00050	10.6	89.4

Table 6.3 summarizes the parameters obtained from fitting the data of the various reduced catalysts with the theoretical FEFF model of an fcc metallic Pd cluster and the FEFF model of PdO. For 0.5% Pd and 1% Pd, the first Pd–Pd distance is larger than that for Pd foil. The coordination number of the first Pd–Pd shell for 1% Pd and 2% Pd samples was close to 12 (the same as Pd foil). For the 0.5% Pd sample, the coordination number of the first Pd-Pd was around 6.2. According to the relation between metal dispersion and first-shell coordination number established by Jentys [37], the first Pd-Pd coordination number of 6.2 observed for 0.5% Pd/ZrO_2 corresponds to a Pd dispersion higher than 0.8. This means that this sample has a small average Pd particle size (1-2 nm), which is consistent with the H_2 chemisorption data.

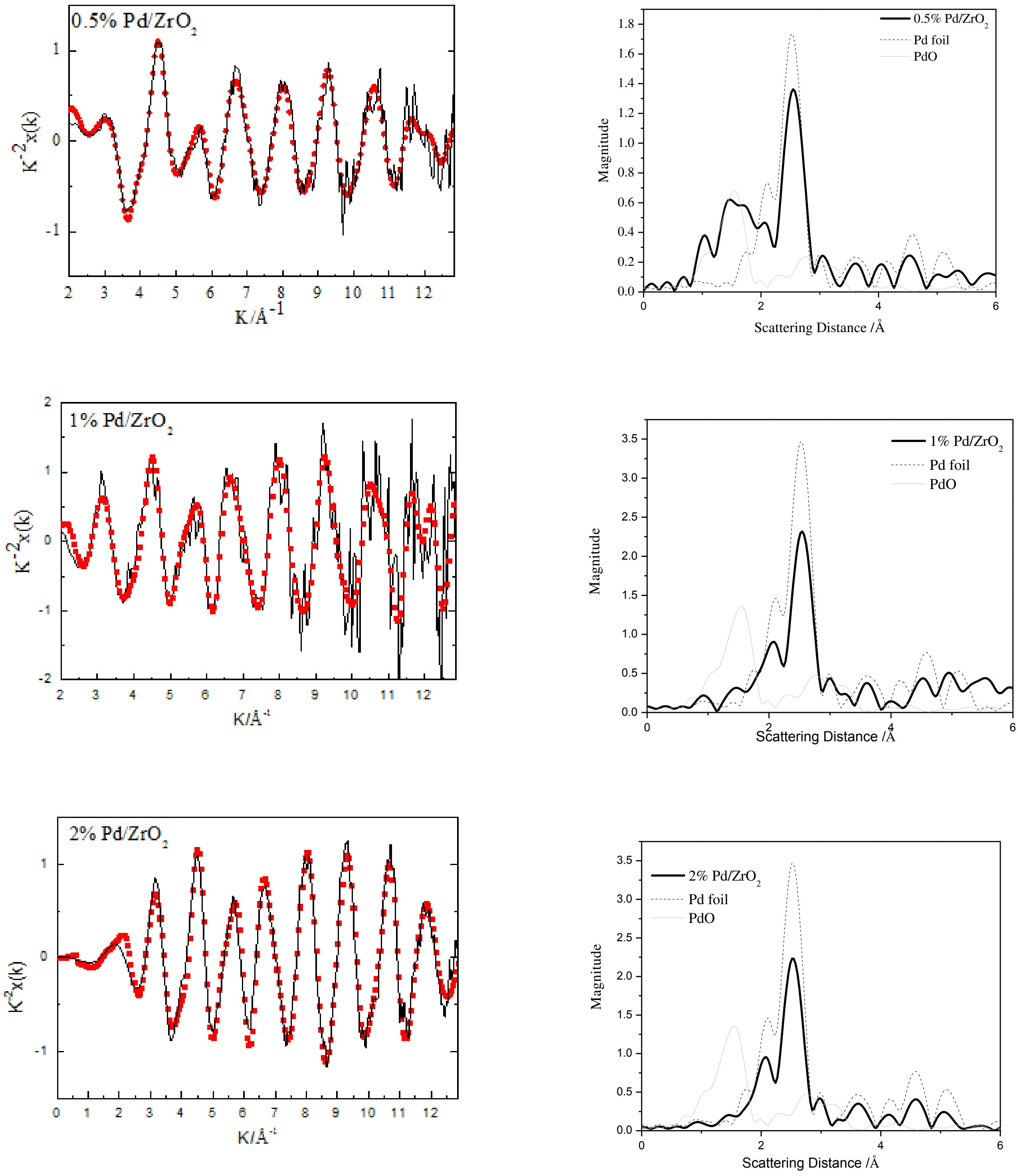

Figure 6-1. EXAFS refinement fits for ex situ reduced (at 473 K) Pd/ZrO$_2$ catalysts in R- and k-spaces. Note that the magnitudes of the Pd foil and PdO (shown as references) in the first R-space plot for 0.5% Pd/ZrO$_2$ were scaled down by a factor of 2 to be similar in magnitude to the 0.5%Pd/ZrO$_2$ sample.

Table 6-3. EXAFS parameters of Pd–Pd interactions for Pd/ZrO2 catalysts and Pd foil reduced at 473 K.

Sample Description	CN		R (Å)		e_0 (eV)	σs2 (x10^{-3} Å^2)		r-factor
	Pd-Pd	Pd-O	Pd-Pd	Pd-O		Pd-Pd	Pd-O	
Pd foil	12	-	2.740	-	0.929	5.68	-	0.00901
0.5% Pd	6.2 (0.6)	1.7 (0.3)	2.756 (0.006)	2.022 (0.004)	1.616	7.52 (0.8)	5.6 (3.8)	0.040133
1% Pd	10.7 (0.8)	-	2.748 (0.002)	-	0.642	7.75 (0.6)	-	0.0095599
2% Pd	10.3 (0.7)	-	2.742 (0.007)	-	0.616	7.28 (0.5)	-	0.0118531
1%PdAg	4.78 (0.5)	0.3 (0.8)	2.750 (0.003)	2.010 (0.001)	5.436	10.09 (0.01)	9.95 (0.07)	0.0120261

6.3.2. Aqueous phase hydrogenation of phenol on Pd/ZrO_2 catalysts

As a result of the weak acidity of ZrO_2 in water, deoxygenation was not observed on any of the ZrO_2-supported Pd catalysts studied. It also appears that the oxophilic sites of ZrO_2, represented by Zr^{4+} and Zr^{3+} cations near the perimeter of the metal particles, do not play a role in water, as these sites were shown to increase the selectivity to deoxygenated products in gas phase phenol HDO at 573 K and 1 bar H_2 [38]. Under our conditions, phenol was selectively hydrogenated to cyclohexanone (>90%) at conversions lower than 24%, with the only other product being cyclohexanol (Table 1SI, Supporting Information). The high selectivity to cyclohexanone on Pd agrees well with earlier reports [18,39]. A theoretical study [32] showed that the barrier for further hydrogenation of adsorbed cyclohexanone is significantly higher than that for desorption. Benzene, as observed in gas-phase HDO of phenol (via rapid dehydration of the unstable cyclohexadienol intermediate) on Pd/ZrO_2 [18], was not observed in the aqueous phase. This is attributed to the much lower reaction temperature

(≤ 473 K) and the positive impact of water on the stability of tautomeric and dienolic intermediates [31].

6.3.3. Kinetic Measurements

Rates normalized to the number of surface Pd atoms (estimated based on H_2 chemisorption data, TOF), increased with decreasing Pd dispersion (Table 6.4). On 1% and 2% Pd/ZrO_2 which contain relatively large particles, a dominant fraction of the surface consists of terraced (111) and (100) planes. On 0.5% Pd/ZrO_2 having a high Pd dispersion (D = 0.86), the fraction of corner/edge/step atoms becomes significant, and can account for a total of more than 80% of the surface atoms at D = 0.76 (based on a cuboctahedron model) [40]. These results indicate that the aqueous phase hydrogenation of phenol on Pd/ZrO_2 is a structure-sensitive reaction, likely requiring large ensembles of surface atoms, which are more prevalent on terraces of large particles. Similar observations were reported for phenol hydrogenation and deoxygenation over nickel nanoparticles of different sizes (5–22 nm) supported on SiO_2 [30]. In comparison, a TOF of 1.7 s^{-1} was obtained on a commercial 1%Pd/C catalyst containing Pd particles with 51% dispersion [6], at 473 K and 50 bar H_2 with a more concentrated phenol solution than used here (Table 6.4).

Table 6-4. Turnover frequencies (TOFs) for aqueous phase phenol hydrogenation on Pd/ZrO_2 with various Pd loadings. Reaction conditions: 50 bar of H_2, 463 K, stirring speed of 680 rpm and 0.30 M of phenol.

	Dispersion	**TOF (s^{-1})**
0.5% Pd/ZrO_2	0.86	1
1% Pd/ZrO_2	0.35	3
2% Pd/ZrO_2	0.08	6
1% PdAg/ZrO_2	0.11	9

Figure 6.2 shows the Arrhenius plots (using TOFs) for hydrogenation of phenol over Pd/ZrO_2. The apparent activation energies for 1% Pd/ZrO_2 and 2% Pd/ZrO_2 samples are similar, ~81 kJ mol^{-1}, while for 0.5% Pd (the least active), the measured activation energy is significantly lower (60 kJ mol^{-1}). We note that the less active catalyst has a lower activation barrier. We will return to discuss possible reasons for this observation after we have shown the kinetic orders in the reactants for the different Pd/ZrO_2 catalysts. In comparison, the activation energy reported at similar reaction conditions was ~70 kJ/mol on the commercial 1%Pd/C [6].

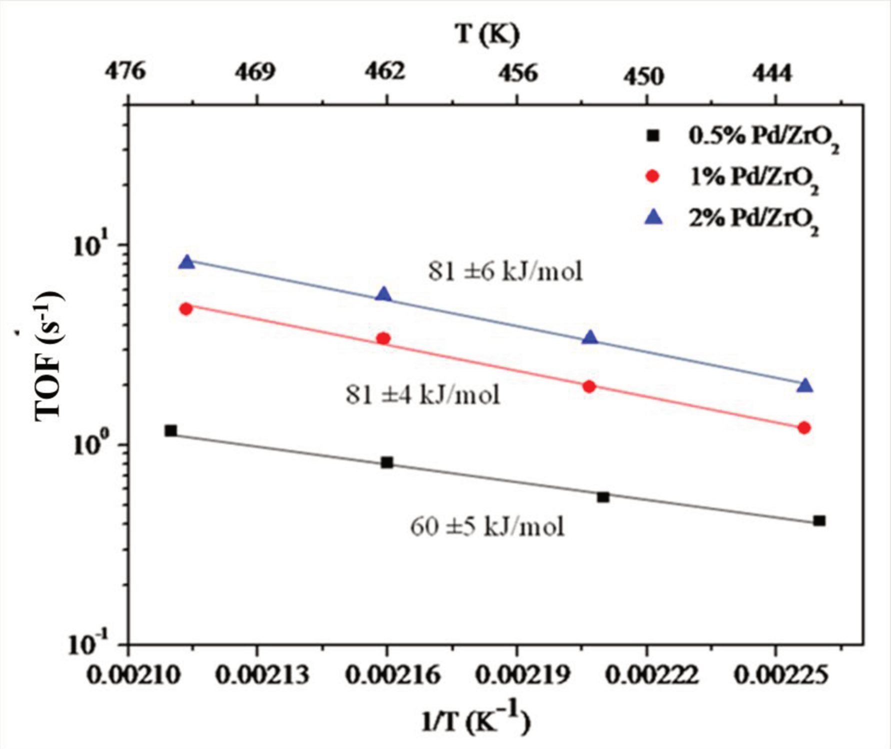

Figure 6-2. Arrhenius plots (443–473 K) for aqueous phase phenol hydrogenation on Pd/ZrO_2 catalysts with varying Pd dispersions. Reaction conditions: phenol (2.26 g), 80 mL of water, 0.5% Pd/ZrO_2 (0.3 g), 1% Pd/ZrO_2 (0.25 g) or 2% Pd/ZrO_2 (0.20 g), 50 bar H_2, stirred at 680 rpm.

The reaction orders in both phenol and H_2 were evaluated via the power-rate-law formalism (Eq. 6.1):

$$r_{a0}=kC_{phenol}^{\alpha}\,P_{H2}^{\beta} \qquad \textbf{6.1}$$

where r_{a0} is the initial rate of phenol hydrogenation, k is the apparent reaction rate constant, C_{phenol} is the phenol concentration and P_{H2} is the hydrogen pressure.

Log-Log plots for data measured on 0.5% and 1% Pd are shown in Fig. 2SI (Appendix II). The regressed reaction orders are listed in Table 6.5, α and β for phenol and H_2, respectively. As the catalyst with 1% and 2% of Pd showed comparable TOFs and identical activation energies, we assume that reaction orders for 2% Pd/ZrO_2 are similar to those measured on 1% Pd/ZrO_2.

Table 6-5. Reaction orders (Eq. 6.1) in phenol (α) and H_2 (β) for reaction at 463 K.[a]

	α	β
0.5% Pd/ZrO_2	0.49±0.03	0.28±0.03
1% Pd/ZrO_2	0.93±0.03	1.12±0.08

[a]From initial rates measured for concentration ranges of 0.1–0.8 M phenol and H_2 pressures ranges of 30-50 bar.

At 463 K, the reaction order with respect to phenol was ~1 for 1% Pd/ZrO_2 and ~0.5 for 0.5% Pd/ZrO_2. The first order in phenol observed for 1% Pd (> 6 nm average Pd particle size) indicates a low coverage of phenol and phenol-derived surface species, while the smaller phenol order observed for 0.5% Pd (1–2 nm average Pd particle size) indicates a higher surface coverage of phenol and/or phenol-derived intermediates, suggesting, in turn, stronger adsorption of phenol-derived intermediates on the much smaller Pd particles.

The reaction order with respect to H_2 partial pressure was ~1.1 for 1% Pd/ZrO_2, and ~0.28 for 0.5% Pd/ZrO_2 (Table 6.5). The higher reaction order with respect to H_2 could suggest a lower H*-coverage on 1% Pd/ZrO_2, whereas the low reaction order of 0.3 could point to a higher H* coverage on 0.5% Pd/ZrO_2. The higher coverages of intermediates derived from phenol and hydrogen on 0.5% Pd/ZrO_2, as discussed above, may be attributed to a greater portion of sites being located on steps and corners of the small Pd particles. Such sites with higher degrees of coordinative unsaturation bind H and phenol more strongly than atoms on terrace planes [41].

The rate-determining step (RDS) for phenol hydrogenation is the surface reaction between adsorbed phenol and intermediates derived from it (phenoxy or partially hydrogenated phenol/phenoxy [32]), and bound hydrogen. Despite the higher coverages of both reactive intermediates on 0.5% Pd/ZrO_2 than on 1% Pd/ZrO_2, the TOF was lower for 0.5% Pd/ZrO_2, indicating that the rate constant (k_{rds}) for the RDS must be significantly smaller on 0.5% Pd than on 1% Pd. Considering that the apparent activation energy ($E_{a,app}$) was remarkably higher for 1% and 2% Pd than on the less active 0.5% Pd (Fig. 6.2), a possible explanation could be that the transition state (TS) is much more stabilized relative to the adsorbed intermediate on highly under-coordinated corner/edge atoms prevalent on 0.5% Pd/$ZrO_{2.}$ However, stronger binding of the TS leads also to smaller entropy of activation, which more than offsets the effect of a lower enthalpy of activation, causing smaller rate constant and TOF on 0.5% Pd/ZrO_2. Overall, we deduce that the higher enthalpic stabilization of the TS relative to the adsorbed state on small Pd particles than on large particles is accompanied with more reduced degrees of freedom and, thus, less favorable entropy factors.

6.3.4. Effect of Ag addition

From the XRD patterns (Fig. 3SI), it is not possible to identify any Ag phases, probably due to its low content. Only the monoclinic and tetragonal ZrO_2 phases are observed. The high-resolution XPS Pd 3d and Ag 3d spectra (Fig. 6.3) provide information about the electronic state of the metal components on the surface. Unfortunately, the Pd 3d spectral region suffers from the interference of the more intense Zr 3p doublet [42]. For the untreated sample (as calcined), the binding energy of the Pd 3d5/2 was 338.0 eV, which was 1.2 eV higher than with PdO (336.8 eV) [33]. This small feature is tentatively attributed to PdO_2 [43] or to metal-support interaction [44]. After the treatment at 473 K in H_2 atmosphere, the peak at 338.0 eV disappeared. This is an indication that Pd particles were reduced under these conditions. Even when exposing to an oxidative atmosphere (synthetic air), Pd^0 on ZrO_2 surface was stable against re-oxidation, in agreement with Okumura et al. [44].

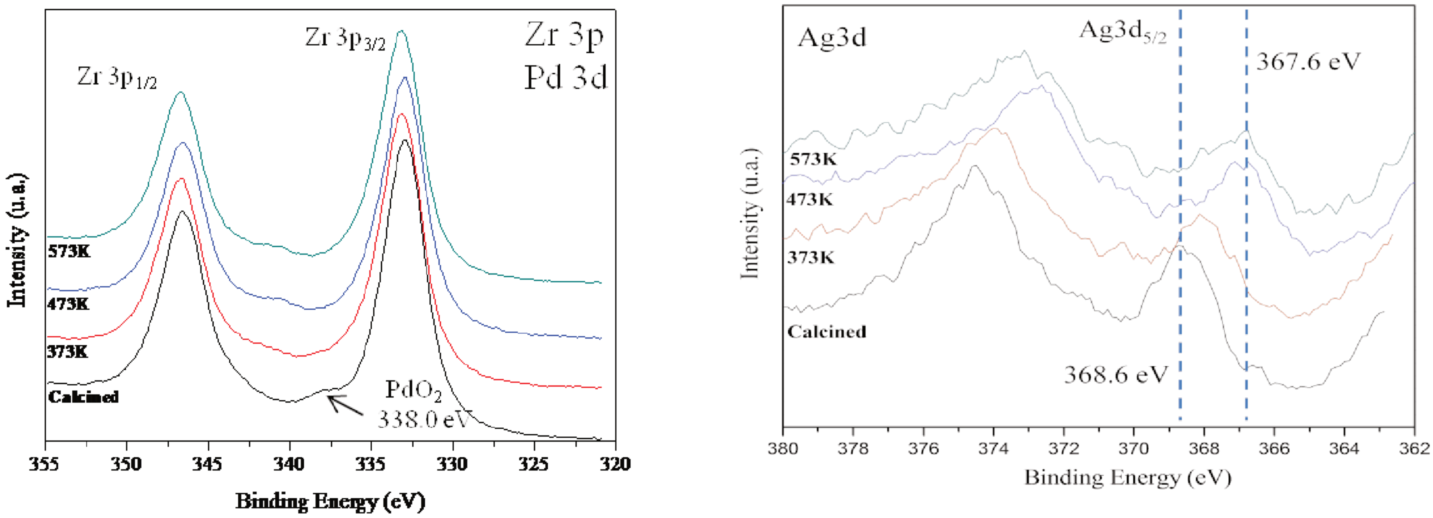

Figure 6-3. High energy resolution photoemission spectra of 1%PdAg/ZrO_2

The binding energy of Ag $3d_{5/2}$ for the calcined sample was 368.6 eV, which is shifted −0.6 eV from bulk Ag (368.0 eV). After the reduction at 573 K, the binding energy of Ag $3d_{5/2}$ became 367.6 eV, which differs from the binding energy of bulk metallic Ag of 368.2 eV [45], suggesting the formation of a PdAg alloy [46]. The core level shifts relative to pure Pd and Ag depend on changes in the charge around the probed atom. Generally, the core level binding energy of the central atom increases (indicating electron depletion), if neighboring elements have a higher electronegativity. Since the electronegativity of Pd is higher than that of Ag, Ag is expected (as observed) to shift to higher binding energies, Pd to lower. Therefore, we conclude that an intimate mixture between Pd and Ag must have been formed upon reduction.

EXAFS measurement was performed on ex situ reduced PdAg/ZrO_2 to verify the formation of bimetallic particles. The Fourier transforms of the $k^2\chi$ and r-space data (Pd K-edge) are presented in Fig. 6.4. The R-space data for this sample show a small peak related to Pd–O bond and a bigger one associated to reduced Pd-Pd. Table 6.3 also presents the parameters obtained from fitting the EXAFS data of the PdAg reduced catalysts. For PdAg, the first Pd–Pd distance was found to be shifted to a slightly longer interatomic distance when compared with pure Pd foil. This is taken as an indication of the presence of heteroatomic bonding in the Pd−Ag. Ideally, in the case of alloying, it is expected that the nearest neighbor distance should be an intermediate value between the two monometallic distances (Pd–Pd and Ag–Ag in bulk metals are 2.751 and 2.889 Å

[47]). In general, a more significant shift can be observed with an increase in the amount of Ag [48].

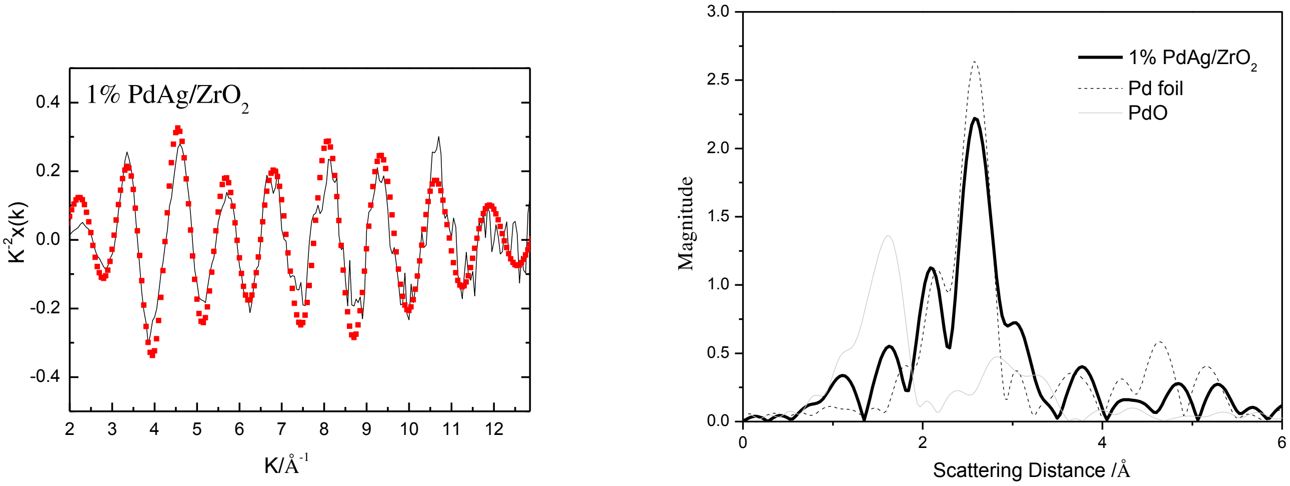

Figure 6-4. EXAFS refinement fits for ex situ reduced (at 473 K) 1%PdAg/ZrO$_2$ sample in R- and k-spaces.

Fig. 6.5 shows the representative TEM image of a passivated PdAg/ZrO$_2$, with the corresponding electron dispersive spectroscopy (EDS) and chemical mapping of the Pd, Ag and Zr elements. The chemical mapping of the bimetallic passivated sample shows that Ag and Pd have a similar distribution, although both isolated and aggregated particles were observed.

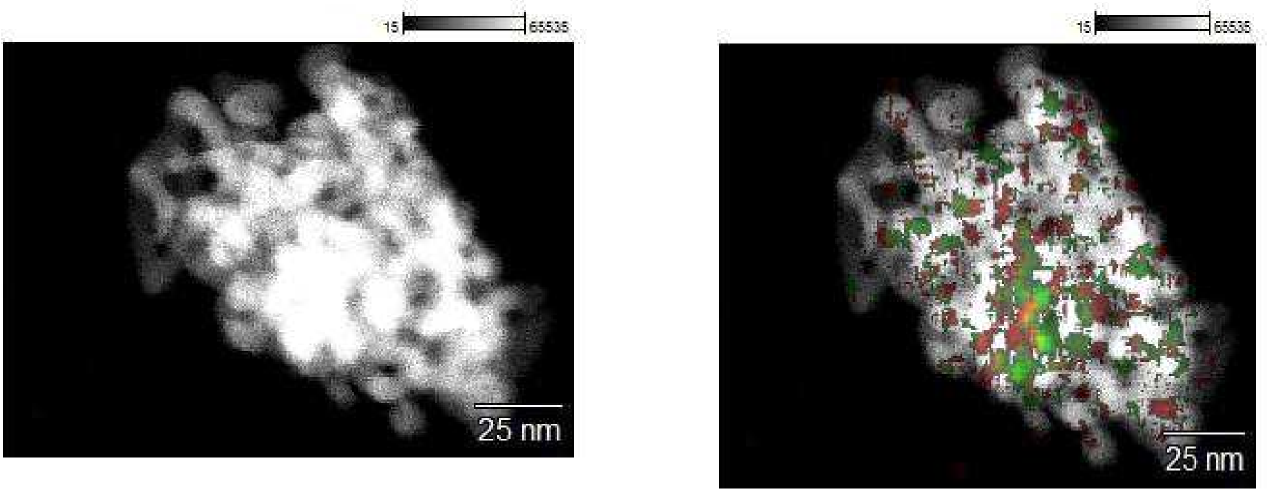

Figure 6-5. Representative TEM picture and elemental mapping using energy dispersive spectroscopy (EDS) of PdAg/ZrO_2. Green area: Pd; brown are: Ag; White area: Zr.

6.3.5. Phenol hydrogenation on PdAg/ZrO_2

The addition of Ag increased the TOF for aqueous phase hydrogenation of phenol by more than a factor of 2 at 463 K (Table 6.4), without changing the selectivity (i.e., cyclohexanone is still the dominant product with >95% selectivity), compared to the monometallic Pd catalyst (Table 2SI, Supporting Information). The apparent activation energy was 57 kJ mol^{-1} on PdAg/ZrO_2, whereas it was 81 kJ mol^{-1} on 1%Pd/ZrO_2 (Fig. 6.6). Thus, the difference in the activity between 1%Pd/ZrO_2 and PdAg/ZrO_2 was greater at lower temperatures. The decreased activation energy in PdAg catalyst is similar to that reported for the activation energy of ethene hydrogenation on Pd/SiO_2 and PdAg/SiO_2 [49].

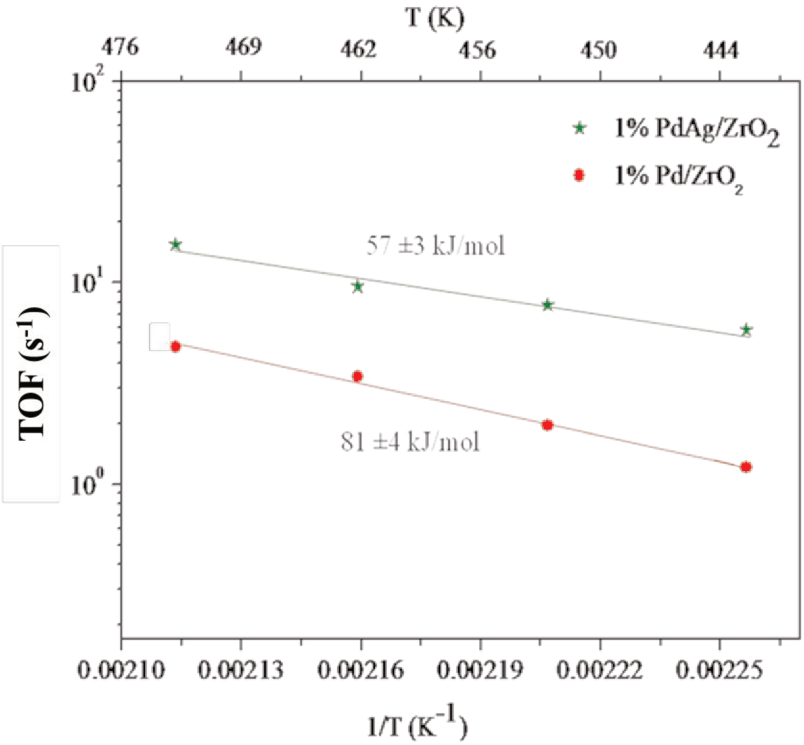

Figure 6-6. Activation energies measured between 443 and 473 K. Reaction conditions: phenol (2.26 g), 80 mL of water, 1% Pd/ZrO_2 (0.25 g) and 1% Pd-0.5%Ag/ZrO_2 (0.20 g), 50 bar H_2, stirred at 680 rpm.

The reaction orders in phenol and H_2 for phenol hydrogenation on $PdAg/ZrO_2$ are compiled in Table 6.6 (see Fig. 4SI for the plots). The low reaction order with respect to phenol (0.18) indicates a much higher surface coverage of phenol and/or phenol-derived intermediates on Pd in the presence of Ag neighbors compared to 1% Pd/ZrO_2. For $PdAg/ZrO_2$, the smaller reaction order observed with respect to H_2 (i.e., ~0.1 on $PdAg/ZrO_2$ compared to ~1.1 on 1% Pd/ZrO_2) points to the fact that the H* coverage at the active sites is also higher for PdAg than for Pd alone. The similar activation energies (~ 60 kJ mol^{-1}) and the small reaction orders in phenol and H_2 measured for 1% $PdAg/ZrO_2$ and 0.5% Pd/ZrO_2 suggest at first sight that diluting Pd with Ag has the same effect as decreasing the Pd particle size in monometallic Pd/ZrO_2 catalysts, i.e., strengthening the binding with the reactant, though the reason for the lower activation energy in the alloy case differs drastically from the impact of coordinatively unsaturated sites (CUS) in small Pd particles.

Table 6-6. Reaction orders in phenol (α) and H_2 (β) for reaction at 463 K.[a]

	α	β
1% Pd/ZrO_2	0.93±0.03	1.12±0.08
1% $PdAg/ZrO_2$	0.18±0.01	0.09±0.004

[a] From initial rates measured for concentration ranges of 0.1–0.8 M phenol and H_2 pressures ranges of 30-50 bar.

6.4. Conclusions

The aqueous phase hydrogenation of phenol is a structure-sensitive reaction on ZrO_2-supported Pd catalysts. Turnover frequencies increased by an order of magnitude with decreasing Pd dispersion (from 85% to 8%). The decreasing activation energies and higher coverages (reflected by reaction orders in phenol and H_2) with decreasing particle size on different Pd/ZrO_2 catalysts suggest that the lower rates on small Pd particles (1-2 nm) than on large particles result from unfavorable activation entropy. This is caused by too strong binding of species on corner and edge atoms. The addition of Ag to Pd/ZrO_2 (yielding a Pd-Ag alloy) significantly increased the TOF of the reaction, by lowering the energy of activation compared to the monometallic Pd counterpart via enhancing the electron density on Pd.

Acknowledgments

K.A.R. was supported by the National Council for Scientific and Technological Development (CNPq, Conselho Nacional de Desenvolvimento Científico e Tecnológico) of the Brazilian federal government under the Ministry of Science and Technology. H.S., O.Y.G., D.M.C. and J.A.L were supported by the U.S. Department of Energy, Office of Science, Office of Basic Energy Sciences, Division of Chemical Sciences, Geosciences, and Biosciences. The XPS and TEM analyses were performed by Drs. Mark Engelhard and Libor Kovarik, respectively, using resources at EMSL, a DOE Office of Science User Facility sponsored by the Office of Biological and Environmental Research and located at Pacific Northwest National Laboratory (PNNL), a multi-program national laboratory operated for DOE by Battelle Memorial Institute. This research also used resources of the Advanced Photon Source (APS), an Office of

Science User Facility operated for the U.S. Department of Energy (DOE) Office of Science by Argonne National Laboratory, and was supported by the U.S. DOE under Contract No. DE-AC02-06CH11357, and the Canadian Light Source and its funding partners. The authors would like to acknowledge Dr. Mahalingam Balasubramanian (APS) for his help with the measurements at Beamline Sector 20, Mr. Meng Wang (PNNL) for his help with some of the XAFS measurements, and Dr. John L. Fulton (PNNL) for his comments and suggestions on the XAFS data of the paper.

Reference

[1] E. Furimsky, Appl. Catal. A Gen. 199 (2000) 147–190.https://doi.org/10.1016/S0926-860X(99)00555-4

[2] J. Wildschut, F.H. Mahfud, R.H. Venderbosch, H.J. Heeres, Ind. Eng. Chem. Res. 48 (2009) 10324–10334.https://doi.org/10.1021/ie9006003

[3] H. Wang, J. Male, Y. Wang, ACS Catal. 3(2013) 1047−1070.https://doi.org/10.1021/cs400069z

[4] H.Y. Zhao, D. Li, P. Bui, S.T. Oyama, Appl. Catal. A Gen. 391 (2011) 305–310.https://doi.org/10.1016/j.apcata.2010.07.039

[5] A. Gutierrez, R.K. Kaila, M.L. Honkela, R. Slioor, A.O.I. Krause, Catal. Today 147 (2009) 239–246.https://doi.org/10.1016/j.cattod.2008.10.037

[6] C. Zhao, J. He, A.A. Lemonidou, X. Li, J.A. Lercher, J. Catal. 280 (2011) 8–16.https://doi.org/10.1016/j.jcat.2011.02.001

[7] X.L. Zhu, L.L. Lobban, R.G. Mallinson, D.E. Resasco, J. Catal. 281 (2011) 21–29.https://doi.org/10.1016/j.jcat.2011.03.030

[8] V. N. Bui, D. Laurenti, P. Afanasiev, C. Geantet, Appl. Catal. B Environ. 101 (2011) 239–245.https://doi.org/10.1016/j.apcatb.2010.10.025

[9] V. N. Bui, D. Laurenti, P. Delichere, C. Geantet, Appl. Catal. B Environ. 101 (2011) 246–255.https://doi.org/10.1016/j.apcatb.2010.10.031

[10] G.S. Foo, A.K. Rogers, M.M. Yung, C. Sievers, ACS Catal. 6 (2016) 1292–1307.https://doi.org/10.1021/acscatal.5b02684

[11] F.E. Massoth, P. Politzer, M.C. Concha, J.S. Murray, J. Jakowski, J. Simons, J. Phys. Chem. B 110 (2006) 14283–14291.https://doi.org/10.1021/jp057332g

[12] J. Sun, A. M. Karim, H. Zhang, L. Kovarik, X. S. Li, A. J. Hensley, J. McEwen, Y. Wang, J. Catal. 306 (2013) 47–57.https://doi.org/10.1016/j.jcat.2013.05.020

[13] J. Wildschut, I. Melián-Cabrera, H.J. Heeres, Appl. Catal. B Environ. 99 (2010) 298–306.https://doi.org/10.1016/j.apcatb.2010.06.036

[14] P.T.M. Do, A.J. Foster, J.G. Chen, R.F. Lobo, Green Chem. 14 (2012) 1388–1397.https://doi.org/10.1039/c2gc16544a

[15] Y. Hong, H. Zhang, J. Sun, A.M. Karim, A.J.R. Hensley, M. Gu, M.H. Engelhard, J.-S. McEwen, Y. Wang, ACS Catal. 4 (2014) 3335–3345.https://doi.org/10.1021/cs500578g

[16] C.R. Lee, J.S. Yoon, Y.-W. Suh, J.-W. Choi, J.-M. Ha, D.J. Suh, Y.-K. Park, Catal. Commun. 17 (2012) 54–58.https://doi.org/10.1016/j.catcom.2011.10.011

[17] P.M. Mortensen, J.D. Grunwaldt, P.A. Jensen, A.D. Jensen, ACS Catal. 3 (2013) 1774–1785.https://doi.org/10.1021/cs400266e

[18] P. M. de Souza, R. C. Rabelo-Neto, L. E. P. Borges, G. Jacobs, B. H. Davis, U. M. Graham, D. E. Resasco, F. B. Noronha, ACS Catal. 5 (2015) 7385−7398.https://doi.org/10.1021/acscatal.5b01501

[19] A.R. Ardiyanti, A. Gutierrez, M.L. Honkela, A.O.I. Krause, H.J. Heeres, Appl. Catal. A Gen. 407 (2011) 56−66.https://doi.org/10.1016/j.apcata.2011.08.024

[20] J.H. Sinfelt, Bimetallic Catalysts: Discoveries, Concepts, and Applications (Exxon Monographs Series), First edition, Wiley, New York, 1983.

[21] X. Zhang, T. Wang, L. Ma, Q. Zhang, Y. Yu, Q. Liu, Catal. Commun. 33 (2013) 15–

19.https://doi.org/10.1016/j.catcom.2012.12.011

[22] L. Nie, P.M. De Souza, F.B. Noronha, W. An, T. Sooknoi, D.E. Resasco, J. Mol. Catal. A Chem. 388-389 (2014) 47–55.https://doi.org/10.1016/j.molcata.2013.09.029

[23] Y. Jin, A.K. Datye, E. Rightor, R. Gulotty, W. Waterman, M. Smith, M. Holbrook, J. Maj, J. Blackson, J. Catal. 203 (2001) 292–306.https://doi.org/10.1006/jcat.2001.3347

[24] E.A. Sales, J. Jove, M.D.J. Mendes, F. Bozon-Verduraz, J. Catal. 195 (2000) 88–95.https://doi.org/10.1006/jcat.2000.2967

[25] S. Echeandia, B. Pawelec, V.L. Barrio, P.L. Arias, J.F. Cambra, C.V. Loricera, J.L.G. Fierro, Fuel 117 (2014) 1061–1073.https://doi.org/10.1016/j.fuel.2013.10.011

[26] E. Shin, M.A. Keane, Ind. Eng. Chem. Res. 39 (2000) 883–892.https://doi.org/10.1021/ie990643r

[27] N. Mahata, V. Vishwanathan, J. Catal. 196 (2000) 262–270.https://doi.org/10.1006/jcat.2000.3041

[28] N. Mahata, K. V. Raghavan, V. Vishwanathan, C. Park, M.A. Keane, Phys. Chem. Chem. Phys. 3 (2001) 2712–2719.https://doi.org/10.1039/b100237f

[29] S. Scirè, S. Minicò, C. Crisafulli, Appl. Catal. A Gen. 235 (2002) 21–31.https://doi.org/10.1016/S0926-860X(02)00237-5

[30] P.M. Mortensen, J.D. Grunwaldt, P.A. Jensen, A.D. Jensen, Catal. Today 259 (2016) 277–284.https://doi.org/10.1016/j.cattod.2015.08.022

[31] Y. Yoon, R. Rousseau, R.S. Weber, D. Mei, J.A. Lercher, J. Am. Chem. Soc. 136 (2014) 10287−10298.https://doi.org/10.1021/ja501592y

[32] G. Li, J. Han, H. Wang, X. Zhu, Q. Ge, ACS Catal. 5 (2015) 2009−2016.https://doi.org/10.1021/cs501805y

[33] Z.A. Chase, J.L. Fulton, D.M. Camaioni, D. Mei, M. Balasubramanian, V. Pham, C. Zhao, R.S. Weber, Y. Wang, J.A. Lercher, J. Phys. Chem. C 117 (2013) 17603–17612.https://doi.org/10.1021/jp404772p

[34] G. Teufer, Acta Crystallogr. 15 (1962) 1187–1187.https://doi.org/10.1107/S0365110X62003114

[35] W. Khaodee, B. Jongsomjit, S. Assabumrungrat, P. Praserthdam, S. Goto, Catal. Commun. 8 (2007) 548–556.https://doi.org/10.1016/j.catcom.2006.08.001

[36] A. Ali, W. Alvarez, C.J. Loughran, D.E. Resasco, Appl. Catal. B Environ. 14 (1997) 13–22.https://doi.org/10.1016/S0926-3373(97)00008-8

[37] A. Jentys, Phys. Chem. Chem. Phys. 1 (1999) 4059–4063.https://doi.org/10.1039/a904654b

[38] C.A. Teles, R.C. Rabelo-Neto, G. Jacobs, B.H. Davis, D.E. Resasco, F.B. Noronha, ChemCatChem, DOI: 10.1002/cctc.201700047.https://doi.org/10.1002/cctc.201700047

[39] H. Liu, T. Jiang, B. Han, S. Liang, Y. Zhou, Science 27 (2009) 1250–1252.https://doi.org/10.1126/science.1179713

[40] H. Shi, X. Li, G. L. Haller, O. Y. Gutiérrez, J. A. Lercher, J. Catal. 295 (2012) 133–145.https://doi.org/10.1016/j.jcat.2012.08.005

[41] J.P. Boitiaux, J. Cosyns, S. Vasudevan, Appl. Catal. 6 (1983) 41–51.https://doi.org/10.1016/0166-9834(83)80186-9

[42] M. Faticanti, N. Cioffi, S. De Rossi, N. Ditaranto, P. Porta, L. Sabbatini, T. Bleve-Zacheo, Appl. Catal. B Environ. 60 (2005) 73–82.https://doi.org/10.1016/j.apcatb.2005.02.022

[43] K. Otto, L. P Haack, J. E. deVries, Appl. Catal. B Environ. 1 (1992) 1-12.https://doi.org/10.1016/0926-3373(92)80003-I

[44] K. Okumura, T. Kobayashi, H. Tanaka, M. Niwa, Appl. Catal. B Environ. 44 (2003) 325–331.https://doi.org/10.1016/S0926-3373(03)00101-2

[45] A. Pachulski, R. Schödel, P. Claus, Appl. Catal. A Gen. 400 (2011) 14–24.https://doi.org/10.1016/j.apcata.2011.03.019

[46] R.N. Lamb, B. Ngamsom, D.L. Trimm, B. Gong, P.L. Silveston, P. Praserthdam, Appl. Catal. A Gen. 268 (2004) 43–50.https://doi.org/10.1016/j.apcata.2004.03.041

[47] W. Huang, R. F. Lobo, J. G. Chen, J. Mol. Catal. A Chem. 283 (2008) 158–165.https://doi.org/10.1016/j.molcata.2007.12.017

[48] K. Mori, M. Dojo, H. Yamashita. ACS Catal. 3 (2013) 1114−1119.https://doi.org/10.1021/cs400148n

[49] H. Zea, K. Lester, A.K. Datye, E. Rightor, R. Gulotty, W. Waterman, M. Smith, Appl. Catal. A Gen. 282 (2005) 237–245.https://doi.org/10.1016/j.apcata.2004.12.026

7. CHAPTER VII

7.1. Hydrodeoxygenation of phenol over metal supported niobia catalysts

ABSTRACT- This work studied the performance of Rh, Pd and Ni supported on Nb_2O_5 catalysts for the HDO of phenol in vapor phase at 300°C. The effect of the reduction temperature on the selectivity to deoxygenated products was also investigated. In general, an increase in the reduction temperature favored benzene selectivity and decreased the reaction rate. The reduction in the rates may be related to the strong metal-support interaction (SMSI) promoted by the high reduction temperatures. For Pd sample the increase in the benzene selectivity probably was due to a partial coverage of this metal by NbO_x, which increases the Pd-Nb_2O_5 surface. This leads to the adsorption of the phenol though its oxygen present in C-O bond, which promotes the hydrogenation of the carbonyl function of the tautomer intermediate. The presence of NbO_x in this sample was confirmed by TPR analysis. For the sample impregnated with Rh the reduction temperature did not changes the benzene selectivity, however there is an indication of the SMSI effect in this sample after high reduction temperature. According to the TPR-XANES the Rh is fully reduced for both reduction conditions studied. In addition, the XPS data showed that the molar concentration of Rh at the surface did not change during the reduction process. Ni sample was not fully reduced after the treatment at 300°C, as observed in TPR XANES at Ni K-edge. For this sample, after higher reduction temperatures there is no nickel oxide, which improved the oxophilicity of this sample and consequently the benzene selectivity.

Keywords: Biomass; Hydrodeoxygenation; Bio-oil; Phenol; Niobium oxide.

7.2. Introduction

The bio oil obtained from fast pyrolysis of biomass may be converted into different fuels, such as, diesel, gasoline and others , which makes it an attractive option to be used as a renewable fuel [1, 2]. Unfortunately, the bio oils are not very attractive for direct fuel applications due to their properties, such as, high viscosity, low heating value, thermal instability. In order to be used as a fuel in engine vehicles, the bio oil has to be upgrading though the hydrodeoxygenation (HDO) process [3-5]. Due to the complex composition of the bio oil several HDO studies use aromatics model compounds, such as, phenol [6, 7], guaiacol [8] and others, as representative of lignin fraction.However, the development of an appropriated catalyst for a HDO reaction is a challenge.

Teles et al. [9] investigated different metals in the HDO reaction, they used phenol as a model compound. The neutral supported-SiO_2 was chosen to better understand the metal effect in this reaction. According to the authors more oxophilic metals, such as, Ru, Co and Ni favor the direct dehydroxylation of phenol followed by hydrogenolis, while Pt, Pd and Rh promote mainly phenol tautomerization. In general, three routes can be considered for HDO reaction: (i) hydrogentation (HYD) (ii) direct deoxygenation route (DDO) and (iii) tautomerization [10-12]. Tan et al. [13] showed that on a strong oxophilic metal, such as Ru or Fe, the direct deoxygenation is the favorable path, while on weaker oxophilic metals, the direct deoxygenation become less favorable and the tautomerization-hydrogenation-dehydration mechanism is the favorable path. They conclude that the oxophilicity of the metal surface can regulate what reaction path is more favorable.

The support also has an important effect over the HDO routes. De Souza et al. [12] tested the performance of Pd catalysts supported on SiO_2, Al_2O_3, TiO_2, ZrO_2, CeO_2 and $CeZrO_2$ for HDO of phenol (reduction and reaction temperature = 300°C, P = 1 atm, and H_2/phenol molar ratio 60). According to the authors the product distribution is significantly affected by the type of support. Benzene was the major product over Pd/TiO_2 and Pd/ZrO_2, while cyclohexanone was a major product over Pd/SiO_2, Pd/Al_2O_3, Pd/CeO_2 and Pd/$CeZrO_2$. The differences in the selectivity were related to the presence of oxophilic sites, which is represented by incompletely coordinated cations present in ZrO_2 and TiO_2.

Recently, some studies reported that niobia support promotes the deoxygenation activity for the HDO reaction. Experimental and theoretical studies showed that NbOx species play a key role in C-O bond cleavage of biomass derived aldol adducts [14]. According to the DFT calculation performed by Xia et al. [14], the Nb-O-Nb chains in both NbOx and $NbOPO_4$ have a strong ability to break the C=O bond on the (tetrahydro) furan ring, as this process can efficiently relieve the surface tension of the oxide bonding network. Shao et al. [15] studied Pd-loaded on niobium oxide dispersed on silica for the hydrodeoxygenation of biomass-related compounds.

Pd/10%Nb_2O_5/SiO_2 was very active for the HDO reaction of 4-(2-furyl)-3-buten-2-one, palmitic acid and diphenyl ether. They also observed a significant promotion effect of NbOx species on C-O bond cleavage. Zhuang et al. [16] investigated the HDO of butyric acid at Nb_2O_5 (001) surface using DFT calculations. The interaction of the molecule and the surface Lewis acid may suppress the C-C bond cleavage and promote the C-O bond, which favors the deoxygenation pathway to produce butane. Barrios et al. [17] compared the performance of Pd supported on SiO_2 and Nb_2O_5 for the HDO of phenol. The reaction rate for HDO of phenol over Pd/Nb_2O_5 was higher than that observed for silica supported catalyst. Also, Pd/Nb_2O_5 favored the benzene selectivity.

Thus, the objective of this work is to investigate different metals (Ni, Pd and Rh) supported on Nb_2O_5 in the gas phase phenol HDO reaction, aiming to observed the effect of the these metals supported on Nb_2O_5 in the HDO reaction. As the niobium oxide is a reduced supported that is known have a strong interation with the supported metals, a systematic study was performed using phenol as a model compound of the bio oil to investigate the effect of the different metals and the reduction temperature on this reaction.

7.3. Results and Discussion

7.3.1. Catalyst Characterization

Table 7.1 shows the Pd, Rh and Ni metal loadings of the studied catalysts. The metal content was close to the nominal value for all samples. Table 7.1 also presents the textural properties of the calcined samples (BET surface area and pore volume). The support showed an area of 110 m^2 g^{-1}, similar to that obtained by Lebarbier et al. [18] for the niobic acid calcined at the 400°C.

The samples with 1 wt.% of metal (Pd and Rh) have approximately the same surface area of the support, while it decreased to for the catalyst impregnated with Ni. However, the pore volume was similar for all the samples, independently of the metal loading.

Table 7-1. Chemical composition, BET surface area and pore volume of the niobia supported catalysts.

Samples	Metal Loading (wt.%)	BET area (m^2 g^{-1})	Pore Volume* (cm^3 g^{-1})
Nb_2O_5	-	110	0.165
Pd/Nb_2O_5	1.01	98	0.159
Rh/Nb_2O_5	0.85	101	0.160
Ni/Nb_2O_5	5.14	85	0.136

*BJH Adsorption cumulative volume of pores between 15.000 Å and 3000.000 Å diameter.

The conversion of cyclohexanol to benzene was used as a probe reaction to titrate the oxophilic sites based on the mechanism of tautomerization of phenol. The reaction rate for cyclohexanol conversion at different reduction temperatures are listed in Table 7.2. After reduction at 300°C, the following order of reaction rate was observed: Pd/Nb_2O_5 > Rh/Nb_2O_5> Ni/Nb_2O_5. Increasing the reduction temperature increased the reaction rate for Ni/Nb_2O_5, while for Pd/Nb_2O_5 and Rh/Nb_2O_5 it still almost the same.

Table 7-2. Reaction rate for the conversion of cyclohexanol to benzene.

Sample	Tr (°C)	Reaction rate (mmol/(min.g_{CAT}))
Pd/Nb_2O_5	300	0.198
	500	0.192
Rh/Nb_2O_5	300	0.040
	500	0.038
Ni/Nb_2O_5	300	0.016
	500	0.030

7.3.2. In situ XRD

Fig. 7.1 shows the diffractograms obtained during reduction of niobia supported catalysts. For all samples, the diffractogram at room temperature exhibits broad diffraction lines associated with amorphous niobia phase [18]. The lines characteristic of palladium oxide, rhodium oxide or nickel oxide were not detected. For Pd/Nb_2O_5 and

Rh/Nb_2O_5, no changes on the diffractograms were observed when the samples were heated to 400°C. Further increase in the temperature to 500°C led to the appearance of the lines characteristic of the TT niobia phase (PDF 28-0317). The typical lines of Pd^0 and Rh^o were not detected during the reduction up to 500°C, indicating that small Pd^0 and Rh^o crystallite size were obtained on niobia. For Ni/Nb_2O_5, the line attributed to metallic Ni appeared at 300^oC and it increased in intensity as the temperature was increased to 500^oC.

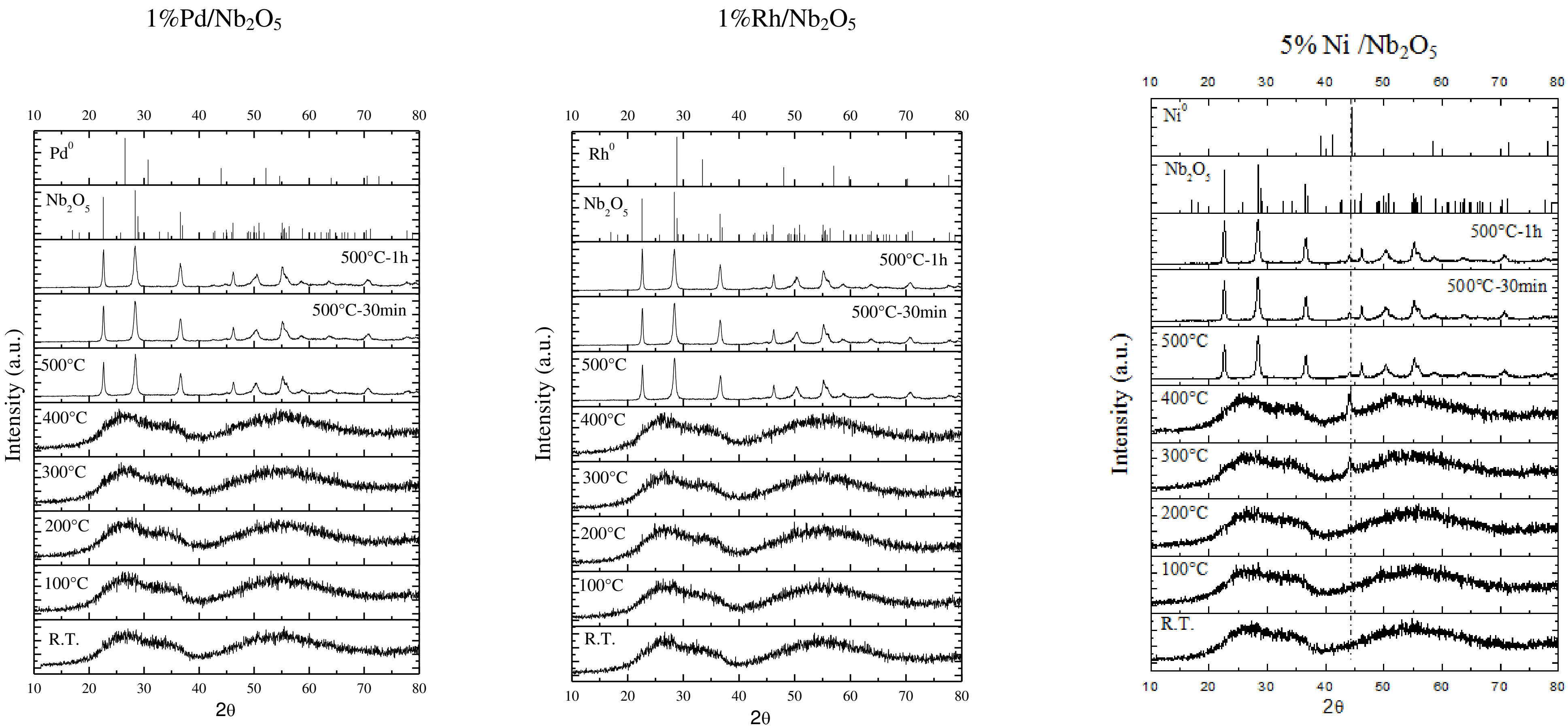

Figure 7-1. XRD diffractogram for in situ reduction of Pd/Nb_2O_5, Rh/Nb_2O_5 Ni/Nb_2O_5 at different temperatures.

The average crystallite size of Ni^0, calculated from XRD data using the Scherrer equation, increased from 12 to 24 nm when the reduction temperature increased from 300 to 500°C, which suggests that metal sintering occurred. The diffractograms did not provide any information about the reduction of palladium and rhodium oxides. Then, TPR and in situ XANES were carried out and the results are discussed in the next section.

7.3.3. TPR and in situ XANES experiments

TPR profiles of Pd/Nb_2O_5, Rh/Nb_2O_5, and Ni/Nb_2O_5 are shown in Fig. 7.2. For Pd/Nb_2O_5, a hydrogen consumption is observed at room temperature (R.T.) followed by a negative peak around 100°C. The H_2 uptake at R.T can be ascribed to the reduction PdO species, while the negative peak is related to the PdH_x decomposition [19].

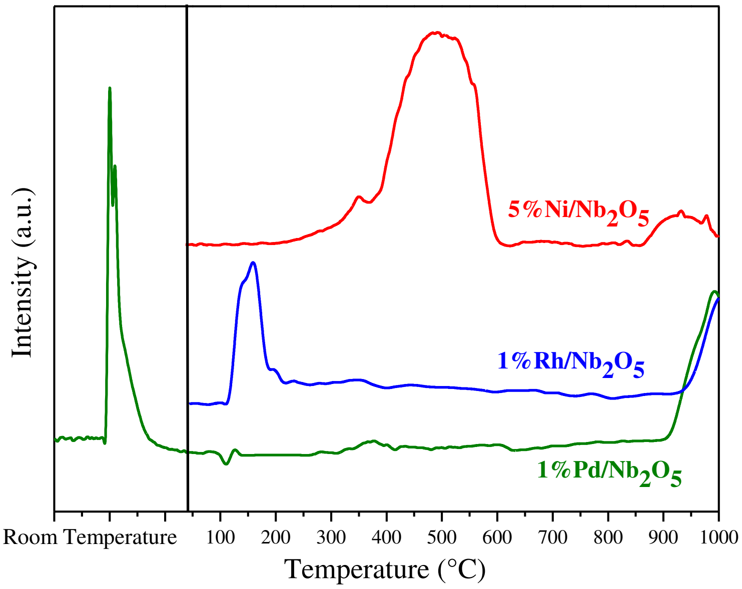

Figure 7-2. TPR profiles for niobia supported catalysts.

The formation of hydride species may occur during the reduction of PdO to Pd^o, followed by the absorption of hydrogen into the palladium structure. The reduction profile of Pd/Nb_2O_5 sample also exhibits a broad peak between 300 – 400 °C and a hydrogen consumption above 800°C. This hydrogen uptake at high temperature in the

TPR profile of metal supported on niobia catalysts has been attributed to the reduction of Nb_2O_5 [19-22]. The TPR profile of Rh/Nb_2O_5 exhibits a peak at 180°C and a hydrogen uptake above 800°C. As reported in the literature [23], the low temperature peak corresponds to the reduction of Rh_2O_3 to metallic Rh and the peak at high temperature is associated with the reduction of niobia, as observed for the Pd sample. For Ni/Nb_2O_5 sample, a broad reduction peak is observed between 300 and 600°C, which is attributed to the reduction of Ni^{2+} to Ni^0. The hydrogen uptake related to the Nb_2O_5 reduction is also displayed above 850°C.

The H_2 consumption calculated from the TPR profiles are reported in Table 7.3. The experimental hydrogen uptake was higher than that of the hydrogen consumption expected for the complete reduction of the metal oxide for Pd and Ni supported catalysts, suggesting a partial reduction of Nb_2O_5 to NbO_x promoted by the metal formed.

Table 7-3. H_2 consumption below 500°C on the TPR profile of niobia supported catalysts and reduction degree of Nb_2O_5.

Samples	**Theoretical Consumption[a] (μmol H_2/gcat)**	**Experimental Consumption (μmol H_2/gcat)**	**Experimental/ Theoretical**	**Degree of niobium oxide reduction (%)**
Pd/Nb_2O_5	108	149	1.38	0.2
Rh/Nb_2O_5	360	354	0.98	~0.0
Ni/Nb_2O_5	1084	1809	1.67	4.0

[a] Theoretical H_2 consumption considering total reduction of PdO, NiO, Rh_2O_3 (μmol H_2/gcat)

The TPR-XANES spectra at the Pd K-edge, Rh K-edge and Ni K-edge obtained during the reduction under a 5% H_2 in He mixture from 25 to 300°C of niobia supported catalysts are shown in Fig. S1 (Appendix III). Snapshots of XANES spectra at specific reduction temperatures are provided in Fig. 7.3.

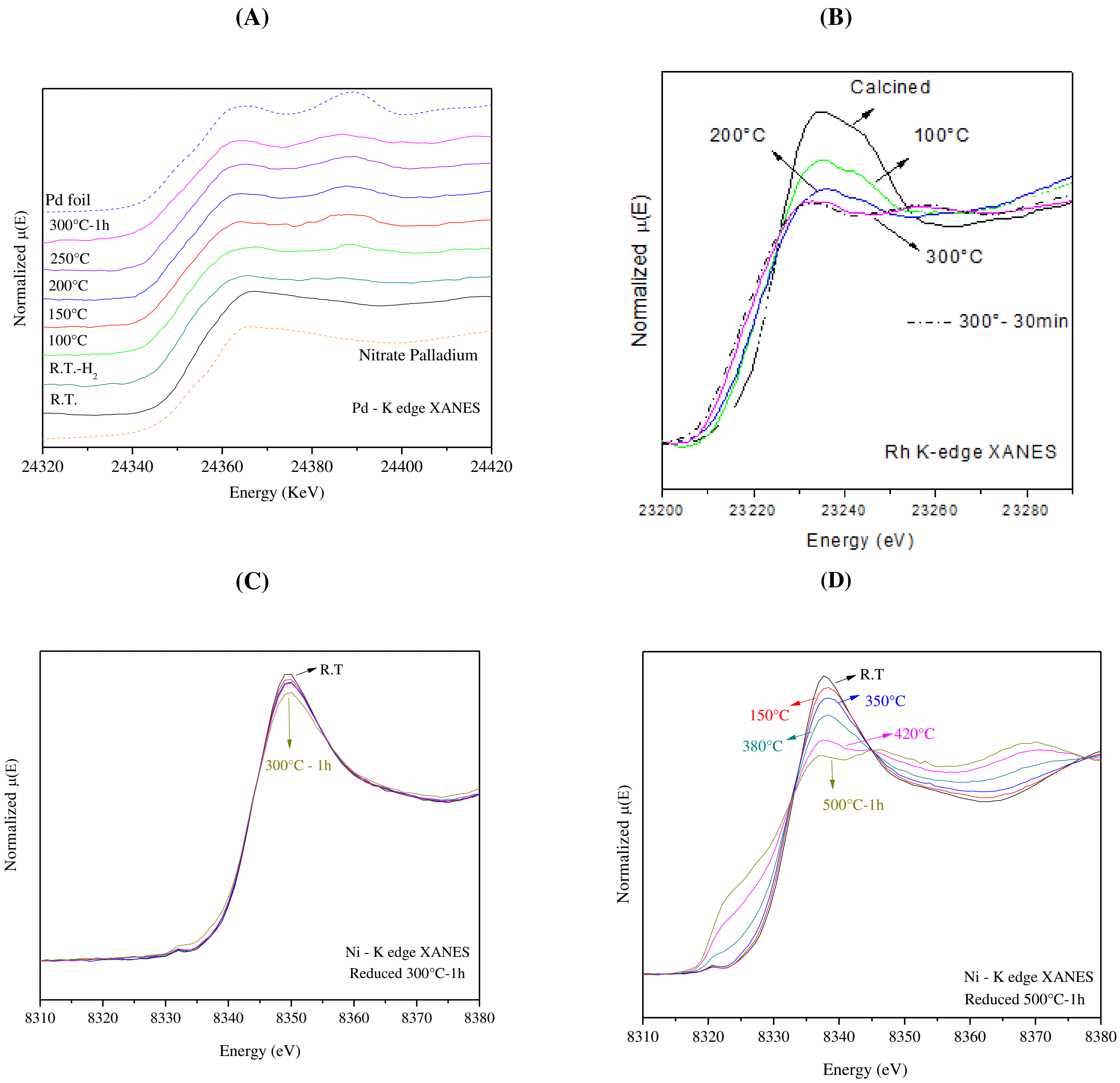

Figure 7-3. Snapshots of XANES profiles at different temperatures for (A) 1%Pd/Nb_2O_5, (B) 1%Rh/Nb_2O_5 and (C) 5%Ni/Nb_2O_5 reduced at 300° for 1h and (D) 5%Ni/Nb_2O_5 reduced at 500° for 1h.

For Pd/Nb_2O_5, the XANES spectra at 25°C after hydrogen flow already reveals the appearance of a peak at around 24350 eV, indicating that PdO is partially reduced at room temperature. This result agrees very well with the TPR profile. At 100°C, palladium oxide is completely reduced. The XANES spectra of Rh/Nb_2O_5 sample shows that the reduction of rhodium oxide begins at 100°C and it is totally reduced around 300°C. Ferreira-Aparicio et al. [24] showed that a Rh/Al_2O_3 catalyst was progressively reduced in the same temperature range (100-250°C). The XANES spectra at Ni-K edge of Ni/Nb_2O_5 catalyst (Figure 7.3c) only slightly change during reduction at 300°C, indicating that a large amount of Ni remained oxidized. However, NiO was completely reduced after treatment under 5% H_2 in He mixture at 500°C (Figure 7.3d). The evolution of the Ni species during reduction calculated by the linear combination of Ni K-edge XANES spectra is shown in Fig. 7.4. When the temperature achieved 300°C, only 10% of Ni was in the metallic state and the amount of Ni^o increased up to 20% after 1h at 300°C under the reduction mixture. However, Ni/Nb_2O_5 catalyst was completely reduced after reaching 500°C. These results are in agreement with the TPR experiment.

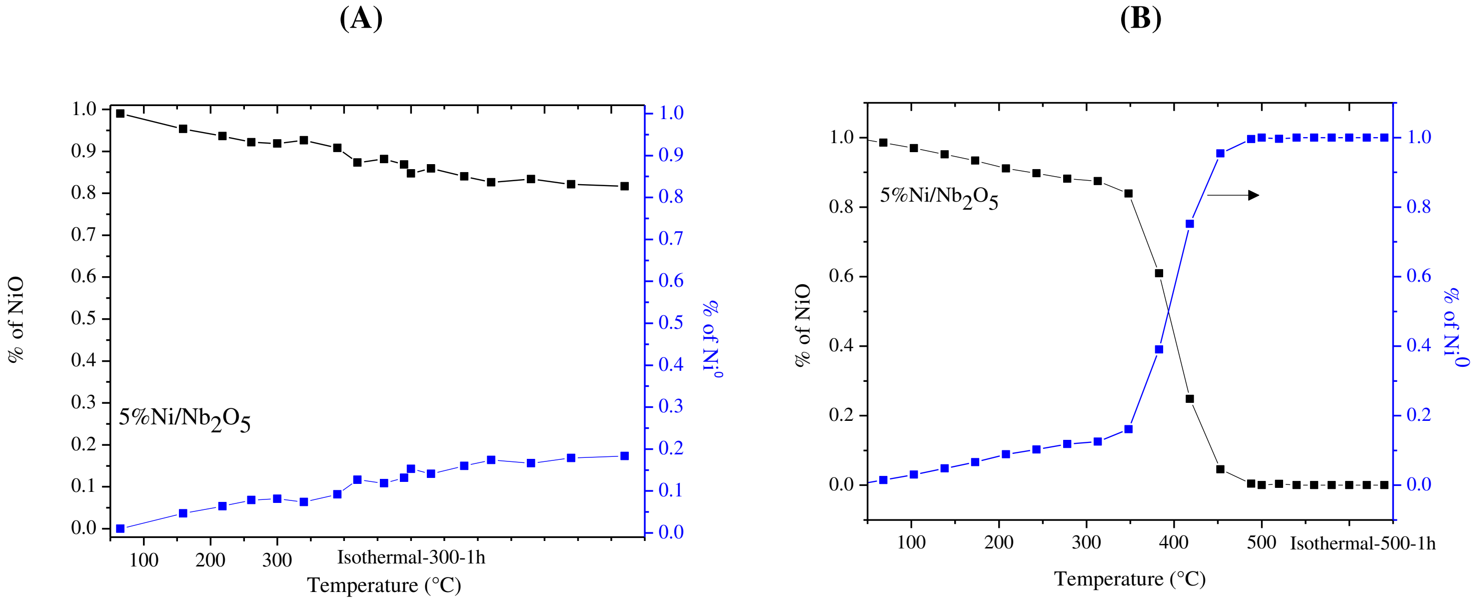

Figure 7-4. Linear combination fittings of TPR-XANES profiles at the Ni K-edge of Ni/Nb_2O_5 catalyst reduced at (A) 300°C; (B) 500°C.

The TPR and in situ XANES experiments were carried out using mixture containing 5% H_2 in He, which did not allow the complete reduction of Ni/Nb_2O_5 catalyst at 300°C. In order to improve NiO reduction at low temperature, this catalyst was reduced under pure hydrogen at 300°C (10°C/min) for 1h. Then, the sample was cooled to room temperature under Ar and passivated under a 5% O_2 in N_2 mixture (30 mL/min) at 0°C. After this, the TPR-XANES spectra as a function of reduction temperature were performed and the results are shown in Fig. 7.5. The reduction under pure hydrogen significantly increased the fraction of metallic Ni to 60%.

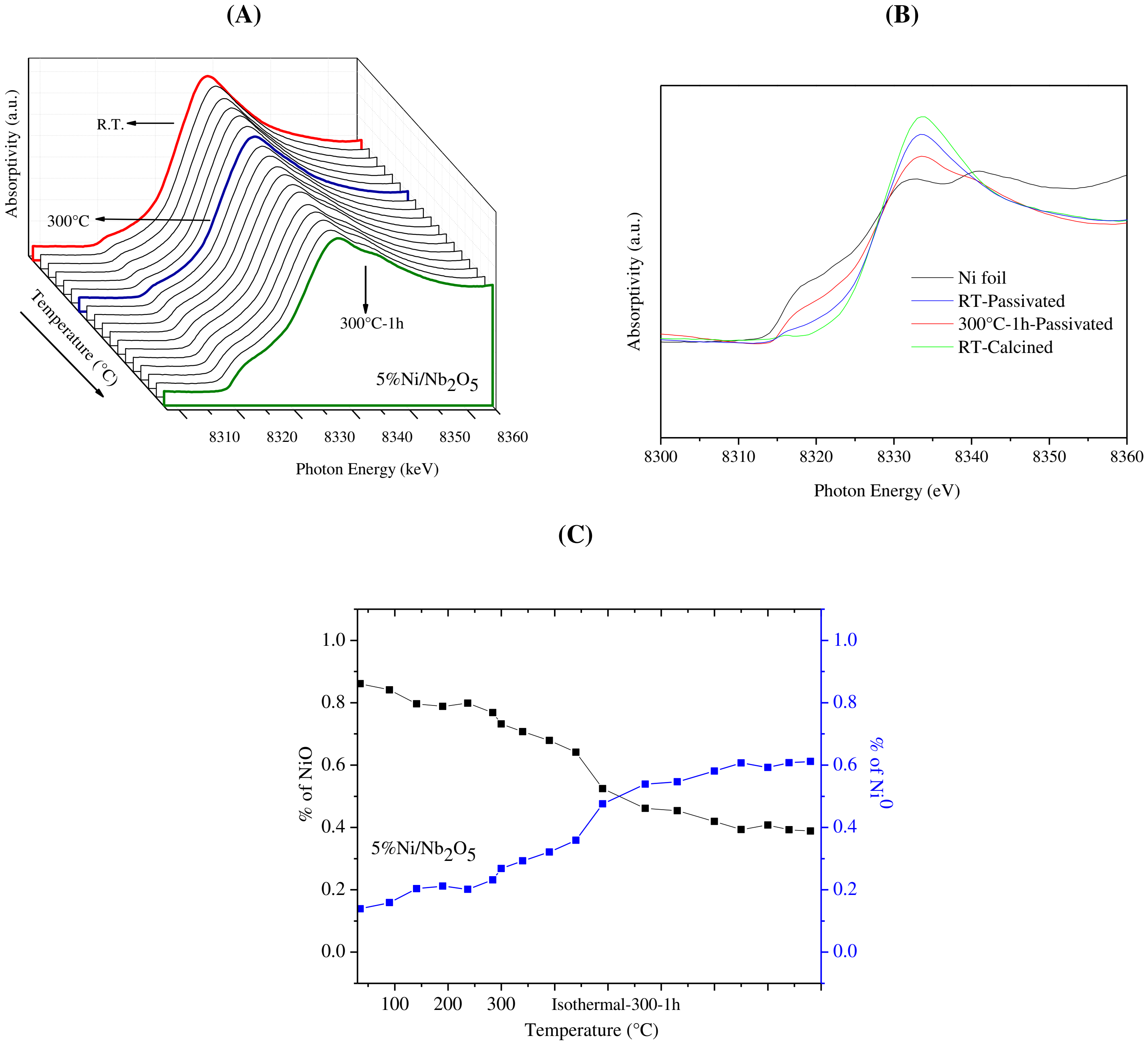

Figure 7-5. (A) TPR-XANES profiles for 5%Ni/Nb_2O_5 of the passived sample; (B) Compration of the XANES profiles for 5%Ni/Nb_2O_5 of the calcinated samples, passived sample at RT, passived sample at 300°C after 1h of reduction (C) Linear combination fittings of TPR-XANES profiles at the Ni K-edge of Ni/Nb_2O_5 passived.

7.3.4. TPR-XANES at the Nb K-edge

Aiming to determine the oxidation state of Nb after reduction at different temperatures, TPR-XANES analysis was performed at the Nb K-edge. TPR-XANES spectra obtained during reduction from 25 to 300°C are shown in Fig. S2 and snapshots of XANES spectra at the initial and final reduction temperature are provided in Fig. 7.6.

For all samples, the following peaks were observed: (i) a weak pre edge absorption shoulder around 18,982 eV, which can be assigned to an electronic transition from the Nb orbital 1s to the orbital 4d [25] ; (ii) an absorption edge around 18,996 eV, which is, in part, due to an electronic transition from the Nb orbital 1s to the orbital 5p [25] and (iii) a strong edge peak around 19,005, which is due to low-energy scattering ressonance of photoelectrons by neighboring atoms [26]. Fig. S3 display the TPR-XANES spectra obtained during reduction to 500°C and snapshots of XANES spectra at the initial and final stages of reduction are shown in Fig. 7.7.

According to the literature [25,27] the XANES from niobium oxides significantly differ from Nb metal. The Nb profile is shifted toward higher energies with an order of the increase in valence values (0 - $^{+}4$ - $^{+}5$). Cartier et al. [25] reported the XANES spectra of reference samples (standards) corresponding to four niobium oxidation state and its respective first derivateve profiles. The authors showed that niobium threshold energy E_0 is shifted from 18986 eV (Nb^0) to 19006 eV (Nb^{5+}) as Nb formal valence increases. In general, for all the temperature reductions almost no changes in peaks intensities and in the first derivate profiles were observed after the pre treatment. Then, the niobium reduction, it was not observed in the XANES analysis.

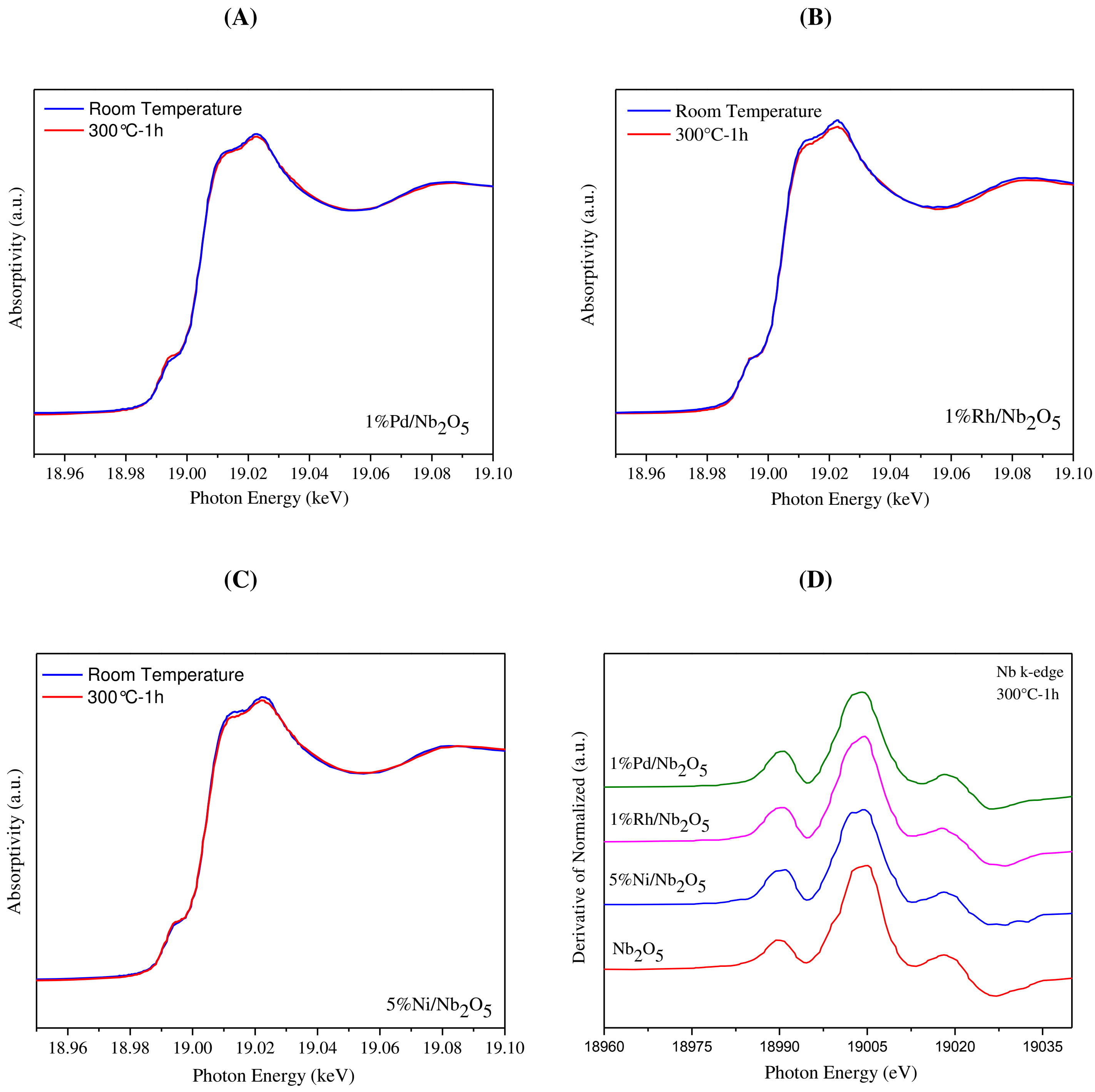

Figure 7-6. Snapshots of XANES spectra at the Nb K-edge at room temperature (blue line); 300°C (red line) for (A) Pd/Nb$_2$O$_5$; (B) Rh/Nb$_2$O$_5$; (C) Ni/Nb$_2$O$_5$. (D) Comparation of the first derivated profile.

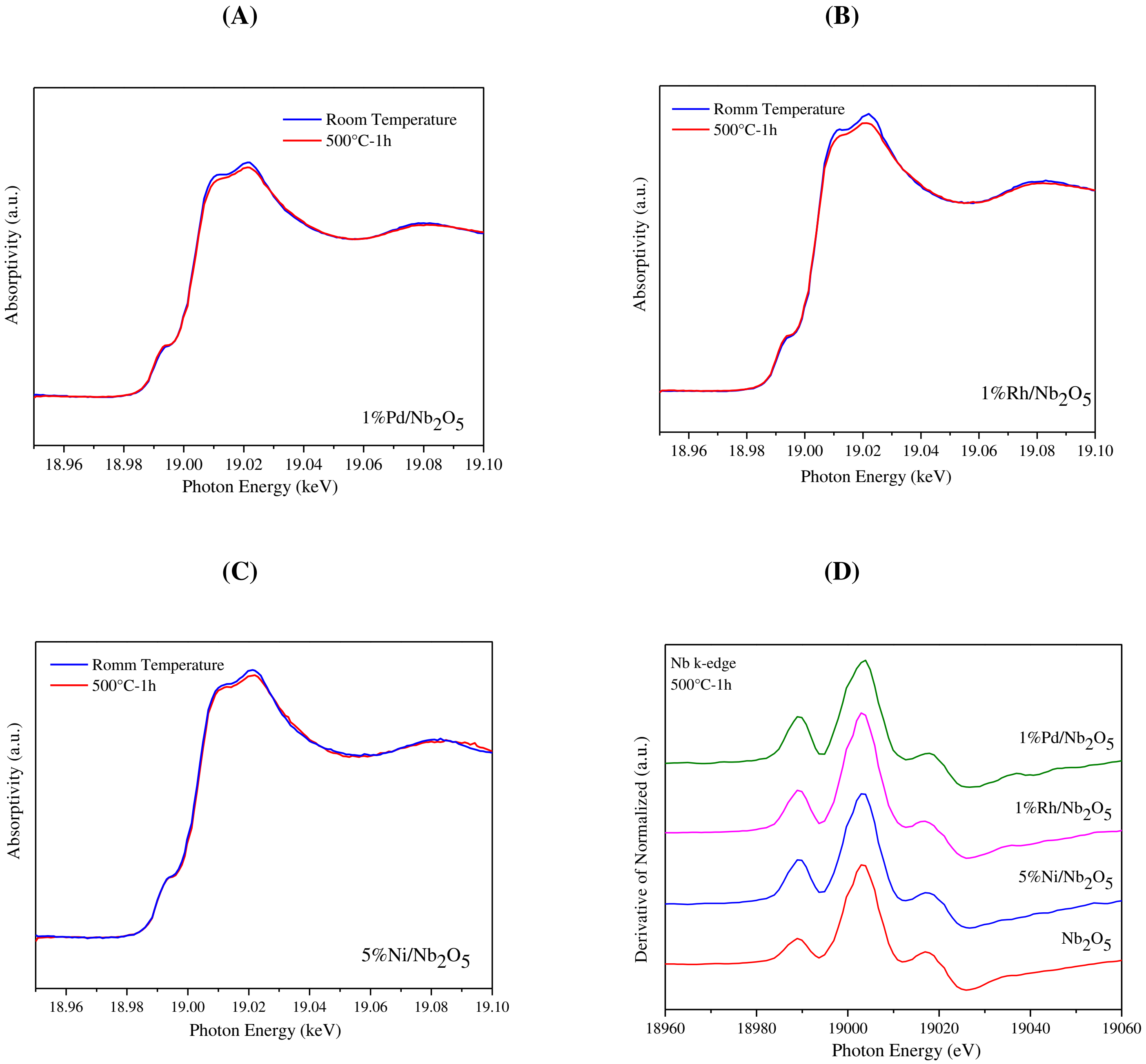

Figure 7-7. Snapshots of XANES spectra at the Nb K-edge at room temperature (blue line); 500°C (red line) for (A) Pd/Nb$_2$O$_5$; (B) Rh/Nb$_2$O$_5$; (C) Ni/Nb$_2$O$_5$; (D) Comparation of the first derivated profile.

7.3.5. In situ x-ray photoelectron spectroscopy (XPS)

Fig. 7.8 shows the XP spectra of Pd 3d, Rh 3d, Ni 2p core levels of the calcined samples and after reduction under H$_2$ flow at different temperatures. The Pd 3d spectrum of the calcined sample displays two peaks at 336.8 and 338.1 eV, which are assigned to PdO and PdO_2 , respectively [28](Fig. 7.8a).

After reduction at 100°C, the peaks attributed to palladium oxide disappeared and a new peak assigned to Pd^0 is observed at 335.2 eV [29], indicating that palladium oxide was completely reduced at this temperature. This result agrees very well with the results from TPR and XANES experiments. Increasing the reduction temperature to 400°C did not change the spectra. At 500°C it was observed a shift in the XPspectra of the Pd, which may be due to the charge transfer from the partially reduced NbOx to Pd [30, 31]. Similar results consistent with a charge transfer between the Ti species and metal were obtained by Chang Lee et al. [32], which was related to the SMSI phenomenon.

For Rh/Nb_2O_5 calcined catalyst (Fig. 7.8b) the binding energy of the $Rh(3d_{5/2})$ peak was at 310.0 eV. This B.E. is attributed to oxidized Rh particles (Rh^{3+} oxidation state) [33]. The peaks related to the rhodium oxide Rh (Rh_2O_3) are still present on the spectrum after reduction at 100°C. However, they are no longer detected after reduction at 200°C. At this temperature, the peak attributed to Rh^0 appears at 307.3 eV ($3d_{5/2}$) [34, 35], which also agrees with the XANES result. For pure Rh metal foil, $Rh(3d_{5/2})$ and $Rh(3d_{3/2})$ peaks occur at 307.0 and 311.8 eV, respectively [33].

The Ni 2p spectrum of the calcined Ni-based catalyst showed a peak at 856.3 eV and a satellite peak at 859.7 eV, with a spin-orbit splitting of 871.5eV, indicating the presence of Ni_2O_3 [36, 37]. The spectra remained unchanged during the reduction at 100 and 200°C. After reduction at 300°C, the spectrum exhibits only the Ni 2p3/2 peak at 852.5 eV that corresponds to Ni^0 [38], which indicates that nickel oxide is completely reduced at the surface at this low temperature. However, the extent of the reduction of the bulk is still too low at 300°C, as revealed by TPR and in situ XANES experiments.

Fig. 7.9 shows the Nb 3d spectra at different reduction temperatures for all catalysts. For the calcined samples, the peak at 207.5 eV is attributed to the Nb $3d_{5/2}$ binding energy of Nb_2O_5 [36,38]. No changes were observed on the spectra during the reduction at different temperatures for all catalysts. The binding energies of the O 1s peaks showed a peak, the sharp one located at 529.6 eV and the low one located at 531.9 eV, which is assigned to O_2 in Nb-oxides and surface oxygen, respectively [39] .

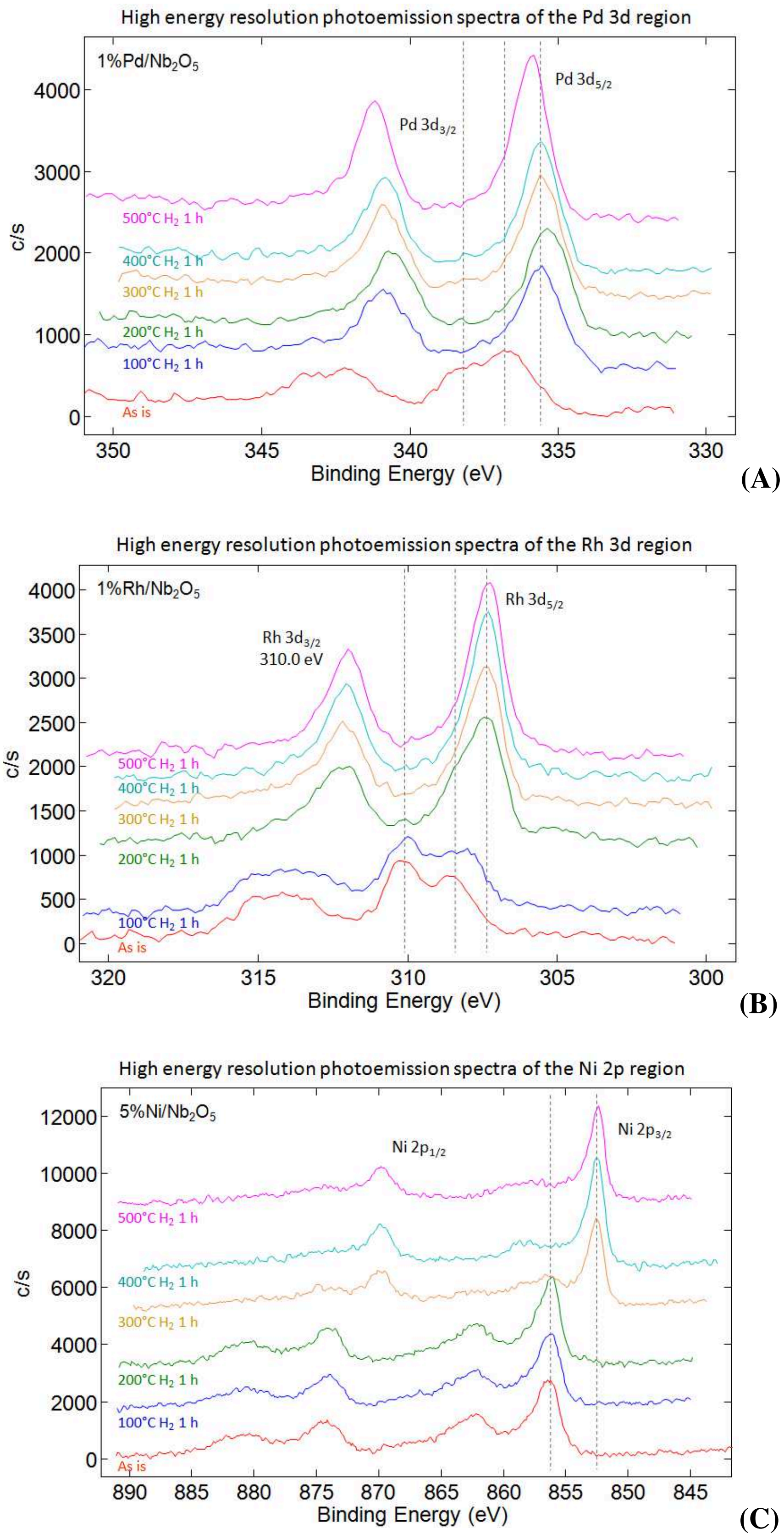

Figure 7-8. XPS spectrum for (A) Pd/Nb_2O_5; (B) Rh/Nb_2O_5; (C) Ni/Nb_2O_5.

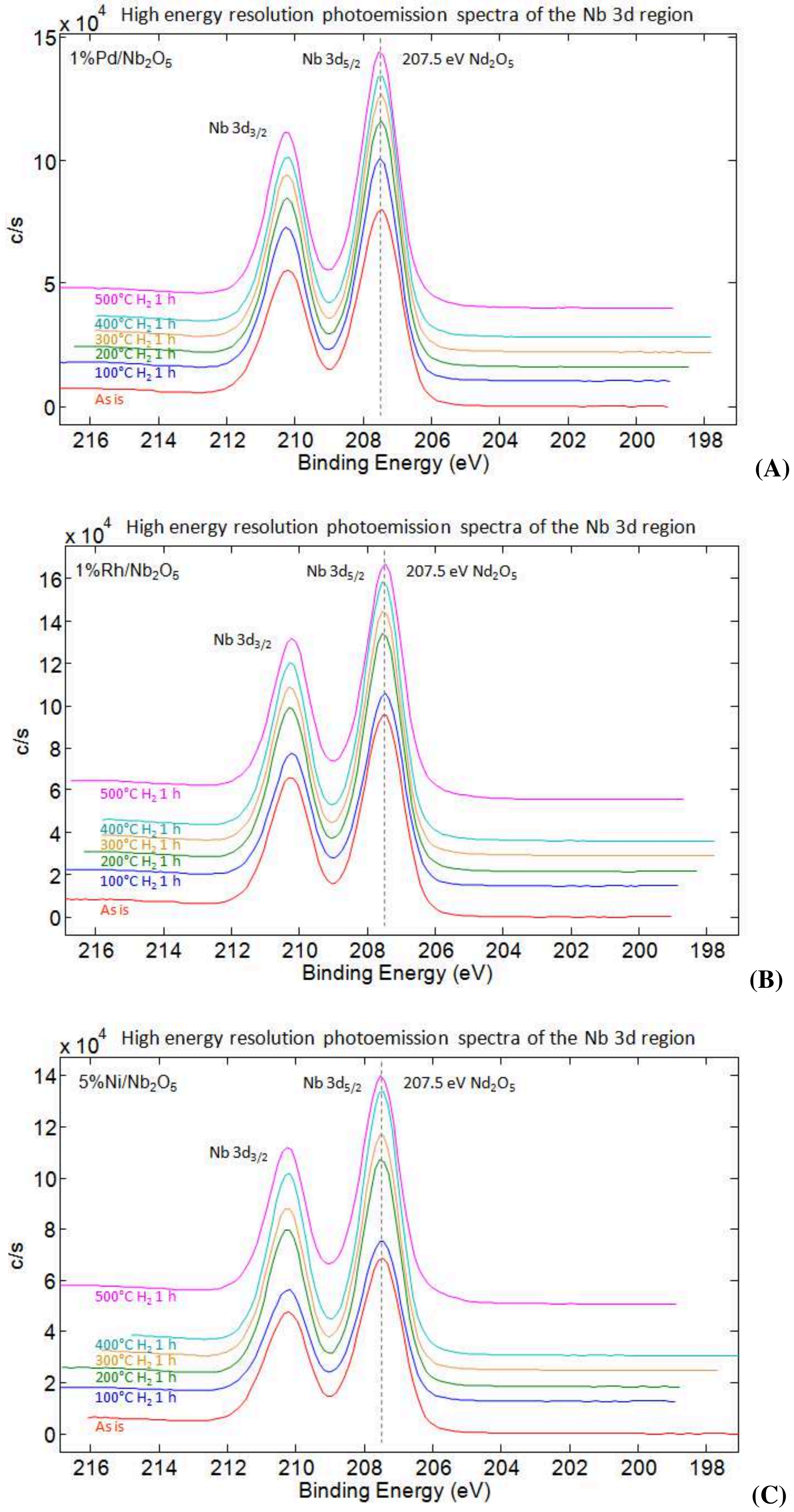

Figure 7-9. XPS spectrum for (A) Pd/Nb_2O_5; (B) Rh/Nb_2O_5; (C) Ni/Nb_2O_5.

The surface chemical compositions determined from XPS peaks are summarized in Table 7.4 [40]. A significant change of Ni surface compositions (around 50%) was observed for Ni/Nb_2O_5 when this sample was submitted to reduction under H_2 at different temperatures, while the Pd3d/Nb3d and Rh3d/Nb3d ratios were constant.

Table 7-4. Surface composition (at.%) derived from the XPS analyses

	Atomic Concentration				
	1%Rh/ Nb_2O_5				
	C1s	**O1s**	**Nb3d**	**Rh3d**	**Rh3d/Nb3d**
Calcined	3.68	67.7	28.33	0.28	0.011
100°C in H_2/Ar	3.39	73	23.34	0.28	0.013
200°C in H_2/Ar	3.86	70.83	25.06	0.25	0.011
300°C in H_2/Ar	1.45	72.07	26.23	0.24	0.01
400°C in H_2/Ar	0.02	73.23	26.5	0.26	0.011
500°C in H_2/Ar	0.08	73.23	26.39	0.3	0.013
	1%Pd/ Nb_2O_5				
	C1s	**O1s**	**Nb3d**	**Pd3d**	**Pd3d/Nb3d**
Calcined	3.88	72.68	23.22	0.22	0.009
100°C in H_2/Ar	3.55	69.9	26.27	0.28	0.011
200°C in H_2/Ar	4.21	70.78	24.77	0.25	0.01
300°C in H_2/Ar	2.03	71.96	25.76	0.25	0.01
400°C in H_2/Ar	0.52	74.53	24.7	0.25	0.01
500°C in H_2/Ar	0.73	72.28	26.66	0.33	0.012
	5%Ni/Nb_2O_5				**Ratio [Metal/Nb]**
	C1s	**O1s**	**Ni2p**	**Nb3d**	**Ni2p/Nb3d**
Calcined	4.04	68.11	2.89	24.96	0.12
100°C in H_2/Ar	5.03	69.91	2.37	22.69	0.1
200°C in H_2/Ar	5.53	66.97	2.39	25.1	0.1
300°C in H_2/Ar	1.99	69.43	2.1	26.47	0.08
400°C in H_2/Ar	0.35	71.38	1.86	26.4	0.07
500°C in H_2/Ar	0.86	72.94	1.59	24.61	0.06

7.3.6. HDO of phenol reaction

The reaction rate for HDO of phenol and the selectivity to products at low phenol conversion (around 10%) for all catalysts reduced at 300 and 500°C are listed in Tables 7.5 and 7.6, respectively. The niobium oxide-support was also tested but it was inactive under the reaction conditions used.

Table 7-5. Reaction rate for HDO of phenol and product distribution at low conversion after reduction of niobia supported catalysts at 300°C.

Sample	W/F (h)	Conversion (%)	Rate of HDO (mmol.min^{-1}.g$_{cat}$$^{-1}$)	Selectivity (%)		
				Benzene	Ano+Eno	ONE
Pd/Nb_2O_5	0.0190	5.6	0.78	72.4	2.3	25.3
Rh/Nb_2O_5	0.0535	10.34	0.31	92.6	4.3	3.1
Ni/Nb_2O_5	0.0800	8.33	0.08	60.2	9.6	30.2

Table 7-6. Reaction rate for HDO of phenol and product distribution at low conversion after reduction of niobia supported catalysts at 500°C.

Sample	W/F (h)	Conversion (%)	Rate of HDO (mmol.min^{-1}.g$_{cat}$$^{-1}$)	Selectivity (%)		
				Benzene	Ano+Eno	ONE
Pd/Nb_2O_5	0.2770	8.6	0.023	91.9	2.6	5.5
Rh/Nb_2O_5	0.5349	14.4	0.032	93.8	1.4	2.3
Ni/Nb_2O_5	1.0698	16.0	0.017	97.0	1.0	1.3

All the samples were more active when reduced at 300°C than 500°C and similar result were observed by Brown et al. [41]. The authors studied the changes in the catalytic properties of Pt and Rh supported on Nb_2O_5 caused by the increase of the reduction temperature from 250°C to 500°C for the hydrogenolysis of 2-methybutane and n-pentane. The high reduction temperature decreased the rates of hydrogenolysis reaction, which was attributed to the strong metal-support interaction (SMSI). According to Caballero et al. [42] the SMSI effect is characterized by oxide moieties from the support that migrate over the metallic particles, blocking the surface and modifying its adsorption and catalytic properties.

Regarding product distribution, benzene was the main product formed independently of the metal and the reduction temperature. Significant amounts of cyclohexanone and cyclohexane were also produced over the Pd/Nb_2O_5 and Ni/Nb_2O_5 catalysts reduced at 300°C. When these samples were reduced at 500°C the selectivity to benzene increased, which as close to 95%. Only small amounts of cyclohexanone and cyclohexane were formed after reduction at high temperature. Rh/Nb_2O_5 catalyst exhibited the highest selectivity to benzene after reduction at 300°C, however an increase in the reduction temperature did not change the benzene selectivity for this sample.

7.3.7. The effect of the type of the metal and niobia support for HDO of phenol

HDO reaction requires a metallic site for hydrogenation/dehydrogenation as well as a support that adsorbs the oxy compound and promotes deoxygenation reaction [43, 44]. Therefore, the type of metal and support plays a key role on the HDO of phenol. However, there are only a few studies about the effect of the type of the metal on HDO of phenol [45, 9, 7]. The performance of Ru/C, Pd/C and Pt/C catalysts was compared for the HDO of phenol in liquid phase [45]. The selectivity to deoxygenated products followed the order: Ru/C > Pd/C > Pt/C. According to Mortensen et al. [45], the highest deoxygenation activity was due to the stronger interaction between the Ru and oxygen atom than with Pt or Pd. Teles et al. [9] investigated the effect of the type of the metal on silica supported catalysts for the HDO of phenol in gas phase. Hydrogenated products (cyclohexanone and cyclohexanol) were mainly formed on Pt/SiO_2, Pd/SiO_2 and Rh/SiO_2 catalysts, whereas large amounts of hydrogenolysis products (C5-C6 hydrocarbons and methane) were produced over Co/SiO_2, Ni/SiO_2 and mainly Ru/SiO_2 catalysts. According to the authors, more oxophilic metals such as Ru, Co and Ni promotes the direct dehydroxylation of phenol followed by hydrogenolysis. The following order for selectivity to deoxygenated products as a function of the binding energies of atomic oxygen was obtained: Ru >> Co > Ni > Rh > Pd = Pt. These results clearly demonstrated that stronger binding of oxygen from the carbonyl group to metal favors the formation of deoxygenated products. Recently, Teles et al. [7] studied the effect of the type of the metal over zirconia supported catalysts for HDO of phenol. They reported that the selectivity to deoxygenated products for zirconia supported catalysts did not followed the same trend observed for silica supported catalysts from their previous study. Ni/ZrO_2 exhibited a higher selectivity to deoxygenated products than Rh/ZrO_2 catalyst, whereas the opposite result was observed for the same metals supported on silica. These results demonstrate the important role of the type of the support for HDO of phenol. In this case, the oxophilic sites of the zirconia support also contributed to the deoxygenation activity of the catalysts.

In our work, the selectivity to benzene for the catalysts reduced at 300°C followed the order: Rh > Pd > Ni. This trend was completely different from that one expected for the oxophicity of the metals [9]. This may be related to the participation of the niobia support on the HDO of phenol or/and to the fact that at lower reduction temperature the nickel is not totally reduced, as observed in the TPR-XANES analysis. The presence of nickel oxide may decrease the oxophilicity of this sample. Recently, Barrios et al. [18] studied the HDO of phenol in gas phase over Pd/SiO_2 and Pd/Nb_2O_5 catalyst. The high activity and selectivity to deoxygenated products of Pd/Nb_2O_5 for HDO of phenol is likely due to the strong interaction between the oxophilic sites represented by Nb^{5+}/Nb^{4+} cations and the oxygen from the phenol molecule. This promotes hydrogenation of the carbonyl group, leading to the formation of benzene. Xia et al. [16] proposed that the stronger bond strength between Nb and oxygen from the phenol molecule reduces the C-O bond dissociation barriers and favors C-O bond cleavage. Therefore, the high selectivity to deoxygenated products over niobia supported catalysts in our work is likely due to stronger interaction of Nb – O, which promotes the deoxygenation.

In this work, the effect of the reduction temperature in the activity and selectivity was evaluated. During the catalytic tests, the reaction rates measured for samples reduced at 300°C were around 10 times higher than the ones observed when the samples were reduced at 500°C [46]. The decrease in the activity observed may be a consequence of the active phase sintering or/and a partial coverage of the active phase by the support. For Pd/Nb_2O_5 and Rh/Nb_2O_5, the ratios of Rh3d/Nb3d and Pd3d/Nb3d observed in the XPS analysis were constant during all the reduction process, which is an indication that these metals did not suffer sintering on the catalyst surface. According to Chang et al. [47] Pd/Al_2O_3 remained at modest dispersion under the severe reduction condition, which was not observed for Pd/TiO_2. The authors showed that the reduced support materials blocked the surface of the metal crystallites at high-temperature reduction. Tauster et al. [34] exposed that the reduction of noble metals supported on TiO_2 at 500°C decreased the hydrogen and carbon monoxide sorption to near zero, however electron microscopy and x-ray diffraction show that the loss of this sorption capacity is not due to metal agglomeration. This effect was related to the chemical interaction between the noble metal and the support. For Ni/Nb_2O_5 the XPS analysis showed a decrease in the Ni2p/Nb3d ratios, which also can be interpreted as a metal sintering. This metal sintering was confirmed by the XRD in situ analysis. However, these effects did not decrease the reaction rates in the same intensity than observed for the noble metals.

In general the reduction temperature also affected the selectivity obtained in the HDO reaction. Teles et al. [7] reported that for the catalysts that do not exhibit significant hydrogenolysis reaction (Pt/ZrO_2, Pd/ZrO_2, Rh/ZrO_2), the changes in product distribution are not due to the different metal dispersion. For these catalysts, the hydrogenation was the main reaction, which is considered an insensitive structure-reaction. According to Griffin et al. [48] the activity and selectivity observed during the deoxygenation of m-cresol over Pt catalysts is dependent on the choice of support and reaction conditions. The combined experimental−computational results reported by them highlighted the effects between hydrogenation catalysts and reducible metal oxide supports. The authors showed that the reactivity of Pt/TiO_2 and Pt/C is driven by the metallic phase at lower temperatures, while contributions from the TiO_2 support enhance deoxygenation at higher temperatures.

When higher reduction temperature was used (Tr=500°C) all the samples showed similar selectivities for benzene, around 95%, independently of the supported metal. Similar result was observed by Xia et al. [49] in the hydrodeoxygenation of furan-derived adducts to liquid alkanes. According to them because of the significant promotional effect of NbOx species on C-O cleavage, expensive metals like Pt and Pd, or much cheaper, such as Ni, can be loaded on $NbOPO_4$ and used as a multifunctional catalysts for the efficient hydrodeoxygenation of biomass-derived oxygenates.

For Pd and the Ni samples, the reduction at higher temperature favored the benzene selectivity, while for Rh this selectivity was similar independently of the reduction temperature. According to Teles et al. [9] the DDO is promoted over Rh catalyst, since the presence of CH_4 was reported, however this route is not favored over Pd samples. Some points were observed for Rh/Nb_2O_5: (i) Independently of the reduction temperature this metal is fully reduced, also (ii) there is no difference between the reaction rate of the cyclohexanol to benzene for the sample reduced at 300°C or 500°C and (iii) there is a decrease in the HDO rate after reduction at 500°C, which is an indication of SMSI effect [50]. Similar conditions was observed for Pd/Nb_2O_5, however this sample showed an increase in the benzene selectivity. The XPS analysis indicated a difference between the Pd on the surface reduced at 300° and 500°C. After reduction at 500°C, the XPS profile showed an transfer of electrons from Nb_2O_5 to Pd, which may affected the oxidation state of the Pd and improves the benzene selective. The strong metal-support interaction may favor the formation a Pd-Nb_2O_5 interface, which leads to the adsorption of the phenol though its oxygen present in C-O bond. This type of adsorption promotes the hydrogenation of the carbonyl function of the tautomer intermediate [46].

The Ni sample showed the biggest improvement in the benzene selectivity after the reduction at 500°C. The TPR-XANES in Ni edge showed that after reduction at 500°C all the nickel is reduced, while at Tr=300°C a large portion of this metal is oxide. The increase in the Ni metallic composition leads to a higher reaction rate measured for dehydration of cyclohexanol over the Ni/Nb_2O_5, which may be relate to the oxophilicity of the sample [44]. In general, an increase in the oxophilicity may justify the higher benzene selectivity after reduction at 500°C.

7.4. Conclusion

The objective of this work was to study different metal catalysts supported on Nb_2O_5 with the aim of obtaining selective catalysts for hydrodeoxygenation reaction and elucidating the structure–property relationships in this system. The reduction temperature affected the activity and selectivity of the studied catalysts. For all the samples the metal surface was covered by NbO_x species, especially at high reduction temperature, as indicated by the decrease observed in the reaction rate.The influence of the metal/support interaction in the selectivity was also observed. In general, the presence of Nb_2O_5 as support favored the benzene formation at all reduction temperature. For reduction temperature at 300°C the tautomerization-hydrogenation-dehydration path was presented, manily for Pd and Ni samples, while the hydrogenation of the aromatic ring was disfavored after the reduction at 500°C. In general, the reduction temperature of 500°C promoted the metal-support interaction, which improved the oxophilicity of the samples and favor benzene formation. The absence of CH_4 is an indication that the hydrogenolysis of benzene was inhibited independent of the reduction temperature used.

Acknowledgments

We acknowledge the support of CNPq, CAPES and FAPEMIG and the CBMM for the acid niobic. We also thank LNLS for the use of XDS and DXAS beamlines. The XPS analyses were performance by Drs. Mark Engelhard, using resources at EMSL, a DOE Office of Science User Facility sponsored by the Office of Biological and Environmental Research and located at Pacific Northwest National Laboratory.

Reference

[1] G.W. Huber, J.A. Dumesic, An overview of aqueous-phase catalytic processes for production of hydrogen and alkanes in a biorefinery, 111 (2006) 119–132.https://doi.org/10.1016/j.cattod.2005.10.010

[2] E.C. Vagia, A.A. Lemonidou, Thermodynamic analysis of hydrogen production via autothermal steam reforming of selected components of aqueous bio-oil fraction, Int. J. Hydrogen Energy. 33 (2008) 2489–2500. doi:10.1016/j.ijhydene.2008.02.057.https://doi.org/10.1016/j.ijhydene.2008.02.057

[3] P.M. Mortensen, J.D. Grunwaldt, P.A. Jensen, K.G. Knudsen, A.D. Jensen, A review of catalytic upgrading of bio-oil to engine fuels, Appl. Catal. A Gen. 407 (2011) 1–19. doi:10.1016/j.apcata.2011.08.046.https://doi.org/10.1016/j.apcata.2011.08.046

[4] S. Sreekumar, M. Balakrishnan, K. Goulas, G. Gunbas, F.D. Toste, Upgrading Lignocellulosic Products to Drop-In Biofuels via Dehydrogenative Cross-Coupling and Hydrodeoxygenation Sequence, 94720 (2015) 2609–2614. https://doi.org/doi:10.1002/cssc.201500754.

[5] H.Y. Zhao, D. Li, P. Bui, S.T. Oyama, Applied Catalysis A : General Hydrodeoxygenation of guaiacol as model compound for pyrolysis oil on transition metal phosphide hydroprocessing catalysts, 391 (2011) 305–310. https://doi.org/10.1016/j.apcata.2010.07.039.

[6] P.M. De Souza, R.C. Rabelo-Neto, L.E.P. Borges, G. Jacobs, B.H. Davis, T. Sooknoi, D.E. Resasco, F.B. Noronha, Role of keto intermediates in the hydrodeoxygenation of phenol over Pd on oxophilic supports, ACS Catal. 5 (2015) 1318–1329. doi:10.1021/cs501853t.https://doi.org/10.1021/cs501853t

[7] A. Camila, A. Teles, R.C. Rabelo-neto, G. Jacobs, B.H. Davis, D.E. Resasco, C.A. Teles, R.C. Rabelo-neto, G. Jacobs, B.H. Davis, D.E. Resasco, Hydrodeoxygenation of phenol over zirconia supported catalysts . The effect of metal type on reaction mechanism and catalyst deactivation, (n.d.). doi:10.1002/cctc.201700047. https://doi.org/10.1002/cctc.201700047

[8] V.N. Bui, G. Toussaint, D. Laurenti, C. Mirodatos, C. Geantet, Co-processing of pyrolisis bio oils and gas oil for new generation of bio-fuels: Hydrodeoxygenation of guaïacol and SRGO mixed feed, Catal. Today. 143 (2009) 172–178. doi:10.1016/j.cattod.2008.11.024.https://doi.org/10.1016/j.cattod.2008.11.024

[9] C. A. Teles, R. C. Rabelo-Neto, J. R. de Lima, L. V. Mattos, D. E. Resasco, F. B. Noronha, The Effect of Metal Type on Hydrodeoxygenation of Phenol Over Silica Supported Catalysts, Catal. Letters. 146 (2016) 1848–1857. doi:10.1007/s10562-016-1815-5.https://doi.org/10.1007/s10562-016-1815-5

[10] V.N. Bui, D. Laurenti, P. Afanasiev, C. Geantet, Hydrodeoxygenation of guaiacol with CoMo catalysts . Part I : Promoting effect of cobalt on HDO selectivity and activity, Applied Catal. B, Environ. 101 (2011) 239–245. doi:10.1016/j.apcatb.2010.10.025.https://doi.org/10.1016/j.apcatb.2010.10.025

[11] A.J.R. Hensley, Y. Wang, J. Mcewen, Phenol deoxygenation mechanisms on Fe (110) and Pd (111), ACS Catal. 5 (2015) 523–536. doi: 10.1021/cs501403w. https://doi.org/10.1021/cs501403w

[12] P.M. De Souza, R.C. Rabelo-neto, L.E.P. Borges, G. Jacobs, B.H. Davis, D.E. Resasco, F.B. Noronha, Hydrodeoxygenation of phenol over Pd catalysts. Effect of support on reaction mechanism and catalyst deactivation, ACS Catal., 7 (2017) 2058–2073.https://doi.org/10.1021/acscatal.6b02022

[13] Q. Tan, G. Wang, L. Nie, A. Dinse, C. Buda, J. Shabaker, D.E. Resasco, Different Product Distributions and Mechanistic Aspects of the Hydrodeoxygenation of m-Cresol over Platinum and Ruthenium Catalysts, ACS Catal. 5 (2015) 6271–6283. doi:10.1021/acscatal.5b00765.https://doi.org/10.1021/acscatal.5b00765

[14] Q. Xia, Q. Cuan, X. Liu, X. Gong, G. Lu, Y. Wang, Pd/NbOPO4 Multifunctional Catalyst for the

Direct Production of Liquid Alkanes from Aldol Adducts of Furans, Biomass Conversion (2014) 9755–9760. doi:10.1002/anie.201403440.https://doi.org/10.1002/anie.201403440

[15] Y. Shao, Q. Xia, X. Liu, G. Lu, Y. Wang, Pd/Nb2O5/SiO2 catalyst for the Direct Hydrodeoxygenation of Biomass-Related Compounds to Liquid Alkanes under Mild Conditions, CHEMSUSCHEM (2015) 1761–1767. doi:10.1002/cssc.201500053.https://doi.org/10.1002/cssc.201500053

[16] X.J. Zhuang, Q.N. Xia, Y.Q. Wang, S.C.E. Tsang, X.Q. Gong, Hydrodeoxygenation of butyric acid at multi-functional Nb2O5 catalyst: A density functional theory study, Int. J. Hydrogen Energy. 41 (2016) 18502–18508. doi:10.1016/j.ijhydene.2016.08.220.https://doi.org/10.1016/j.ijhydene.2016.08.220

[17] A.M. Barrios, C.A. Teles, P.M. De Souza, R.C. Rabelo-neto, G. Jacobs, B.H. Davis, L.E.P. Borges, F.B. Noronha, Hydrodeoxygenation of phenol over niobia supported Pd catalyst, In press (2017) 115-124. https://doi.org/10.1016/j.cattod.2017.03.034

[18] V. Lebarbier, M. Houalla, T. Onfroy, New insights into the development of Bronsted acidity of niobic acid, Catal. Today. 192 (2012) 123–129. doi:10.1016/j.cattod.2012.02.061. https://doi.org/10.1016/j.cattod.2012.02.061

[19] F.B. Noronha, D.A.G. Aranda, A.P. Ordine, M. Schmal, The promoting effect of Nb2O5 addition to Pd/Al2O3 catalysts on propane oxidation, 57 (2000) 275–282. https://doi.org/10.1016/S0920-5861(99)00337-5.

[20] T.U.Z. Hu, H. Nakamura, K. Kunimori, H. Asano, Ethane hydrogenolysis and hydrogen chemisorption over niobia-promoted rhodium catalysts: A new phase by a strong rhodium-niobia interaction, J. Catal. 112 (1988) 478–488. doi:10.1016/0021-9517(88)90163-7.https://doi.org/10.1016/0021-9517(88)90163-7

[21] T.U. Z. Hu, H. Nakamura, K. Kunimori, Y. Yokoyama, H. Asano, M. Soma, Structural transformation in Nb2O5-promoted Rh catalysts during calcination and reduction treatments, J. Catal. 119 (1989) 33–46. doi:10.1016/0021-9517(89)90132-2.https://doi.org/10.1016/0021-9517(89)90132-2

[22] I.E. Wachs, Y. Chen, J.-M. Jehng, L.E. Briand, T. Tanaka, Molecular structure and reactivity of the Group V metal oxides, Catal. Today. 78 (2003) 13–24. doi:10.1016/S0920-5861(02)00337-1.https://doi.org/10.1016/S0920-5861(02)00337-1

[23] L. G.. Appel, A. Frydman, C. A. C. Perez, J. G. Eon, D. G. Castner, CH. T. Campbell, M. Sshmal, XPS Studies on Ce/Al2O3 and on Co-Rh / Nb2O5 Catalysts, Phys. stat. sol.477 (1995) 192. doi: 10.1002/pssb.2221920217.https://doi.org/10.1002/pssb.2221920217

[24] P. Ferreira-Aparicio, I. Rodríguez-Ramos, A. Guerrero-Ruiz, Methane interaction with silica and alumina supported metal catalysts, Appl. Catal. A Gen. 148 (1997) 343–356. doi:10.1016/S0926-860X(96)00237-2.https://doi.org/10.1016/S0926-860X(96)00237-2

[25] C. Cartier, T. Hammouda, M. Boyet, O. Mathon, D. Testemales, B. N. Moine, Evidence for Nb2+ and Ta3+ in silicate melts under highly reducing conditions : A XANES study, American Mineralogist 100 (2015) 2152–2158.https://doi.org/10.2138/am-2015-5330

[26] M. R. Antonio, I. Song, H. Yamaha, Coordination and Valence of Niobium in TiO2–NbO2 solid solutions through X-Ray Absorption Spectroscopy, Journal of solid state chemistry 93 (1991) 183–192.https://doi.org/10.1016/0022-4596(91)90287-R

[27] K. Sasaki, L. Zhang, R.R. Adzic, Niobium oxide-supported platinum ultra-low amount electrocatalysts for oxygen reduction, Physical Chemistry Chemical Physics 10 (2008) 159–167. doi:10.1039/b709893f.https://doi.org/10.1039/B709893F

[28] T. Fleisch, An XPS study of metal-support interactions on Pd/SiO2 and Pd/La2O3, J. Catal. 87 (1984) 398–413. doi:10.1016/0021-9517(84)90200-8.https://doi.org/10.1016/0021-9517(84)90200-8

[29] W.J. Shen, Y. Ichihashi, H. Ando, Y. Matsumura, M. Okumura, M. Haruta, Effect of reduction temperature on structural properties and CO/CO2 hydrogenation characteristics of a Pd-CeO2 catalyst, Appl. Catal. A Gen. 217 (2001) 231–239. doi:10.1016/S0926-860X(01)00608-1.https://doi.org/10.1016/S0926-860X(01)00608-1

[30] S. C. Fung, XPS Studies of Strong Metal-Support Interactions, J. of Catal. 76 (1982) 225–230. https://doi.org/10.1016/0021-9517(82)90251-2.https://doi.org/10.1016/0021-9517(82)90251-2

[31] S. Chien, B. N. Shelimov, D. E. Resasco, E. H. Lee, G. L. Haller, Characterization of the Interaction between Rhodium and Titanium Oxide by XPS, J. Catal. 77 (1982) 301–303.https://doi.org/10.1016/0021-9517(82)90172-5

[32] D.C. Lee, J.H. Kim, W.J. Kim, Selective hydrogenation of 1,3-butadiene on TiO2 -modified Pd/SiO2 catalysts, 244 (2003) 83–91. https://doi.org/10.1016/S0926-860X(02)00597-5

[33] K. Polychronopoulou, J.L.G. Fierro, A.M. Efstathiou, The phenol steam reforming reaction over MgO-based supported Rh catalysts, J. Catal. 228 (2004) 417–432. doi:10.1016/j.jcat.2004.09.016.https://doi.org/10.1016/j.jcat.2004.09.016

[34] S.J. Tauster, S.C. Fung, R.L. Garten, Strong Metal-Support Interactions. Group 8 Noble Metals Supported on TiO2, J. Am. Chem. Soc. 100 (1978) 170–175. doi:10.1021/ja00469a029.https://doi.org/10.1021/ja00469a029

[35] S. Chuang, SI Pien, Infrared study of the CO insertion reaction on reduced, oxidized, and sulfided Rh/SiO2 catalysts, J. Catal. 135 (1992) 618–634. doi:10.1016/0021-9517(92)90058-P.https://doi.org/10.1016/0021-9517(92)90058-P

[36] K.V.R. Chary, K. Sri, P. Venkat, R. Rao, K. Seetha, R. Rao, M. Papadaki, Characterization and catalytic properties of niobia supported nickel catalysts in the hydrodechlorination of 1,2,4-trichlorobenzene, Journal of Molecular Catalysis A: Chemical 223 (2004) 353–361. doi:10.1016/j.molcata.2003.09.049.https://doi.org/10.1016/j.molcata.2003.09.049

[37] A.P. Grosvenor, M.C. Biesinger, R.S.C. Smart, N.S. McIntyre, New interpretations of XPS spectra of nickel metal and oxides, Surf. Sci. 600 (2006) 1771–1779. doi:10.1016/j.susc.2006.01.041.https://doi.org/10.1016/j.susc.2006.01.041

[38] P.C. Kemeny, N.J. Shevchik, Primary XPS spectra of Ni and final state effects, Solid State Commun. 17 (1975) 255–258. doi:10.1016/0038-1098(75)90287-2. https://doi.org/10.1016/0038-1098(75)90287-2

[39] Ö.D. Coşkun, S. Demirel, G. Atak, The effects of heat treatment on optical, structural, electrochromic and bonding properties of Nb2O5 thin films, J. Alloys Compd. 648 (2015) 994–1004. doi:10.1016/j.jallcom.2015.07.053.https://doi.org/10.1016/j.jallcom.2015.07.053

[40] E.B. Fox, S. Velu, M.H. Engelhard, Y.H. Chin, J.T. Miller, J. Kropf, C. Song, Characterization of CeO2-supported Cu-Pd bimetallic catalyst for the oxygen-assisted water-gas shift reaction, J. Catal. 260 (2008) 358–370. doi:10.1016/j.jcat.2008.08.018.https://doi.org/10.1016/j.jcat.2008.08.018

[41] C.K. Ronald Brown, Influence of strong metal-support interaction on exchange with deuterium and other reactions of hydrocarbons. Part 1. - Studies with Rh/TiO2 and Rh/SiO2, J. Chem. Soc. Faraday Trans. 91 (1995) 741–748. doi:10.1039/ft9969200281.https://doi.org/10.1039/FT9969200281

[42] A. Caballero, J.P. Holgado, V.M. Gonzalez-delacruz, S.E. Habas, T. Herranzb, M. Salmeron, In situ spectroscopic detection of SMSI effect in a Ni/CeO2 system : hydrogen-induced burial and dig out of metallic nickel, ChemComm 46 (2010).1097-1099 doi:10.1039/b920803h. https://doi.org/10.1021/cs501853t

[43] P.M. De Souza, R.C. Rabelo-neto, L.E.P. Borges, G. Jacobs, B.H. Davis, T. Sooknoi, D.E. Resasco, F.B. Noronha, Role of Keto Intermediates in the Hydrodeoxygenation of Phenol over Pd on Oxophilic Supports, ACS Catal 5 (2015) 1318-1329. doi:10.1021/cs501853t.https://doi.org/10.1021/cs501853t

[44] P.M. De Souza, L. Nie, L.E.P. Borges, F.B. Noronha, D.E. Resasco, Role of Oxophilic Supports in the Selective Hydrodeoxygenation of m -Cresol on Pd Catalysts, Catal Lett 144 (2014) 2005–2011. doi:10.1007/s10562-014-1337-y.https://doi.org/10.1007/s10562-014-1337-y

[45] P.M. Mortensen, J.D. Grunwaldt, P.A. Jensen, A.D. Jensen, Screening of catalysts for hydrodeoxygenation of phenol as a model compound for bio-oil, ACS Catal. 3 (2013) 1774–1785. doi:10.1021/cs400266e.https://doi.org/10.1021/cs400266e

[46] I. Nowak, M. Ziolek, Niobium Compounds: Preparation, Characterization, and Application in Heterogeneous Catalysis, Chem. Rev. (1999), 99, 3603−3624. doi: 10.1021/cr9800208.https://doi.org/10.1021/cr9800208

[47] T. -C. Chang, J.-J. Chen, C.-T. Yeh, Temperature-Programmed Reduction and Temperature-Resolved Sorption studies of strong metal-support interaction in supported palladium, J. Catal. 96 (1985) 51–57.https://doi.org/10.1016/0021-9517(85)90359-8

[48] M.B. Griffin, G.A. Ferguson, D.A. Ruddy, M.J. Biddy, G.T. Beckham, J.A. Schaidle, Role of the Support and Reaction Conditions on the Vapor-Phase Deoxygenation of m-Cresol over Pt/C and Pt/TiO2 Catalysts, ACS Catal. 6 (2016) 2715–2727. doi:10.1021/acscatal.5b02868.https://doi.org/10.1021/acscatal.5b02868

[49] Q.N. Xia, Q. Cuan, X.H. Liu, X.Q. Gong, G.Z. Lu, Y.Q. Wang, Pd/NbOPO4 multifunctional catalyst for the direct production of liquid alkanes from aldol adducts of furans, Angew. Chemie - Int. Ed. 53 (2014) 9755–9760. doi:10.1002/anie.201403440.https://doi.org/10.1002/anie.201403440

[50] S.-Y. Wang, S.H. Moon, M.A. Vannice, The Effect of SMSI (Strong Metal-Support Interaction) on CO Adsorption and Hydrogenation on Pd Catalysts, J. Catal. 71 (1981) 167–174.https://doi.org/10.1016/0021-9517(81)90212-8

8.CHAPTER VIII

8.1. Hydrodeoxygenation of phenol over doped cerium oxide: The effect of niobium addition

ABSTRACT- This work investigated the effect of doping cerium oxide catalyst with niobium for gas phase hydrodeoxygenation (HDO) of phenol at 300°C. The incorporation of niobium altered the lattice parameters of the oxides, favored the reduction of the cerium and increased the selectivity to deoxygenated products (benzene). Small amounts of niobium affected the surface area of the support and promoted the formation of smaller nickel particles, which disfavored the hydrogenolysis of benzene. As the amount of Nb increased, the surface area was negatively affected, while the formation of oxygen vacancy was favored, as observed in the XANES and XPS analysis. In situ XRD and Raman analysis indicated that the high niobium concentration leads to Nb_2O_5 oxide with hexagonal structure, while the XPS analysis indicated an enrichment of the surface by Nb. In general, the presence of Nb promoted the formation of Ni- Nb_2O_5 interface, providing a lower C−O bond scission barrier during the DDO route, which leads to an improvement in the benzene selectivity.

Keywords: Phenol; Bio-oil; Hydrodeoxygenation; cerium oxide; niobium addition; oxygen vacancy.

8.2. Introduction

The oxygen content in pyrolytic bio-oil is high up to 50%, which leads to undesirable properties, such as low energy density, thermal and chemical instability and lower calorific power [1]. The upgrading of bio-oil by hydrodeoxygenation (HDO) is a potential route to the final production of renewable fuels, since this process eliminates oxygen and stabilizes the product [2]. The HDO reaction may be perform in gas or liquid phase, however the liquid treatments have some disadvantages, such as, the consumption of solvent, the cost of high pressure equipment and the difficulties to separate catalyst, char, products, solvent and non-reacted lignin from the reaction media [3].

The bio-oil obtained from biomass pyrolysis is a complex mixture of reactive compounds. Phenolic compounds represent the major part of the lignin fraction of the bio-oil [4], which explains the use of these reagents as model compounds of the bio-oil [5]. In this work, the HDO reaction was studied in the gas phase using phenol as a model compound.

Several transition metals and their combinations have been studied in HDO reactions [6-9]. According to the literature, bifunctional catalysts containing a combination of support oxophilicity and an active metal phase is the most beneficial for this process [10]. The metal particles are responsible for hydrogenation/dehydrogenation reactions [11], while the activation of oxy-compounds is promoted by the valence of an oxide support [12].

The supports play an important role in the HDO reaction process, since it can improve the dispersion and stability of the active phase. de Souza et al. [6] investigated the effect of the type of support (SiO_2, Al_2O_3, TiO_2, ZrO_2, CeO_2 and $CeZrO_2$) on the performance of Pd-based catalysts for the hydrodeoxygenation of phenol at 500°C using a fixed bed reactor. Pd/TiO_2 and Pd/ZrO_2 favored the formation of benzene, while cyclohexanone was a major product over the other supports (Pd/SiO_2, Pd/Al_2O_3, Pd/CeO_2 and Pd/$CeZrO_2$). The high selectivity to benzene over Pd/TiO_2 and Pd/ZrO_2 catalysts was related to the oxophilic sites of these supports represented by low-coordinated Ti^{4+}/ Ti^{3+} and Zr^{4+}/Zr^{3+} cations near the periphery of metal particles. Although the Pd/CeO_2 and Pd/$CeZrO_2$ catalysts were poorly selective to deoxygenated products, these samples showed the best stability for the HDO reaction.

Over the past several years, CeO_2-containing materials have been intense studied as catalysts of heterogeneous reactions. The presence of cerium in the catalyst is justified by the possible improvement in the reaction activity and selectivity caused by the presence of the redox couple Ce^{4+}-Ce^{3+}. Schimming et al. [13] investigated the hydrodeoxygenation of guaiacol over bulk ceria and ceria–zirconia oxide with different elemental compositions. Ceria–zirconia catalysts without fully reduced metal particles are active for the studied reaction, benzene was formed as the completely deoxygenated product, but the final deoxygenation step is much slower than the hydrogenation. According to the authors Ce-oxide dissociates hydrogen and creates oxygen vacancy sites under mild conditions, which is a requirement for HDO catalysts. The presence of zirconium causes a slight strain in the ceria–zirconia crystal lattice and facilitates structural relaxation after the formation of an oxygen vacancy.

Several cerium mixed oxides Ce–M–O (with M = Eu, Pr, Sm, Nd) were recently investigated with the aim of improving oxygen mobility of this oxide [14]. The distortion of the O_2 sub lattices caused by the presence of another element in the mixed oxides permits a higher mobility of lattice oxygen. Thus, besides zirconium [15-17], another promoting metal can be added to the cerium oxides structure aiming to favors the HDO reaction, although so far there is no reports in the HDO reaction. Niobium is potential metal to be add to the cerium oxide, since this transition metal strongly favors the deoxygenation of phenolic compounds over HDO reaction conditions [8]. Similar system has been studying for another reaction [18-21]. In general, interactions among different components of mixed oxides strongly affect their structure and catalytic performance.

Therefore, this work aims to investigate the effects of Nb addition on the ceria structure and the effects on activity and selectivity over gas phase hydrogenation of phenol, using nickel as a metallic phase. The structural modification promoted by Nb addition in different environments was studied by in situ X-ray photoelectron spectroscopy (XPS), and in situ X-ray absorption spectroscopy (XAS) and X-ray diffraction (XRD) experiments.

8.3. Results and discussion

8.3.1. Nb-doped cerium oxides

Table 8.1 shows the metal loadings and the textural properties of the calcined oxides. The samples were calcined at 600°C during 6h. In general, the samples have different specific surface areas. $Ce_{0.90}Nb_{0.10}O_2$ exhibited the highest specific area, around 50 m^2g^{-1}. As the Nb concentration increased the BET area decreased, which also was observed by Stošić et al. [22].

Figure 8.1 shows the diffractograms obtained during calcination process of the precipitated oxides under air flow. For $Ce_{0.90}Nb_{0.10}O_2$ is noteworthy that the wet precipitate already displayed reflections of CeO_2, with fluorite structure. Similar results were observed by Chen et al. [23]. $Ce_{0.80}Nb_{0.20}O_2$ and $Ce_{0.30}Nb_{0.70}O_2$ are amorphous at room temperature and the presence of diffraction peaks started at 300°C and 400°C, respectively.

Table 8-1. Chemical composition determined by XRF and surface area of the calcined samples.

Samples	CeO_2 (%)	Nb_2O_5(%)	Ce/Nb	BET area (m^2 g^{-1})
$Ce_{0.30}Nb_{0.70}O_2$	16.4	83.4	0.4	17
$Ce_{0.80}Nb_{0.20}O_2$	68.7	30.5	5	30
$Ce_{0.90}Nb_{0.10}O_2$	86.5	13.4	15	51

The Ce-rich samples ($Ce_{0.80}Nb_{0.20}O_2$ and $Ce_{0.90}Nb_{0.10}O_2$) showed peaks related to CeO_2 below 600°C. For $Ce_{0.30}Nb_{0.70}O_2$ was observed only peaks relate to Nb_2O_5 at this temperature range. For all the samples the $CeNbO_{4-x}$ phase was observed up to 600°C, with x range of $0.0<x<0.25$ [24], which may be related to the composition of each sample.Thompson et al. [25] reported that the Nb-doped precipitated was readily oxidized to yield several different phases upon heating, depending on the heating regime, according to the Equation 8.1.

$$Ce^{3+}NbO_4 + x_{1/2}\,O_2 \rightarrow Ce^{3+}{}_{1-2x}\,Ce^{4+}{}_{2x}\,NbO_{4+x} \qquad \textbf{8.1}$$

The formation of $CeNbO_{4.08}$ phase was observed for $Ce_{0.90}Nb_{0.10}O_2$ at 900°C , while $Ce_{0.80}Nb_{0.20}O_2$ showed the presence of a less oxygenated structure, $CeNbO_4$. According to the Eq. 8.1, it indicates a higher concentration of Ce^{3+} in $Ce_{0.80}Nb_{0.20}O_2$ structure. A higher amount of niobium favored the formation of the structure $CeNb_5O_{14}$ on $Ce_{0.30}Nb_{0.70}O_2$ sample at high temperatures [26]. Figure 1S (Appendix IV) shows the diffractograms obtained during calcination process of the precipitated solid under inert atmosphere. According to Bayliss et al. [27] the single phase $CeNbO_4$ was only obtained by growth under argon, while the synthesis in air yielded $CeNbO_{4.08}$ as a minor phase. However, in this work, the atmosphere did not change significantly the final phase observed.

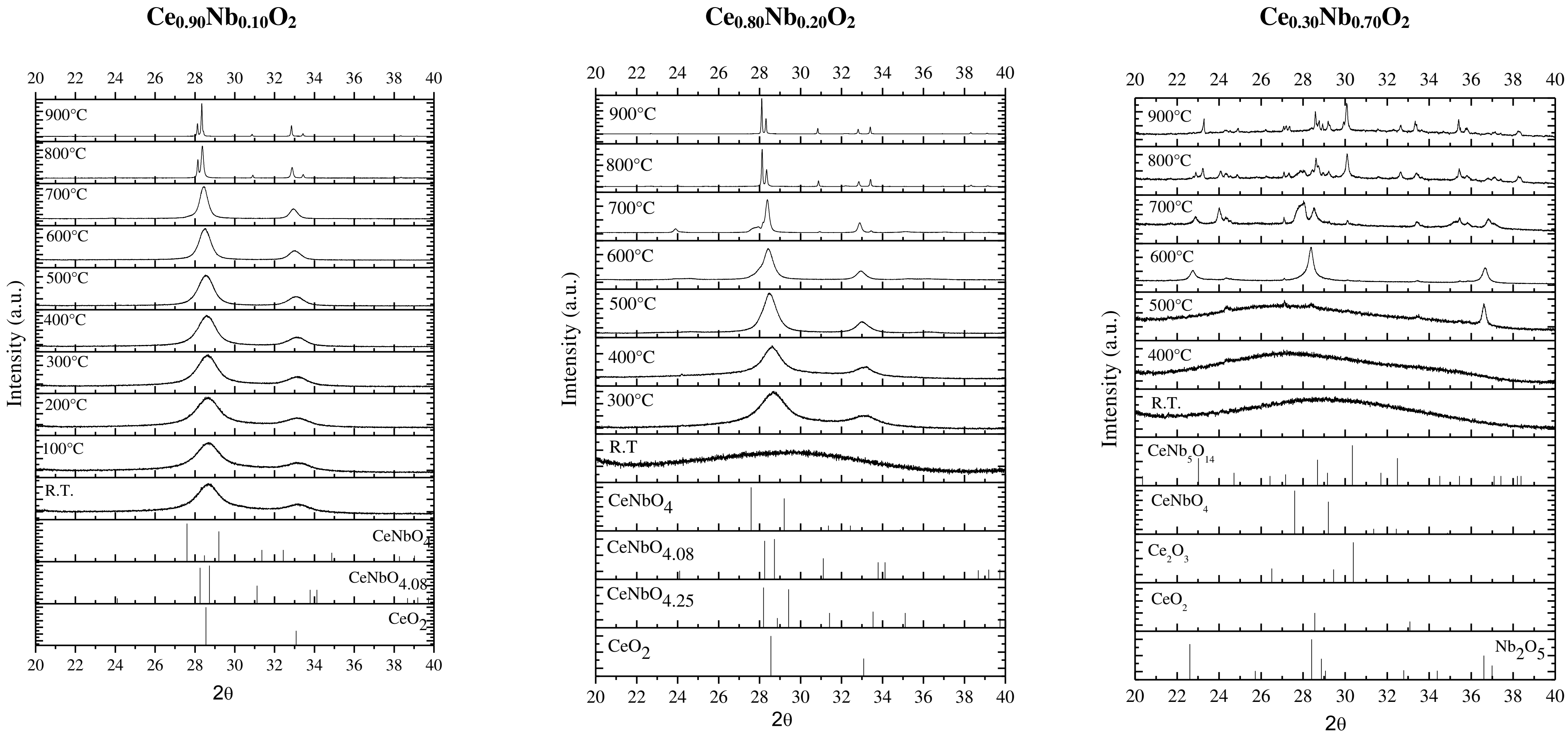

$Ce_{0.90}Nb_{0.10}O_2$ $Ce_{0.80}Nb_{0.20}O_2$ $Ce_{0.30}Nb_{0.70}O_2$

Figure 8-1. XRD diffractogram for in situ calcination of $Ce_{0.90}Nb_{0.10}O_2$, $Ce_{0.80}Nb_{0.20}O_2$ and $Ce_{0.30}Nb_{0.70}O_2$ at different temperatures in air oxidant atmosphere).

Following, the samples were calcined at 600°C, cooled down to room temperature. This calcination temperature was chosen to favor the formation of CeO_2 structure. Figure 8.2 showed the XRD profile of the calcineted samples at room temperature. For $Ce_{0.90}Nb_{0.10}O_2$ and $Ce_{0.80}Nb_{0.20}O_2$ only the diffraction peaks of CeO_2 with fluorite structure were observed. The literature showed other cases of metal-doped CeO_2 with similar results [15, 28, 29]. This may be an indication that the doped species were highly dispersed in CeO_2 [15]. For the sample doped with the highest amount of niobium, only peaks related to the Nb_2O_5 phase were observed. Fig. 8.2(b) shows a zoom in the range of $2\theta = 27.5$ and 30^o. A soft shift in the peak related to the CeO_2 structure ($2\theta \sim 28.70$) was observed for $Ce_{0.90}Nb_{0.10}O_2$ and $Ce_{0.80}Nb_{0.20}O_2$, however for $Ce_{0.30}Nb_{0.70}O_2$ the peak assigned to the Nb_2O_5 structure showed a significant shift to lower 2θ value (28.54) [15].

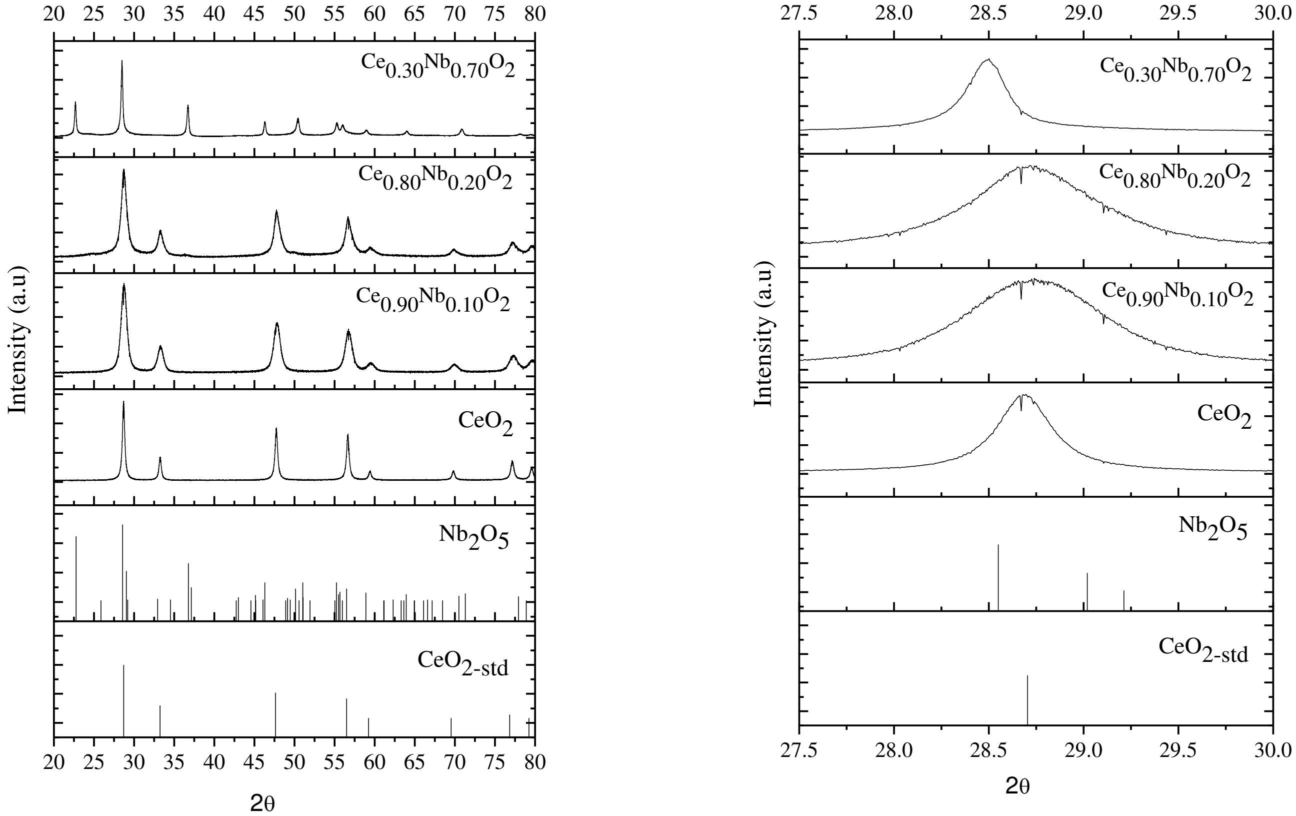

(A) **(B)**

Figure 8-2. XRD diffractogram for calcined: CeO_2, $Ce_{0.9}Nb_{0.1}O_2$, $Ce_{0.8}Nb_{0.2}O_2$ and $Ce_{0.30}Nb_{0.70}O_2$ at room temperature.

Raman spectra of the calcined oxides are shown in Figure 8.3. The Raman spectra of the niobium oxalate calcined at 500°C (Nb_2O_5) presented a band around 690 cm^{-1} due to NbO_6 octahedra [30-31]. According to Pittman and Bell [32] the presence of the orthorhombic or hexagonal Nb_2O_5 crystal phases gives rise to the Raman peak at 692cm^{-1}. For this sample a band at 230 cm^{-1} also was observed, which are characteristic of Nb-O-Nb bond [30, 31]. The Raman spectrum of $Ce_{0.30}Nb_{0.70}O_2$ showed a main band around 690 cm^{-1}, which is a confirmation that the NbO_6 octahedra structure prevails for this sample. This result is in good agreement with XRD analysis (Fig. 8.2).

The Raman spectra of the CeO_2 exhibited a band at 464 cm^{-1}, it is due to the Raman-active F_{2g} mode of CeO_2 [33]. Fluorite structure of CeO_2 have only a single allowed Raman mode, which has F_{2g} symmetry and can be viewed as a symmetric breathing mode of the O atoms around cerium [34]. The Raman spectrum of $Ce_{0.90}Nb_{0.10}O_2$ and $Ce_{0.80}Nb_{0.20}O_2$ oxides showed a main band around 464 cm^{-1}, as reposted before it is attributed to the F_{2g} vibration of the fluorite type lattice of the CeO_2 [29]. A small systematic shift in this Raman band to lower frequency was observed in all doped samples, which may be an indication of the incorporation of Nb in the ceria structure [34]. Vidal et al. observed [35] that the incorporation of Zr or Pr into the fluorite structure of CeO_2 induced a shift to lower frequency of the main band around 460 cm^{-1}.

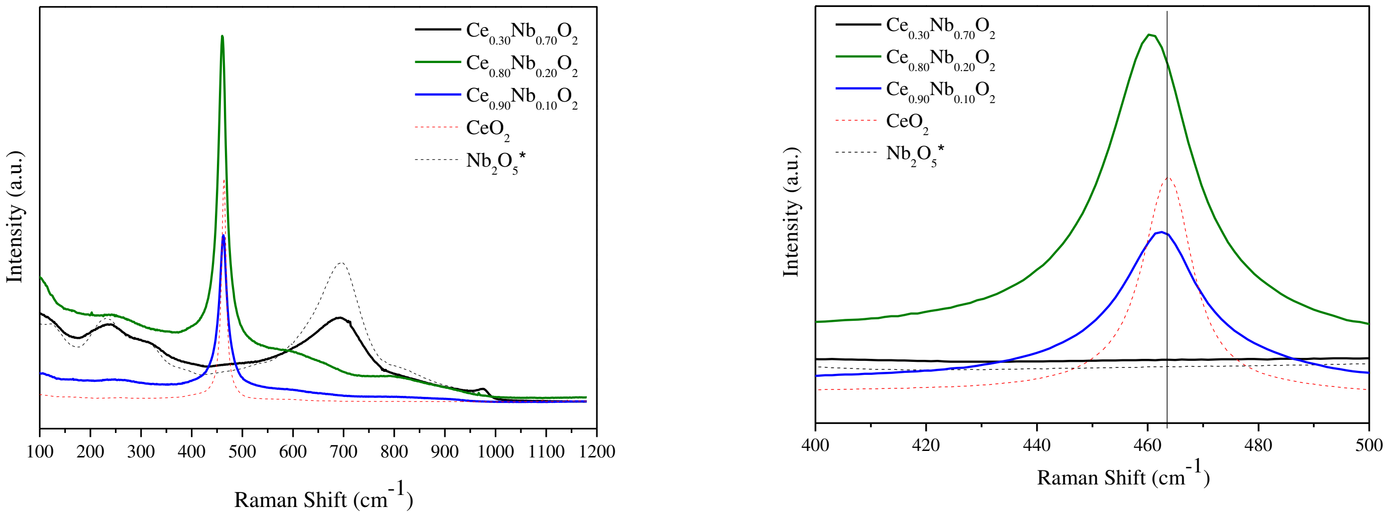

Figure 8-3. Raman spectra of CeO_2, $Ce_{0.90}Nb_{0.10}O_2$, $Ce_{0.80}Nb_{0.20}O_2$ and $Ce_{0.30}Nb_{0.70}O_2$. (* Nb oxalate calcined. 500°C)

8.3.2. Transmission Electron Microscopy (TEM)

The morphology of the calcined powder samples has been observed by TEM. Fig. 8.4 shows the representative TEM image of a cerium doped oxide, with the corresponding electron dispersive spectroscopy (EDS) and chemical mapping of the Nb and Ce for $Ce_{0.90}Nb_{0.10}O_2$ and $Ce_{0.80}Nb_{0.20}O_2$. The materials consisted of a highly porous substance formed of agglomerated crystalline particles. The chemical mapping of the $Ce_{0.90}Nb_{0.10}O_2$ sample shows that Nb and Ce have a similar distribution. This is an indication that there is not a segregation of the metals. For $Ce_{0.80}Nb_{0.20}O_2$ the presence of isolated and aggregated particles were observed.

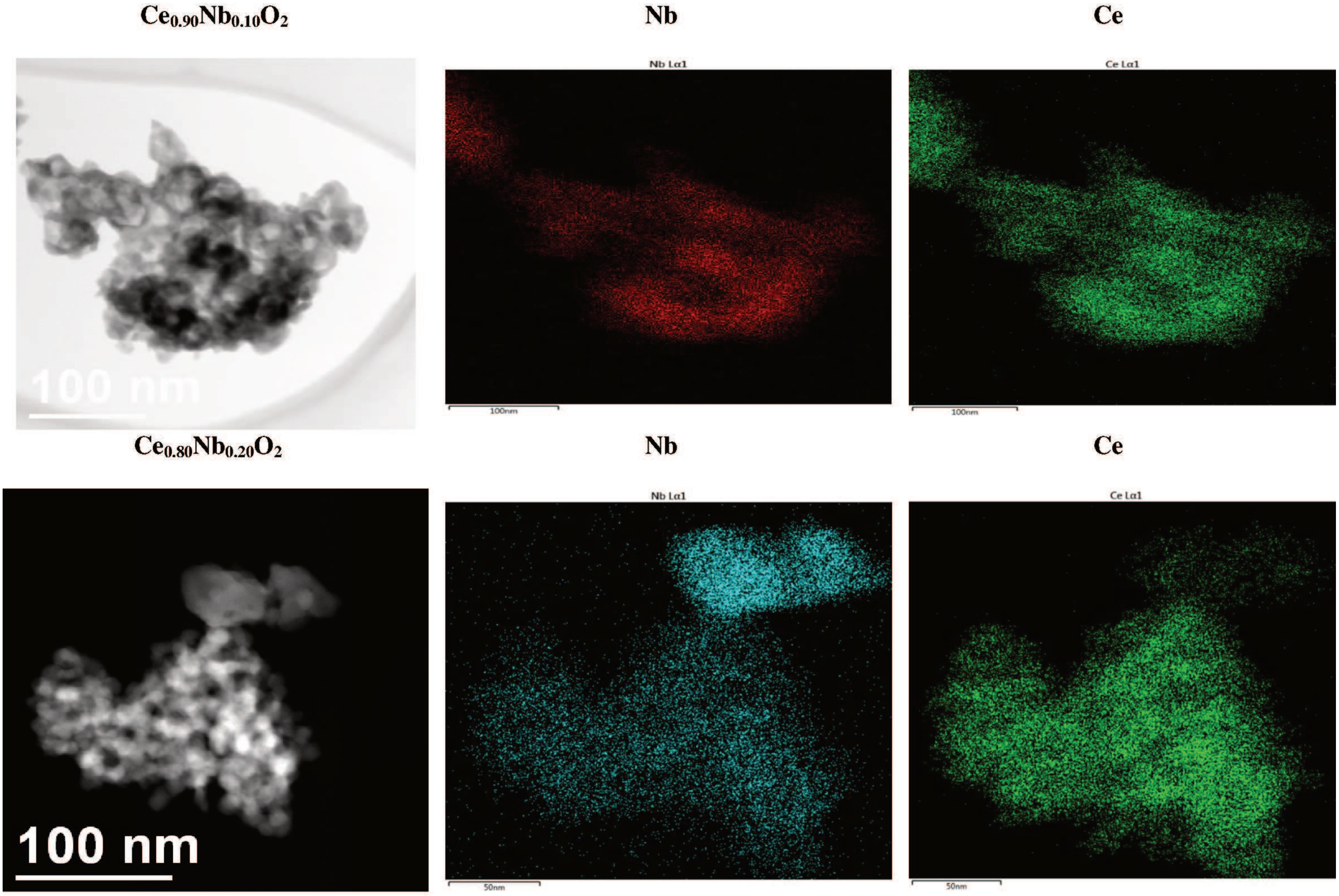
$Ce_{0.90}Nb_{0.10}O_2$ **Nb** **Ce**

$Ce_{0.80}Nb_{0.20}O_2$ **Nb** **Ce**

Figure 8-4- TEM/EDS analysis of $Ce_{0.90}Nb_{0.10}O_2$ and $Ce_{0.80}Nb_{0.20}O_2$

Fig. 8.5 shows the representative TEM image for $Ce_{0.30}Nb_{0.70}O_2$. TEM analysis showed a more organized and amourphous morphology for $Ce_{0.30}Nb_{0.70}O_2$ calcined powder samples, which is related to the Nb_2O_5 structure. The XRD analysis also indicated the presence of only peaks related to this structure. The electron dispersive spectroscopy (EDS) analysis and chemical mapping of the Nb and Ce indicated that Nb and Ce have a similar distribution.

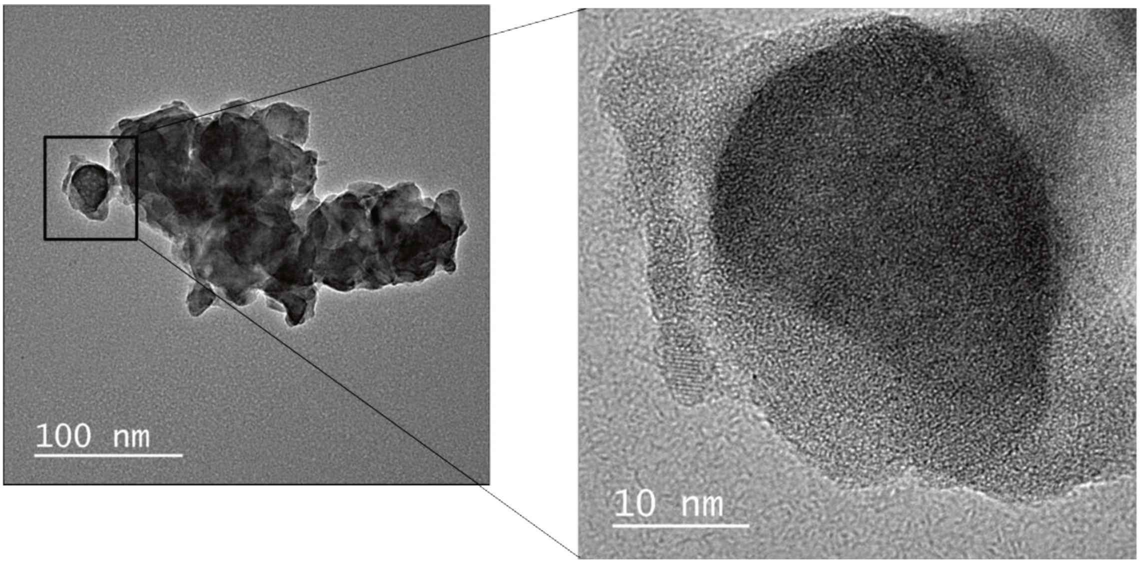

Figure 8-5- HR-TEM of calcined $Ce_{0.30}Nb_{0.70}O_2$

8.3.3. $Ni/Ce_xNb_{1-x}O_2$ catalysts

Table 8.2 shows the BET surface area of the supported Ni catalysts. The addition of nickel caused a slightly decrease in the surface area. The surface area values followed the values observed for the pure oxides. Fig. 8.6 shows the TPR profiles obtained for nickel-supported catalysts. All the samples showed a peak in the 300-500°C temperature range, which corresponds to the reduction of NiO [36]. For Ni/CeO_2, this peak is located at 340°C but it is shifted to higher temperature (380°C) as Nb is added to ceria. In general, low temperature peaks are attributed to the reduction of large NiO particles [37]. Ni/CeO_2 also showed a peak around 800°C, which is likely due to the partial reduction of Ce^{4+} to Ce^{3+} [38].

Table 8-2. BET surface area.

Samples	**BET area (m^2 g^{-1})**
Ni/$Ce_{0.30}Nb_{0.70}O_2$	15
Ni/$Ce_{0.80}Nb_{0.20}O_2$	28
Ni/$Ce_{0.90}Nb_{0.10}O_2$	44
Ni/CeO_2	20
Ni/Nb_2O_5	7

According to the literature [39], the TPR profile of CeO_2 generally exhibits two peaks. The first one at around 530°C is attributed to the surface reduction of CeO_2, and the second one at 950°C is related to the reduction of bulk ceria and the formation of Ce_2O_3. The addition of niobium to ceria led to the disappearance of the hydrogen consumption at high temperature and the presence of a shoulder at lower temperature (450 – 550°C). This shoulder may be related to the promotion of the cerium reduction caused by the presence of niobium. For Ni/Nb_2O_5 the peak between 300-500°C shift to higher temperatures values. This may be related to a strong Ni–niobium oxide interaction [40-41].

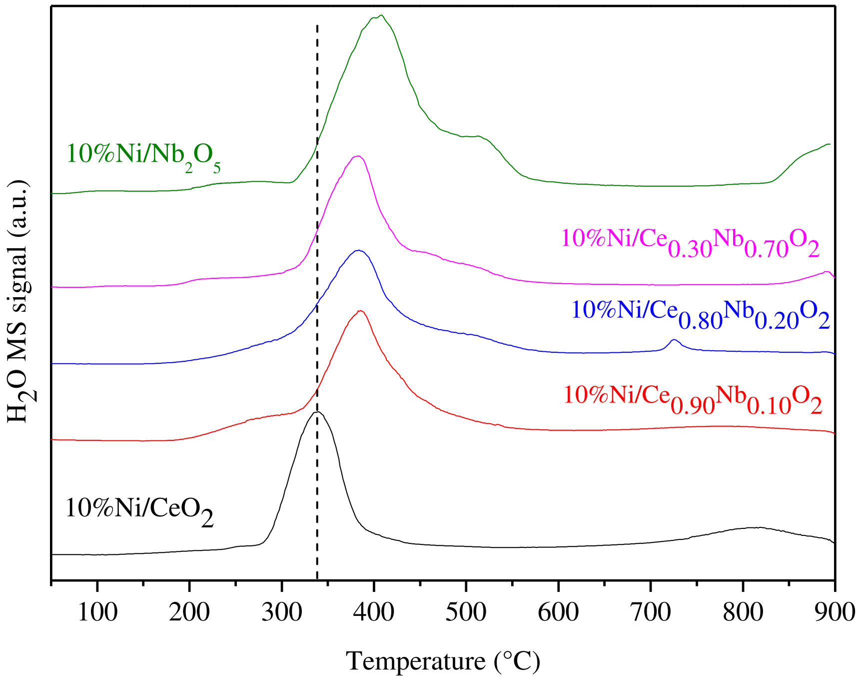

Figure 8-6. TPR profiles of Ni supported catalysts.

Figure 8.7 shows the XRD diffractograms of calcined Ni-supported samples. All the samples exhibit lines characteristic of NiO at 2θ = 37.31 and 43.37° at room temperature. For Ni/CeO_2, Ni/$Ce_{0.90}Nb_{0.10}O_2$ and Ni/ $Ce_{0.80}Nb_{0.20}O_2$, it is also observed the lines corresponding to CeO_2 with cubic structure (2θ = 28.69° and 47.73°), while lines related to Nb_2O_5 were only observed for Ni/$Ce_{0.30}Nb_{0.70}O_2$ and Ni/Nb_2O_5.

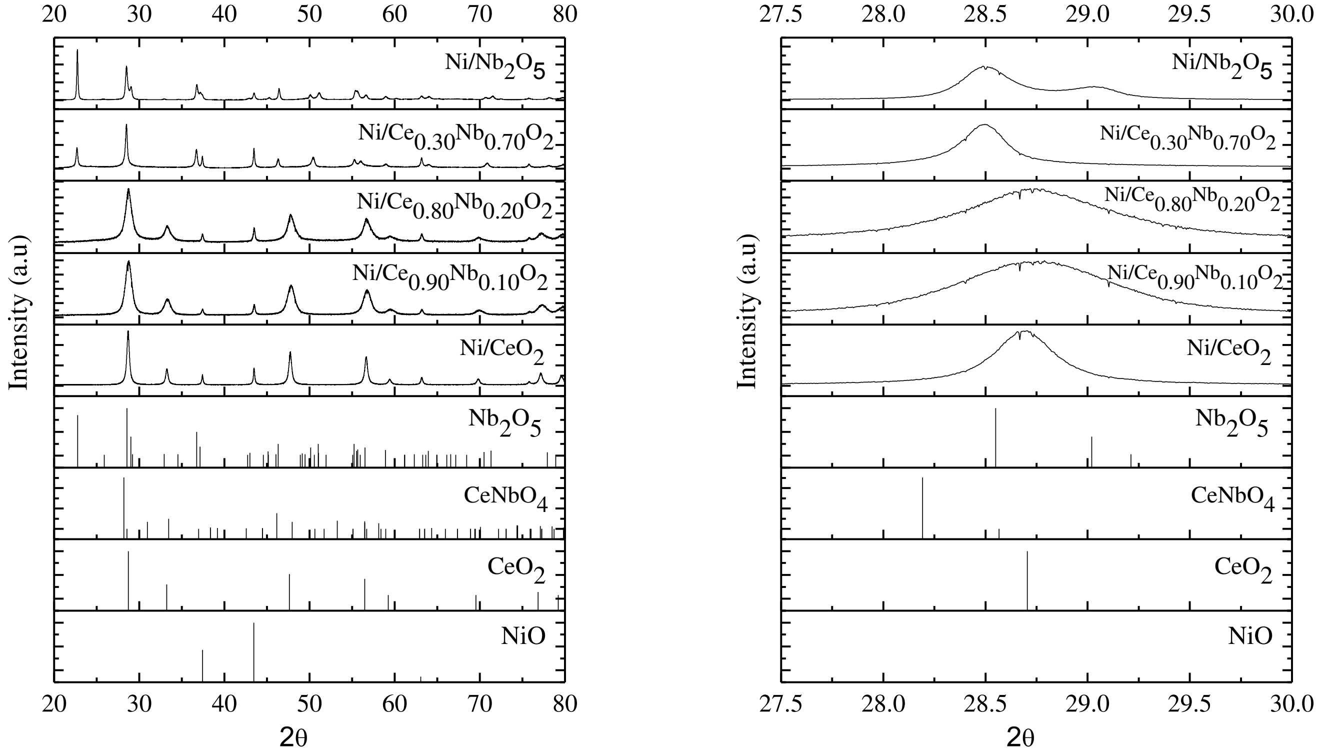

Figure 8-7. Diffractogram of Ni-supported calcined samples: (A) 2θ = 10 – 90°; (B) 2θ= 27.5 - 29.5°.

The lattice parameters of the catalysts powder from the XRD data were calculated using the UNITCELL software package [42-43]. For the calculation of the lattice parameters, as Ni/$Ce_{0.90}Nb_{0.10}O_2$ and Ni/$Ce_{0.80}Nb_{0.20}O_2$ showed only phases corresponding to CeO_2, the cubic structure was used. For Ni/$Ce_{0.30}Nb_{0.70}O_2$ the hexagonal structure was applied, since the main peaks observed in the diffractograms were related to Nb_2O_5 with hexagonal structure. The lattice parameter calculated for pure CeO_2 sample was a=5.412Å, which matches well with the lattice parameter of bulk Ni/CeO_2 reported on literature[44]. For Ni/$Ce_{0.90}Nb_{0.10}O_2$ and Ni/$Ce_{0.80}Nb_{0.20}O_2$ with cubic structure the values of the unit cell parameter decreased, which is in good agreement with effective ionic radii considerations (Ce^{4+}=0.96 A° and Nb^{5+} =0.7A°). In the case of the formation of a solid solution between CeO_2 and niobium, the niobium ionic radius will occupies the position of the larger Ce^{4+}, which may favor the decrease of the cell volume. Doping CeO_2 lattice with Nb will induce a uniform strain in the lattice as the material is elastically deformed. This effect causes the d-spacing to change and the diffraction peaks to shift to a new 2θ position, as observed in the XRD analysis. Similar results were observed by Aneggi et al. [45] that reported a cubic structure for $CeZrO_2$ with a smaller cell parameter than ceria, in agreement with the introduction of the smaller Zr^{4+} in the lattice. For Ni/$Ce_{0.30}Nb_{0.70}O_2$ with hexagonal structure mainly, the unit cell parameter a and c showed an increase compared to values observed for Nb_2O_5. As the ionic radii of cerium is larger than niobium, this may be an indication of addition of cerium in the crystal structure of niobium oxide.

Table 8-3. Refined crystallographic parameters in the Rietveld analysis of synchrotron X-ray powder diffraction data of doped oxide.

Sample	Structure	a	b	c	Cell Volume
Ni/CeO_2	Cubic	5.41213±0.00024	-	-	158. 5275±0.0209
Ni/$Ce_{0.90}Nb_{0.10}O_2$	Cubic	5.37689±0.00024	-	-	155.4507±0.0206
Ni/$Ce_{0.80}Nb_{0.20}O_2$	Cubic	5.38268±0.00024	-	-	155.9539±0.0207
Ni/$Ce_{0.30}Nb_{0.70}O_2$	Hexagonal	25.13184±0.00197	-	4.01152±0.00037	2194.2622±0.3791
Ni/Nb_2O5	Hexagonal	22.89501±0.00182	-	3.90883±0.00036	1774.4320±0.3257

In situ XRD measurements of the catalysts also were conducted under atmospheric pressure and reducing atmosphere. The diffractograms of the Ni-supported catalysts are presented in Figure 8.8. For Ni/CeO_2, the diffractograms remained unchanged when the sample was heated from 25 to 200 °C. At 300°C, the lines characteristic of NiO were no longer observed, whereas a new line corresponding to metallic Ni appears at 2θ=44.44°. Similar behavior was observed for Ni/$Ce_{0.90}Nb_{0.10}O_4$ and Ni/$Ce_{0.80}Nb_{0.20}O_4$. However, besides the nickel reduction, for Ni/ $Ce_{0.80}Nb_{0.20}O_4$ after 1h at 500°C the presence of peaks relates to Ce_2O_3 around 2θ=31.02° also was observed, which indicates reduction of Ce^{4+} to Ce^{3+}. This may be an indication that the presence of niobium favors the reduction of cerium oxide, as indicated by the TPR analysis. For Ni/$Ce_{0.30}Nb_{0.70}O_4$ and Ni/ Nb_2O_5 the reduction of nickel was also observed around 300°C, however, the structure of support remains unchanged, with the profiles showing hexagonal Nb_2O_5 structure with peaks at $2\theta=22.68$ and 28.487 (JCPDS- 7-61).

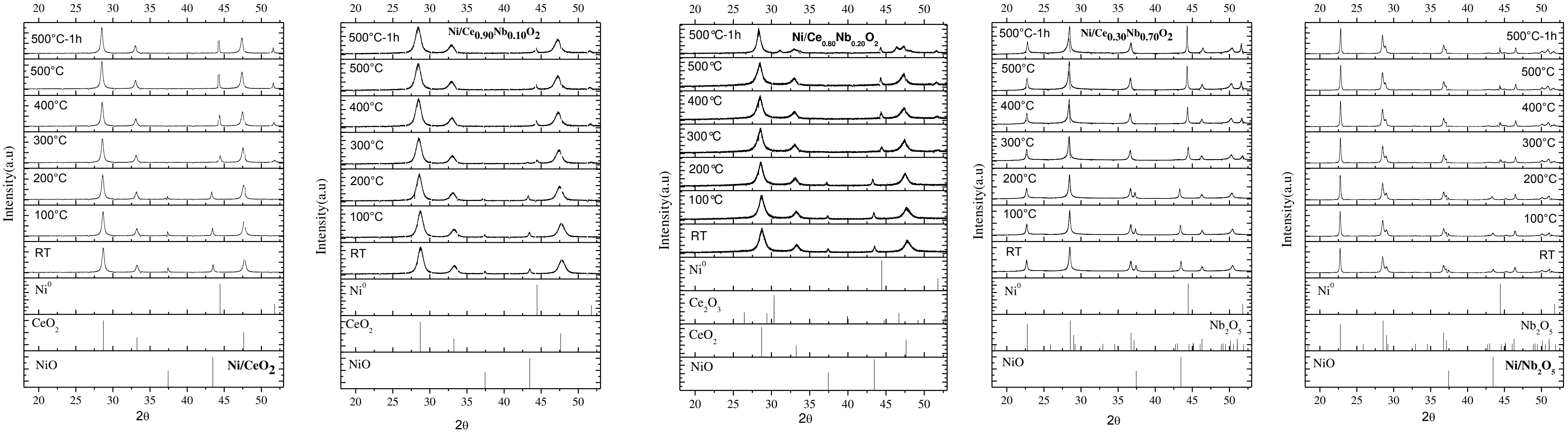

Figure 8-8. XRD diffractogram for in situ reduction of Ni impregnated CeO_2, $Ce_{0.9}Nb_{0.1}O_2$, $Ce_{0.8}Nb_{0.2}O_2$, $Ce_{0.30}Nb_{0.70}O_2$ and Nb_2O_5 at different temperatures.

Table 8.4 presents the particle size of the metallic nickel and cerium oxide estimated based on Scherrer Equation. In general, the addition of Nb decreased the crystallite sizes of ceria, which is in agreement with the absence of CeO_2 crystallographic peaks for $Ni/Ce_{0.3}Nb_{0.7}O_2$ in the XRD analysis.. The Ni crystallite size increased during reduction from an initial value of 30nm to final values around 60 nm for Ni/CeO_2, $Ni/Ce_{0.8}Nb_{0.2}O_2$, $Ni/Ce_{0.3}Nb_{0.7}O_2$ and Ni/Nb_2O_5. However, for $Ni/Ce_{0.9}Nb_{0.1}O_2$ smaller NiO particles (around 23nm) were observed and the sintering process did not happen during the reduction of this sample. According to Richardson et al. [46] nickel clusters rapidly agglomerate into metallic nickel crystallites due to the small distances between NiO crystallites in bulk NiO. Thus, as $Ni/Ce_{0.9}Nb_{0.1}O_2$ has a more disperse NiO oxide, which may hinders the agglomeration of the nickel nanoparticles during the reduction.

Table 8-4. Ni^0 and CeO_2 particle size estimation based on Scherrer Equation.

Temp (°C)	**Ni^0 particle size (nm)**				
	Ni/CeO_2	**$Ni/Ce_{0.9}Nb_{0.1}O_2$**	**$Ni/Ce_{0.8}Nb_{0.2}O_2$**	**$Ni/Ce_{0.3}Nb_{0.7}O_2$**	**Ni/Nb_2O_5**
RT*	38	28	30	38	31
300	33	22	29	37	36.
400	46	23	33	45	33
500	57	23	44	53	51
500-1h	60	23	47	61	57
	CeO_2 particle size (nm)				
R.T	21	9	10	-	-
500-1h	22	9	8	-	-

*NiO oxide particle size

XPS technique provided information about the oxidation states for all elements on the surface as well as their surface concentration. The XP spectra of $Ni2p_{3/2}$, Nb3d, and Ce3d core electron levels for the calcined samples and after reduction at 500°C are shown in Fig. 8.9 [47]. The Ni 2p spectra for all the calcined catalysts show the main peak with two clearly visible components, one at lower BE values, c.a. 853-854 eV, related to Ni^{2+} with octahedral coordination (O_h) and another at higher BE values of 854-855 eV, which can be assigned to low-coordination Ni^{2+} cations [47-48]. For Nb3d the binding energy values reported in the literature [49] for the different niobium oxidation states at Nb3d5/2 bands were: 202.0 eV for metallic niobium, 204.4 eV for NbO, 206.4 eV for NbO_2, and 207.9 eV for Nb_2O_5. For $Ni/Ce_{0.90}Nb_{0.10}O_2$ and $Ni/Ce_{0.80}Nb_{0.20}O_2$ two Nb species were identified. These species correspond to Nb^{4+} and Nb^{5+} with Nb 3d5/2 binding energy around 206.1 and 207.2 eV, respectively. According to You et al. [19], Nb^{4+} in the $NbOx/CeO_2$ catalysts should be formed by the redox reaction between Ce^{3+} (oxygen vacancy) and Nb^{5+} on the CeO_2 surface. For the sample with the highest amount of Nb the presence of Nb^{4+} was not observed, because higher Nb content favored the formation of Nb^{5+} [19]. The Ce 3d spectra is composed by two multiplets (v and u). These multiplets correspond to the spin-orbit split of $3d_{5/2}$ and $3d_{3/2}$ core holes. The u''' is the most representative peak of Ce^{4+} state [50], while v' and u' lines indicate the presence of Ce^{3+} ions. $Ni/Ce_{0.90}Nb_{0.10}O_2$, $Ni/Ce_{0.80}Nb_{0.20}O_2$ and Ni/CeO_2 calcined showed mainly Ce^{4+} on the surface, while no cerium was observed over $Ni/Ce_{0.3}Nb_{0.7}O_2$ surface.

The Ni 2p3/2 core level spectra of catalysts after reduction process (at 500°C for 1h) showed binding energies characteristic of Ni^0 and Ni^{2+} (B.E. = 852.2 eV and 855 eV, respectively). It was clear that none of the samples were completely reduced after the reduction protocol applied [51]. This absence of full reduction may be caused by the use of diluted hydrogen flow in this analysis, and can also be related to strong metal-support interaction, in which a partial reduction of the support oxide and of the NiO clusters can lead to a recovering by the support in some degree. $Ni/Ce_{0.90}Nb_{0.10}O_2$ showed the lowest intensity for the Ni^0 peak, which may be related to small Ni particles observed for this sample. Smaller nickel particles have a stronger interaction with the support, therefore the Ni particles become less reducible [37]. After the reduction, the position of the Nb3d peaks shifted to lower B.E, as the amount of Nb decreased. This shift is highlighted by dash line in the Figure 8.7, which is an indication that the surface niobium was reduced to NbOx during the reduction treatment. After the pre-treatment at 500°C for 1h in diluted H_2 all the samples showed the reduction of Ce^{4+} to Ce^{3+}, which is in agreement with the XRD and TPR analysis. According to the intensity of the peak u''' the reduction degree decreased in the following order: $Ni/Ce_{0.30}Nb_{0.70}O_2$ > $Ni/ Ce_{0.8}Nb_{0.2}O_2$ > $Ni/ Ce_{0.9}Nb_{0.1}O_2$ > Ni/CeO_2. For $Ni/ Ce_{0.30}Nb_{0.70}O_2$ only Ce^{3+} was observed in its surface.

Before reduction

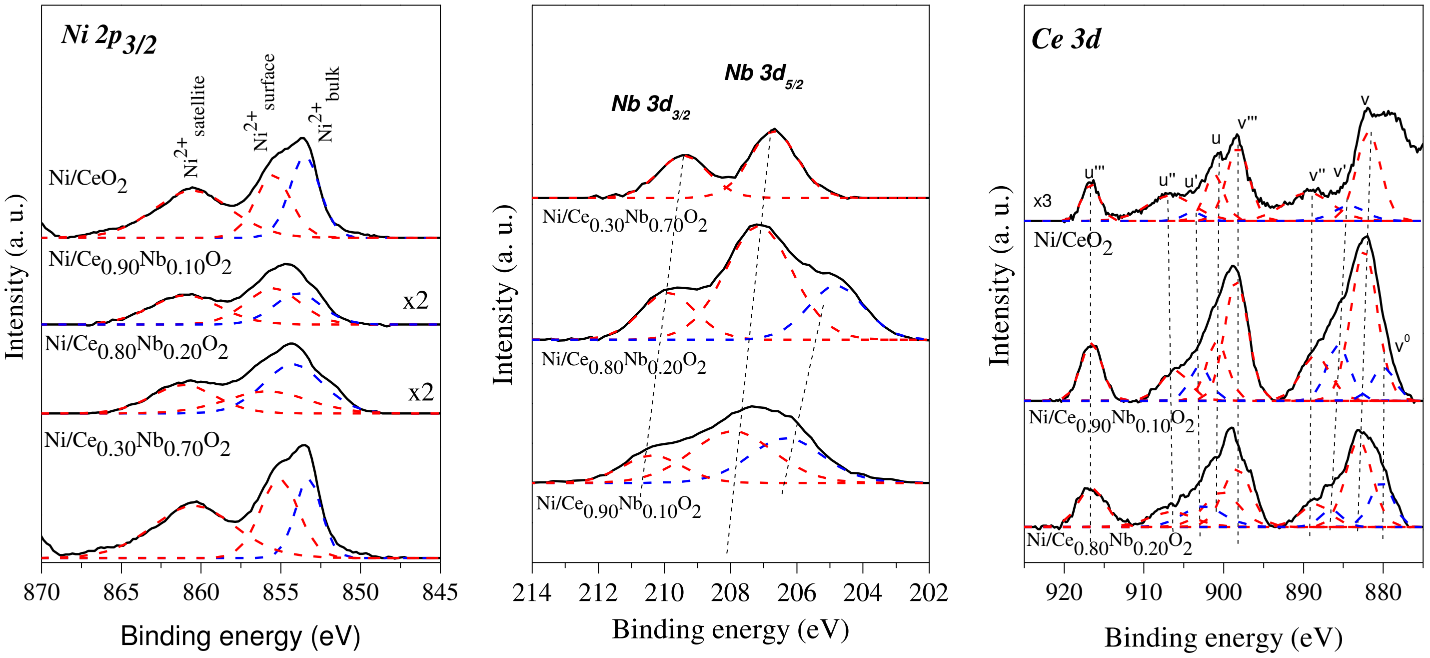

After reduction

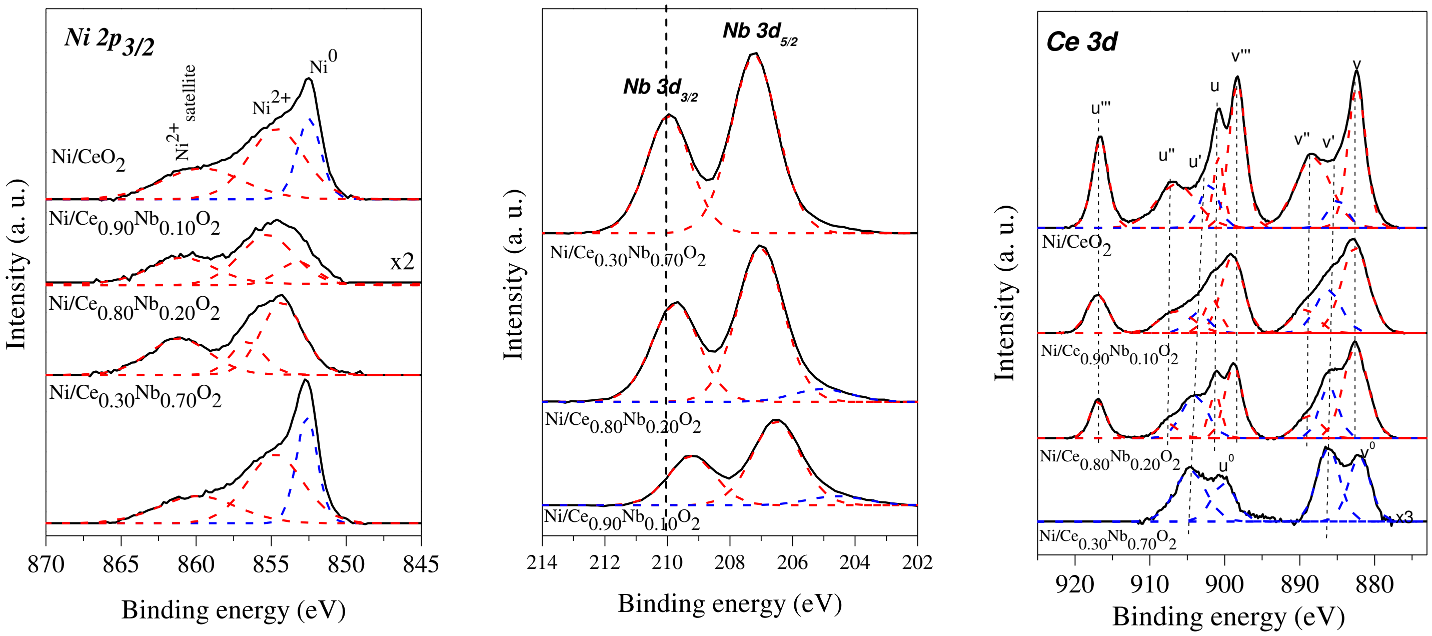

Figure 8-9. XP spectra of the Ni-supported catalysts before and after reduction in diluted H_2 at 500°C.

Table 8.5 lists the surface composition derived from the XPS analyses. The ratio of Ni_{surf}/Ni_{bulk} was calculated based on Pedra et al. [47]. The surface Ce/Nb ratios indicated that the addition of niobium decreased the concentration of surface cerium oxide species on calcined samples. After reduction treatment, almost all the catalysts showed a strong decrease in the intensity of the Ni 2p3/2 core level, which decreases the surface exposition of metallic Ni. This decrease may be an indicative of sintering phenomena of nickel particles during the reduction process and/or coverage of metallic particles by the support. Surface exposition of metallic nickel decreases in the order: Ni/CeO_2> $Ni/Ce_{0.30}Nb_{0.70}O_2$>~ Ni/ $Ce_{0.9}Nb_{0.1}O_2$ > Ni/ $Ce_{0.8}Nb_{0.2}O_2$. The presence of Nb promoted the formation of oxygen vacancy on the catalysts surface, which was confirmed by an increase in $Ce^{3+}/(Ce_{total})$ rate. The followed order of Ce^{3+} concentration was observed: Ni/CeO_2< Ni/ $Ce_{0.9}Nb_{0.1}O_2$ < Ni/ $Ce_{0.8}Nb_{0.2}O_2$ < $Ni/Ce_{0.30}Nb_{0.70}O_2$. For $Ni/Ce_{0.30}Nb_{0.70}O_2$ the niobium concentration over the surface increased after the reduction.

Table 8-5. Surface composition (at %) derived from the XPS analyses

	Surface Composition							
	Calcined				**Ratios**			
	Ni	**Ce**	**Nb**	**O**	**Ce3d/Nb3d**	**Nb/Ce+Nb+Ni**	**Ni/support**	
Ni/CeO_2	36.43	8.58	-	63.57	1	-	3.24	
Ni/ $Ce_{0.9}Nb_{0.10}O_2$	19.34	11.91	22.43	58.24	0.53	0.53	0.19	
Ni/ $Ce_{0.8}Nb_{0.20}O_2$	7.17	7.61	29.34	55.87	0.26	0.66	0.07	
$Ni/Ce_{0.30}Nb_{0.70}O_2$	29.64	0	8.57	61.79	0.0	0.22	3.45	
	After reduction				**Ratios**			
	Ni	**Ce**	**Nb**	**O**	**$Ce^{3+}/(Ce_T)$**	**Nb/Ce+Nb+Ni**	**Ni/support**	**$Ce^{3+}/(Ce_T+Nb_T)$**
Ni/CeO_2	9.5	34.2	-	55.3	0.11	-	0.27	-
$Ni/Ce_{0.90}Nb_{0.10}O_2$	2.53	18.5	26.59	52.37	0.17	0.55	0.02	0.03
$Ni/Ce_{0.80}Nb_{0.20}O_2$	5.1	14.45	21.22	59.2	0.27	0.52	0.05	0.04
$Ni/Ce_{0.30}Nb_{0.70}O_2$	6.3	3.3	44.2	46.3	1.00	0.82	0.13	0.04

8.3.4. XAS analysis

8.3.3.1. In-situ XANES spectra at Nb K-edge

Aiming to evaluate the oxidation state of Nb before and after the reduction process at different temperatures, TPR-XANES analysis was performed. Snapshots of XANES spectra at the initial and final stages of reduction are provided in Fig. 8.10. The XANES spectra were quite similar for all calcined and reduced samples: a pre-edge absorption and two peaks in the post-edge region. The pre-edge absorption feature was observed around 18996 eV, which is related to, in part, an electronic transition from the Nb 1s-orbital to the 5p orbital [52]. The two features located at around 19005 and 19017 eV reflect the low-energy scattering resonances of photoelectrons by neighboring atoms [53]. Figure 8.11 presents a comparison of the XANES spectrum in the Nb k-edge for all the samples after the reduction at 500°C for 1h. According to the literature [53-54] the XANES spectra of niobium oxides significantly differ from Nb metal.

The Nb spectra is shifted toward higher energies with an order of the increase in valence values. Cartier et al. [54] showed that niobium threshold energy E_0 is shifted from 18986 eV (Nb^0) to 19006 eV (Nb^{5+}) as Nb formal valence increases. Fig. 8.11 reveals a shift in the first derivative peak at 19013 eV for Ni/Nb_2O_5 to lower photon energy as the Nb content decreased. In addition, it is also observed the appearance of a small peak around 18986 eV. These results indicate the reduction of Nb^{5+} species to a lower oxidation state, which is good agreement with XPS data for reduced samples.

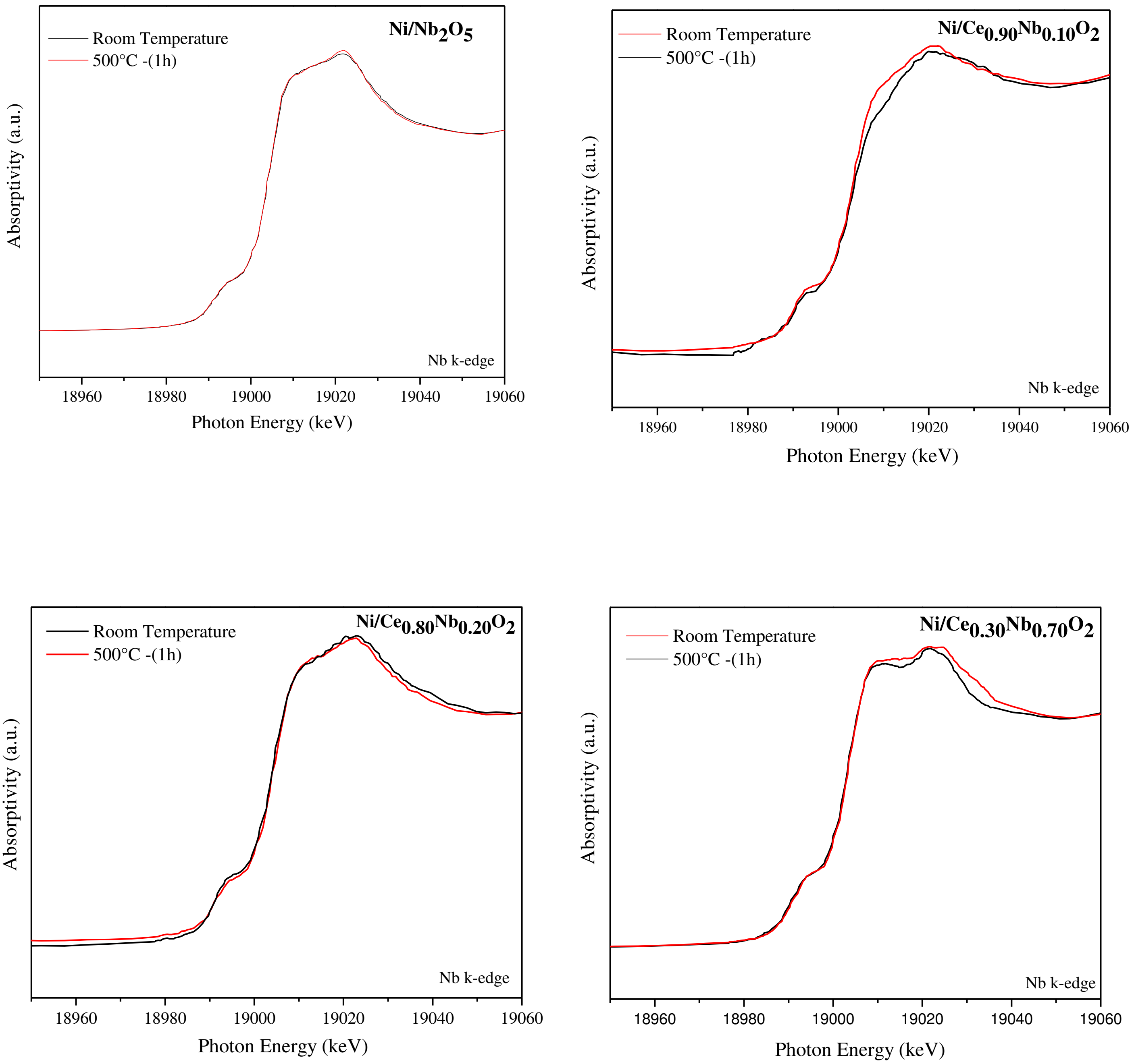

Figure 8-10. Snapshots of XANES profiles at the Nb K-edge at (black) ~Room temperature; (red line) ~500°C complete reduction of (above right).

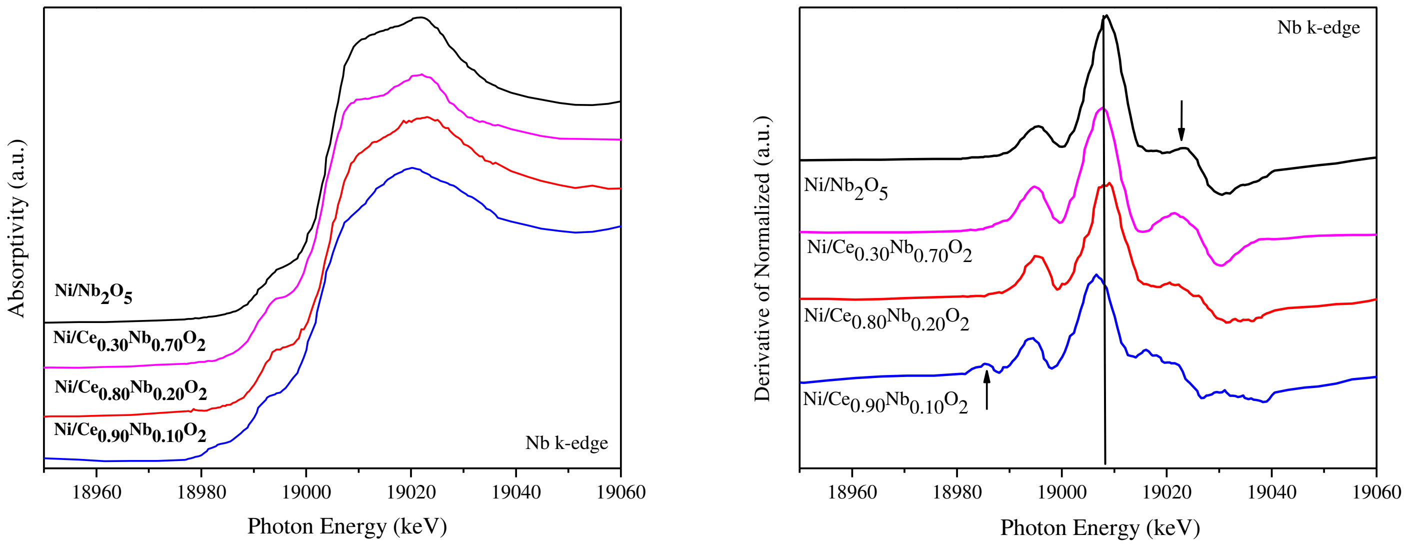

Figure 8-11. Comparation of the Snapshots of normalized Nb K-edge XANES profiles and first differential Nb K-edge XANES at the Nb K-edge at~500°C complete reduction.

8.3.3.2. In-situ XANES spectra at Ce LIII-edge

Fig. 8.12 shows the in situ XANES spectra at Ce L_{III}-edge and the corresponding linear combination fittings of these spectra during reduction of the catalysts. CeO_2 standard and $Ce(NO_3)_3$ spectrums were used as references for the linear combination fittings. At room temperature, all samples showed two peaks (5728.3 and 5735.3 eV) [55], which are related to Ce^{4+} species (Fig. 8.12). These peaks correspond to absorption into the 5d level with no occupancy in the 4f level in either the initial or final state [56]. During reduction, a new peak appears at 5717.8 eV that is associated with 4f occupancy in the initial state. This peak is an indicative of the presence of Ce^{3+} in the sample [57]. The concentration of the Ce^{3+} in the sample is related to the amount of Nb added to the catalyst. Figure 8.14 showed a comparison among the samples before and after the reduction process.

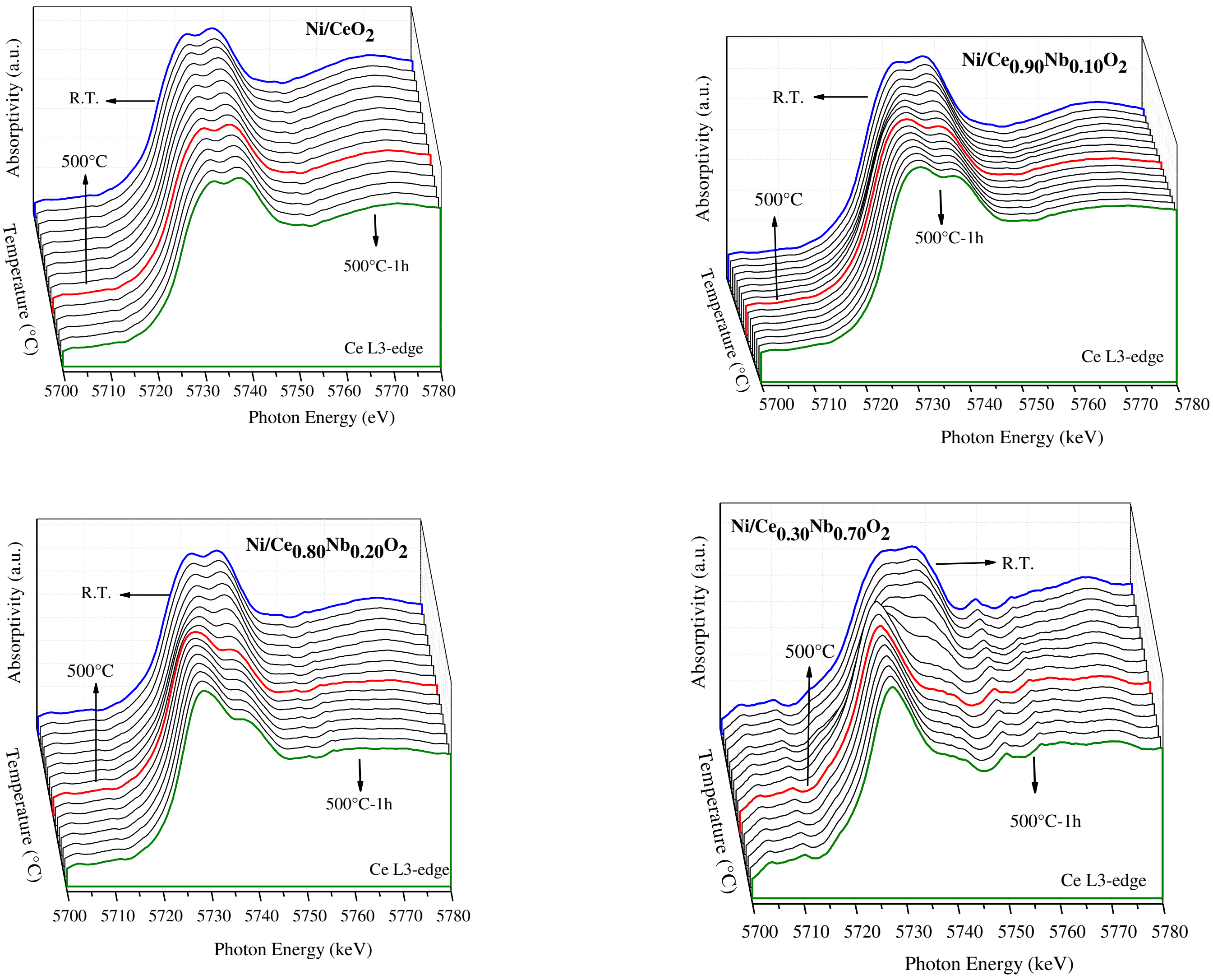

Figure 8-12. TPR- XANES profiles at the Ce L3-edge for the studied samples.

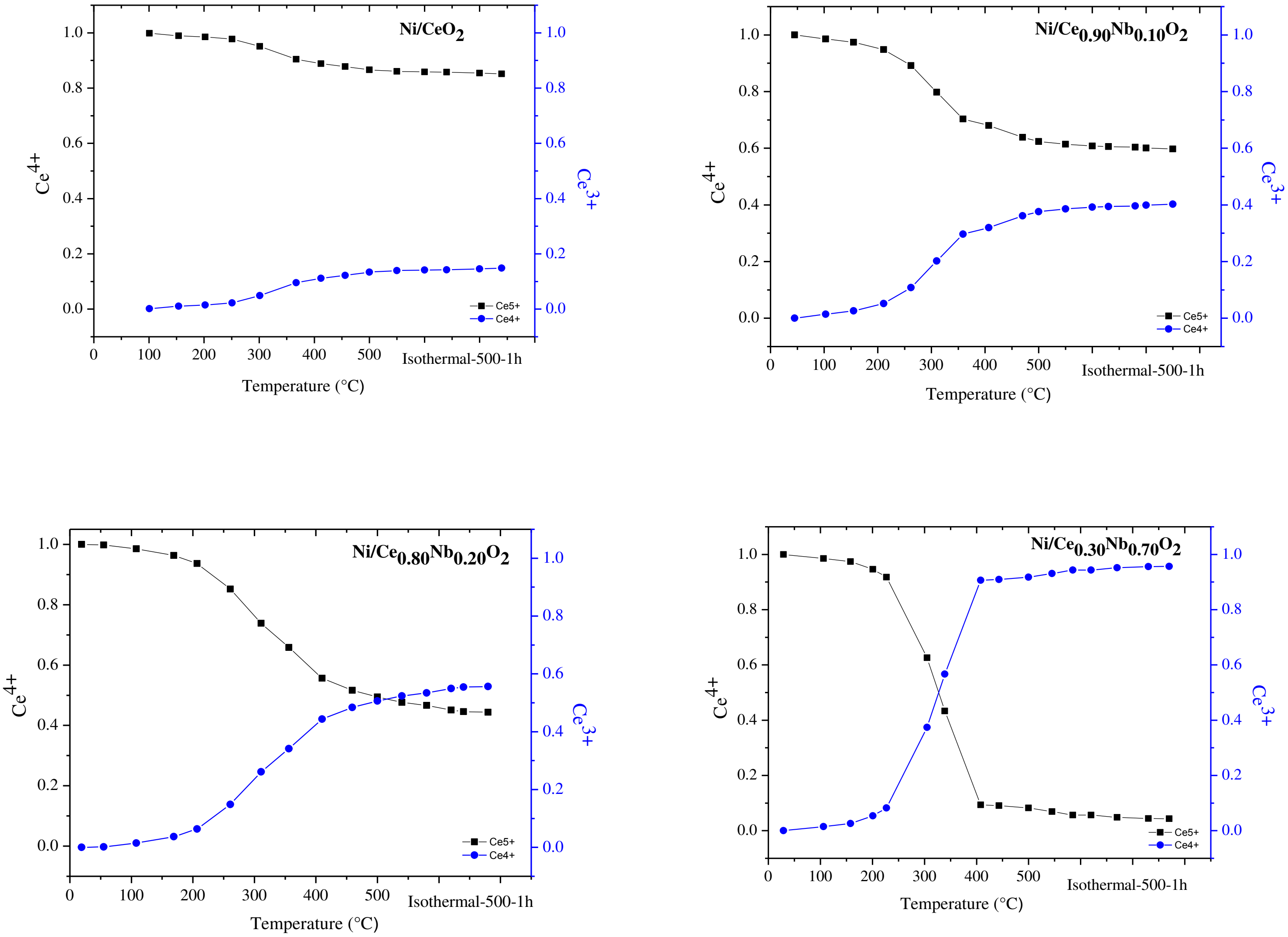

Figure 8-13- Linear combination fittings of TPR-XANES profiles at the Ce L3-edge for the studied samples.

For Ni/CeO$_2$ catalyst, the reduction of Ce^{4+} to Ce^{3+} species started at 250°C. The beginning of ceria reduction began at lower temperature for Ni/Ce$_{0.90}$Nb$_{0.10}$O$_2$ catalyst (200°C). Furthermore, a higher fraction of Ce^{3+} species was obtained in this catalyst after reduction at 500°C. Increasing the Nb content facilitates the reduction temperature of Ce^{4+} to Ce $^{3+}$, by increasing the amount of Ce^{3+} formed and decreasing the temperature of reduction. The following reduction order was observed: Ni/Ce$_{0.30}$Nb$_{0.70}$O$_2$ > Ni/ Ce$_{0.80}$Nb$_{0.20}$O$_2$ >Ni/ Ce$_{0.90}$Nb$_{0.10}$O$_2$ > Ni/CeO$_2$. The addition of Zr to ceria also lowered the temperature of reduction and increased the extent of Ce reduction [57]. This was attributed to the incorporation of zirconia into the ceria lattice.

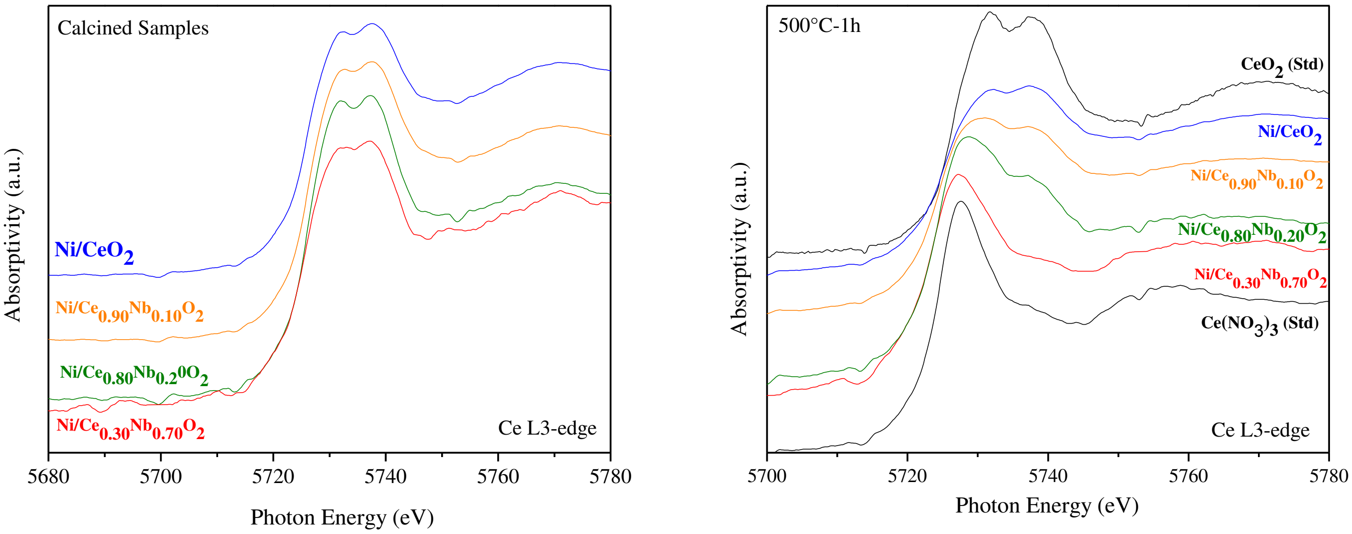

Figure 8-14. Comparison of the Snapshots of normalized Ce L3-edge XANES spectra before and after the reduction at 500°C.

8.3.3.3. In-situ XANES and EXAFS spectra at Ni K-edge

In situ XANES spectra at Ni K-edge and the corresponding linear combination fittings of these spectra during reduction of the catalysts are shown in Fig. 8.15. The initial spectrum of the oxidized catalyst and the Ni foil were used as references for the linear combination fittings. The Ni-K edge XANES spectra for the calcined samples correspond to the presence of NiO [58]. The intensity of the white line decreased as the reduction temperature increased up to 500°C, which suggests the progressive reduction of NiO to metallic Ni. There were no significant changes on XANES spectra during reduction for 1 h. Fig. 8.15 also shows the changes in the Ni species during reduction for all catalysts. The NiO to Ni^o reduction starts at 280°C for Ni/CeO_2 and this temperature increased as the Nb content increased, indicating that NiO reducibility slightly decreased when Nb was added to ceria. At 500°C, complete reduction of NiO was observed for all catalysts.

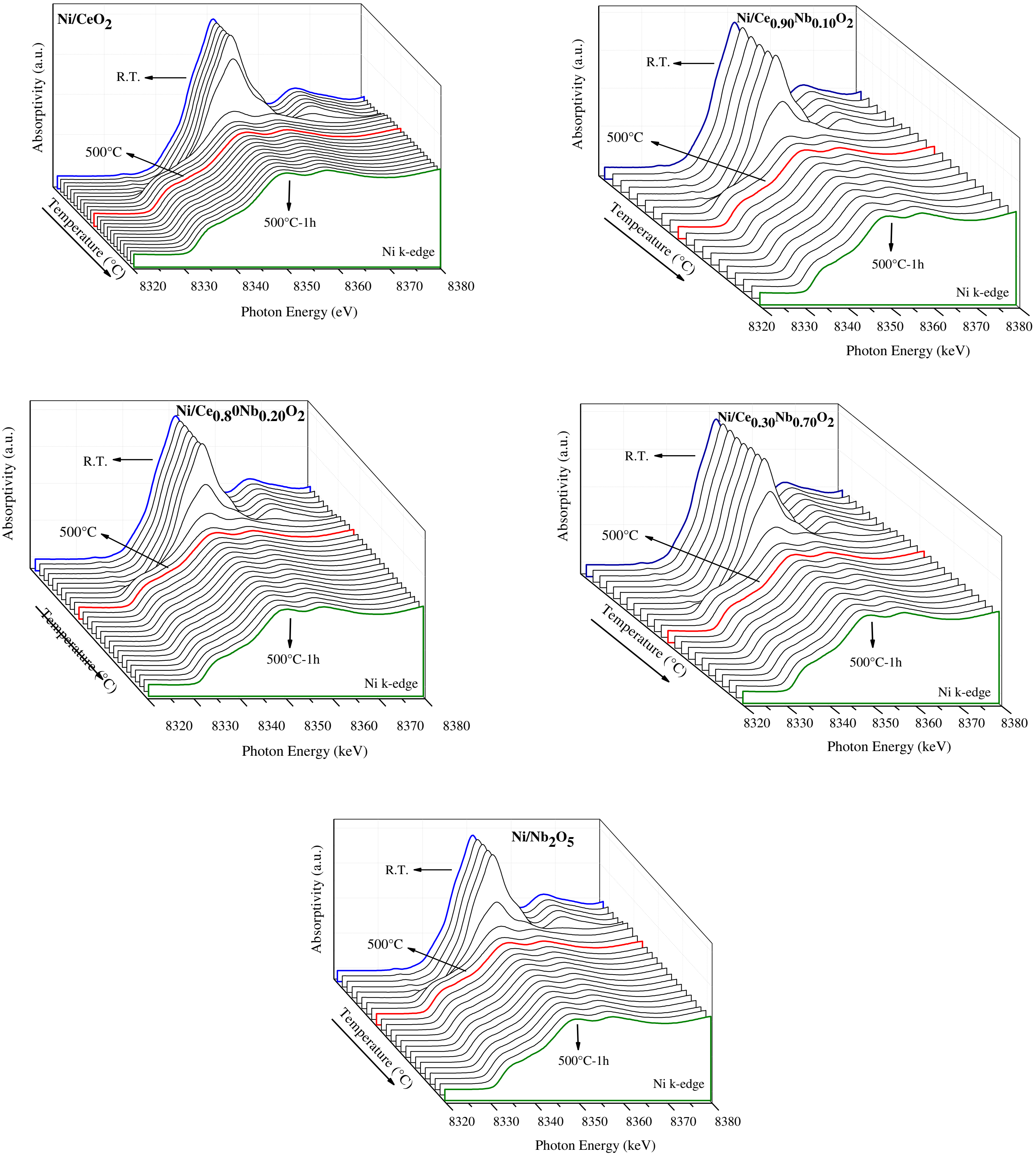

Figure 8-15. Comparation of the Snapshots of normalized Ni K-edge XANES profiles before and after the reduction at~500°C.

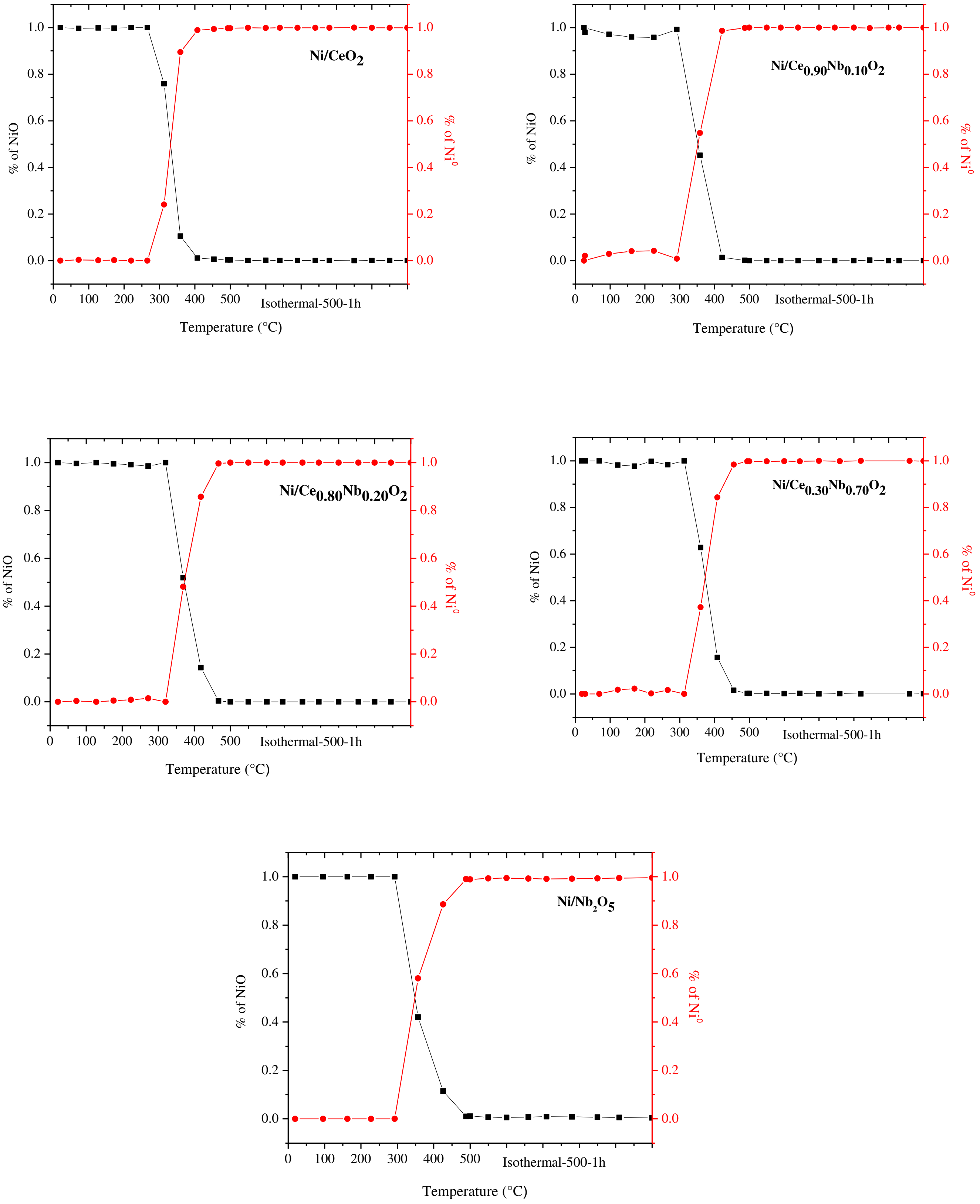

Figure 8-16- Linear combination fittings of TPR-XANES profiles at the Ni K-edge for the studied samples.

Snapshots of EXAFS spectra at the initial and final stages of reduction are provided in Fig. 8.17. The initial spectra (spectrum of calcined sample) are dominated by the Ni-O bond. For all the samples, the EXAFS spectra following reduction at ~500°C are dominated by a single peak located between 2 and 2.5 angstroms in the phase-uncorrected Fourier transform magnitude spectra, which can be assigned to the first Ni-Ni shell. XRD in situ data also indicated the presence of Ni metallic after reduction at 500°C for 1h .

The raw k^2-weighted $\chi(k)$ spectra (solid black line) filtered and (red filled circles) fitted k^2-weighted $\chi(k)$ spectra of the reduced catalysts are shown in Fig. 8.18. According to these pictures there are not differences in the spectra of the doped oxide compared with Ni/CeO_2 and Ni/Nb_2O_5.

EXAFS fitting parameters of all catalysts, as well as for the Ni foil reference are given in Table 8.6. The goodness of fit parameter was less than 0.009, indicating a good fit. The coordination number of the first Ni-Ni shell for all the samples determined by curve-fitting was around 12. This result agrees very well with the Ni^o crystallite size determined by in situ XRD (Table 8.4). Also, all the samples had similar Ni-Ni distance, around 2.48Å. The Debye-Waller factors for the samples are a little higher for the Ni particles obtained after reduction than for Ni foil, which can be related with a slightly more disordered structure.

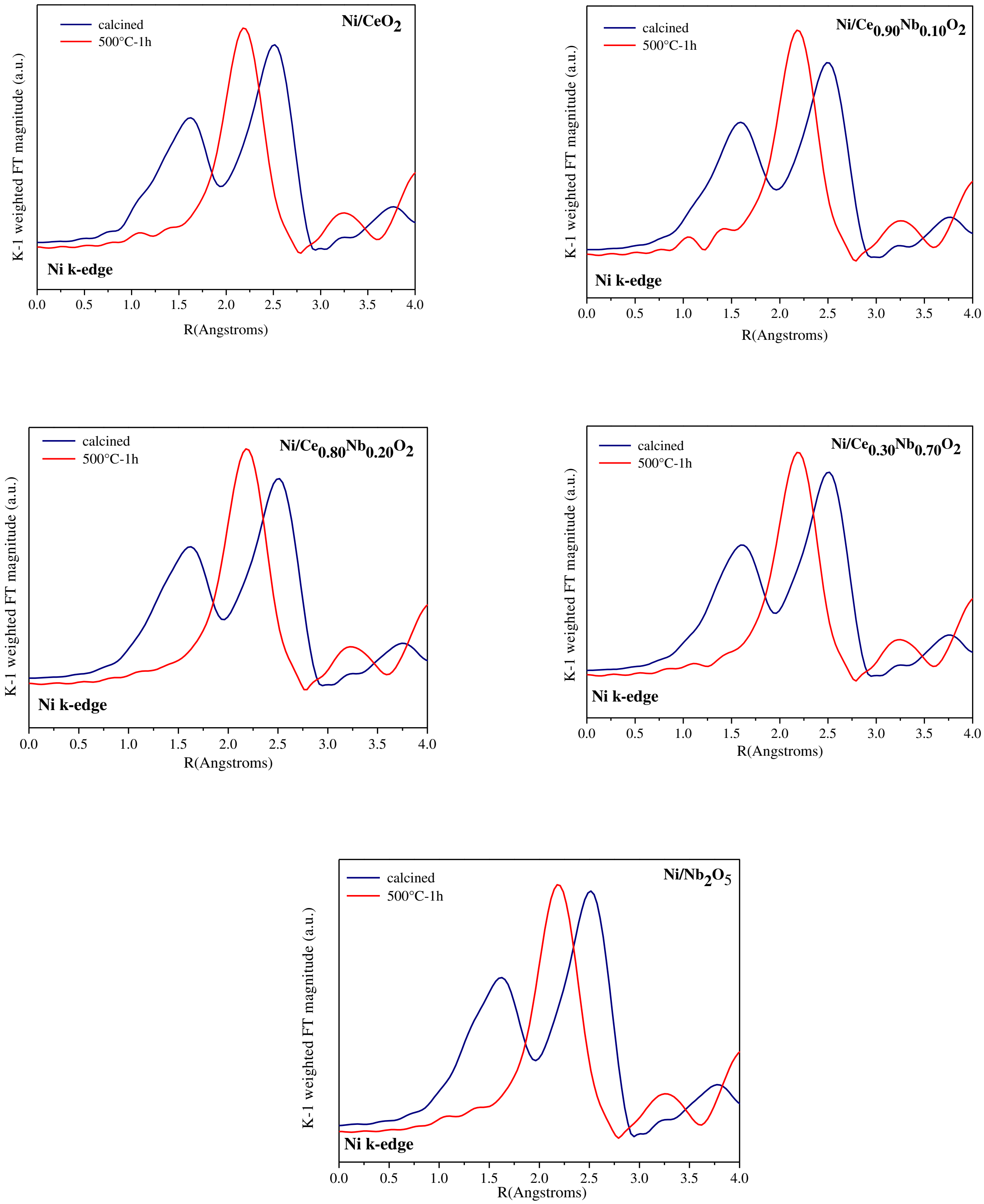

Figure 8-17. Snapshots of EXAFS profiles at the Ni K-edge at (blue line) ~R.T; (red line) ~500°C complete reduction of studied catalysts.

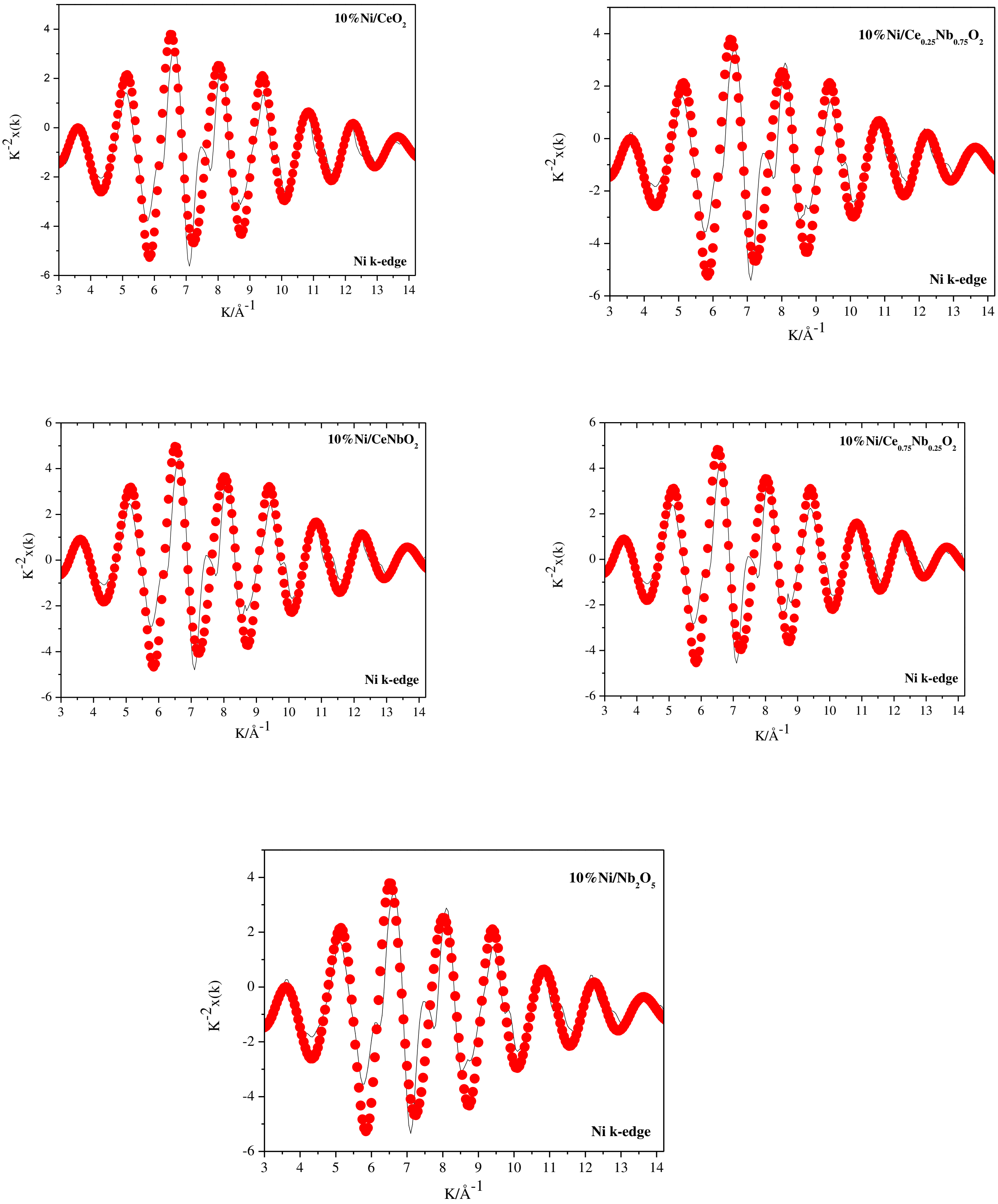

Figure 8-18. EXAFS fits for in situ reduced (at 500°C) Ni catalysts in k-spaces.

Table 8-6. EXAFS parameters of Ni–Ni interactions for the studied catalysts and Ni foil reduced at 500°C.

Sample	C.N. (Ni-Ni)	R (Å) (Ni-Ni)	$e_{0\,(eV)}$	σ^2 (Å2)	r-factor
Ni^{foil}	12	2.48293 (0.0015)	6.425 (0.66)	0.00600 (0.0004)	0.0084878
Ni/CeO_2	11.79 (0.75)	2.48248 (0.0017)	6.445 (0.71)	0.00658 (0.0005)	0.0088707
$Ni/Ce_{0.9}Nb_{0.1}O_2$	11.85 (0.76)	2.48166 (0.0017)	6.197 (0.71)	0.00647 (0.0005)	0.0089239
$Ni/Ce_{0.8}Nb_{0.2}O_2$	12.08 (0.78)	2.48192 (0.0018)	6.205 (0.72)	0.00639 (0.0005)	0.0090888
$Ni/Ce_{0.30}Nb_{0.70}O_2$	11.72 (0.74)	2.4829 (0.0017)	6.371 (0.71)	0.00646 (0.0005)	0.0089992
Ni/Nb_2O_5	11.79 (0.75)	2.4827 (0.0017)	6.486 (0.69)	0.0066 (0.0005)	0.0083676

8.3.5. HDO of phenol over $Ni/Ce_xNb_{1-x}O_2$ catalysts

The phenol conversion and product yield for HDO of phenol at 300°C over all the catalysts as a function of W/F are shown in Fig. 8.19. For Ni/CeO_2 catalyst, methane was the dominant product for W/F > 0.4 h. Cyclohexanone (ONE), cyclohexanol (OL) and benzene were also formed. The addition of 10% of Nb changed significantly the product distribution. In this case, the yield to benzene increased and the formation of methane strongly decreased. Increasing the Nb content favored the formation of benzene, while the production of methane and oxygenated compounds was inhibited. For $Ni/Ce_{0.30}Nb_{0.70}O_2$ and Ni/Nb_2O_5 catalyst, only benzene was formed in the whole range of W/F studied. The selectivity to products for HDO of phenol at 300°C over all the catalysts as a function of phenol conversion are shown in Fig. 8.20.

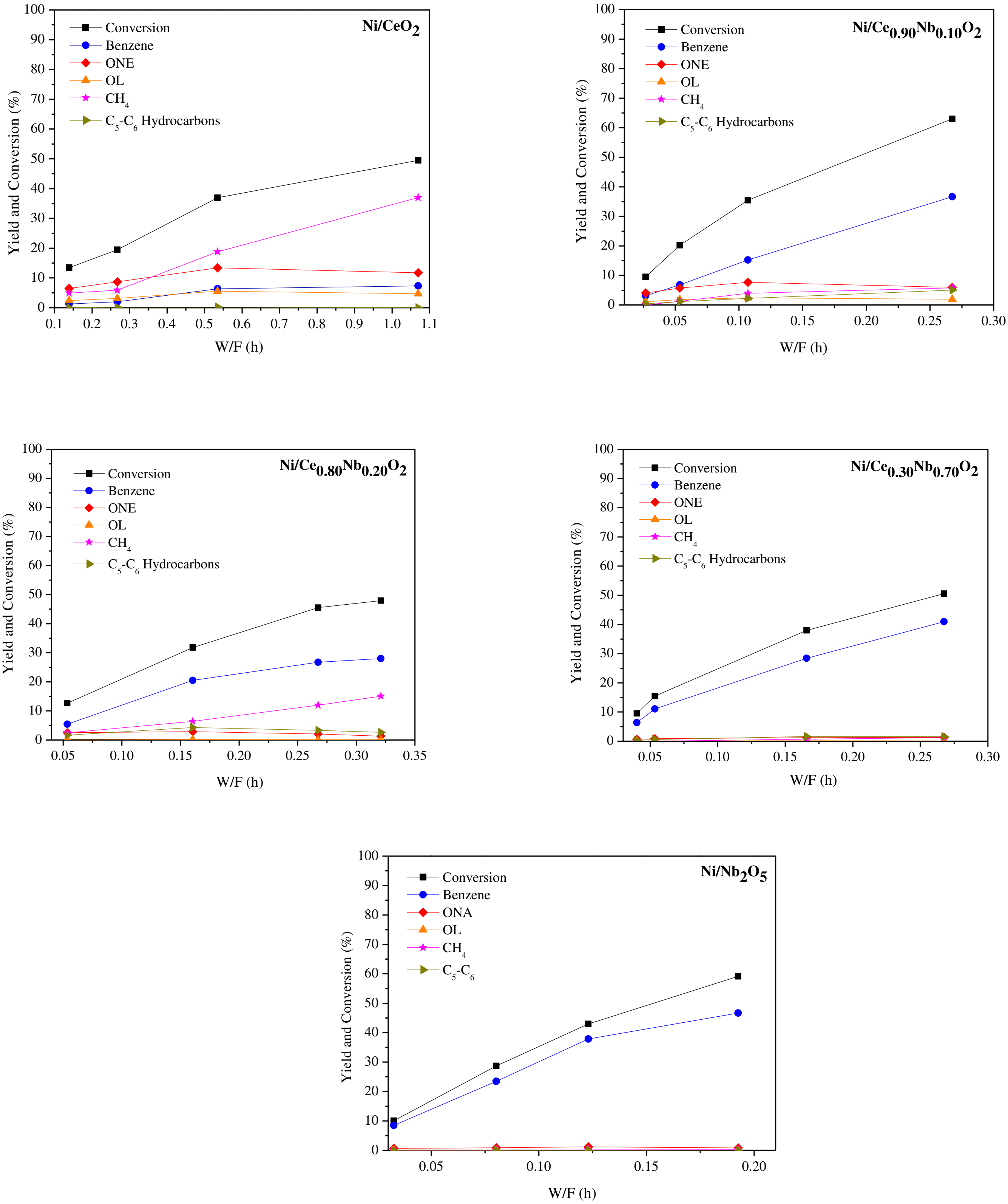

Figure 8-19- Phenol conversion and yield of products as a function of W/F over the studied samples. Reaction conditions: T = 500°C; p = 1 atm; and H_2/phenol molar ratio = 60.

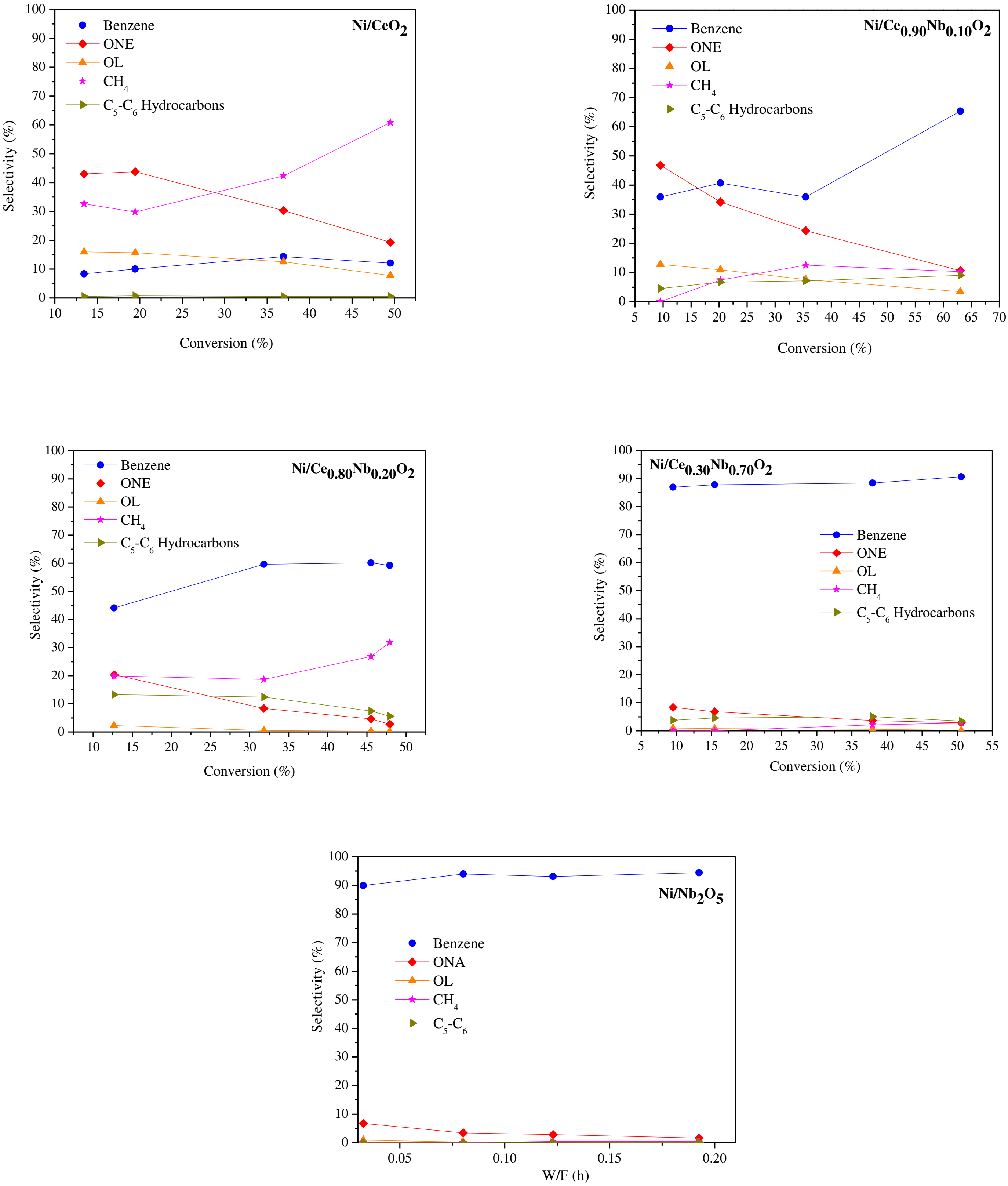

Figure 8-20. Selectivity to products as a function of phenol conversion over. Reaction conditions: T = 500°C; p = 1 atm; and H_2/phenol molar ratio = 60.

The reaction rate for HDO of phenol and the selectivity to products at low phenol conversion (around 13%) were shown in Table 8.7. Regarding product distribution, Ni/CeO_2 catalyst exhibited a low selectivity to benzene and a significant formation of cyclohexanone and methane. The addition of Nb to ceria significantly increased the selectivity to benzene and reduced the formation of methane and cyclohexanone. The results indicate that an increase in the Nb concentration improved the formation of benzene, which is an indication that this metal significantly impacts the adsorptive and catalytic properties of the catalysts.

Table 8-7. Reaction Temp: 300°C; H_2/phenol = 60 molar ratio; phenol mass flow (L/h)= 2.91179E-06 .

Samples	**W/F (h)**	**Reaction rate (mmol/(min.g$_{CAT}$))**	**X* (%)**	**Selectivity (%)**				
				Benzene	**Ano+Eno**	**ONA**	**Methane**	**Cyclohexanol**
Ni/CeO_2	0.14	0.199	13.4	8.38	0	43.02	32.62	15.98
$Ni/\ Ce_{0.9}Nb_{0.1}O_2$	0.02	0.735	9.54	35.93	4.54	46.76	0	12.75
$Ni/\ Ce_{0.8}Nb_{0.2}O_2$	0.05	0.488	12.67	44.09	13.29	20.38	19.94	2.27
$Ni/Ce_{030}Nb_{0.70}O_2$	0.05	0.409	9.53	86.92	3.77	8.35	0	0.94
Ni/Nb_2O_5	0.03	0.55	10.1	89.96	2.4	6.74	0	0.90

*Conversion

8.3.6. The effect of supports with different compositions

Three reaction pathways have been reported in the literature for the HDO of phenol [59-60]: (i) Hydrogenation of the C_{Arom}-C (HYD) bond of the aromatic ring of phenol followed by dehydration of the cyclohexanol formed, (ii) the direct deoxygenation (DDO) and (iii) tautomerization-hydrogenation-dehydration. DDO route involves high dissociation energy of the C-O bond of the aromatic ring in the phenol molecule and thus, it may occur depending on reaction temperature and catalyst used. Chen et al. [61] studied the hydrodeoxygenation of m-cresol on silica supported Ni, Pd and Pt catalysts. According to the authors the oxygen removal is mainly through a direct deoxygenation (DDO). The phenol tautomerization-hydrogenation-dehydration was observed over Pd-catalysis. The keto-tautomer intermediate 2,4-cyclohexadienone may be hydrogenated at the ring to produce 2-cyclohexen-1-one, which is further hydrogenated (e.g., to cyclohexanone and cyclohexanol), or with the oxophilic support, it can be preferentially hydrogenated at the carbonyl group. This produces 2,4-cyclohexadienol, which is subsequently dehydrated to benzene.

The results obtained in the present work revealed that for the studied nickel supported samples, the product distribution is influenced by the composition of the support. For all the samples, both reaction pathways (tautomerization and direct deoxygenation) might take place. The favored pathway over Ni/CeO_2 was the tautomerization, as ONE and OL were the products most produced. Mortensen et al. [62] also studied Ni/CeO_2 catalysts over the HDO of phenol, according to the authors the Ni/CeO_2 catalyst had practically no activity for deoxygenation. Scission of the C-C bond by hydrogenolysis of the phenol group over Ni catalyst yielding methane also was reported by Teles et al. [7 and 63]. Tan et al. [64] showed that the direct dehydroxylation of m-cresol over the Ru(0001) surface forms an unsaturated hydrocarbon surface species C_7H_7*, which can be an intermediate for the production of C-C bond breaking products CH_4 and C_2-C_5 hydrocarbons.

The presence of niobium affects the structural properties of the new oxide, which leads to higher surface area and more disperse nickel particles. According to the Table 8.7, probably CH_4 is directly formed from benzene breaking rather than from its hydrogenation products, which also was reported by Tan et al. [64] in HDO of m – cresol. The hydrogenolysis reaction proceeds by cleaving C-C bonds to form CxHy and CH_x species. In general, the hydrogenolysis of alkanes has been considered a structure sensitive reaction and a decrease in activity with decreasing particle size has been observed [65]. The positive effect of the niobium addition over the benzene selectivity is more evident for Ni/$Ce_{0.30}Nb_{0.70}O_2$.

As a support, Nb_2O_5 intensely favors the HDO products, independent of the metals used. According to Xia et al. [66], the high catalytic activity of $NbOPO_4$ for the direct hydrodeoxygenation reaction can be ascribed to the better adsorption capability of surface Nb^{5+}. Correlation between the C–O bond dissociation barriers and their corresponding adsorption energies shows that stronger M^{5+}–O (M=Nb, Re) bond strength leads to easier the C–O bond cleavage. Barrios et al. [8] also showed that the superior performance of niobia supported catalyst for HDO of phenol is likely due to the presence of oxophilic sites represented by Nb^{5+}/Nb^{4+} cations. According to the authors the strong interaction with the oxygen of the phenol molecule promotes hydrogenation of the carbonyl function of the tautomer intermediate.

According to the XRD analysis presented in this work the octahedral structure of Nb_2O_5 prevailed for $Ni/Ce_{0.30}Nb_{0.70}O_2$, which also was confirmed by the Raman analysis. The XPS analysis also indicated a higher Nb concentration on the $Ni/Ce_{0.30}Nb_{0.70}O_2$ surface. The Nb_2O_5 structural may favor the formation a Ni-Nb_2O_5 interface, which leads to the adsorption of the phenol though its oxygen present in C-O bond. This type of adsorption promotes the hydrogenation of the carbonyl function of the tautomer intermediate. Therefore, a complete HDO of phenol reaction pathways over the studied samples is proposed in Figure 8.21, representing the main reaction route for each sample.

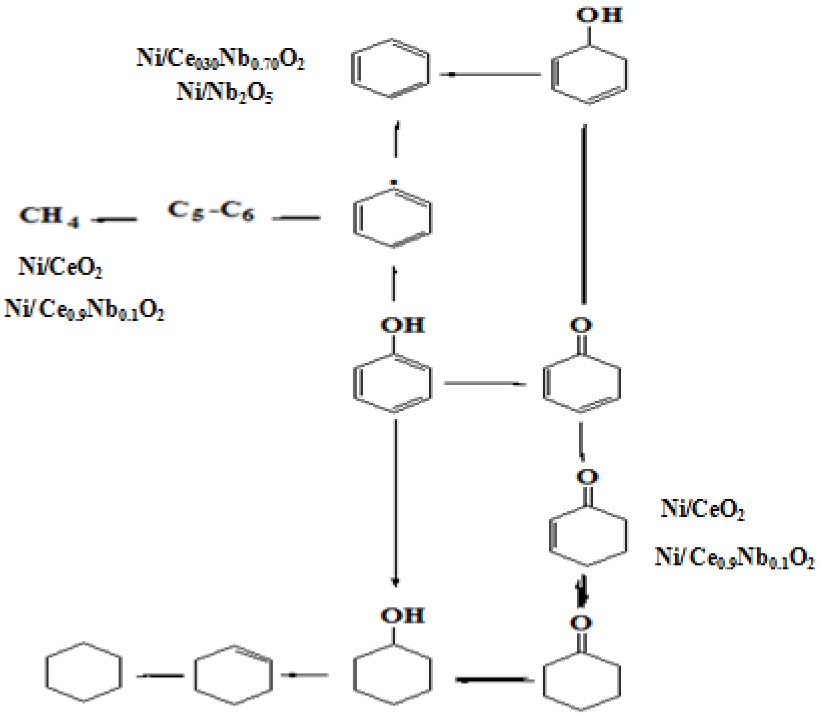

Figure 8-21- Reaction pathways for HDO of phenol over supported metal catalysts

8.3.7. Stability analysis

Phenol conversion and product distributions as a function of TOS (24h) for all catalysts are shown in Figure 8-22. All the samples showed similar initial conversion (around 60-65) and deactivated mainly during the first 6 h of TOS. The stability of the catalysts defined by Eq. (3.13) was calculated and the results are listed in Table 8-8 (deactivation parameter – DP). In general the deactivation degree was favored by the presence of Nb.The presence of cerium as a support did not favored the catalyst stability for Ni impreganed samples. De Souza et al. [6] reported that Pd supported on the CeO_2 and $CeZrO_2$ were more stable for the HDO reaction at similar conditions used in this study. According to the authors under reactions conditions phenoxy and intermediate species remains adsorbed on the Lewis acid sites, blocking those sites and inhibiting further reactant adsorption. The authors related the lower degree of deactivation of Pd/CeO_2 and $Pd/CeZrO_2$ catalysts to the higher density of oxygen vacancies of these supports. The formation of oxygen vacancies expose additional cationic sites that turn over oyxgenate intermediates and/or allow facile desorption of oxygenate products. In general, they reported that the adsorption strength also contributed to catalyst deactivation. The stronger adsorption between the carbonyl function with oxides such as TiO_2, ZrO_2, SiO_2, and Al_2O_3 resulted in an accumulation of O-containing byproducts and led to catalyst deactivation. Thus, in this study the presence of a more oxofilic metal (Ni) [7] may favor the accumulation of O-containing byproducts and promoted the desactivation process.

There were also changes in the product distribution along the reaction (Figure 8.22). For all the samples the selectivity to ONE increased, while the benzene decreased during 24 h. However, this effect is stronger for the samples doped with niobium. Iniaially for $Ni/Ce_{030}Nb_{0.70}O_2$ and Ni/Nb_2O_5 the only products observed were benzene and a small amount of ONA, however after the first hour the selctiviy of ONA and CH_4 increased. The presence of CH_4 may be related to the destruion of the Ni-Nb interatction caused by the presence of H_2O produced in the reaction [67].

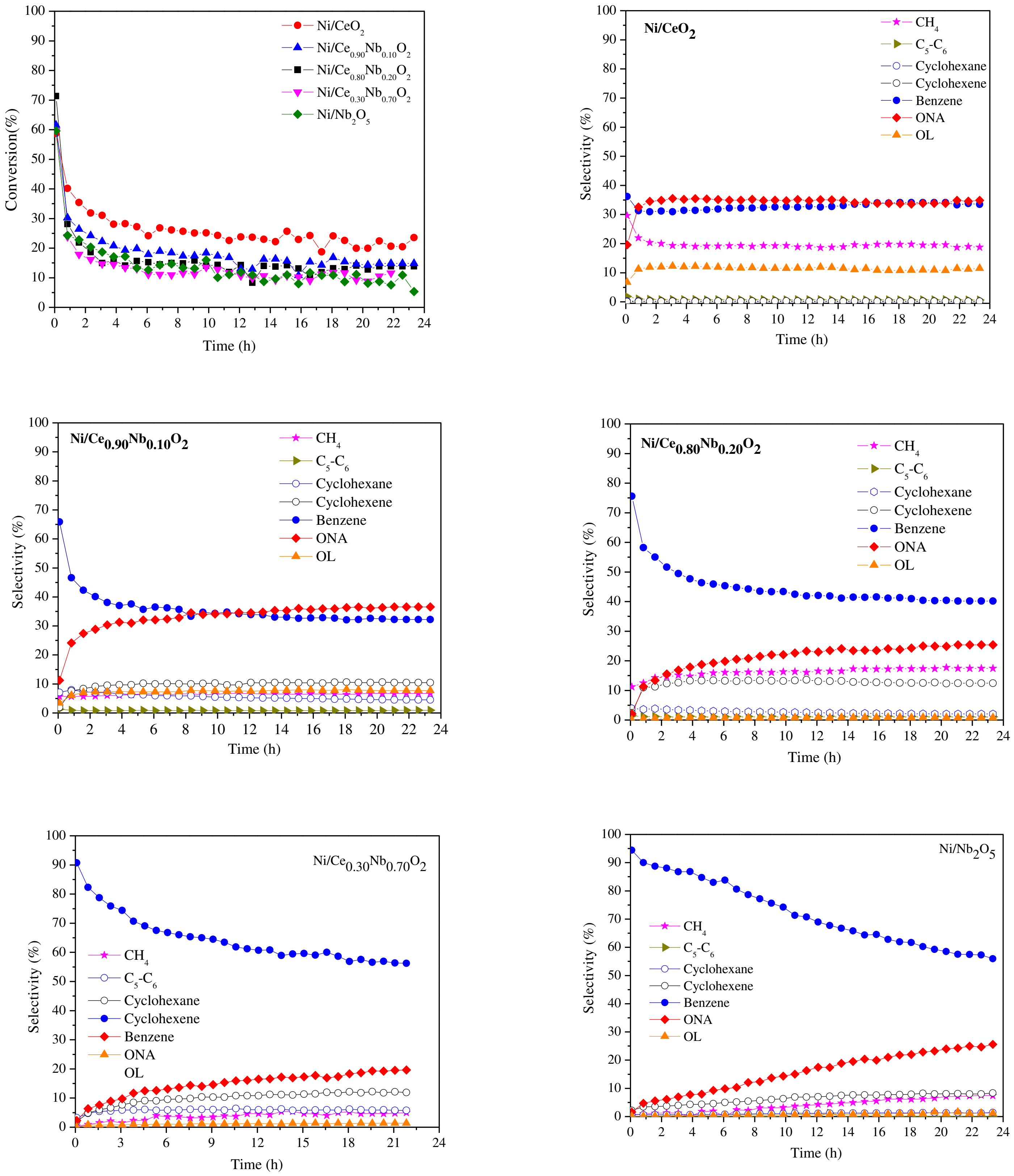

Figure 8-22- Conversion of phenol (A) and selectivity to products as a function of TOS for: (B) Ni/CeO$_2$; (C) Ni/Ce$_{0.9}$Nb$_{0.1}$O$_2$; (D) Ni/Ce$_{0.8}$Nb$_{0.2}$O$_2$; (E) Ni/Ce$_{0.8}$Nb$_{0.2}$O$_2$; (F) Ni/Ce$_{0.3}$Nb$_{0.7}$O$_2$ (G) Ni/Nb$_2$O$_5$.

Table 8-8- Deactivation parameters (DP) of the studied samples

Samples	**Dp**
Ni/CeO_2	0.17
$Ni/Ce_{0.90}Nb_{0.10}O_2$	0.17
$Ni/Ce_{0.80}Nb_{0.20}O_2$	0.12
$Ni/Ce_{0.30}Nb_{0.70}O_2$	0.14
Ni/Nb_2O_5	0.10

8.4. Conclusions

The objective of this work was to study the effect of the niobium addition in CeO_2 structure with the aim of obtaining selective nickel catalysts for hydrodeoxygenation reaction. The deoxygenation capacity of the samples was enhanced in the presence of niobium, suggesting that adsorptive and catalytic properties of Ni/CeO_2 were modified. For Ni/CeO_2 the reaction mechanism based on the tautomerization prevailed at small W/F. This sample promoted the hydrogenation of the ring, producing preferentially cyclohexanone and cyclohexanol. However, at higher conversions, CH_4 was the most favored product for Ni/CeO_2 , which is related to the tendency of nickel to breaking C-C. Smaller nanoparticle nickel size strongly affected the selectivity of methane, which is desfavored by the addition of small amounts of niobium, due to the formation of an oxide with higher surface area. The hexanol structure of Ni/Nb_2O_5 and $Ni/Ce_{0.30}Nb_{0.70}O_2$ favors the formation of a $Ni\text{-}Nb_2O_5$ interface, which leads to the adsorption of the phenol though its oxygen and promotes the benzene selectivity.

Reference

[1] Wang, W.; Yang, Y.; Luo, H.; Hu, T.; Liu, W. CATCOM 2011, 12 (6), 436–440. https://doi.org/10.1016/j.catcom.2010.11.001

[2] Elliott, D. C. Energy and Fuels 2007, 21 (3), 1792–1815.https://doi.org/10.1021/ef070044u

[3] Olcese, R.; Bettahar, M.; Malaman, B.; Dufour, A. Applied Catal. B, Environ. 2012, 115–116, 63–73.https://doi.org/10.1016/j.apcatb.2011.12.005

[4] Zhao, H. Y.; Li, D.; Bui, P.; Oyama, S. T. Appl. Catal. A Gen. 2011, 391 (1–2), 305–310.https://doi.org/10.1016/j.apcata.2010.07.039

[5] Gutierrez, A.; Kaila, R. K.; Honkela, M. L.; Slioor, R.; Krause, A. O. I. Catal. Today 2009, 147 (3–4), 239–246.https://doi.org/10.1016/j.cattod.2008.10.037

[6] Souza, P. M. De; Rabelo-neto, R. C.; Borges, L. E. P.; Jacobs, G.; Davis, B. H.; Resasco, D. E.; Noronha, F. B. 2017, ACS Catal. 2017, *7* (3), 2058–2073.https://doi.org/10.1021/acscatal.6b02022

[7] Teles, C. A.; Rabelo-Neto, R. C.; de Lima, J. R.; Mattos, L. V.; Resasco, D. E.; Noronha. F. B. Catal. Letters 2016, 146 (10), 1848–1857.https://doi.org/10.1007/s10562-016-1815-5

[8] Barrios, A. M.; Teles, C. A.; Souza, P. M. De; Rabelo-neto, R. C.; Jacobs, G.; Davis, B. H.; Borges, L. E. P.; Noronha, F. B. Catalysis Today 2017, 302, 115-124. https://doi.org/10.1016/j.cattod.2017.03.034

[9] Hong, Y.; Zhang, H.; Sun, J.; Ayman, K. M.; Hensley, A. J. R.; Gu, M.; Engelhard, M. H.; Mcewen, J.; Wang, Y.

ACS catalysis 2014, (4), 3335-3345.https://doi.org/10.1021/cs500578g

[10] Mortensen, P. M.; Grunwaldt, J. D.; Jensen, P. A.; Knudsen, K. G.; Jensen, A. D. Appl. Catal. A Gen. 2011, 407 (1–2), 1–19.https://doi.org/10.1016/j.apcata.2011.08.046

[11] Lee, C. R.; Yoon, J. S.; Suh, Y. W.; Choi, J. W.; Ha, J. M.; Suh, D. J.; Park, Y. K. Catal. Commun. 2012, (17), 54–58.https://doi.org/10.1016/j.catcom.2011.10.011

[12] Souza, P. M. de; Rabelo-neto, R. C.; Borges, L. E. P.; Jacobs, G.; Davis, B. H.; Graham, U. M.; Resasco, D. E.; Noronha, F. B. ACS catalysis 2015, (5), 7385-7398.https://doi.org/10.1021/acscatal.5b01501

[13] Schimming, S. M.; Lamont, O. D.; Kçnig, M.; Rogers, A. K.; Amico, A. D. D.; Yung, M. M.; Sievers, C. ChemSusChem 2015, (8), 2073–2083.https://doi.org/10.1002/cssc.201500317

[14] Gaálová, J.; Mesnard, D.; Mikulova, J.; Ã, S. R.; Ge, F.; Kappenstein, C.; Duprez, D. Journal of Solid State Chemistry 2006, (179), 2511–2520. https://doi.org/10.1016/j.jssc.2006.04.051

[15] Zhang, Z.; Wang, Y.; Lu, J.; Wang, M.; Li, M.; Liu, X.; Wang, F. ACS Catal. 2016, (6), 8248–8254.https://doi.org/10.1021/acscatal.6b02134

[16] Ayastuy, J. L.; Iglesias-González, A.; Gutiérrez-Ortiz, M.A; Chemical Engineering Journal 2014, (244), 372–381.https://doi.org/10.1016/j.cej.2014.01.077

[17] Kurnatowska, M.; Mista, W.; Mazur, P.; Kepinski, L. Applied Catalysis B: Environmental 2014, (148), 123–135.https://doi.org/10.1016/j.apcatb.2013.10.047

[18] Liu, Y.; Luo, L.; Gao, Y.; Huang, W. Applied Catalysis B: Environmental 2016, (197), 214–221.https://doi.org/10.1016/j.apcatb.2016.03.011

[19] You, R.; Zhang, X.; Luo, L.; Pan, Y.; Pan, H.; Yang, J.; Wu, L.; Zheng, X.; Jin, Y.; Huang, W. Journal of Catalysis 2017, (348), 189–199.https://doi.org/10.1016/j.jcat.2016.12.012

[20] Li, N.; Huber, G. W. J. Catal. 2010, (270), 48–59.https://doi.org/10.1016/j.jcat.2009.12.006

[21] Hori, C. E.; Permana, H.; Ng, K. Y. S.; Brenner, A.; More, K.; Rahmoeller, K. M.; Belton, D. Appl. Catal. B-Environmental 1998, (16), 105–117. https://doi.org/10.1016/S0926-3373(97)00060-X

[22] Stošić, D.; Bennici, S.; Rakić, V.; Auroux, A. Catal. Today 2012, (192), 160–168. https://doi.org/10.1016/j.cattod.2011.10.040

[23] Chen, P.; Chen, I. J. Am. Ceram. Soc. 1992, (76), 1577-1583.

[24] Negas, T.; Roth, R.S.; McDaniel, C.L.; Parker, H.S.; Olson, C.D. Mat. Res. Bull 1977, (12), 1161–1171.https://doi.org/10.1016/0025-5408(77)90170-2

[25] Thompson, J. G.; Withers, R. L.; Brink, F. J. Journal of Solid State Chemistry 1999 (143), 122–131.https://doi.org/10.1006/jssc.1998.8096

[26] Chretien, A. ; Bodiot, D. Compt. Rend., Ser. C 1966, (263), 882.

[27] Bayliss, R. D.; Pramana, S. S.; An, T.; Wei, F.; Kloc, C. L.; White, A. J. P.; Skinner, S. J.; White, T. J.; Baikie, T. Journal of solid state chemistry 2013, (204), 291–297.https://doi.org/10.1016/j.jssc.2013.06.022

[28] Damyanova, S.; Pawelec, B.; Arishtirova, K. Applied Catalysis A: General 2008, (337), 86–96.https://doi.org/10.1016/j.apcata.2007.12.005

[29] Reddy, B. M.; Khan, A. J. Phys. Chem. B 2003, (107), 5162–5167.https://doi.org/10.1021/jp0344601

[30] Wachs, I. E.; Jehng J.; Hardcastle F., Solid State lonics 1989, (32), 904-910. https://doi.org/10.1016/0167-2738(89)90374-3

[31] Mamede, A.; Payen, E.; Granger, P.; Florea M.; Pârvulescu V. I. AIChE Journal 2008, (54), 1303–1312.https://doi.org/10.1002/aic.11468

[32] Pittman, R. M.; Bell, A. T. Structure 1993, (2), 12178–12185.

[33] Graham, G. W.; Weber, W. H.; Peters, C. R.; Usmen, R.; Journal of Catalysis 1991, (313), 310–313.https://doi.org/10.1016/0021-9517(91)90113-I

[34] Mcbride, J. R.; Hass, K. C.; Poindexter, B. D.; Weber, J. Appl. Phys. 1994, (76), 2435.https://doi.org/10.1063/1.357593

[35] Vidal, H.; Kašpar, J.; Pijolat, M.; Colon, G.; Bernal, S.; Cordón, A.; Perrichon, V.; Fally F. Applied Catalysis B: Environmental 2000, (27), 49–63.https://doi.org/10.1016/S0926-3373(00)00138-7

[36] Moraes, T. S.; Neto, R. C. R.; Ribeiro, M. C.; Mattos, L. V.; Kourtelesis, M.; Verykios, X.; Noronha, F. B. Top. Catal. 2015, (281–294).https://doi.org/10.1007/s11244-015-0369-x

[37] Dong, W.; Roh, H.; Jun, K.; Park, S.; Oh, Y. Applied Catalysis A: General 2002, (226), 63–72.https://doi.org/10.1016/S0926-860X(01)00883-3

[38] Biswas, P.; Kunzru, D. International Journal of Hydrogen Energy 2007, (32), 969–980.https://doi.org/10.1016/j.ijhydene.2006.09.031

[39] Leitenburg, C. De.; Trovarelli, A.; Llorca, J.; Cavani, F.; Bini, G. Applied Catalysis A: General 1996, (139), 161–173.https://doi.org/10.1016/0926-860X(95)00334-7

[40] Chary, K. V. R.; Lakshmi, K. S.; Rao, P. V. R.; Rao, K. S. R.; Papadaki, M. Journal of Molecular Catalysis A: Chemical 2004, (223), 353–361.https://doi.org/10.1016/j.molcata.2003.09.049

[41] Wojcieszak, R.; Jasik, A.; Monteverdi, S.; Ziolek, M.; Bettahar, M. M. J. Mol. Catal. A Chem. 2006, 256 (1–2), 225–233.https://doi.org/10.1016/j.molcata.2006.04.053

[42] Kumar, E.; Selvarajan, P.; Balasubramanian, K. Recent Res. Sci. Technol. 2010, 2 (4), 37–41.

[43] Ciambelli, P.; Cimino, S.; Lisi, L.; Faticanti, M.; Minelli, G.; Pettiti, I.; Porta, P. Applied Catalysis B: Environmental 2001, (33), 193-705.https://doi.org/10.1016/S0926-3373(01)00163-1

[44] Yue, L.; Zhang, X. Journal of Alloys and Compounds 2009, (475), 702–705.https://doi.org/10.1016/j.jallcom.2008.07.096

[45] Aneggi, E.; Leitenburg, C. De; Dolcetti, G.; Trovarelli, A. Catalysis Today 2006, (114), 40–47.https://doi.org/10.1016/j.cattod.2006.02.008

[46] Richardson, J. T.; Scates, R.; Twigg, M. V. Applied Catalysis A: General 2003, (246), 137–150.https://doi.org/10.1016/S0926-860X(02)00669-5

[47] Preda, I.; Mossanek, R. J. O.; Abbate, M.; Alvarez, L.; Méndez, J.; Gutiérrez, A.; Soriano, L. Surf. Sci. 2012, 606 (17–18), 1426–1430.https://doi.org/10.1016/j.susc.2012.05.005

[48] Uhlenbrockt, S.; Scharfschwerdtt, C.; Neumannt, M.; Illing, G.; Freund, H.J. J. Phys.: Condens. Matter 1992, (4), 7973–7978.https://doi.org/10.1088/0953-8984/4/40/009

[49] Kuznetsov, M V, Razinkin, A. S.; Shalaeva, E. V. Journal of Structural Chemistry 2009, 50 (3), 536–543.https://doi.org/10.1007/s10947-009-0079-y

[50] Beche, E.; Charvin, P.; Perarnau, D.; Abanades, S.; Flamant, G. Surf. Interface Anal. 2008, (40), 264–267.https://doi.org/10.1002/sia.2686

[51] Iriondo, A.; Barrio, V. L.; Cambra, J. F.; Arias P. L.; Güemez, M. B.; Navarro R. M.; Sánches-Sánchez M. C; Fierro, J. L. G. Top Catal 2008, (49), 46–58.https://doi.org/10.1007/s11244-008-9060-9

[52] Antonio, R.; Song, I.; Yamada, H.; Journal of Solid State Chemistry 1991, (192), 183–192.https://doi.org/10.1016/0022-4596(91)90287-R

[53] Sasaki, K.; Zhang, L.; Adzic, R. R. Phys.Chem. Chem.Phys. 2008, (10), 159–167.https://doi.org/10.1039/B709893F

[54] Cartier, C.; Hammouda, T.; Boyet, M.; Mathon, O.; Testemales, D.; Moine, B. American Mineralogist 2015, (100), 2152–2158.https://doi.org/10.2138/am-2015-5330

[55] Zhang, J.; Wu, Z.; Liu, T.; Hu, T.; Z.; Ju. X. Synchrotron Rad. 2001, (8), 531–532. https://doi.org/10.1107/S0909049500016022

[56] Zhang, F.; Wang, P.; Koberstein, J.; Khalid, S.; Chan, S. Surface Science 2004, (563), 74–82.https://doi.org/10.1016/j.susc.2004.05.138

[57] Overbury, S. H.; Huntley, D. R.; Mullins, D. R.; Glavee, G. N. Catalysis Letters 1998, (51), 133–138.https://doi.org/10.1023/A:1019086428874

[58] Pandya, K. I.; Hoffman, R. W.; Mcbreen, J.; O'Grady, W. E. J. Electrochem. Soc. 1990, 137 (2), 2–7.https://doi.org/10.1149/1.2086450

[59] Mortensen, P. M.; Grunwaldt, J.; Jensen, P. A.; Knudsen, K. G.; Jensen, A. D. Applied Catal. A, Gen. 2011, 407 (1–2), 1–19.https://doi.org/10.1016/j.apcata.2011.08.046

[60] Bui, V. N.; Toussaint, G.; Laurenti, D.; Mirodatos, C.; Geantet, C. Catal. Today 2009, 143 (1–2), 172–178.https://doi.org/10.1016/j.cattod.2008.11.024

[61] Chen, C.; Chen, G.; Yang, F.; Wang, H.; Han, J.; Ge, Q.; Zhu, X. Chem. Eng. Sci. 2015, (135), 145–154.https://doi.org/10.1097/01.ccm.0000473963.28374.ae

[62] Mortensen, P. M.; Grunwaldt, J.; Jensen, P. A.; Jensen, A. D. ACS Catal. 2013, (3), 1774−1785.https://doi.org/10.1021/cs400266e

[63] Teles, C. A.; Rabelo-neto, R. C.; Jacobs, G.; Davis, B. H.; Resasco, D. E.; Noronha, F.B. ChemCatChem 2017, 9 (14) 2850-2863. https://doi.org/10.1002/cctc.201700047

[64] Tan, Q.; Wang, G.; Nie, L.; Dinse, A.; Buda, C.; Shabaker, J.; Resasco, D. E. ACS Catal. 2015, 5 (11), 6271–6283.https://doi.org/10.1021/acscatal.5b00765

[65] Flaherty, D. W.; Iglesia, E. J. Am. Chem. Soc. 2013, 135 (49), 18586–18599.https://doi.org/10.1021/ja4093743

[66] Zhuang, X. J.; Xia, Q. N.; Wang, Y. Q.; Tsang, S. C. E.; Gong, X. Q. Int. J. Hydrogen Energy 2016, 41 (41), 18502–18508.https://doi.org/10.1016/j.ijhydene.2016.08.220

[67] Anderson, J.B.F.; Burch, R. Applied Catalysis, 1986 (21), 179-185https://doi.org/10.1016/S0166-9834(00)81338-X

CHAPTER IX

9.1. Conclusion

- ✓ Initially, we conclude that without methane the thermodynamic equilibrium indicated that a high ratio of H_2 to phenol and medium temperatures contributed to a greater selectivity for benzene. This equilibrium is reached over Pd samples at higher temperatures. However, when methane was add to the calculations this product was the only one observed, which was expected because CH_4 is a very stable compound.

- ✓ For HDO reaction in gas phase, alloying Pd with less oxophilic metals (Zn, Cu and Ag) favored the selectivity to hydrogenated products. For PdSn, as tin oxide should exhibit an oxophilicity similar to Zr^{4+} cations it promoted the formation of benzene. Once Sn^{n+} is located at or near the metal particles, it favors the adsorption of the keto-tautomer of phenol through its carbonyl group, which increases hydrogenation of the C=O bond.

- ✓ Different metals supported in Nb_2O_5 also were studied in a HDO gas phase. The reduction temperature affected the activity and selectivity of the different metallic Nb_2O_5-supported by the promotion of the SMSI effect. After reduction at 773K, nickel supported in Nb_2O_5 showed similar benzene selectivity than rhodium and palladium.

- ✓ The niobium addition in CeO_2 structure favored the deoxygenation suggesting that adsorptive and catalytic properties of Ni/CeO_2 were modified. The octahedral Nb_2O_5 structure for the sample with more niobium may favored the formation a Ni-Nb_2O_5 interface which leads to the adsorption of the phenol though its oxygen and promoted the benzene formation.

- ✓ In a liquid phase, Pd catalysts with different metal loading showed that the hydrogenation of phenol in a liquid phase is a structure sensitive reaction. The addition of Ag increased the TOF of the reaction, by lowering the energy of activation compared to the monometallic Pd counterpart via enhancing the electron density on Pd.

- ✓ For future studies we recommended the investigation of nickel supported on Nb_2O_5 and on cerium doped oxide catalysts in a liquid phase. Also, must be relevant investigated the effect of Ni particles size over different supports in a HDO reaction. It will be important to obtain materials with controlled shape and size, which allows a better understanding of the influence of these characteristics on the reaction..

APPENDIX I

I. Hydrodeoxygenation of phenol over zirconia supported Pd bimetallic catalysts: The effect of second metal on catalyst deactivation.

Table 1SI: TPR Areas

Samples	Area 1st peak	Area 2st Peak	Area median of the loop
Pd/ZrO_2	3.11324E-09	1.81094E-09	1.21491E-11
PdAg/ZrO_2	3.21861E-09	4.92907E-09	1.23107E-11
PdCu/ZrO_2	2.90879E-09	1.88061E-09	1.02089E-11
PdSn/ZrO_2	2.74139E-09	1.50592E-09	6.25254E-12
PdZn/ZrO_2	3.71993E-09	1.9035E-09	9.69169E-12

Loop Volume : 0.00025mL

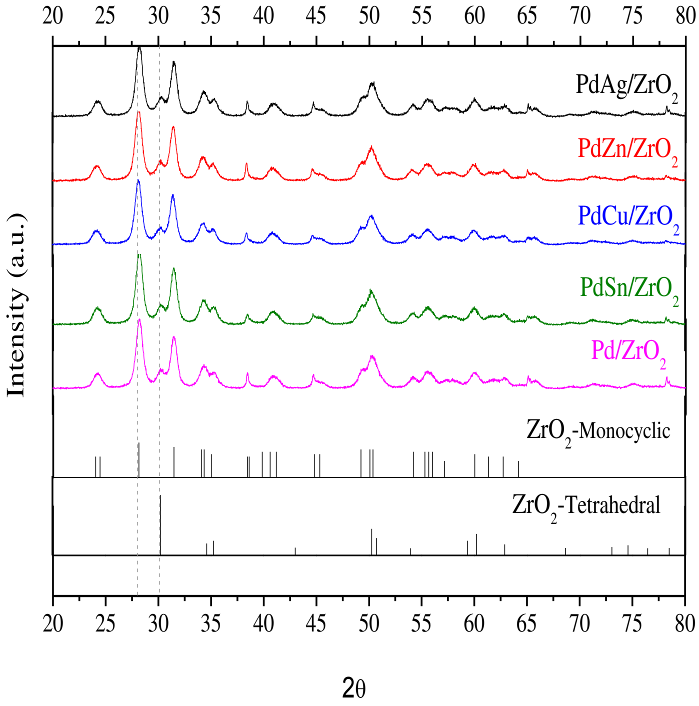

Figure S1. XRD patterns of Pd/ZrO_2 and PdMe/ZrO_2 catalysts (Me=Ag, Sn, Cu and Zn).

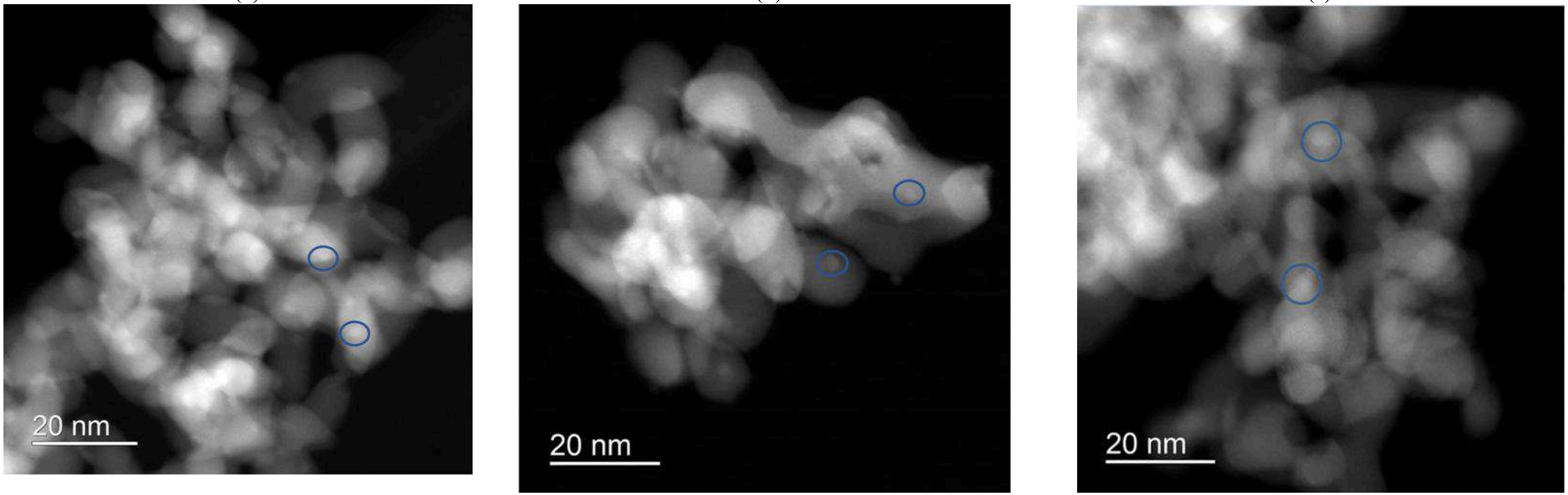
(a) (b) (c)

Figure S2- STEM image of (a) Pd/ZrO_2 ; (b) $PdAg/ZrO_2$ (c) $PdSn/ZrO_2$ catalysts.

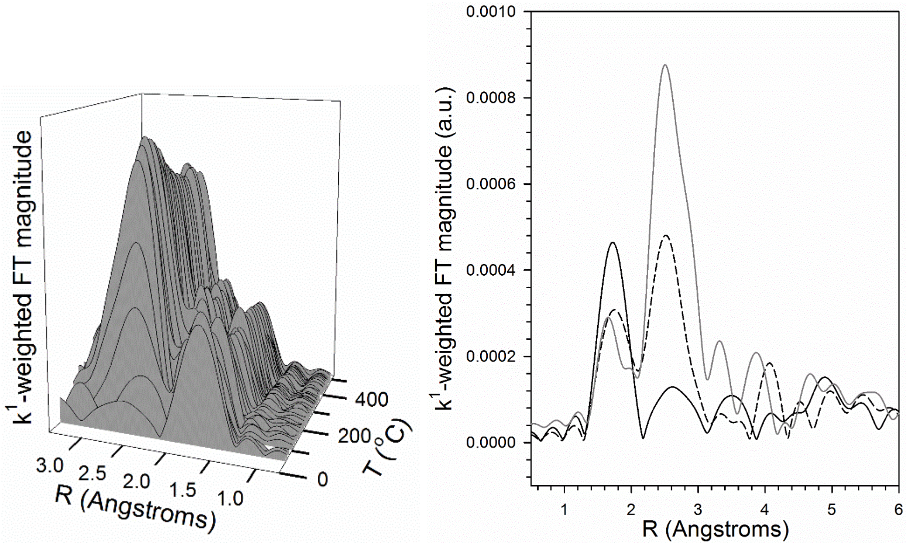

Figure S2. (right) TPR-EXAFS k^1-weighted Fourier transform magnitude spectra at the Ag K-edge of the Pd-Ag catalyst as a function of temperature (left) EXAFS profiles at the Ag K-edge at (solid black line) ~331K; (dashed line) partial reduction; and (solid gray line) ~771K complete reduction of the PdAg catalyst.

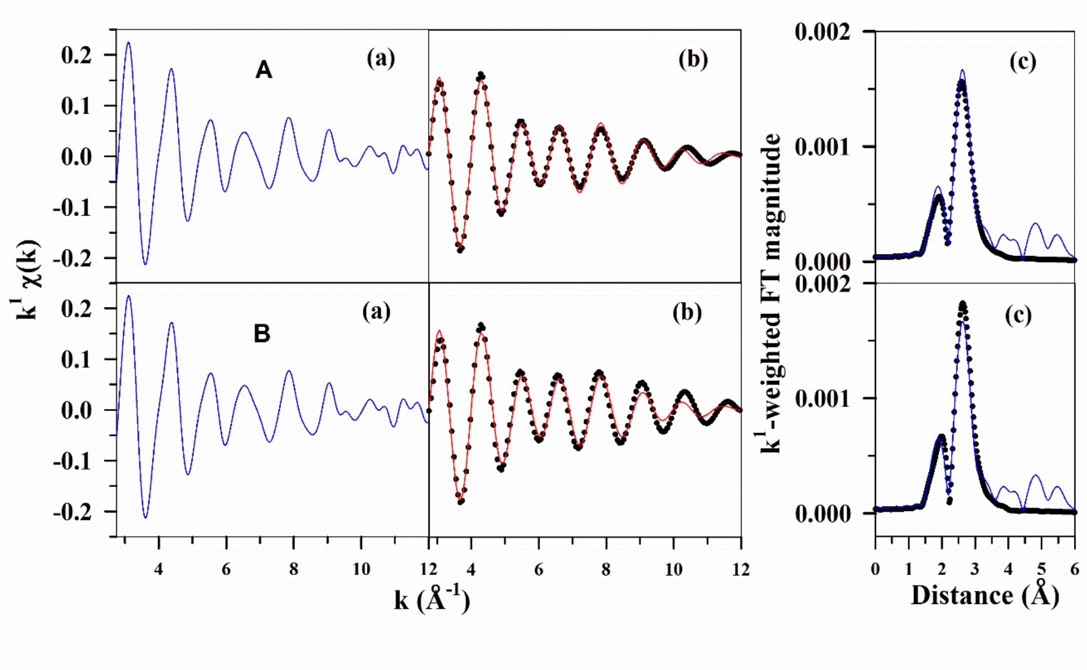

Figure S4. (left, a) raw k^1-weighted χ(k) spectra; (middle, b) (solid line) filtered and (filled circles) fitted k^1-weighted χ(k) spectra; and (right, c) (solid line) raw and (filled circles) fitted k^1-weighted Fourier Transform magnitude spectra of (I) Pd-Ag (separate fitting) and (II) Pd-Ag (combination fitting). Fittings were conducted over the first Pd–M(M = Pd and/or Ag) coordination shell.

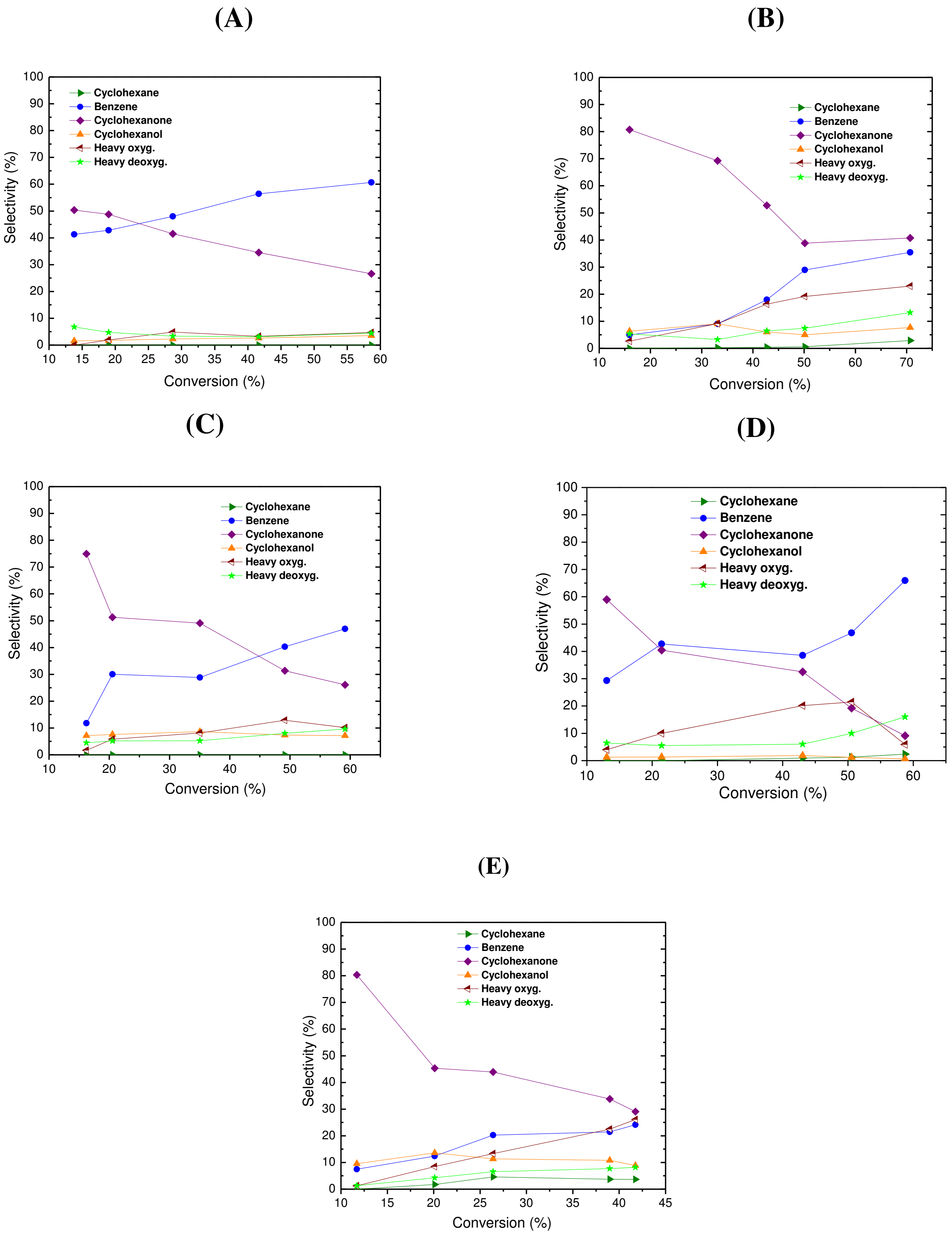

Figure S4. Selectivity to products as a function of phenol conversion over: (A) Pd/ZrO_2; (B) PdAg/ZrO_2; (C) PdCu/ZrO_2; (D) PdSn/ZrO_2; (E) PdZn/ZrO_2. Reaction conditions: T = 573 K; p = 1 atm; and H_2/phenol molar ratio = 60.

APPENDIX II

II. Aqueous phase hydrogenation of phenol catalyzed by Pd and PdAg on ZrO_2

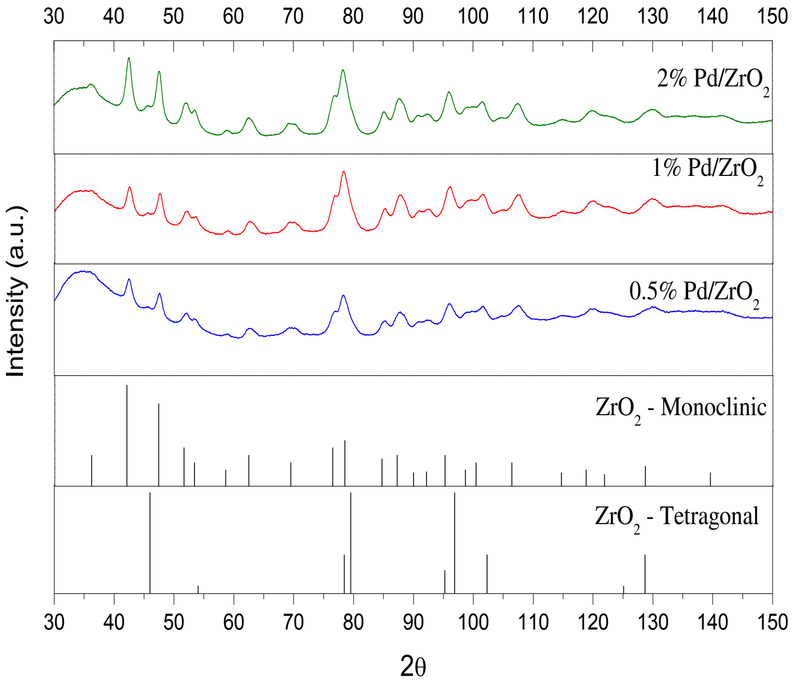

Figure 1SI. XRD patterns of the Pd/ZrO_2 samples with different Pd loadings.

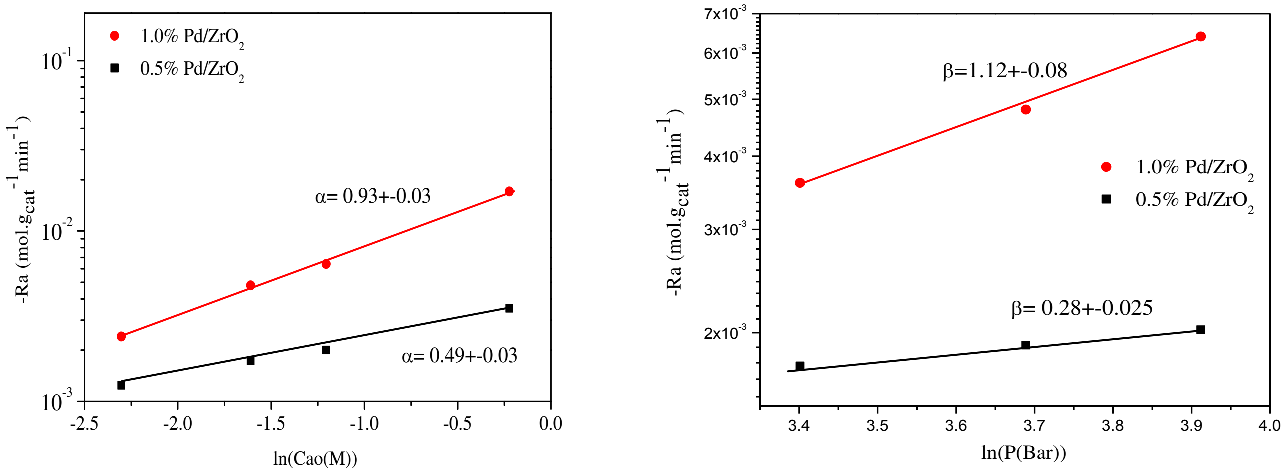

Figure 2SI. Effects of H_2 partial pressure at 0.30 M of phenol (left) and phenol concentration (right) at 50 bar of H_2 on the rate of HDO of phenol over 1% Pd/ZrO_2 and 0.5% Pd/ZrO_2 catalysts at 463 K.

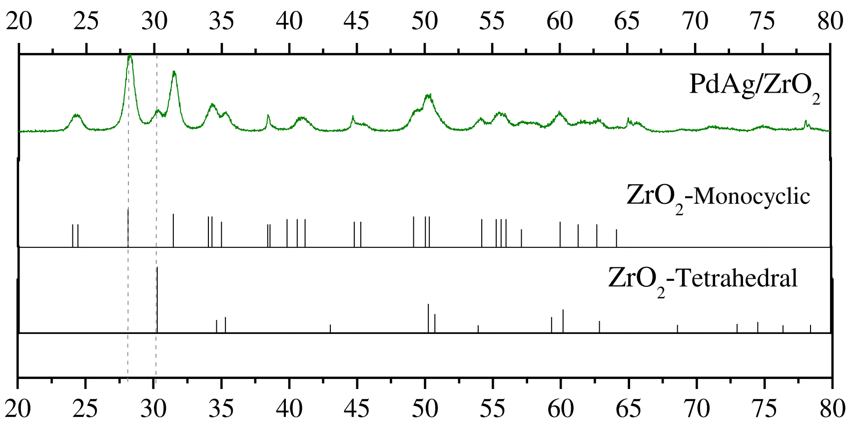

Figure 3SI.XRD patterns of the 1%PdAg/ZrO_2sample.

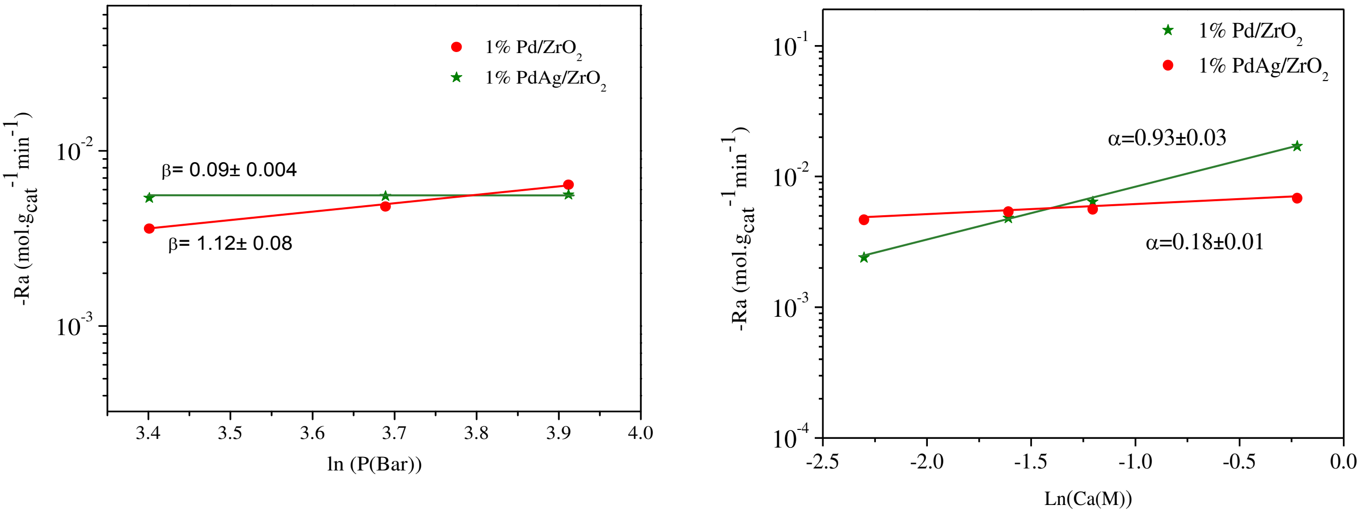

Figure 4 SI. Effects of phenol concentration at 50 bar of H_2 (left) and hydrogen partial pressure at phenol concentration of 0.30 M (right) on the rate of phenol hydrogenation over 1% Pd/ZrO_2 and 1% PdAg/ZrO_2 catalysts at 463 K.

Table 1SI.Phenol hydrogenation over 1%Pd/ZrO_2 at different temperatures. Reaction conditions: 50 bar H_2, 0.30 M phenol concentration (in water), catalyst mass 15-20 mg.

T (K)	**Time (min)**	**Catalyst mass (mg)**	**Conversion (%)**	**Selectivity (%)**	
				Cyclohexanone	**Cyclohexanol**
443	15	20	2	100	0
	30		7	100	0
	45		10	98	2
	90		19	97	3
453	15	20	10	100	0
	30		16	98	2
	45		22	97	3
	60		24	96	4
463	15	15	8	100	0
	30		14	95	5
	45		22	95	5
	60		24	94	6
473	15	10	6	100	0
	30		16	95	5
	45		24	92	8

Table 2SI. Comparison of the product selectivities on 1% Pd-0.5%Ag/ZrO_2 at different temperatures.P (H_2) = 50 bar and C(phenol)= 0.30 M.

		1%Pd-0.5%Ag/ZrO_2	
T (K)	**Time (min)**	**Selectivity (%)**	
		Cyclohexanone	**Cyclohexanol**
473	15	96	4
	30	96	4
	45	98	2
	60	98	2
463	15	93	7
	30	97	3
	45	98	2
	60	99	1
453	15	97	3
	30	98	2
	45	98	2
	60	98	2
443	10	-	-
	30	98	2
	45	99	1
	60	-	-

Exclusion of internal mass transfer limitations

Regarding the internal mass transport limitation, we used the Weisz-Prater number to evaluate its impact [1]:

$$N_{W-P} = \frac{\Re {R_p}^2}{C_s D_{eff}}$$

where $\Re$ is the reaction rate per unit volume of catalyst, R_p is catalyst particle radius, C_s is the reactant concentration at the external surface of the particle, and D_{eff} is the effectivediffusivity in the pores of the catalyst.

On the most active catalyst (2%Pd/ZrO_2), $\Re$,the reaction rate normalized to the pore volume (0.15 cm^3g^{-1}) was 6×10^{-4}mol$s^{-1}cm^{-3}$ at 463 K. R_p, catalyst particle radius, can be estimated from the TEM images to be <0.2μmon average.In the absence of external transport limitation, the surface concentration can be assumed to be equal to the bulk concentration, 3.0×10^{-4}mol cm^{-3}. D_{eff}, the effective diffusivity in the pores of ZrO_2, is not available. A number of relevant estimates are given below. Diffusion coefficient was reported to be ~$10^{-5}cm^2$ s^{-1} for phenol in water at r.t. [2]; intraparticle diffusivity of phenol in packed columns (particles having 10-32 nm pore diameter) was determined to be also on the order of $10^{-5}cm^2$ s^{-1}at 295 K [3]; for smaller pores of 7 nm average size, the effective diffusion coefficient was on the order of 10^{-7} to 10^{-8} cm^2 s^{-1} [4].D_{eff} with Similar orders of magnitude were reported for diffusion of phenol from aqueous solutions to activated carbon [5].

A Weisz-Prater number less than 0.3 typically indicates negligible internal mass transfer limitations [1]. The Weisz-Prater number, using lower-bound estimates for D_{eff}[6] and upper-bound estimates for $\Re$ and R_p,was calculated to be 0.08 on the most active catalyst, which indicates that the reactions are free of internal mass transfer limitations.

Notes and references

[1] M.A. Vannice, Kinetics of Catalytic Reactions; Springer: New York, 2005.https://doi.org/10.1007/b136380

[2] R. Niesner, A. Heintz, J. Chem. Eng. Data 45 (2000) 1121-1124.https://doi.org/10.1021/je0000569

[3] F. Gritti, G. Guiochon, AICHE J. 57 (2011) 346-358.https://doi.org/10.1002/aic.12280

[4] H. Moon, S.K. Kook, H.C. Park, Korean J. Chem. Eng. 8 (1991) 168-176.https://doi.org/10.1007/BF02706679

[5] C.O.M. Miller, C.W. Clump, AICHE J. 16 (1970) 169-172.https://doi.org/10.1002/aic.690160204

[6] At reaction temperatures, D_{eff} was expected to be higher than those measured here at near-ambient or temperatures slightly above room temperature.

APPENDIX III

III. Hydrodeoxygenation of phenol over metal supported niobia catalysts

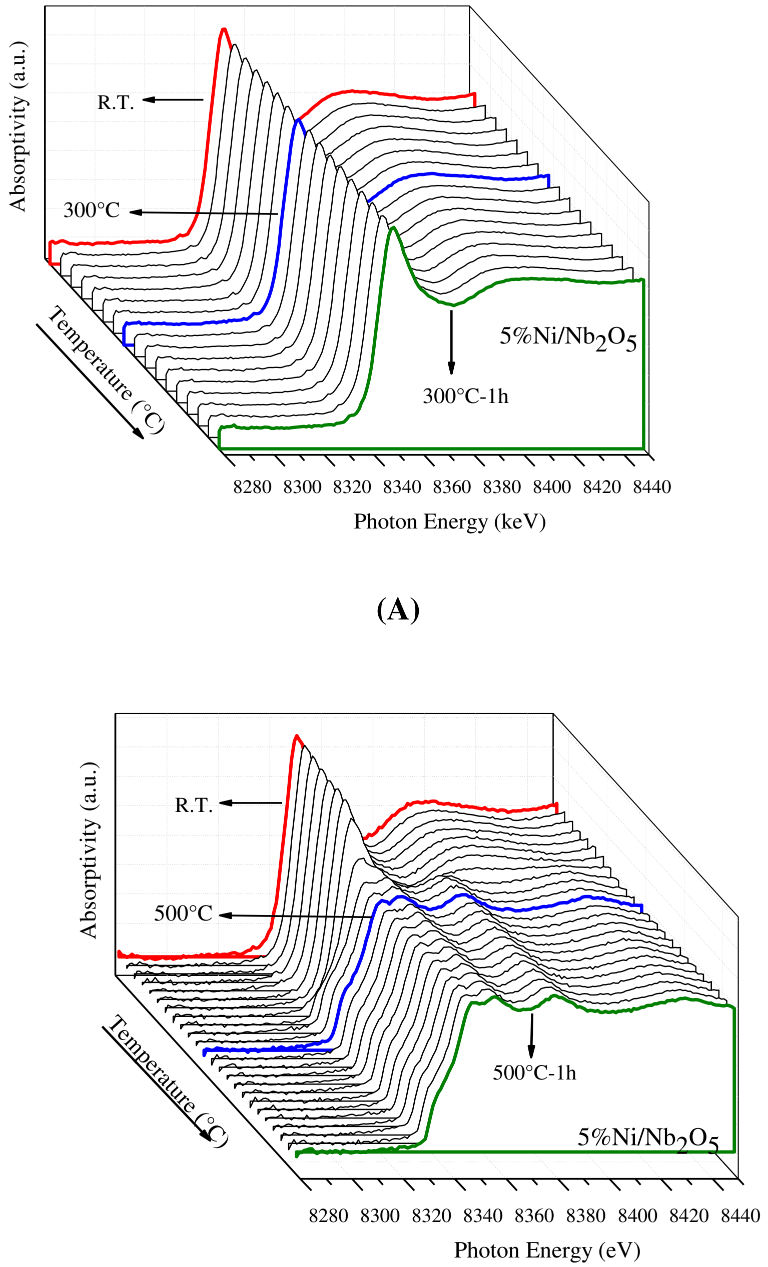

(A)

(B)

Figure S1. TPR-XANES profiles as a function of temperature at the (A) Ni K-edge – 300°C; (B) Ni-Kedge – 500°C.

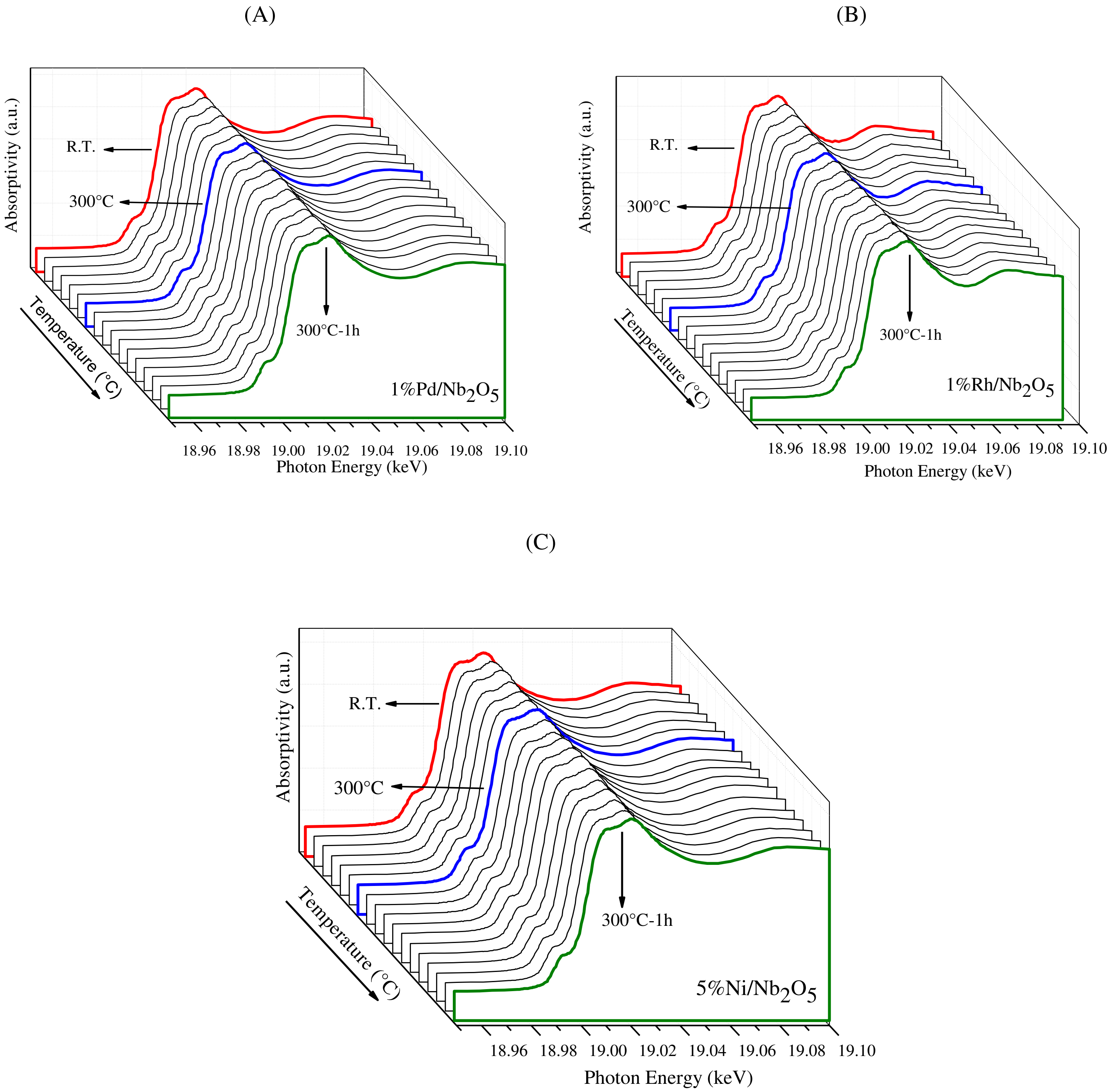

Figure S2. TPR-XANES profiles as a function of temperature up to 300°C at the Nb K-edge for (A) Pd/Nb_2O_5; (B) Rh/Nb_2O_5; (C) Ni/Nb_2O_5.

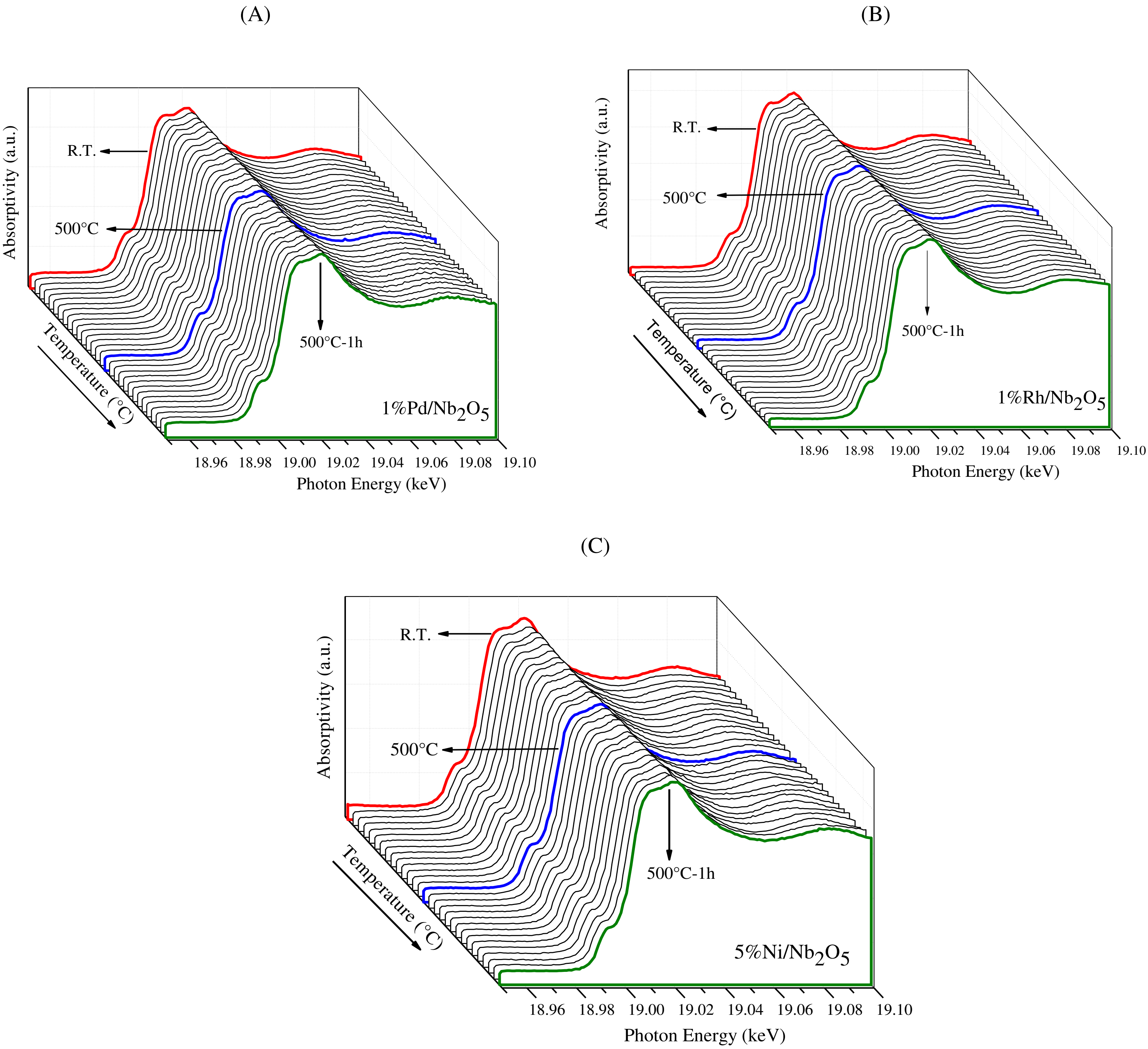
(A)

(B)

(C)

Figure S3. TPR-XANES profiles as a function of temperature up to 500°C at the Nb K-edge for (A) Pd/Nb_2O_5; (B) Rh/Nb_2O_5; (C) Ni/Nb_2O_5.

APPENDIX IV

IV. Hydrodeoxygenation of phenol over doped cerium oxide: The effect of niobium addition

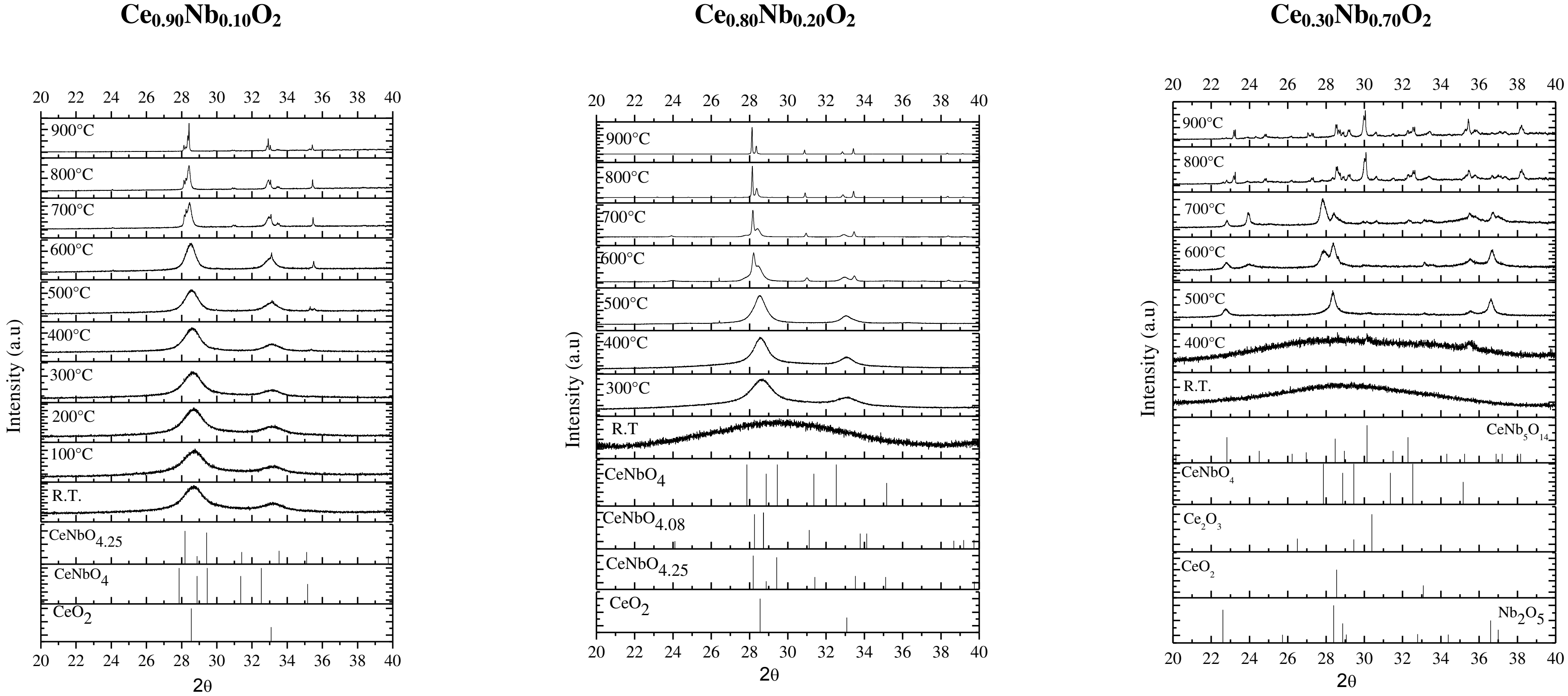

Figure 1S: XRD diffractogram for in situ calcination of $Ce_{0.9}Nb_{0.1}O_2$, $Ce_{0.8}Nb_{0.2}O_2$ and $Ce_{0.30}Nb_{0.70}O_2$ at different temperatures in He (inert atmosphere).

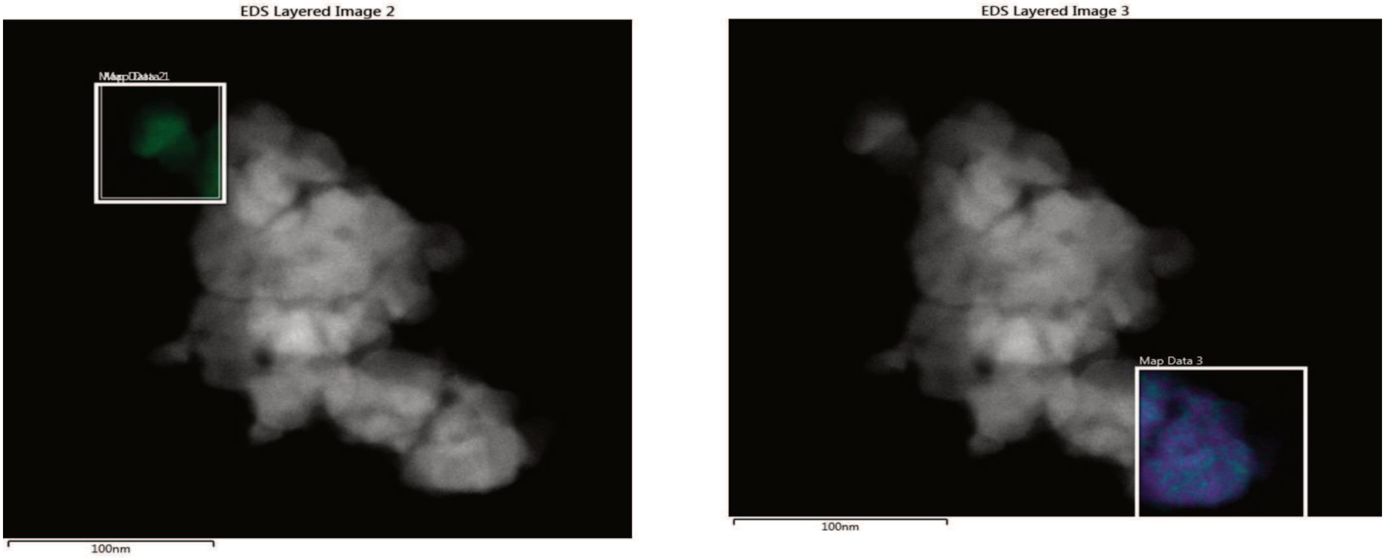

Figure 2S: TEM/EDS analysis of $Ce_{0.30}Nb_{0.70}O_2$